ION BEAM EXTRACTION FROM ELECTRON CYCLOTRON RESONANCE ION SOURCES AND THE SUBSEQUENT LOW ENERGY BEAM TRANSPORT

By

Daniel Winklehner

A DISSERTATION

Submitted to
Michigan State University
in partial fulfillment of the requirements
for the degree of

Physics - Doctor of Philosophy

2013

ABSTRACT

ION BEAM EXTRACTION FROM ELECTRON CYCLOTRON RESONANCE ION SOURCES AND THE SUBSEQUENT LOW ENERGY BEAM TRANSPORT

By

Daniel Winklehner

Electron Cyclotron Resonance Ion Sources (ECRIS) are capable of delivering high currents of Highly Charged Ions (HCIs) to heavy ion accelerators (e.g.: to the future FRIB). The use of a sextupole magnet for confinement of the plasma inside the source imposes a unique triangular structure on the beam. This, together with the multitude of ion species that are extracted at the same time and the high axial magnetic field at the plasma aperture, resulting from additional confining solenoids, make the simulation and design of ECRIS extraction systems particularly challenging. The first objective of this thesis was to refine and test a semi-empirical simulation model of the formation and extraction of HCIs from ECR ion sources as well as their transport through the subsequent Low Energy Beam Transport (LEBT) system. To this end, a set of utility functions was written to simplify performing the simulations.

In the LEBT system, another interesting, yet so far unanswered, question arises: The influence of space-charge effects on the beam and the level of space-charge compensation in the ECRIS beam line.

This interesting topic quickly became the second main objective of the thesis. A Retarding Field Analyzer (RFA) was built and systematic measurements of the neutralization level in ECRIS LEBT systems were done for the first time as part of this thesis (this intensity and pressure regime was previously not well explored). The measured neutralization levels for typical ECRIS beams were found to be between 0 and 50 % and agreed reasonably well with

a simple formula developed by Gabovich *et al.* for highly neutralized proton and H^- beams after it was re-derived and extended in this thesis for low neutralization and multiple species. Preliminary tests of the refined and integrated simulation model for the ECR ion sources VENUS and SuSI and their respective low energy beam transport systems include comparisons of measured beam currents, cross sections and emittances with the simulation results. These tests suggest that the model is suited for the simulation of ion beam extraction and transport for medium to high charge states of medium to heavy ions, but not for the lowest charge states and lightest ions (He^{1+}, protons).

Finally, as an example application of the developed software, a variable-energy (300 kV - 3 MV) electrostatic accelerator was simulated and redesigned for the DIANA project, a new proposed underground laboratory for nuclear astrophysics.

Dedicated to my grandmother, Dr. Sigilde Kösner.

ACKNOWLEDGMENTS

First and foremost I would like to express my gratitude towards my adviser Daniela Leitner. She was always there to discuss ideas and answer my questions. It was a pleasure working with her.

I would further like to thank my guidance committee for their support: Phillip Duxbury, Felix Marti, Michael Syphers, and Kirsten Tollefson.

A lot of this thesis would not have been possible without the help of the many people doing exceptional work here at the NSCL. These include, but are not limited to, the members of the ECR group: Guillaume Machicoane, Dallas Cole, Larry Tobos, and Alain Lapierre, people from the machine shop: Jay Pline and Susan LeCureux, and Ghulam Mujtaba of the electronics department.

Furthermore, I would like to thank Dave Grote, and Damon Todd for their help with WARP.

I would also like to thank Janilee Benitez, Markus Strohmeier, and Claude Lyneis for their support during my time in Berkeley.

There were many people participating in the DIANA collaboration, and it was a pleasure working with all of them. I would especially like to thank Manoel Couder and Alberto Lemut, with whom I worked closest, for the great teamwork and fun times.

My office mates Vincent Bader, Michael Bennett, and Michael Jones were a true source of inspiration (work related and otherwise) during my time at MSU. I will miss our friendly banter.

Last but not least, I would like to thank my family for their continuous support. Amélie, Birgit, Brigitte, Grete, Lucia, Robert, Sigilde, Stefanie, Valentin, I am looking forward to spending more time with you soon!

TABLE OF CONTENTS

LIST OF TABLES

LIST OF FIGURES

KEY TO SYMBOLS AND ABBREVIATIONS

A .... Atomic mass number (sum of neutrons and protons in the nucleus of an atom)

amu .... Atomic mass unit (1/12 of the mass of $^{12}C \approx 1.661 \cdot 10^{-28}$ kg)

ARTEMIS .... A roomtemperature ECRIS (at NSCL)

β .... Relativistic factor beta ($\beta = speed/c$)

c .... Speed of light in vacuum ($\approx 3 \cdot 10^8$ m/s)

DIANA .... Dual Ion Accelerators for Nuclear Astrophysics

e .... Elementary charge ($\approx 1.602 \cdot 10^{-19}$ C)

ϵ_0 .... Vacuum permittivity ($\approx 8.854 \cdot 10^{-12}$ F/m)

ECR(IS) .... Electron Cyclotron Resonance (Ion Source)

eμA .... Electrical micro-Amperes (10^{-6} C/s)

emA .... Electrical milli-Amperes (10^{-3} C/s)

γ .... Relativistic factor gamma ($\gamma = 1/\sqrt{1-\beta^2}$)

IGUN .... A ion source extraction simulation code

K-V .... Kapchinsky-Vladimirsky, a special particle distribution

LBNL .... Lawrence Berkeley National Laboratory

LEBT .... Low Energy Beam Transport (System)

NEC .... National Electrostatics Corporation

NeMo .... Neutralization Monitor, the RFA used in this thesis

NSCL .... National Superconducting Cyclotron Laboratory

PDR .... Preliminary Design Report

pμA .... Particle micro-Amperes (10^{-6} particles/s) pmA .... Particle milli-Amperes (10^{-3} particles/s)

PIC .... Particle-In-Cell, a simulation method

q .... Charge-State (number of electrons missing for neutrality in an atom)

RGA .... Residual Gas Analyzer

RFA .... Retarding Field Analyzer

SOR .... Successive Over-Relaxation, a finite difference method for fieldsolves

SuSI .... Superconducting Source for Ions (at NSCL)

VENUS .... Versatile ECR ion source for NUclear Science (at LBNL)

WARP .... A particle-in-cell simulation code

Z .... Atomic number (number of protons in the nucleus of an atom)

Chapter 1

Introduction

1.1 General Introduction

Since their inception in 1965 [14, pp. 313] electron cyclotron resonance ion sources (ECRIS) have been a field of rapid development. Their ability to produce very high charge state ions of virtually any element make them the injector of choice for many heavy ion accelerator facilities. A few examples are: the 88" Cyclotron at Lawrence Berkeley National Laboratory, the Coupled Cyclotron Facility at Michigan State University or the Facility for Rare Isotope Beams (FRIB) [15] under construction also at Michigan State University. Over time, the demand for more beam current has grown and today's third generation ECRIS are capable of delivering many emA of total extracted beam current and several hundreds of eμA of analyzed currents per species. However, facilities like FRIB already push the performance limits of third generation ECRIS, and it stands to reason that in the future we will need to continue the development of ECR ion sources. In his book '*Electron Cyclotron Resonance Ion Sources and ECR plasmas*' Richard Geller presented simple *scaling laws* stating that the charge state and beam currents extractable from ECR ion sources could be increased by going to higher magnetic field strengths and higher microwave frequencies [14, pp. 394]. A hypothesis that, over the last decades, proved to be reasonably valid, and today efforts are in place to develop a fourth generation ECRIS that will run at the highest fields and frequencies yet, promising further increase in delivered beam current [16, 17]. Of course, many other aspects of ECRIS physics influence the maximal achievable charge state, beam intensities, and stability. Some of those are: Coupling of radio frequency microwaves into the ECR plasma [18,19], the plasma dynamics inside the source in the presence of microwave heating and strong magnetic fields [20,21], the exact structure of the magnetic confinement field [14], gas mixing [14,22], and the position of the extraction aperture [22,23]. In pulsed mode, preglow [24,25] and afterglow [26,27] effects were discovered, which can increase the beam intensity for a brief period. In addition, many detailed studies have been performed including, but not limited to: Precision measurements of the beam energy to determine the plasma potential [28], X-ray measurements [29,30], and measurements of the plasma energy density with a diamagnetic loop [30]. Some of these results will be mentioned in Section 2.2 and chapter 6, but going into the details would go far beyond the scope of this thesis. Instead I will concentrate on the subjects of ion beam extraction and low energy beam transport. At the presently achievable beam intensities, space charge (the repulsion of neighboring beam particles due to their own electric fields) can become an important factor for the *low energy beam transport (LEBT)*. In the case of ECR ion sources, the LEBT has two major functions:

- The transport of the beam with minimal losses and degradation of the beam quality.
- The selection of the desired ion species from the number of species provided by the source.

A very important design tool both for the extraction systems and the LEBT are ion beam transport simulations. However, the simulation of ion beam extraction from an ECRIS plasma is not straight-forward and there are several challenges to overcome:

1. Modeling the extraction process from the plasma itself. This includes considering the plasma electrons, the current density of the extracted ions, and the applied electrostatic

fields which, together, lead to the formation of a plasma meniscus.

2. Modeling the extraction and transport of a multitude of different ion species with different masses and charge states.

3. Modeling the extraction from a region of high longitudinal magnetic field, which introduces an increase in emittance.

4. Taking into account the non-rotationally symmetric beam due to the radial confinement sextupole field in ECR ion sources.

And for the beam transport through the LEBT we have to consider:

5. The asymmetric beam from the extraction simulation.

6. Space charge and space charge compensation in the LEBT.

7. Realistic electrostatic and magnetostatic field maps for the beam optics elements.

Item 1. has been studied extensively in the past and a one dimensional model for the plasma sheath region in the source aperture was developed [31] which could be implemented in computer codes like IGUN [31–33] to successfully simulate the extraction of rotationally symmetric beams from plasma ion sources. Later, simulation codes like IGUN also included items 3 and 4, multi-species extraction and magnetic fields. 3D codes like IBSimu [34], KOBRA3 INP [35] and WARP [36] are now able to include 3D field maps for the electrostatic and magnetostatic fields and one can define arbitrary initial particle distributions. However, the exact spatial and velocity distributions for those initial conditions are still a matter of debate and while the aforementioned plasma simulations can provide some insight, no satisfying solution has been found yet.

In this thesis, I will use a semi-empirical model for the 3D extraction of highly charged ions from an ECRIS using the particle-in-cell code WARP. I will investigate the influence of the extraction of up to 30 different ion species at the same time on the beam dynamics in the extraction system and the beginning of the LEBT.

I will furthermore investigate the level of space charge compensation (interchangeably also called 'space charge neutralization' or simply 'neutralization') in the LEBT of an ECRIS both theoretically and experimentally. The particle distributions obtained from the extraction simulations will then be used as initial conditions for the simulation of the beam transport in the LEBT with neutralization determined by the results of the space charge investigation. Beam diagnostic devices like emittance scanners and beam viewers will be used in experiments to compare the actual measured beam properties of the ECR ion sources VENUS [3, 8, 37] and SuSI [38–40] to the simulations to investigate the applicability of the two models for ECR extraction and space charge compensation for typical ECRIS ion beams.

At the end of the thesis, I will present a practical example of how the developed software and the information from the LEBT studies can be put to use: The high energy electrostatic accelerator of the DIANA project, which has recently completed the preliminary design report (PDR) phase.

1.2 Structure Of The Thesis

Following LaTeX convention, the thesis is structured in *Chapters, Sections,* and *Subsections* and references to these will be labeled thus.

In accordance with the general introduction presented in the preceding section, this thesis will focus on three main topics related to the understanding of the physics and engineering challenges involved with ECRIS beam extraction and the subsequent LEBT:

- Ion extraction from an ECRIS and beam transport: Theory and simulations compared to measurements.
- Space charge and space charge compensation: Theory and measurements.
- The DIANA project: A practical example of a small ECRIS used as the injector source of an electrostatic accelerator.

These three topics are highly convoluted, because space charge has to be included in any realistic simulation effort of beams in the mA current regime. How strong its influence is depends on beam current and space charge compensation, thus space charge compensation becomes an important parameter in the simulations. At the same time, simulations have been performed to confirm the beam parameters (e.g. beam cross section) during the space-charge compensation measurements. Consequently, no individual treatment is possible. Instead a structure has been chosen in which the more general topics are treated first (chapters *2-Theory, 3-Software, 4-Hardware*), followed by detailed chapters on the three topics described above (chapters *5-Space-Charge Compensation Measurements, 6-3D ECR Extraction Model*, and *7-An Example Application: DIANA*) with frequently given references between chapters.

1.3 Conventions Used In This Work

1.3.1 Units

Mostly, I will use the International System of units (SI - *Le Système international d'unités*) in this thesis. The most noticeable exception being the pressure which will generally be given in *Torr* (1 Torr = 133.322 Pa). Also, sometimes it is more intuitive to use the metric sub-unit of a base unit (e.g. mm instead of m for a beam diameter), which I will do freely. Values cited from other works might not be in SI units, either. In all cases, it will be clearly labeled which unit is used. If no units are given, SI units should be assumed (this is mostly the case for presented formulae).

1.3.2 Emittance

Throughout the thesis, I will mostly use the *normalized rms emittance* ϵ_{n-rms} and make clear whenever I use one of the other definitions (e.g. for comparison with literature, other experiments, etc.). See Section 2.1.3 for more information on emittance.

1.3.3 Brightness

In the rare cases I will use brightness (a figure of merit for the beam quality that includes the total beam current) to characterize the beam, it will be a *fractional brightness* including the fraction of the beam encompassed (e.g. $B_{90\%}$ - including 90% of the beam current) See Section 2.1.3 for more information on brightness.

Chapter 2

Theory

2.1 Charged Particle Beams

In this section I will introduce the basic principles of the physics of charged particle beams. However, the fundamentals will only be reviewed briefly and only where it is necessary and helpful in understanding the more specific concepts related to ECR ion sources and low energy, heavy ion beams. Very good treatments of ion beam physics and accelerator physics can be found in textbooks on the topics [41–45] and the descriptions in the following subsections (2.1.1 - 2.1.4) follow the discussion presented in those references.

2.1.1 Equations of motion

The motion of an individual charged particle (charge $q \cdot e$, mass m) due to the *Lorentz force* is governed by *Newton's equation of motion*:

$$\frac{d\vec{P}}{dt} = qe(\vec{E} + \vec{v} \times \vec{B}) \tag{2.1}$$

with $\vec{P}$ the mechanical momentum, $\vec{E}$ and $\vec{B}$ the electric and magnetic fields, and $\vec{v}$ the particle's velocity vector. With

$$\vec{P} = \gamma m \vec{v}$$

we can write the three components of equation 2.1 in Cartesian coordinates:

$$\frac{d}{dt}(\gamma m\dot{x}) = \dot{\gamma}m\dot{x} + \gamma m\ddot{x} = qe(E_x + \dot{y}B_z - \dot{z}B_y) \tag{2.2a}$$
$$\frac{d}{dt}(\gamma m\dot{y}) = \dot{\gamma}m\dot{y} + \gamma m\ddot{y} = qe(E_y + \dot{z}B_x - \dot{x}B_z) \tag{2.2b}$$
$$\frac{d}{dt}(\gamma m\dot{z}) = \dot{\gamma}m\dot{z} + \gamma m\ddot{z} = qe(E_z + \dot{x}B_y - \dot{y}B_x) \tag{2.2c}$$

and in cylindrical coordinates $\vec{r} = (r, \theta, z)$, $\vec{v} = (\dot{r}, r\dot{\theta}, \dot{z})$:

$$\frac{d}{dt}(\gamma m\dot{r}) - \gamma m r\dot{\theta}^2 = qe(E_r + r\dot{\theta}B_z - \dot{z}B_\theta) \tag{2.3a}$$
$$\frac{1}{r}\frac{d}{dt}(\gamma m r^2\dot{\theta}) = qe(E_\theta + \dot{z}B_r - \dot{r}B_z) \tag{2.3b}$$
$$\frac{d}{dt}(\gamma m\dot{z}) = qe(E_z + \dot{r}B_\theta - r\dot{\theta}B_r) \tag{2.3c}$$

where the dot is equivalent to d/dt.

2.1.2 Particle Distributions

Let us consider the beam as an ensemble of particles, moving in largely the same direction. Each individual particle can be described by the three spatial coordinates (x, y, z) and the mechanical momentum coordinates (p_x, p_y, p_z). The beam can then be characterized by the six-dimensional distribution function

$$f(x, y, z, p_x, p_y, p_z, t) \tag{2.4}$$

which defines the beam in six-dimensional phase space. If z is the direction of propagation of the beam, we can assume $p_z \gg p_x, p_y$. This is called *paraxial approximation.* Simply put, it means the velocity component in direction of propagation (z) is much larger than the transversal velocity component (tightly connected to the *transversal temperature* of the beam), which is usually the case. We can use z instead of t as the independent variable and approximate the angles (x', y') of the particle trajectories with the beam axis (sometimes referred to as *design trajectory*) as: $x' = dx/dz \approx p_x/p_z = v_x/v_z$ and $y' \approx v_y/v_z$ (note that for non-relativistic beams $p_{x,y} = mv_{x,y}$). Thus we can express the four-dimensional distribution function for the transversal phase space as

$$f(x, y, x', y') \tag{2.5}$$

2.1.2.1 Liouville's theorem

Liouville's theorem states that the volume of a given number of particles in phase space is constant. If $n(x, y, z, p_x, p_y, p_z, t)$ is the six dimensional phase space density, this can be expressed as

$$\frac{dn}{dt} = 0 \tag{2.6}$$

or alternatively:

$$\iint d^3q d^3p = \text{const.} \tag{2.7}$$

if only conservative forces are present. This is going to be important shortly, when emittance is introduced. If there is no coupling between longitudinal and transversal motion, Liouville's theorem also holds for the four-dimensional transversal subspace and without coupling between the two transversal planes, it even holds for each of the two-dimensional horizontal and vertical subspaces separately:

$$\iiiint dxdydx'dy' = \text{const.}, \quad \iint dxdx' = \text{const.}, \quad \iint dydy' = \text{const.}$$

2.1.2.2 Transversal distribution

Restricting ourselves to paraxial, DC beams, we are mainly interested in the transversal phase-space distribution $f(x, y, x', y')$. In [41] Reiser presents a self-consistent theory for beams with finite velocity spread based on the Vlasov model [46] for systems for which the Liouville theorem holds and collisions between particles can be neglected. The simplest and probably best known solution to the self-consistent model is the *Kapchinsky-Vladimirsky (K-V)* distribution [47]:

$$f(x, y, x', y') = f_0 \cdot \delta \left(\frac{x_b^2 x'^2 + \sqrt{x'^2_b x_b^2 - \epsilon_x^2}\, xx' + x'^2_b x^2}{\epsilon_x^2} + \frac{y_b^2 y'^2 + \sqrt{y'^2_b y_b^2 - \epsilon_y^2}\, yy' + y'^2_b y^2}{\epsilon_y^2} - 1 \right) \tag{2.8}$$

with x_b, y_b the maximum beam extent (b for 'beam') in x and y directions, x'_b, y'_b the maximum angles, and ϵ_x, ϵ_y the (full) beam emittances, which will be discussed shortly. This distribution uniformly fills the surface of the four-dimensional hyper-ellipsoid in the transversal phase-space (note the delta function). It has the interesting property that each projection into one of the two-dimensional subspaces (x-y, x-x', x-y', y-y', y-x' x'-y') is a uniformly filled ellipse.

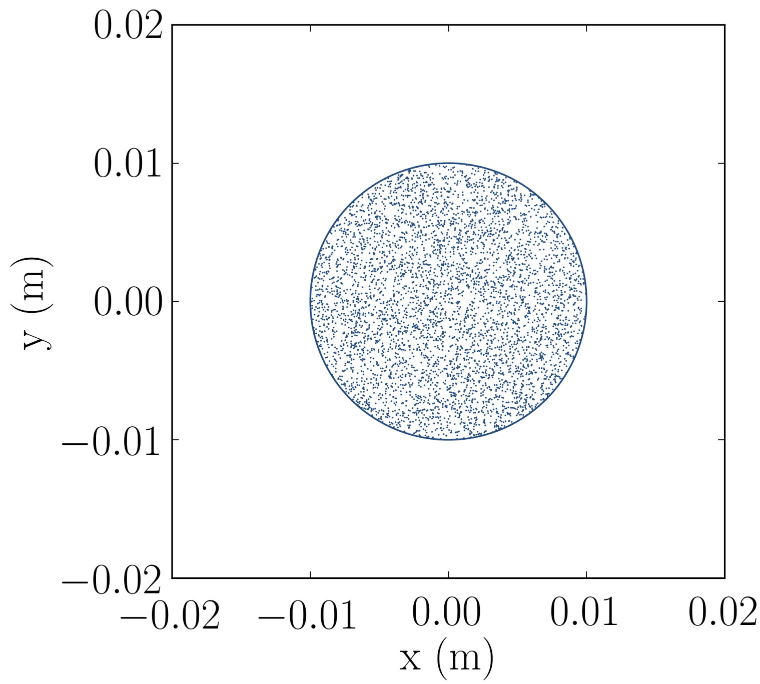

Figure 2.1: Beam cross-section of a K-V distribution. For interpretation of the references to color in this and all other figures, the reader is referred to the electronic version of this dissertation.

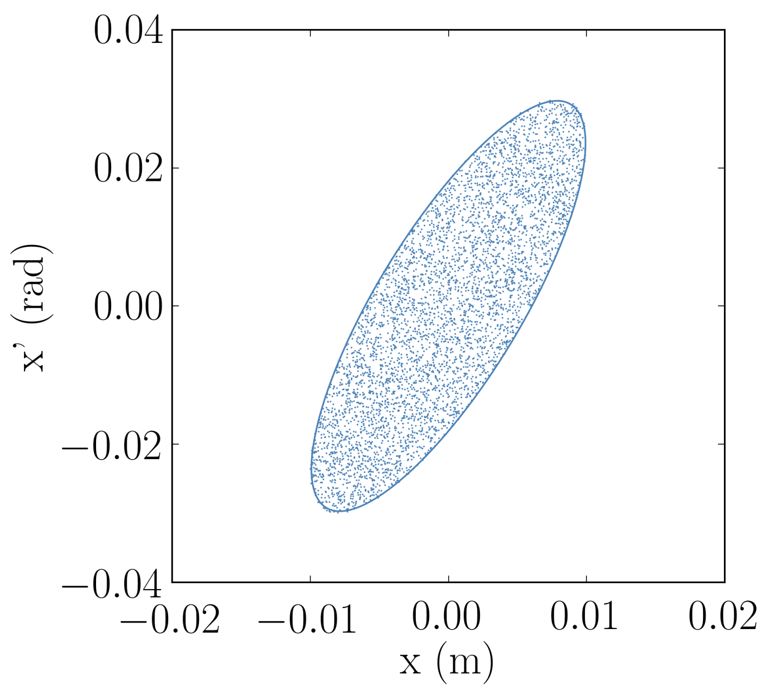

Figure 2.2: Two-dimensional transversal subspace (x-x') of the phase space of a K-V distribution.

In Figures 2.1 and 2.2 the cross-section and x-x' phase-space for the K-V distribution are shown (arbitrary values for beam radius $x_b = y_b$, maximum divergence, and emittance were chosen). Note that in x-y space the beam extents in x and y direction do not necessarily have to be the same. An elliptical beam cross-section is the general form of the K-V distribution and the circular beam was chosen in 2.1 for convenience. The other important property of the K-V distribution is that it is the only solution to the self-consistent model that produces linear self-fields (see Subsection 2.1.4). Of course, other solutions to the Vlasov theory exist that are more realistic (e.g. *waterbag distribution*, *Gaussian distribution*) and if collisions between beam ions are included, a *Maxwell-Boltzmann distribution* turns out to best represent realistic beams. But, the K-V distribution can be used to examine basic properties of beams in transport systems with only horizontal and vertical focusing (electrostatic and magnetic quadrupoles, dipoles) or axially symmetric systems.

2.1.3 Emittance

Emittance and *brightness* of ion beams are values used for quantification of the beam quality. Intuitively, emittance can be understood as the product of beam size and beam divergence, thereby giving us an idea of the transportability of the beam. Brightness relates the beam intensity to the emittance. The *normalized emittance* is particularly helpful when comparing different ion sources and accelerators that operate at different beam energies. All of these will now be discussed in more detail. Generally, the emittance is defined as the phase space area (A) of the two-dimensional projections (x-x', y-y', x-y', y-x') divided by π, e.g.:

$$\epsilon_x = \frac{A_{xx\prime}}{\pi} \quad [\pi\text{-}mm\text{-}mrad] \tag{2.9}$$

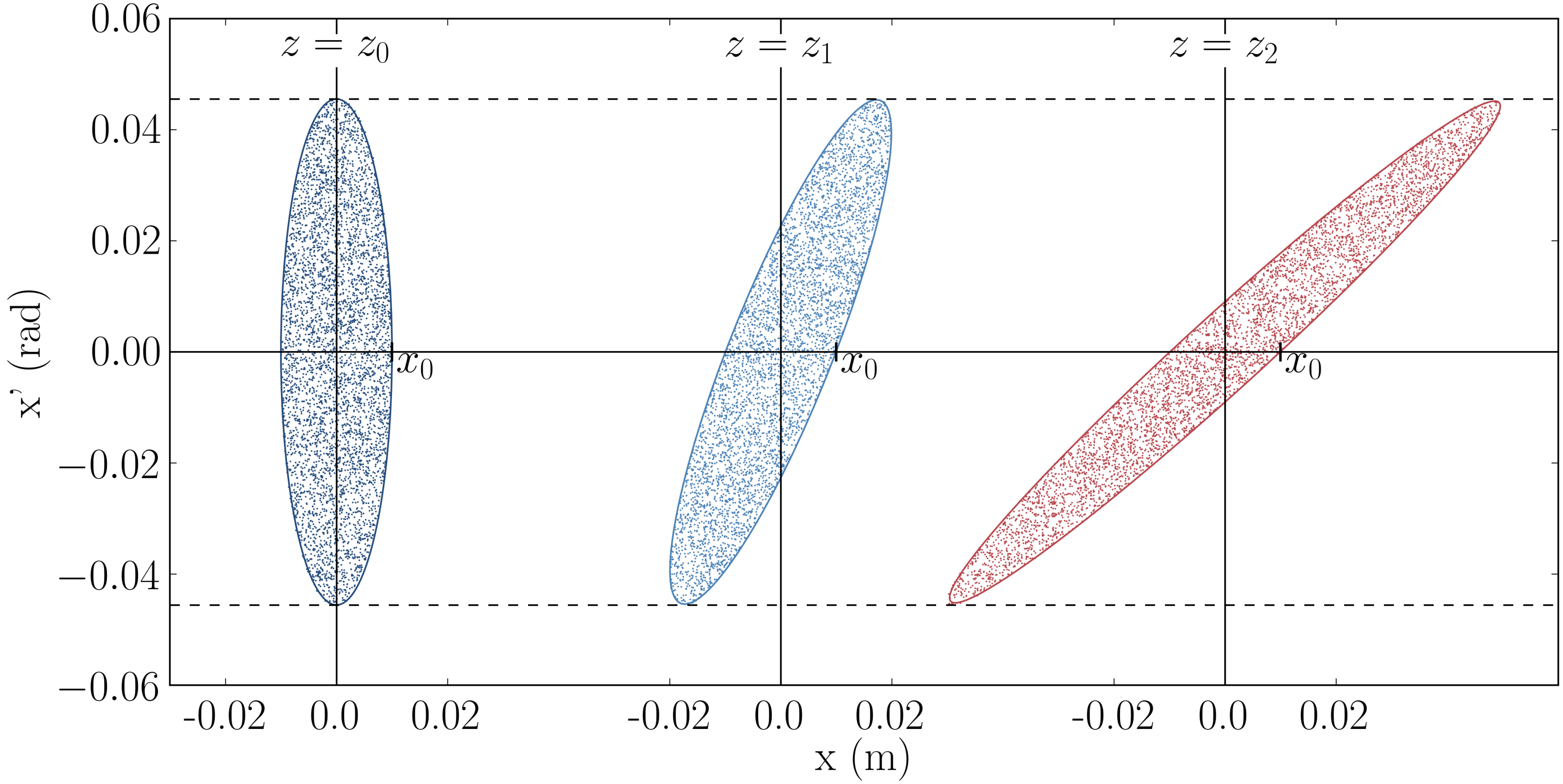

Figure 2.3: Phase space evolution of a K-V beam without space charge in drift space (no applied fields) for three different instances along the beam path (z). Note that the area of all three ellipses is constant, as is the maximum divergence angle x'_b. $x_0 = x_b(z = z_0)$.

This emittance is given in units of π-m-rad or π-mm-mrad. The π in the units is not to be taken as a factor π but as a reminder which definition of emittance is being used (there are others that do not divide by π). This is also the emittance used in the definition of the K-V distribution 2.8. Using Liouville's theorem, we immediately see that if only conservative forces are present the emittances ϵ_x and ϵ_y are conserved. If we allow coupling of the two transverse phase spaces, only the product of the two ($\epsilon_x \cdot \epsilon_y$) is conserved. The evolution of the x-x' phase space of a beam for three different positions along the z-axis (three moments in time) is shown in Figure 2.3. There are no applied fields and no self-fields and the area of the ellipse (and thus the emittance) as well as the divergence are constant. The initial upright ellipse represents a waist in the beam, i.e. the outermost angles $(\pm x_b)'$ - not to be confused with the maximum angles x_b' - are zero. Unfortunately, real beams rarely have perfect elliptical phase spaces. Distortions can be introduced into the beam by the ion source itself, or by fringe fields and higher order aberrations in the focusing elements. Figure 2.4 shows phase space distortions of an originally K-V beam, due to spherical aberrations in a periodic focusing channel. In accordance with Liouville's theorem, the actual area covered by the beam is still constant, but due to the filamentation, if we were to draw an ellipse around the beam that contained all the particles (100% of the beam current) the emittance would be artificially large. It is useful to introduce a new concept of emittance, that better reflects the physical situation of distorted beams: the *rms emittance*.

2.1.3.1 RMS Emittance

If $\langle x^2 \rangle$ is the second moment of our distribution $f(x, y, x', y')$; defined as:

$$\langle x^2 \rangle = \frac{\iiiint x^2 f(x, y, x', y') dx dy dx' dy'}{\iiiint f(x, y, x', y') dx dy dx' dy'} \tag{2.10}$$

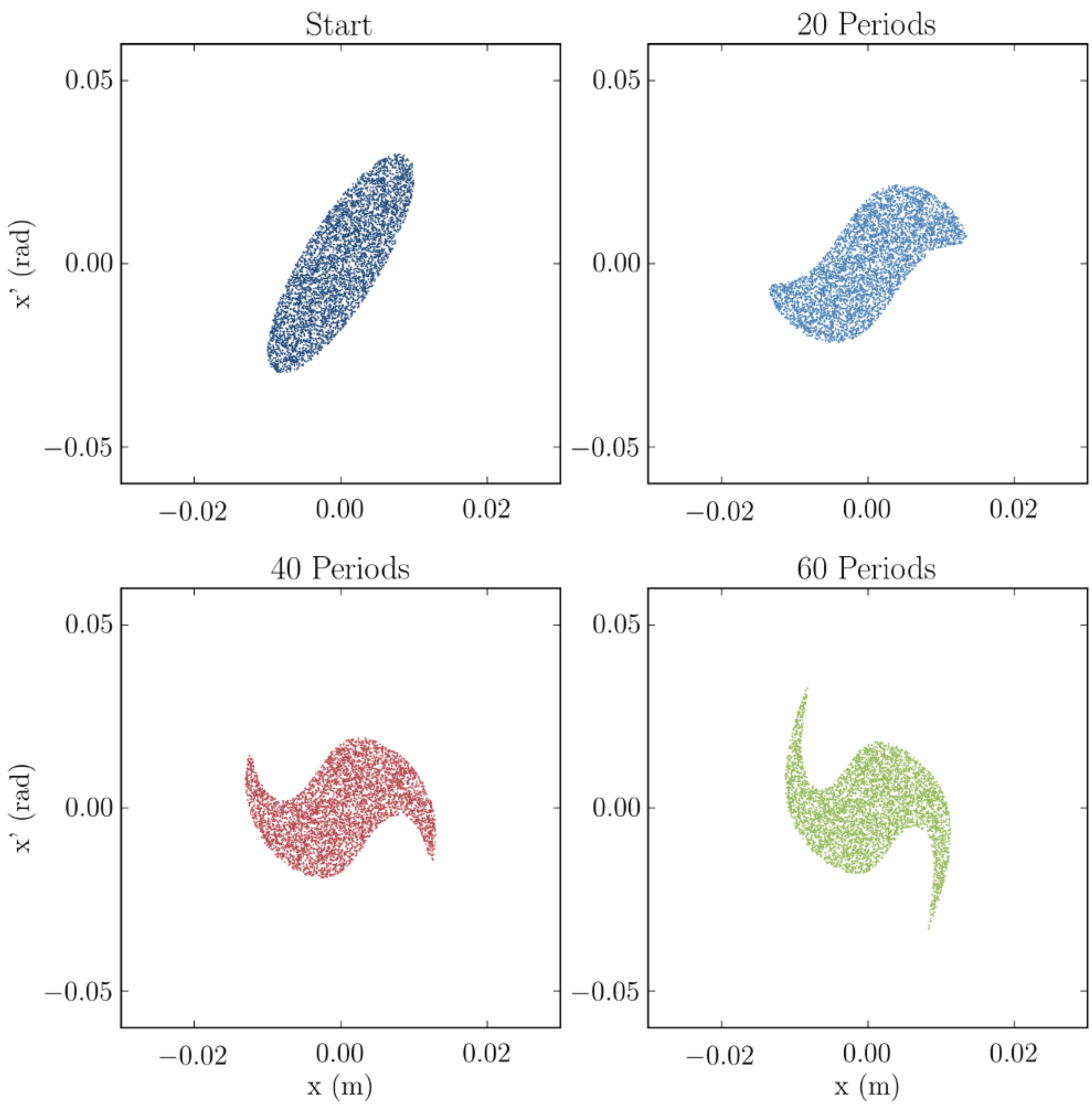

Figure 2.4: Phase space distortion due to spherical aberrations in a periodic thin lens focusing channel. Each period consists of a drift, a thin lens and another drift.

and analogous for $\langle x'^2 \rangle$ and $\langle xx' \rangle$, then the rms emittance can be defined as:

$$\epsilon_{rms} = \sqrt{\langle x^2 \rangle \langle x'^2 \rangle - \langle xx' \rangle^2} \quad [mm\text{-}mrad] \tag{2.11}$$

Because the rms emittance is a purely statistical value, we will use units of m-rad or mm-mrad without the π for ϵ_{rms}. It can be shown, that in the case of the K-V distribution $\epsilon_{x\text{-}full} = 4 \cdot \epsilon_{x\text{-}rms}$, exactly. For other distributions, like the *waterbag distributions* and the *Gaussian distribution* this factor varies from 6 to 16. It should also be noted that combinations of distributions are possible, like Gaussian in transversal direction and uniform in longitudinal direction. In practice, the beam density gets very low towards the outer regions of the Gaussian distribution and it does not make much sense to calculate the 'full' emittance. The same holds for otherwise distorted beams, like the ECRIS beams (as will be seen in Chapter 6). Many people including Reiser [41] have adopted a concept of *effective emittance* which is just $4 \cdot \epsilon_{x\text{-}rms}$. On the other hand, what we are really interested in, is not only the emittance, but to know how much beam current we can transport with a certain emittance. This can be expressed as a *brightness*.

2.1.3.2 Brightness

The brightness is commonly defined by

$$B = \frac{J}{d\Omega} = \frac{dI}{dSd\Omega} \tag{2.12}$$

as current density per unit solid angle. Or in case of the K-V distribution (and waterbag distribution as well)

$$\bar{B} = \frac{2I}{\pi^2 \epsilon_x \epsilon_y} \qquad \left[\frac{A}{m^2\text{-}rad^2}\right] \tag{2.13}$$

the emittances here are the full K-V emittances. As Reiser points out, sometimes the factor $2/\pi^2$ is left out or the rms emittance is used. It is thus very important to be clear and consistent in the definition and usage of emittance and brightness.

2.1.3.3 Fractional Emittance

From an experimentalist point of view, the practical thing to do is often to define an elliptical emittance contour, that envelopes a certain fraction of the beam current, e.g. 90%, and calculate the full emittance of the such defined sub-ensemble of particles (e.g. $\epsilon_{x\text{-}90\%}$). This contour should encompass 'most' of the beam. The brightness can then be defined as

$$B_{90\%} = \frac{2 \cdot 0.9 \cdot I}{\pi^2 \epsilon_{x\text{-}90\%} \epsilon_{y\text{-}90\%}} \tag{2.14}$$

If the beam has a very non-uniform distribution, the so obtained brightness will have a maximum at some percent beam current value. Above the maximum, the emittances increase faster than the current, thereby lowering the brightness. Below the maximum, the emittance decreases slower than the current , thereby lowering the brightness. This can be used as a figure of merit for the quality of the beam after 'cleaning it up' (e.g. collimators).

2.1.3.4 Normalized Emittance

In order for the phase space area (volume) to be invariant also under acceleration, the normalized emittance is defined as:

$$\epsilon_n = \beta \cdot \gamma \cdot \epsilon \tag{2.15}$$

with $\beta = v/c$ and $\gamma = 1/\sqrt{1-\beta^2}$ the relativistic factors. This definition is valid for rms emittance as well as effective or full emittance and lets us compare the quality of beams with different energies.

2.1.3.5 Normalized Brightness

Similarly we define the normalized brightness:

$$B_n = \frac{B}{\beta^2 \gamma^2} \tag{2.16}$$

The conventions for emittance and brightness used throughout this work are listed in the introduction in Section 1.3.

2.1.4 Self Fields

In the discussion of self-fields, it is useful to start out with a simple beam. Hence we will start with an axially symmetric K-V beam in cylindrical coordinates. This means that the paraxial condition applies ($v_r \ll v_b$, $v_\theta \ll v_b$, $v_z \approx v_b$ with v_b the overall beam velocity). At each longitudinal position z, the beam has the charge density $\rho(r, \theta, z)$ and velocity v_z. Associated with a distribution of charged particles is an electric field, the *self electric field*. On the other hand, because the charged particles are in motion, a current can be associated with the beam, which gives rise to a *self magnetic field*. Because the ions are of same sign charge, the self electric field is defocusing and a coasting, perfectly parallel (i.e. zero emittance) ion beam will start diverging given sufficient time. The self magnetic field on the other hand is focusing. It is useful to start the examination of the self fields' effects on the beam with a cylindrical beam. Following Reiser [41, pp. 170], we use the simplifications:

1. The beam cross-section is circular with a sharp edge at radius r_b inside a concentric beam pipe with radius r_p.

2. The beam radius changes slowly with z, so the paraxial assumption holds ($v_x \ll v_b$, $v_y \ll v_b$, $v_z \approx v_b$) and the radial magnetic field component B_r and axial electric field component E_z can be neglected.

3. The potential difference between beam center and drift tube wall is small compared to the voltage equivalent of the particle kinetic energy (several 10 kV).

4. The ion beam density ρ is uniform inside the beam and zero outside. The velocity of all particles is approximately the same (v_b) and therefore the current density is uniform inside the beam and zero outside.

We can then write the charge density as

$$\rho = \frac{I}{r_b^2 \pi v_b}$$

with I the beam current, and get the electric field (which has only a radial component) by application of Gauss's law:

$$E_r = \begin{cases} \frac{I \cdot r}{2\pi\epsilon_0 r_b^2 v_b} & \text{for } r \leq r_b \\ \frac{I}{2\pi\epsilon_0 r v_b} & \text{for } r > r_b. \end{cases} \tag{2.17}$$

By integrating, we obtain the electrostatic potential (assuming a grounded beam pipe, $\phi(r_p) = 0$):

$$\phi(r) = \begin{cases} \Delta\phi \left(1 + 2\ln\frac{r_p}{r_b} - \frac{r^2}{r_b^2}\right) & \text{for } r \leq r_b \\ \Delta\phi \; 2\ln\frac{r_p}{r} & \text{for } r_b \leq r \leq r_p \end{cases} \tag{2.18}$$

with

$$\Delta\phi = \frac{I}{4\pi\epsilon_0 v_b}. \tag{2.19}$$

The magnetic field (which has only an azimuthal component) is obtained by using Ampére's law:

$$B_\theta = \begin{cases} \mu_0 \frac{I \cdot r}{2\pi r_b^2} & \text{for } r \leq r_b \\ \mu_0 \frac{I}{2\pi r} & \text{for } r > r_b. \end{cases} \tag{2.20}$$

As an example, the electrostatic field and potential for a 0.5 mA oxygen beam of charge state $q = 5+$ is shown in Figure 2.5. The self magnetic field of such a low current, non-relativistic beam is negligible.

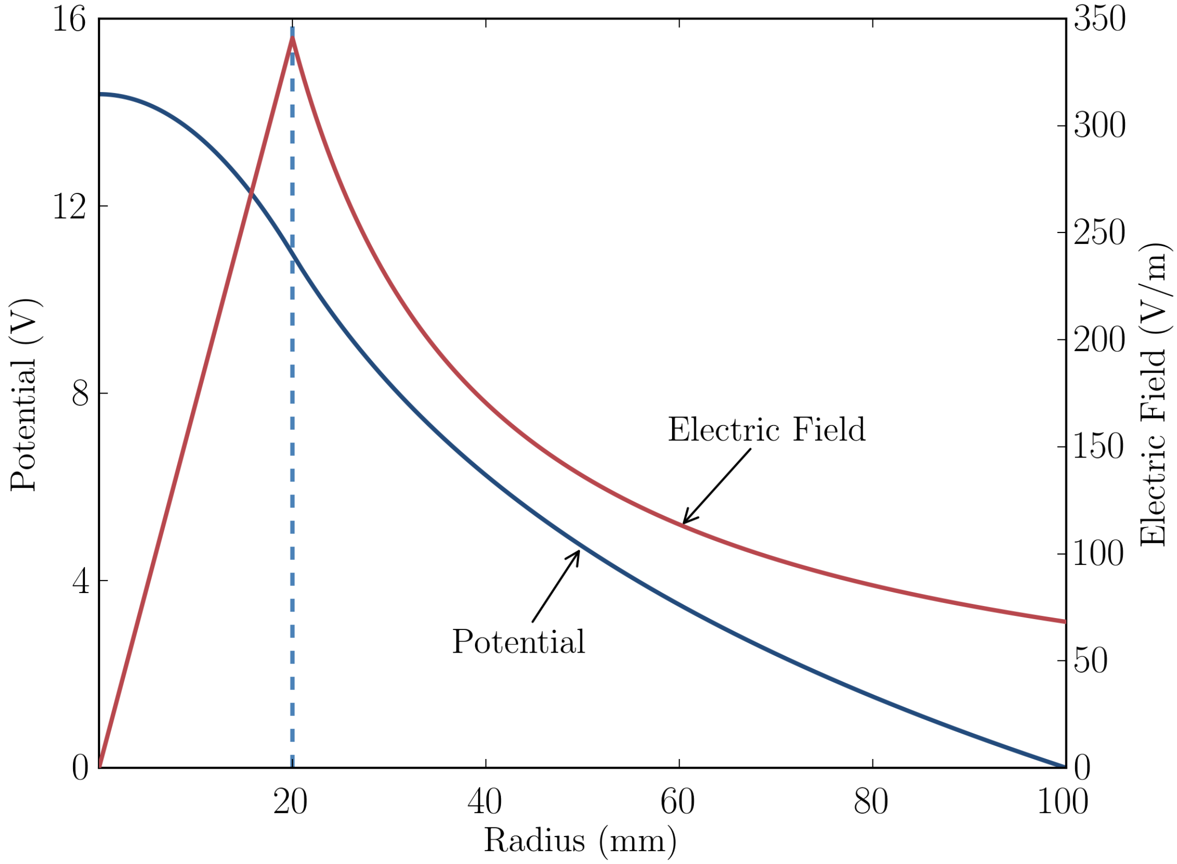

Figure 2.5: Radial beam potential and electrostatic self field of a round 0.5 mA $^{16}O^{6+}$ beam. Beam radius 20 mm, grounded pipe radius 10 cm.

Using the electric and magnetic self fields in the radial force equation 2.3a, Reiser derives the particle trajectory equation [41, p. 175] for a uniform, round beam in drift space:

$$\frac{\mathrm{d}^2 r}{\mathrm{d}z^2} = \frac{K}{r_b^2} r \tag{2.21}$$

with K the *generalized perveance*

$$K = \frac{2qeI}{4\pi\epsilon_0 m_b \beta^3 \gamma^3 c^3} \tag{2.22}$$

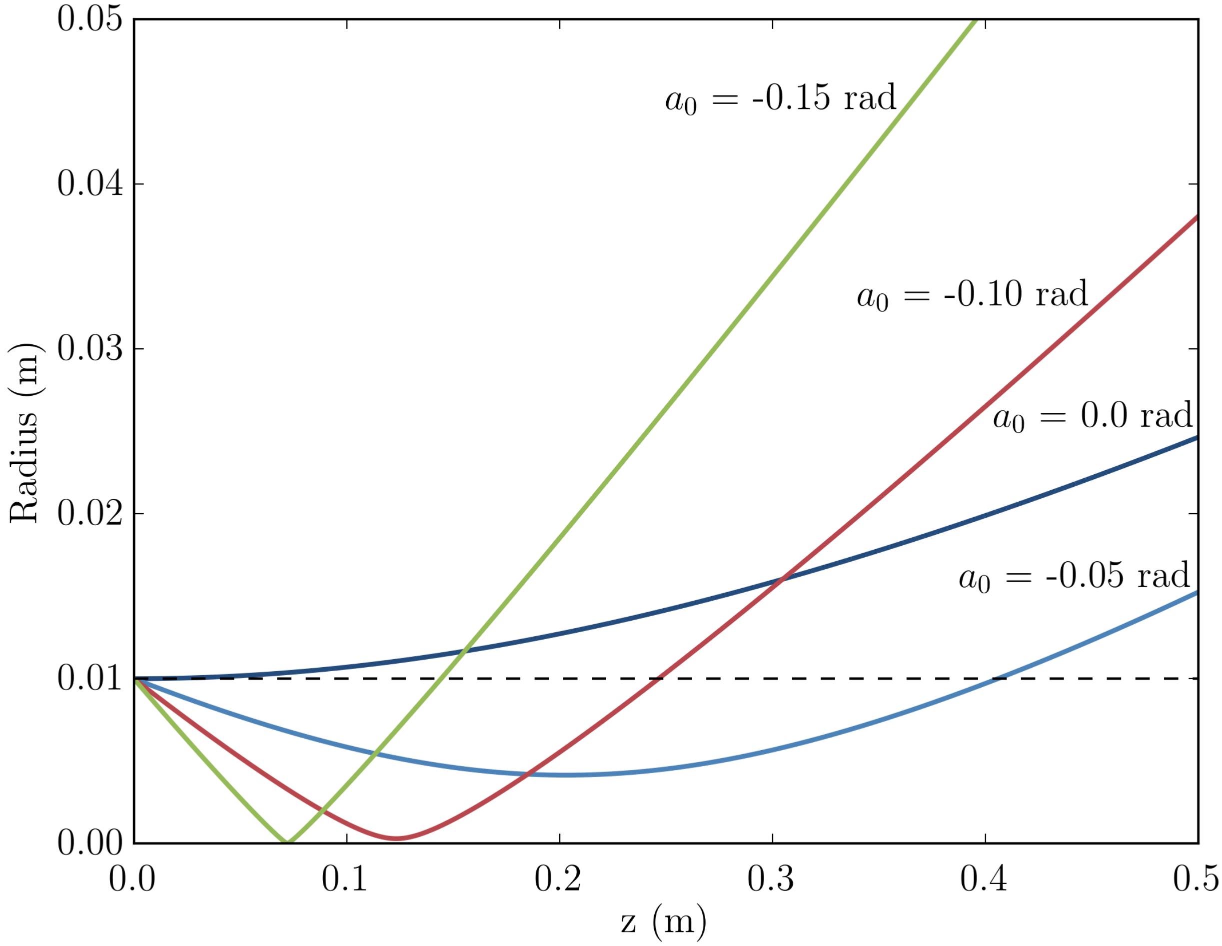

Figure 2.6: Solutions of the envelope equation for a 0.5 mA $^{16}O^{6+}$ beam in drift space for different initial angles $a_0 = r_b'(z = 0)$, initial radius $r_b(z = 0) = 10$ mm, and zero emittance. Note that in the K-V model the self-fields are linear in r and the emittance is constant.

which is connected to the generalized plasma frequency

$$\omega_p^2 = \frac{qeI}{\pi\epsilon_0 m_b c\beta\gamma^3 r_b^2} \tag{2.23}$$

by

$$K = \omega_p^2 \cdot \frac{r_b^2}{2\beta^2 c^2}. \tag{2.24}$$

The generalized perveance is a measure of the importance of space charge for the beam transport. Without space charge compensation, it is always positive, as can easily be seen

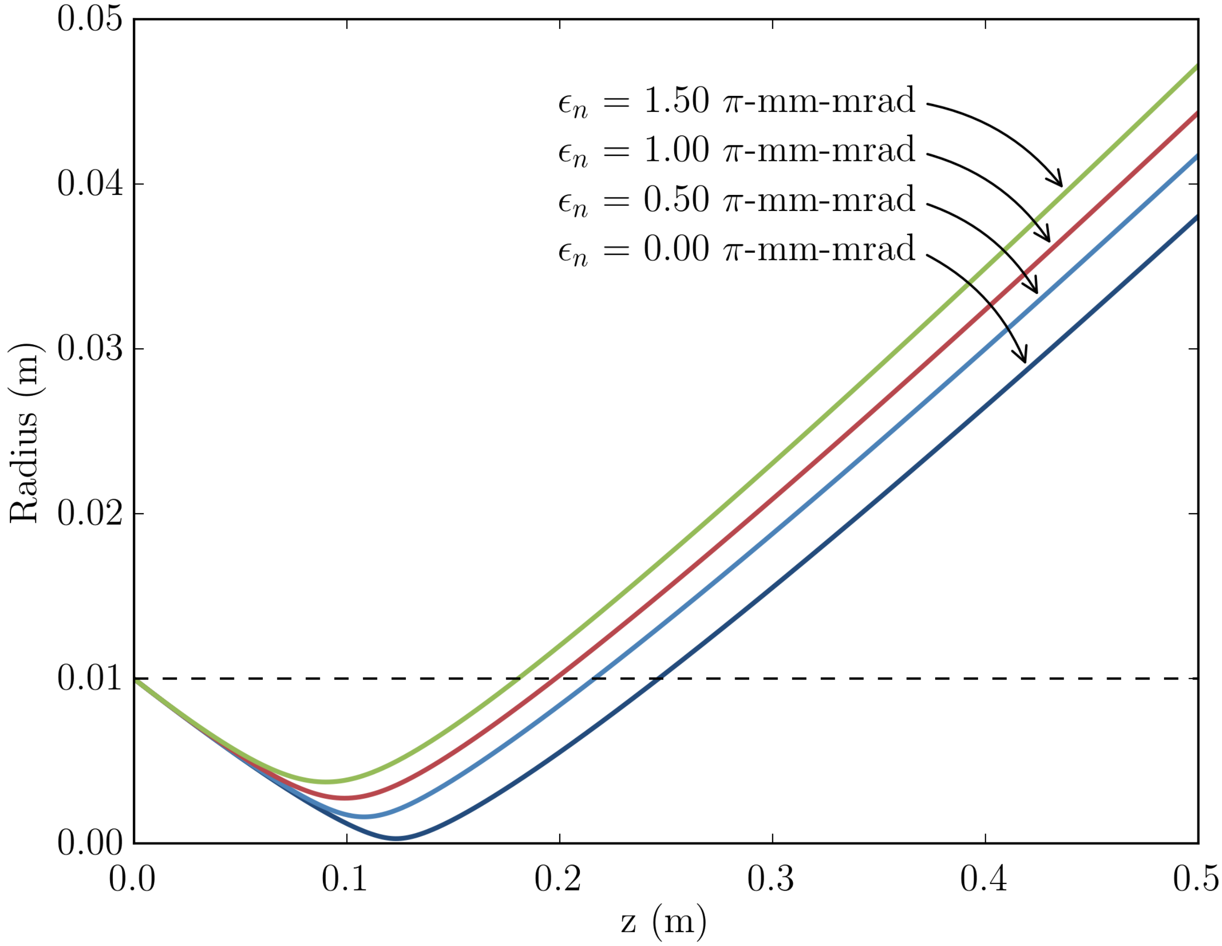

Figure 2.7: Solutions of the envelope equation for a 0.5 mA $^{16}O^{6+}$ beam in drift space for different emittances, initial radius $r_b(z = 0) = 10$ mm and initial angle -0.1 rad. The emittance shown here is the normalized full emittance of the beam ($\epsilon_n = 4\epsilon_{n-rms}$).

from equation 2.22 and thus the net effect of defocusing electric field and focusing magnetic field is a defocusing one. In the next subsection, we will see, that having stationary secondary particles of the opposite charge inside the beam envelope can lead to a net focusing effect. In order to solve equation 2.21, we need an expression for the beam radius. This is given by the beam envelope equation for a beam in drift space [41, p. 181]:

$$\frac{\mathrm{d}^2 r_0}{\mathrm{d}z^2} = \frac{\epsilon^2}{r_b^3} + \frac{K}{r_b} \tag{2.25}$$

with ϵ the beam emittance and $r_b(z)$ the envelope radius varying slowly in z. Depending on the magnitudes of ϵ and K, we speak of *emittance dominated* versus *space-charge dominated* beams. Equations 2.21 and 2.25 represent the equation of motion and envelope equation for the axially symmetric K-V model a drift and examples of the beam envelopes for different initial angles and different emittance values are shown in Figures 2.6 and 2.7, respectively. For completeness, the equations of motion for the more general K-V model of separated horizontal and vertical motion in linear external fields are:

$$x'' + \kappa_x(z)x - \frac{2K}{x_b(x_b + y_b)}x = 0 \tag{2.26a}$$

$$y'' + \kappa_y(z)y - \frac{2K}{y_b(x_b + y_b)}y = 0 \tag{2.26b}$$

with $\kappa_x(z)$ and $\kappa_y(z)$ the focusing functions representing the external fields, and x_b and y_b the semi-axes of the beam cross-section ellipse. $\kappa_x(z)$ and $\kappa_y(z)$ are defined solely by the lattice of the accelerator (the magnets and electrostatic elements used for focusing and bending). x_b and y_b have to be determined from the envelope equations:

$$x_b'' + \kappa_x(z)x_b - \frac{2K}{(x_b + y_b)} - \frac{\epsilon_x^2}{x_b^3} = 0 \tag{2.27a}$$

$$y_b'' + \kappa_y(z)y_b - \frac{2K}{(x_b + y_b)} - \frac{\epsilon_y^2}{y_b^3} = 0 \tag{2.27b}$$

This set of 2×2 coupled differential equations is usually solved numerically and is the basis of many ion beam simulation codes.

We obviously over-simplified the beam in order to obtain these equations. For ECR ion sources, the beam is not round, the ion distribution is not uniform and the beam is also not concentric with the beam pipe (i.e. image fields might occur). One consequence of the nonuniformity is that space-charge forces are no longer linear and thus Liouville's theorem does not hold anymore. Phase space volume and emittance are no longer preserved. Ultimately, the problem of beam transport for many ECRIS beams gets so complex that the only way of obtaining realistic results is by using simulation codes that can treat the three dimensional problem of propagation of particle ensembles with applied and self fields. One of these codes is WARP (a particle-in-cell code) and will be discussed in detail in Section 3.1. We have seen, however, that already with a very simple beam concept, we can pinpoint some of the problems that arise for ions beams with non-negligible self fields and we will continue the analysis in the next subsection by including space charge compensation due to secondary electrons created by the interaction of the beam with the residual gas in the beam line.

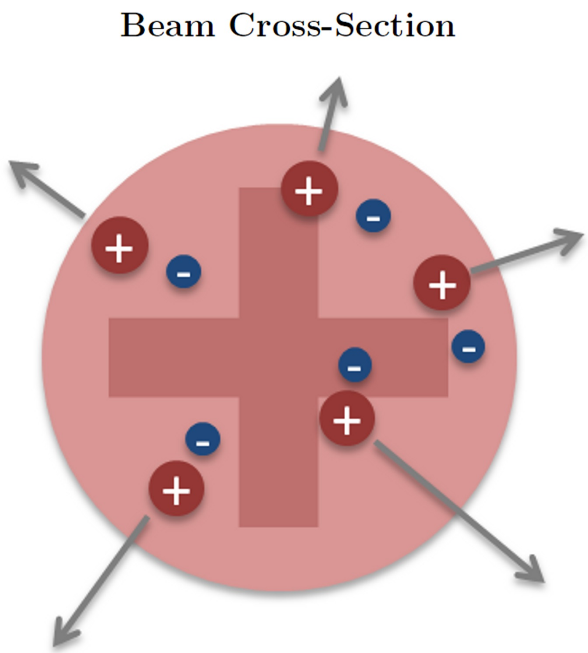

Figure 2.8: Space charge compensation. Beam Cross section view with ions and electrons created from residual gas ionization and charge exchange.

2.1.5 Space Charge Compensation

The pressure in LEBT systems of ECR ion sources is typically between 10^{-5} to 10^{-8} Torr. At these pressures, the interaction of the beam ions (primary ions) and the residual gas molecules is not negligible. The positive beam ions interact with the gas molecules mainly through two processes (assuming only one ion species in the beam) [44]:

$$\underline{\mathrm{A}}^{q+} + \mathrm{X}^0 \rightarrow \underline{\mathrm{A}}^{(q-1)+} + \mathrm{X}^+ \qquad \text{(charge exchange)}$$

$$\underline{\mathrm{A}}^{q+} + \mathrm{X}^0 \rightarrow \underline{\mathrm{A}}^{q+} + \mathrm{X}^+ + e^- \qquad \text{(ionization)}$$

where A is the primary beam ion and X the gas molecule. The underline denotes the fast particle. Both processes create slow secondary ions, which are expelled by the beam space charge potential. Ionization also provides slow secondary electrons, which are captured inside

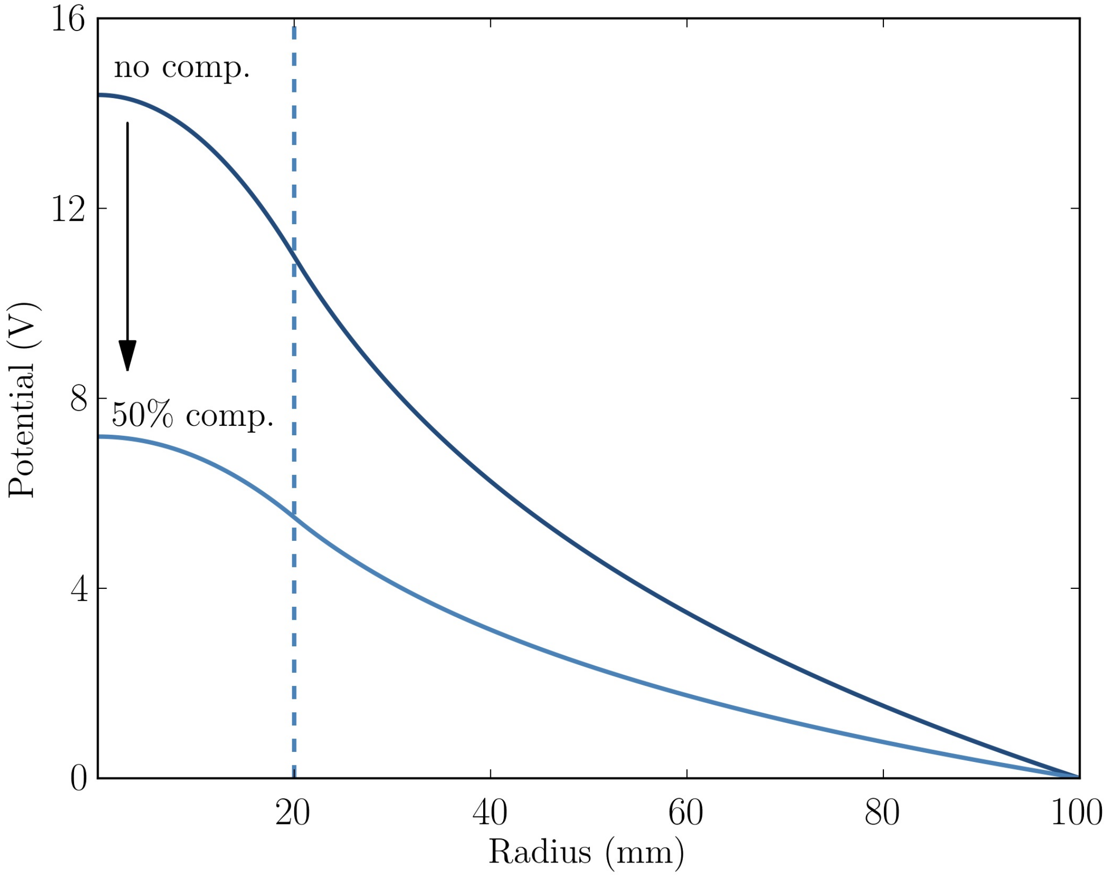

Figure 2.9: Space charge compensation. Change in beam potential from uncompensated beam to 50% compensation. This is for a 2 mA oxygen primary beam with round cross section ($r_b = 20$ mm) and homogeneous charge distribution. The beam pipe ($r_p = 100$ mm) is assumed to be grounded.

the beam space charge potential well and effectively lower said potential well. The process is illustrated in Figures 2.8 and 2.9. In our simple model of a uniformly charged cylindrical beam, the neutralization can be expressed in form of a neutralization-factor f_e modifying the total beam current in equation 2.19:

$$\Delta\phi = \frac{I \cdot (1 - f_e)}{4\pi\epsilon_0 v_b} \tag{2.28}$$

In a similar way, it can be incorporated into the linear beam model presented by M. Reiser [41] by modifying the expression for the generalized perveance:

$$K = \frac{2qeI}{4\pi\epsilon_0 m_b \beta^3 \gamma^3 c^3}\left[1 - \gamma^2 f_e(\tau)\right] \tag{2.29}$$

where β and γ are the relativistic factors, and τ is the time into the beam pulse. Since in ECR LEBTs we are only concerned with non-relativistic beams, we can use $\gamma = 1$ and assume that f_e is a constant in time (steady-state of a DC beam). As an interesting aside, it should be noted that in the case of $f_e > 1/\gamma^2$, K is negative and the beam is self-focusing due to the self magnetic field. This is called *Budker condition* of self-focusing. In the non-relativistic case, the expression for K reduces to:

$$K = \frac{2qeI}{4\pi\epsilon_0 m_b \beta^3 c^3}(1 - f_e) \tag{2.30}$$

We will now see if we can find an analytical expression for the magnitude of f_e depending on beam current, size and neutral gas density. The following derivation follows largely the considerations in the papers written by I. A. Soloshenko et al. [48–50], and M. D. Gabovich [51, 52]. I made an effort, though, to write everything in SI units and not leave out any essential steps in the derivation.

Let us consider the beam to be a plasma consisting of these three species:

- **Primary beam ions** (density n_b, velocity v_b, mass m_b, charge state q, charge $Q_b = q \cdot e$)
- **Secondary ions** (density n_i, velocity v_i, mass m_i, charge $Q_i = e$)
- **Secondary electrons** (density n_e, velocity v_e, mass m_e, charge $Q_e = -e$)

Like in the previous chapter, we start with a uniform cylindrical charge distribution for the primary beam ions. The trapped electrons are also assumed to uniformly fill the beam envelope. As mentioned earlier, the secondary ions are expelled by the beam, but, of course, spend some time inside the beam envelope. The only interaction between the beam and the secondary electrons are Coulomb collisions (no collective processes are taken into consideration). The energy necessary for the secondary electrons to leave the potential created by the beam is then given by:

$$\left(\frac{d\mathrm{E}}{dt}\right)_{out} = L \int_0^{r_b} 2\pi r \; \mathrm{d}r \int_0^{e\varphi(r)} f(\mathrm{E}) \left(e\varphi(r) - \mathrm{E}\right) \; \mathrm{dE} \tag{2.31}$$

with L the length of the beam, r_b the radius, $\varphi(r)$ the potential at radius r, and $f(\mathrm{E})$ the secondary electron energy distribution. On the other hand, a fast beam ($v_b > v_e$) will transfer energy mostly through Coulomb collisions. A good treatment of Coulomb collisions can be found here [53, 54]. In simple classical Coulomb collisions, the rate of transfer of energy per unit length for one beam particle of energy $E_{kin} = m_b v_b^2/2$ to stationary target particles can be written as

$$\frac{\mathrm{dE}}{\mathrm{d}\ell} = n_t \left(\frac{Q_b Q_t}{4\pi\epsilon_0}\right)^2 \frac{4\pi}{m_t v_b^2} \cdot \ln\left|\frac{b_{\mathrm{max}}}{b_{\mathrm{min}}}\right| \tag{2.32}$$

which, for electrons as target species becomes

$$\frac{\mathrm{dE}}{\mathrm{d}\ell} = n_e \frac{q^2 e^4}{4\pi\epsilon_0^2} \frac{1}{m_e v_b^2} \cdot \ln\left|\frac{b_{\mathrm{max}}}{b_{\mathrm{min}}}\right|$$

where b_{min} and b_{max} are appropriate lower and upper limits of the impact parameter, and q the charge state of the primary ion beam. We can now write the energy transfer to the electrons per unit time for the sum of all beam particles $N_b = n_b r_b^2 \pi L$ with velocity v_b as

$$\left(\frac{d\mathrm{E}}{dt}\right)_{in} = \frac{n_b n_e q^2 e^4 r_b^2 L}{4 m_e \epsilon_0^2 v_b} \cdot \ln\left|\frac{b_{\max}}{b_{\min}}\right| \tag{2.33}$$

Since the main contribution to the process comes from small angle scattering, a good choice for $b_{\min}$ is b_{90}, the impact parameter, where the incident particle is scattered by 90°. b_{90} for ion-electron collisions is given by

$$b_{90} = \frac{-qe^2}{4\pi\epsilon_0}\frac{1}{m_r v_b^2} \tag{2.34}$$

with m_r the reduced mass, which for ion-electron collisions is $m_r \approx m_e$. The secondary electrons are not bound to nuclei and essentially form a low density electron plasma. A good value for $b_{\max}$ is then

$$b_{\max} = \frac{v_b}{\omega_{pe}} = \frac{v_b}{e} \cdot \sqrt{\frac{\epsilon_0 m_e}{n_e}} \tag{2.35}$$

with ω_{pe} the electron plasma frequency. We expect the effectiveness of the collisions to fall off because of dielectric effects for $b > b_{\max} = v_b/\omega_{pe}$. Substituting expressions 2.34 and 2.35 for $b_{\min}$ and $b_{\max}$, respectively, we obtain

$$\tilde{\mathcal{L}} = \ln\left(4\pi\epsilon_0^{3/2}\frac{m_e^{3/2} v_b^3}{q e^3 n_e^{1/2}}\right) \tag{2.36}$$

where we call $\tilde{\mathcal{L}}$ a Coulomb logarithm. Hence

$$\left(\frac{d\mathrm{E}}{dt}\right)_{in} = \frac{n_b n_e q^2 e^4 r_b^2 L \tilde{\mathcal{L}}}{4 m_e \epsilon_0^2 v_b} \tag{2.37}$$

In steady-state, expressions 2.31 and 2.37 have to be equal in order to conserve energy:

$$L \int_0^{r_b} 2\pi r \ \mathrm{d}r \int_0^{e\varphi(r)} f(\mathrm{E}) \left(e\varphi(r) - \mathrm{E}\right) \ \mathrm{dE} = \frac{n_b n_e q^2 e^4 r_b^2 L \tilde{\mathcal{L}}}{4 m_e \epsilon_0^2 v_b}$$

or:

$$\int_0^{r_b} r \ \mathrm{d}r \int_0^{e\varphi(r)} f(\mathrm{E}) \left(e\varphi(r) - \mathrm{E}\right) \ \mathrm{dE} = \frac{n_b n_e q^2 e^4 r_b^2 \tilde{\mathcal{L}}}{8\pi m_e \epsilon_0^2 v_b} \tag{2.38}$$

Let us now solve the integrals on the left hand side. At this point, Soloshenko et al. [49] and Gabovich [52] make an approximation for $f(\mathrm{E})$:

$$f(\mathrm{E}) \propto \frac{1}{(e\Phi_i + \mathrm{E})^2} \tag{2.39}$$

with $e\Phi_i$ the ionization energy of the gas molecules. They determine the proportionality constant by requiring:

$$\int_0^{\infty} f(\mathrm{E}) d\mathrm{E} = \frac{\partial n_e}{\partial t} = n_b v_b n_0 \sigma_e$$

with n_0 the neutral gas density, and σ_e the electron creation cross -section. This expression can be readily solved to yield

$$f(\mathrm{E}) = \frac{n_b v_b n_0 \sigma_e \cdot e\Phi_i}{(e\Phi_i + \mathrm{E})^2} \tag{2.40}$$

And the energy integral in equation 2.38 can be solved to:

$$
\begin{aligned}
\int\limits_0^{e\varphi(r)} f(\mathrm{E})\,(e\varphi(r)-\mathrm{E})\;\mathrm{dE} &= \eta\cdot\int\limits_0^{e\varphi(r)} \frac{e\varphi(r)-\mathrm{E}}{(e\Phi_i+\mathrm{E})^2}\;\mathrm{dE} \\
&= \eta\cdot\left[\frac{\varphi(r)^2-\Phi_i^2}{\Phi_i(\Phi_i+\varphi(r))}+1-\ln\left(1+\frac{\varphi(r)}{\Phi_i}\right)\right] \\
&= \eta\cdot\left[\frac{\varphi(r)-\Phi_i}{\Phi_i}+1-\ln\left(1+\frac{\varphi(r)}{\Phi_i}\right)\right] \\
&= \eta\cdot\left[\frac{\varphi(r)}{\Phi_i}-\ln\left(1+\frac{\varphi(r)}{\Phi_i}\right)\right] \qquad (2.41)
\end{aligned}
$$

where η was introduced for convenience as

$$\eta = n_b v_b n_0 \sigma_e \cdot e\Phi_i$$

η is considered constant in r and E in our simplified view of the problem. The potential $\varphi(r)$ inside a homogeneously charged cylinder inside a beam pipe of radius R is given by 2.18:

$$\varphi(r) = \frac{I_b}{4\pi\epsilon_0 v_b}\cdot\left(1+2\ln\frac{r_p}{r_b}-\frac{r^2}{r_b^2}\right)$$

with I_b the beam current and ϵ_0 the vacuum permittivity. Computing $\Delta\varphi = \varphi(r_b)-\varphi(0)$ yields

$$\Delta\varphi = \frac{I_b}{4\pi\epsilon_0 v_b}$$

Since, for our considerations, we are only interested in $\Delta\varphi$, which is independent of the beam pipe radius, we can set $r_p = r_b$, and

$$\varphi(r) = \Delta\varphi\cdot\left(1-\frac{r^2}{r_b^2}\right). \qquad (2.42)$$

Now we can carry out the radial integral in equation 2.38:

$$
\begin{aligned}
\int_0^{r_b} r \cdot \left[\frac{\varphi(r)}{\Phi_i} - \ln\left(1 + \frac{\varphi(r)}{\Phi_i}\right)\right] \, \mathrm{d}r = \\
&= \int_0^{r_b} r \cdot \left\{ \frac{\Delta\varphi}{\Phi_i}\left(1 - \frac{r^2}{r_b^2}\right) - \ln\left[1 + \frac{\Delta\varphi}{\Phi_i}\left(1 - \frac{r^2}{r_b^2}\right)\right]\right\} \, \mathrm{d}r \\
&= \frac{\Delta\varphi}{\Phi_i}\left(\frac{r_b^2}{2} - \frac{r_b^2}{4}\right) - \int_0^{r_b} r \cdot \ln\left[1 + \frac{\Delta\varphi}{\Phi_i}\left(1 - \frac{r^2}{r_b^2}\right)\right] \, \mathrm{d}r \\
&= \frac{\Delta\varphi}{\Phi_i}\frac{r_b^2}{4} - \frac{\Phi_i}{\Delta\varphi}\frac{r_b^2}{2}\left[-\frac{\Delta\varphi}{\Phi_i} + \left(1 + \frac{\Delta\varphi}{\Phi_i}\right)\ln\left(1 + \frac{\Delta\varphi}{\Phi_i}\right)\right] \\
&= \frac{r_b^2}{2}\left[\frac{\Delta\varphi}{2\Phi_i} + 1 - \left(1 + \frac{\Phi_i}{\Delta\varphi}\right)\ln\left(1 + \frac{\Delta\varphi}{\Phi_i}\right)\right]
\end{aligned}
\tag{2.43}
$$

Expanding the logarithm for $\Delta\varphi/\Phi_i < 1$ yields

$$
\ln\left(1 + \frac{\Delta\varphi}{\Phi_i}\right) = \frac{\Delta\varphi}{\Phi_i} - \frac{1}{2}\left(\frac{\Delta\varphi}{\Phi_i}\right)^2 + \frac{1}{3}\left(\frac{\Delta\varphi}{\Phi_i}\right)^3 + \mathcal{O}(4).
$$

Substituting into the solution of equation 2.43, carrying out the multiplication and dropping the terms of order 3 and higher gives

$$
\frac{r_b^2}{2}\left[\frac{\Delta\varphi}{2\Phi_i} + 1 - \left(1 + \frac{\Phi_i}{\Delta\varphi}\right) \cdot \left(\frac{\Delta\varphi}{\Phi_i} - \frac{1}{2}\left(\frac{\Delta\varphi}{\Phi_i}\right)^2 + \frac{1}{3}\left(\frac{\Delta\varphi}{\Phi_i}\right)^3 + \mathcal{O}(4)\right)\right] \approx \frac{r_b^2}{12}\frac{(\Delta\varphi)^2}{\Phi_i^2}.
$$

And thus

$$\begin{aligned}
\int_0^{r_b} r\ \mathrm{d}r \int_0^{e\varphi(r)} f(\mathrm{E})\,(e\varphi(r)-\mathrm{E})\ \mathrm{dE} &= \eta\cdot\frac{r_b^2}{12}\frac{(\Delta\varphi)^2}{\Phi_i^2} \\
&= n_b v_b n_0 \sigma_e e \Phi_i \cdot \frac{r_b^2}{12}\frac{(\Delta\varphi)^2}{\Phi_i^2} \\
&= n_b v_b n_0 \sigma_e e \cdot \frac{r_b^2}{12}\frac{(\Delta\varphi)^2}{\Phi_i} \qquad (2.44)
\end{aligned}$$

Then, 2.38 becomes

$$(\Delta\varphi)^2 = \frac{3q^2\Phi_i n_e e^3 \tilde{\mathcal{L}}}{2\pi m_e v_b^2 n_0 \sigma_e \epsilon_0^2} \qquad (2.45)$$

The only unknown quantity now is the electron density. Here, Gabovich and Soloshenko use quasi-neutrality:

$$n_e = q\cdot n_b + n_i \qquad (2.46)$$

and the secondary ion balance equation (number of secondary ions created in the beam is equal to the number of ions leaving the beam per unit time):

$$2r_b\pi n_i \bar{v}_i = r_b^2\pi n_b v_b n_0 \sigma_i \qquad (2.47)$$

with $\bar{v}_i$ the average secondary ion velocity. Thus the electron density is

$$n_e = q\cdot n_b + \frac{n_b v_b n_0 \sigma_i r_b}{2\bar{v}_i} \qquad (2.48)$$

We can now rewrite 2.45:

$$
\begin{aligned}
(\Delta\varphi)^2 &= \frac{3q^2\Phi_i e^3\tilde{\mathcal{L}}}{2\pi m_e v_b^2 n_0 \sigma_e \epsilon_0^2} \cdot \left(q \cdot n_b + \frac{n_b v_b n_0 \sigma_i r_b}{2\bar{v}_i} \right) \\
&= \frac{3q^2\Phi_i n_b e^3\tilde{\mathcal{L}}}{2\pi m_e v_b^2 \epsilon_0^2} \cdot \left(\frac{q}{n_0\sigma_e} + \frac{v_b \sigma_i r_b}{2\bar{v}_i \sigma_e} \right). \qquad (2.49)
\end{aligned}
$$

Finally, we use the non-relativistic kinetic energy of the primary beam

$$
qeU_0 = \frac{m_b v_b^2}{2},
$$

with U_0 the source voltage, to replace v_b^2 and obtain the formula presented in [49] (but in SI units and for an arbitrary charge-state q of the primary ion beam):

$$
(\Delta\varphi_{neut})^2 = 3\mathcal{L} \cdot \frac{m_b}{m_e} \cdot \frac{\Phi_i}{U_0} \frac{n_b q e^2}{(4\pi\epsilon_0)^2} \left(\frac{q}{n_0\sigma_e} + \frac{v_b \sigma_i r_b}{2\bar{v}_i \sigma_e} \right). \qquad (2.50)
$$

Note that we have absorbed a factor 4π into the definition of $\mathcal{L}$ ($\mathcal{L} = 4\pi\tilde{\mathcal{L}}$) to be consistent with [49]. We also use equation 2.48 to replace the electron density in the Coulomb logarithm (equation 2.36). We now have an explicit expression for $\Delta\varphi$ in terms of quantities either experimentally accessible or calculable by theoretical models. The neutralization factor f_e can now be obtained by substituting the (partially) neutralized $\Delta\varphi_{neut}$ (equation 2.50) into equation 2.28:

$$
f_e = 1 - \frac{\Delta\varphi_{neut}}{\Delta\varphi_{full}} \qquad (2.51)
$$

where (with $\beta c = v_b$ the beam velocity):

$$
\Delta\varphi_{full} = \frac{I}{4\pi\epsilon_0 v_b}
$$

2.1.5.1 Simple Generalization of the Result

One of the drawbacks of Gabovich's result is the assumption of quasi-neutrality which naturally limits the usefulness of the formula to highly neutralized beams. If we modify equation 2.46 to reflect the fact that the electron density is only a fraction of the combined primary and secondary ion densities (corresponding to the level of neutralization) we can write it as:

$$n_e = fe \cdot (q \cdot n_b + n_i) \tag{2.52}$$

This only adds a factor $\sqrt{f_e}$ to the definition of $\Delta\varphi_{neut}$ and the new equation for calculation of the compensation factor is:

$$f_e = 1 - \frac{1}{\Delta\varphi_{full}}\sqrt{f_e}\sqrt{3\mathcal{L} \cdot \frac{m_b}{m_e} \cdot \frac{\Phi_i}{U_0}\frac{n_b q e^2}{(4\pi\epsilon_0)^2}\left(\frac{q}{n_0\sigma_e} + \frac{v_b\sigma_i r_b}{2\bar{v}_i\sigma_e}\right)} \tag{2.53}$$

Using the abbreviation

$$\chi = \frac{1}{\Delta\varphi_{full}} \cdot \sqrt{3\mathcal{L} \cdot \frac{m_b}{m_e} \cdot \frac{\Phi_i}{U_0}\frac{n_b q e^2}{(4\pi\epsilon_0)^2}\left(\frac{q}{n_0\sigma_e} + \frac{v_b\sigma_i r_b}{2\bar{v}_i\sigma_e}\right)} \tag{2.54}$$

we can easily solve for f_e:

$$f_e = 1 + \frac{\chi^2}{2} - \frac{\chi}{2}\sqrt{\chi^2 + 4} \tag{2.55}$$

Note: Technically, we cannot simply replace the electron density inside the Coulomb logarithm anymore, but a quick error propagation study shows that a relative error $\Delta(n_e)_{rel}$ contributes little to $\Delta(\Delta\varphi_{neut})_{rel}$:

$$\Delta(\Delta\varphi_{neut})_{rel} = \frac{\Delta(n_e)_{rel}}{4 \cdot \tilde{\mathcal{L}}} \tag{2.56}$$

which for typical values of 5-15 for $\tilde{\mathcal{L}}$ is a factor 20 - 60 smaller than $\Delta(n_e)_{rel}$ and thus well below other sources of error due to our approximations. Still, a sort of crude *relaxation process* can be used, where f_e is calculated using the full electron density inside $\tilde{\mathcal{L}}$ in a first iteration. This preliminary f_e can then be used inside $\tilde{\mathcal{L}}$ in the second iteration, making sure that the resulting error really is negligible.

2.1.5.2 Multiple Ion Species

In the region between the ECR source and the first dipole magnet, the beam is composed of several ion species with different mass-to-charge ratios m/q. Naturally, we are interested to expand the theoretical model to include multiple ion species, to predict neutralization in those parts of the beam line. Because of the linearity of the K-V model, we can easily generalize equation 2.50 for multiple ion species in the beam. If we assume all species have the same beam radius, this is achieved by summation over all k species in the beam:

$$\sum_{j=1}^{k}\left(\frac{d\mathrm{E}}{dt}\right)_{j,\,in} = \sum_{j=1}^{k}\left(\frac{d\mathrm{E}}{dt}\right)_{j,\,out}. \tag{2.57}$$

With the full potential drop:

$$\Delta\varphi_{full} = \sum_{j=1}^{k}\frac{I_{b,j}}{4\pi\epsilon_0 v_{b,j}}, \tag{2.58}$$

the individual Coulomb logarithms:

$$\mathcal{L}_j = 4\pi \ln\left(4\pi\epsilon_0^{3/2}\frac{m_e^{3/2}v_{b,j}^3}{q_j e^3 n_e^{1/2}}\right), \tag{2.59}$$

the individual ion beam densities

$$n_{b,j} = \frac{I_{b,j}}{eq_j r_b^2 \pi v_{b,j}} \tag{2.60}$$

and the sum expression for the electron density:

$$n_e = f_e \cdot \sum_{j=1}^{k} \left(q_j \cdot n_{b,j} + \frac{n_{b,j} v_{b,j} n_0 \sigma_{i,j} r_b}{2\bar{v}_i} \right), \tag{2.61}$$

we obtain:

$$\begin{aligned} \Delta\varphi_{neut}^2 &= f_e \cdot \frac{3}{m_e} \frac{\Phi_i}{U_0} \frac{e^2}{(4\pi\epsilon_0)^2} \cdot \sum_{j=1}^{k} \left[\frac{q_j n_{b,j}}{n_0} + \frac{r_b n_{b,j} v_{b,j} \sigma_{i,j}}{2\bar{v}_i} \right] \cdot \frac{\sum_{j=1}^{k} I_{b,j} m_{b,j} \mathcal{L}_j}{\sum_{j=1}^{k} \frac{I_{b,j}\sigma_{e,j}}{q_j}} \\ &\equiv fe \cdot \eta^2. \end{aligned} \tag{2.62}$$

And with

$$\chi_{multi} = \frac{\eta}{\Delta\varphi_{full}} \tag{2.63}$$

we can calculate f_e from

$$f_e = 1 - \sqrt{f_e} \cdot \chi_{multi} \tag{2.64}$$

to be (analogous to equation 2.55):

$$f_e = 1 + \frac{\chi_{multi}^2}{2} - \frac{\chi_{multi}}{2} \sqrt{\chi_{multi}^2 + 4}. \tag{2.65}$$

2.1.5.3 Obtaining the Cross-Sections

Clearly, one of the sources of uncertainty in this model are the cross-sections σ_e and σ_i for secondary electron and ion production. Remembering the two processes involved with beam-residual gas-interaction mentioned at the beginning of this subsection, we can rewrite σ_e and σ_i in terms of the actual reactions:

$$\begin{aligned} \sigma_e &= \sigma_{ionization} \\ \sigma_i &= \sigma_{charge-exchange} + \sigma_{ionization} \end{aligned}$$

In the past century, many measurements have been conducted and scaling models and semi-empirical formulae have been developed to address the question of obtaining the ionization and charge-exchange cross-sections. For charge-exchange processes, A. Müller and E. Salzborn presented an overview of previous measurements and scaling laws in 1977 [1]. Based on the data they had collected, they proposed the following scaling law for the charge-exchange cross-section (in cm^2):

$$\sigma_{q,q-k} = A_k \cdot q^{\alpha_k} \cdot \Phi_i^{\beta_k} \quad k = 1, \cdots, 4 \tag{2.66}$$

with q the initial charge-state, k the number of exchanged electrons, Φ_i the ionization energy in eV, and A_k, α_k β_k fit parameters with values listed in Table 2.1.

For the ionization cross-section $\sigma_{ionization}$, the situation is a bit more problematic. Data for proton, helium and lithium beams in the desired range of 10 keV to 100 keV can be found for gaseous hydrogen, helium and lithium targets [55–57], because the cross-sections are interesting for fusion research. For other projectiles and targets, several measurements exist at significantly higher energies. Based on classical and quantum theories, several models have been developed and compared to the existing measurements. A good summary of previous efforts was given by I.D.Kaganovich et al. in several papers between 2003 and 2005 [58–60]. He presented a scaling law that seems to fit the data very well. Unfortunately, most cases we are interested in for ECR ion source low energy beam transport are in energy regimes below the applicability of this scaling law. If the velocity of the incident particle becomes too low, the interaction time of projectile and target electron increases enough for tunneling effects to become an important factor in the ionization process and the Kaganovich fit underestimates the cross-section. But at the same time, the charge-exchange cross sections become much larger than the ionization cross-sections at low velocities. To predict neutralization for different ECR beams, one has to find measured ionization cross-sections and (very carefully) scale known curves to the desired beams. The given references are very helpful in this. Further information can be found in chapter 5 on space-charge compensation measurements in ECR beam lines.

Table 2.1: Müller-Salzborn fit parameters for charge-exchange cross-sections [1].

k	A_k	α_k	β_k
1	$(1.43 \pm 0.76) \times 10^{-12}$	1.17 ± 0.09	-2.76 ± 0.19
2	$(1.08 \pm 0.95) \times 10^{-12}$	0.71 ± 0.14	-2.80 ± 0.32
3	$(5.50 \pm 5.80) \times 10^{-14}$	2.10 ± 0.24	-2.89 ± 0.39
4	$(3.57 \pm 8.90) \times 10^{-16}$	4.20 ± 0.79	-3.03 ± 0.86

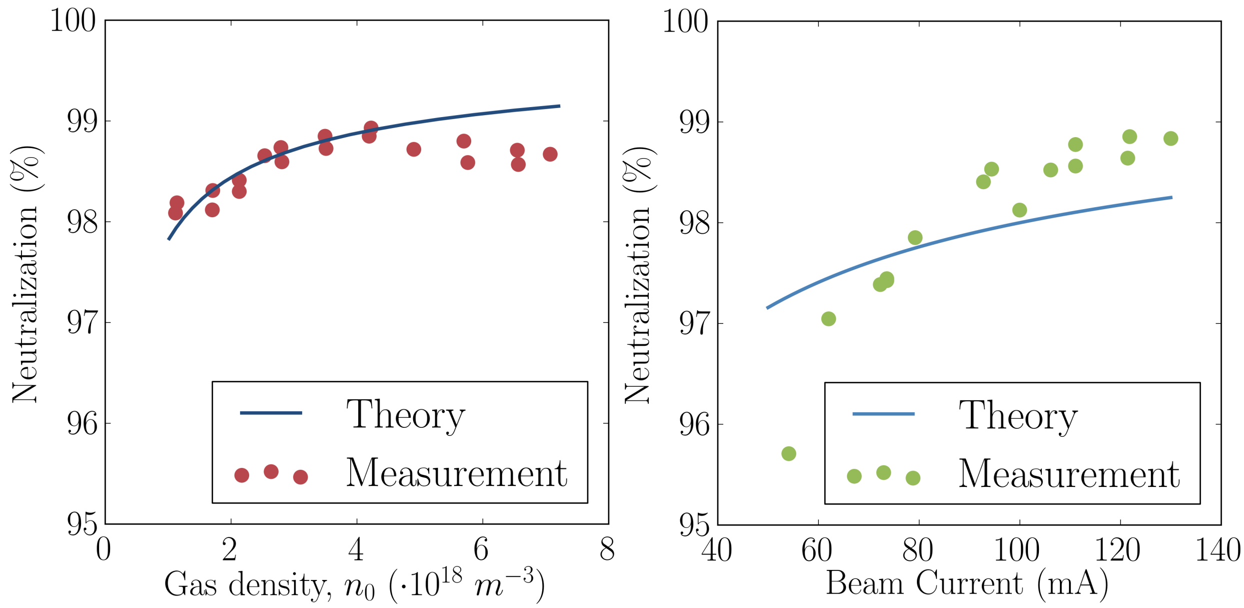

Figure 2.10: Example of theoretical neutralization prediction for a 75 keV proton beam with a 14 mm diameter in H_2 residual gas. Experimental data shown for comparison from [7]. The data was published without errorbars. Left: pressure variation at a constant beam current of 100 mA, right: current variation at a constant gas density of $1.2 \cdot 10^{18}$ m^{-3}.

2.1.5.4 An Example

Using cross-section data from [57] for a 75 keV proton beam going through a residual gas of H_2, we find $\sigma_e \approx 2.2 \cdot 10^{-20}$ m^2 (25% accuracy) and $\sigma_i \approx 3.2 \cdot 10^{-20}$ m^2 (30% accuracy). Figure 2.10 shows the neutralization values calculated with the generalized model (equation 2.55). For comparison, data for the LEDA injector source presented by R. Ferdinand [7] is shown in the graph. As in the measurements, the residual gas was assumed to be H_2, the beam current was varied from 50 mA to 130 mA and the pressure from $2 \cdot 10^{-5}$ to $3 \cdot 10^{-4}$ Torr. The beam diameter was assumed to be 14 mm. The overall agreement is very good and decreasing neutralization with decreasing beam current as well as decreasing residual gas pressure can be observed in both experiment and theory.

2.1.5.5 Some Comments and Limitations of this Model

- The average secondary ion velocity $\bar{v}_i$ obviously depends on the potential well depth of the compensated beam. The dependence goes as the square root of $\Delta\varphi_{neut}$, though making it a fourth root contribution to the calculated $\Delta\varphi_{neut}$.Thus choosing a ion temperature close to the expected $\Delta\varphi_{neut}$ gives good results and even a rather large variation of it does not change the result significantly.

- Gabovich and Soloshenko use a rather simplistic approximation for f(E) following Thomson's theory [61].

- Beam is approximated as a homogeneously charged cylinder. This can be a good approximation for beams like the proton beams from, e.g., the LEDA source [7] (the experimental data in Figure 2.10). For ECR sources the beam shape may have to be taken into account. However, in general, the neutralization will exhibit the following dependencies:

  - Residual gas pressure (lower pressure $\rightarrow$lower neutralization)
  - Beam current (lower beam current $\rightarrow$lower neutralization)
  - Beam diameter (smaller beam diameter $\rightarrow$lower neutralization)

- Charge-exchange and ionization are assumed to produce only ions with $q = 0 \rightarrow 1+$. Ionization cross-sections for $q = 0 \rightarrow 2+$ are generally an order of magnitude lower; charge-exchange, however, may produce higher charge-states with non-negligible probability.

- In the presented model, no collective processes are included (e.g. plasma waves, beam instabilities, etc.) Further information can be found in [48] and Chapter 5 of this thesis.

- For the multiple species approach, in reality the different radii will not be the same, because individual beamlets experience different focusing depending on their mass-to-charge ratio (m/q). This happens when they exit the source, as well as in solenoids or einzel lenses in the LEBT system. Unfortunately, the densities n_b, n_i, and n_e will no longer be uniform in this case and the forces no longer linear so different radii cannot readily be incorporated into the linear theory.

2.2 Electron Cyclotron Resonance Ion Sources

2.2.1 General Overview

Very detailed treatment of ECR ion sources, the plasma physics applicable to those sources and considerations regarding extraction of the beam can be found in the books by R. Geller [14], and I.G.Brown [44, 45]. Furthermore, the development of ECR ion sources is a very active fields and numerous publications are available. Here, I will review a few basic principles of ECR ion sources, the related plasma physics and physics of ion beam extraction. I will give references to related articles where corresponding topics are mentioned. The technological and engineering aspects of the specific ECR ion sources used for experiments in this thesis will be treated in chapter 4.1.

2.2.1.1 ECR Concept

The basic operating principle of the electron cyclotron resonance ion source is that of a plasma ion source: A plasma consisting of ions and electrons is confined by a magnetic field. Highly charged ions are created by successive (step-by-step) *electron impact ionization*. In the ECR source, the electrons circle around the magnetic field lines with their *electron cyclotron resonance frequency*:

$$\omega_{ecr} = \frac{e \cdot B}{m_e} \tag{2.67}$$

with B the magnetic field, m_e the electron mass, and e the electron charge. Microwaves of the same frequency ($2\pi f_{rf} = \omega_{rf} = \omega_{ecr}$) are used to resonantly transfer energy to the electrons ('heat' them). Thus the magnetic field does not only provide the ion confinement, but also the resonance condition necessary for the heating process. Typical frequencies f_{rf}

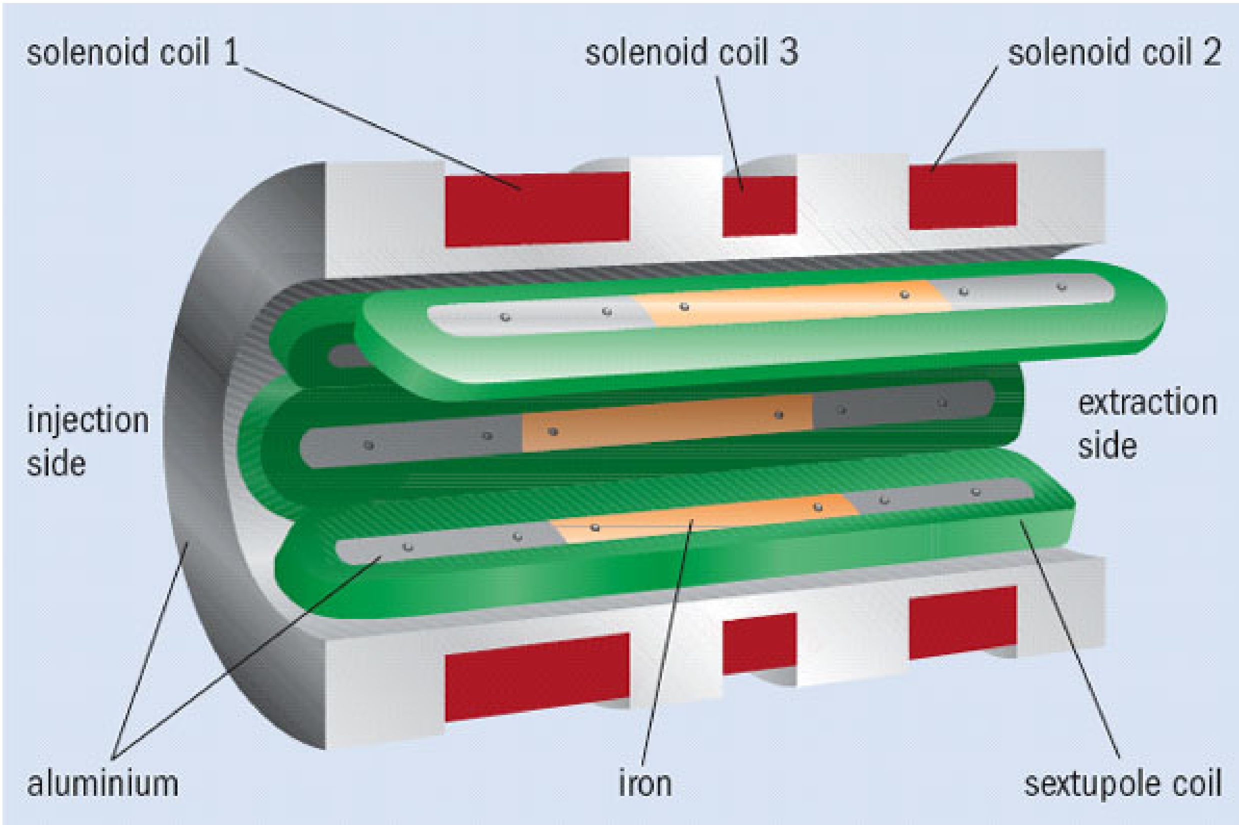

Figure 2.11: The magnet structure of the VENUS ECR ion source. Courtesy of D. Leitner.

go from 2.45 to 28 GHz with corresponding resonance fields from 0.0875 to 1 T.

2.2.2 Magnetic Field Structure

Typically, ECR ion sources consist of a longitudinal mirror field produced by two or more solenoids and a superimposed sextupole (also called a hexapole) magnet. Such a configuration can be seen in Figure 2.11 for the case of the Lawrence Berkeley National Laboratory ECR source VENUS. This type of configuration is often called *minimum-B*, because from the center of the source, the magnetic field strength increases in all directions. The main purpose of the sextupole field is to suppress *magneto-hydrodynamic (MHD)* plasma instabilities [14]. There are ECR sources, with slightly different magnetic field configurations: Some do use only solenoids (e.g. LEDA source), some use higher order multipoles for the

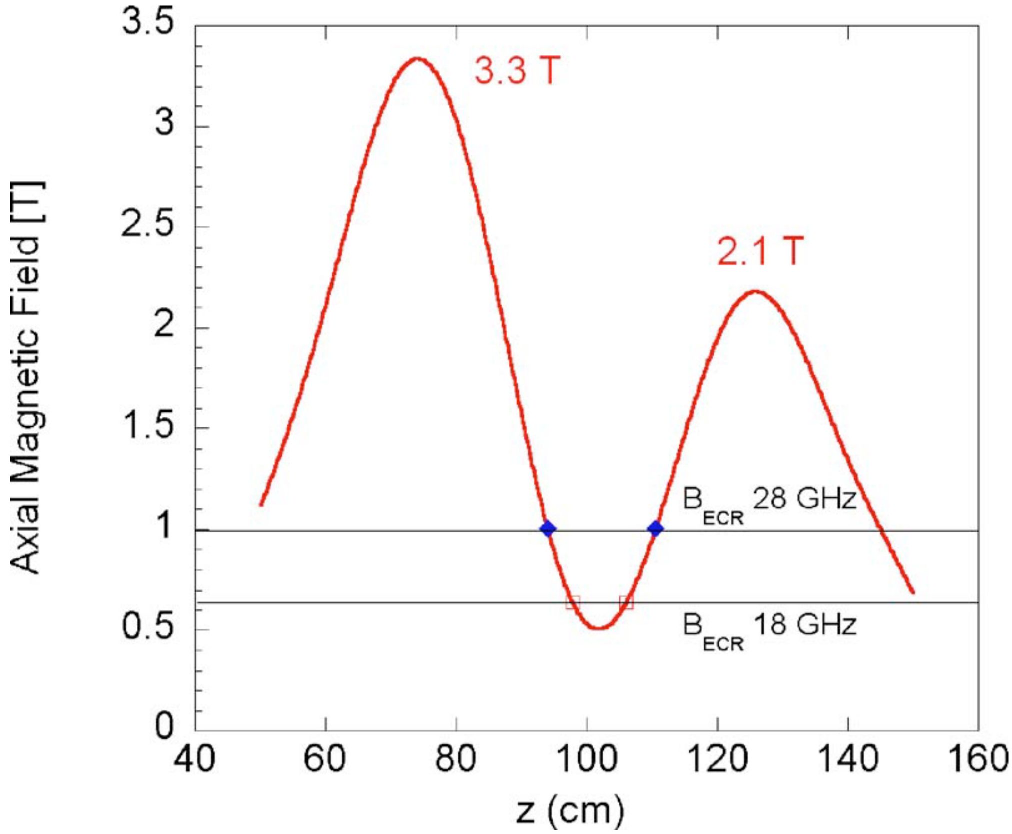

Figure 2.12: Axial Field of the VENUS ECR ion source. It can be seen that the mirror ratios are around 6 at injection (left peak) and 4 at extraction (right peak). Also indicated are the B values that correspond to the two microwave frequencies 18 GHz and 28 GHz used in VENUS. The two corresponding ecr surfaces then form nested shells. Image taken from [8].

radial confinement (octupoles, dodecapoles). Solenoid-only operation is only used when high currents of singly charged ions are desired. For a given rf-frequency, the area of magnetic flux B, where the ecr-condition (equation 2.67) is met forms a closed shell inside the ion source chamber, the *ecr surface*. The longitudinal field $B_z(z)$ on axis of the VENUS source, as well as the points where the ecr condition is met are shown in Figure 2.12. It was experimentally found, that it can be beneficial to use more than one frequency (18 GHz and 28 GHz in case of VENUS) [62]. One important parameter of the magnetic field is the *mirror ratio* $R_m = B_{max}/B_{min}$. As can be seen in Figure 2.12, for VENUS this can be as high as 6 at injection and 4 at extraction. Typical values for other ECR sources are between 2 and 4.

With the mirror ratio, a *loss cone* can be defined and particles inside the loss cone escape the magnetic mirror. Let us consider this for a simple mirror field without radial confinement, collisions, or plasma potential. If α is the angle between $v_\perp$ and $v_\parallel$ of an ion at the center of the source (where $B = B_{min}$), the loss cone is defined by $\sin\alpha_0 = \sqrt{1/R_m}$. A particle with $\alpha < \alpha_0$ is not trapped and escapes the magnetic mirror. In reality many factors contribute to the loss processes and the loss cones can be severely modified. More information can be found in literature on ECRIS magnetic confinement, e.g.: [14, 63–65].

2.2.3 Creation of Highly Charged Ions

As mentioned before, the high charge states of ions in an ECR ion source are achieved by successive electron impact ionization. Two processes occur that work against the ionization process: Charge-exchange with neutral atoms and losses to the walls (due to the loss cone). The whole process can be described by a rate equation [66]:

$$\begin{aligned} \frac{dn_i^q}{dt} &= n_e\langle\sigma v\rangle^{ion}_{q-1\to q} n_i^{q-1} - n_e\langle\sigma v\rangle^{ion}_{q\to q+1} n_i^q \\ &\quad + n_{0,i}\langle\sigma v\rangle^{cx}_{q+1\to q} n_i^{q+1} - n_{0,i}\langle\sigma v\rangle^{cx}_{q\to q-1} n_i^q - \frac{n_i^q}{\tau_i^q} \end{aligned} \tag{2.68}$$

where the terms on the right hand side (in order of appearance) are:

- ionization from charge state $q-1$ to q
- ionization from charge state q to $q+1$
- charge-exchange from charge state $q+1$ to q
- charge-exchange from charge state q to $q-1$
- losses due to escaping from confinement

Here, $\langle \sigma v \rangle$ denotes a rate coefficient depending on cross section for either ionization or charge-exchange and the electron velocity averaged over the electron energy distribution. Cross-sections for electron-impact ionization are more available than those for ion-impact ionization (cf. Section 2.1.5) and semi-empirical formulae have been proposed by Müller and Salzborn [67], and Lotz [68, 69]. A scaling law for charge-exchange has been proposed by Müller and Salzborn [1] (as mentioned in Section 2.1.5).

2.2.4 ECR Heating

In order to strip an electron from a target atom or ion, the *ionization energy* must be provided by the projectile. The higher the charge state of the target ion, the more energy is necessary to free the next electron. For instance, the 1$^{\text{st}}$ ionization potential of ^{40}Ar is $\approx$ 16 eV while the 18$^{\text{th}}$ (stripping the last electron) is $\approx$ 4.5 keV. Consequently, the typical electron energies needed in ECR ion sources are 1 keV to 20 keV (depending on the element). As mentioned earlier, the heating of electrons is achieved by coupling rf-microwaves into the source volume. Resonant heating then occurs on the ecr surface. It is essential that the ecr surface is closed and well within the source volume. In order for the microwaves to penetrate the plasma and reach the ecr surface, the plasma frequency

$$\omega_p = \sqrt{\frac{n_e e^2}{\epsilon_0 m_e}}$$

should be lower than the microwave frequency: $\omega_p < \omega_{rf} = 2\pi f_{rf}$. If this is not the case, we speak of an *overdense plasma*. If the plasma is overdense, the highest charge states are not reached and the plasma can experience turbulence (it is not *quiescent*) [14].

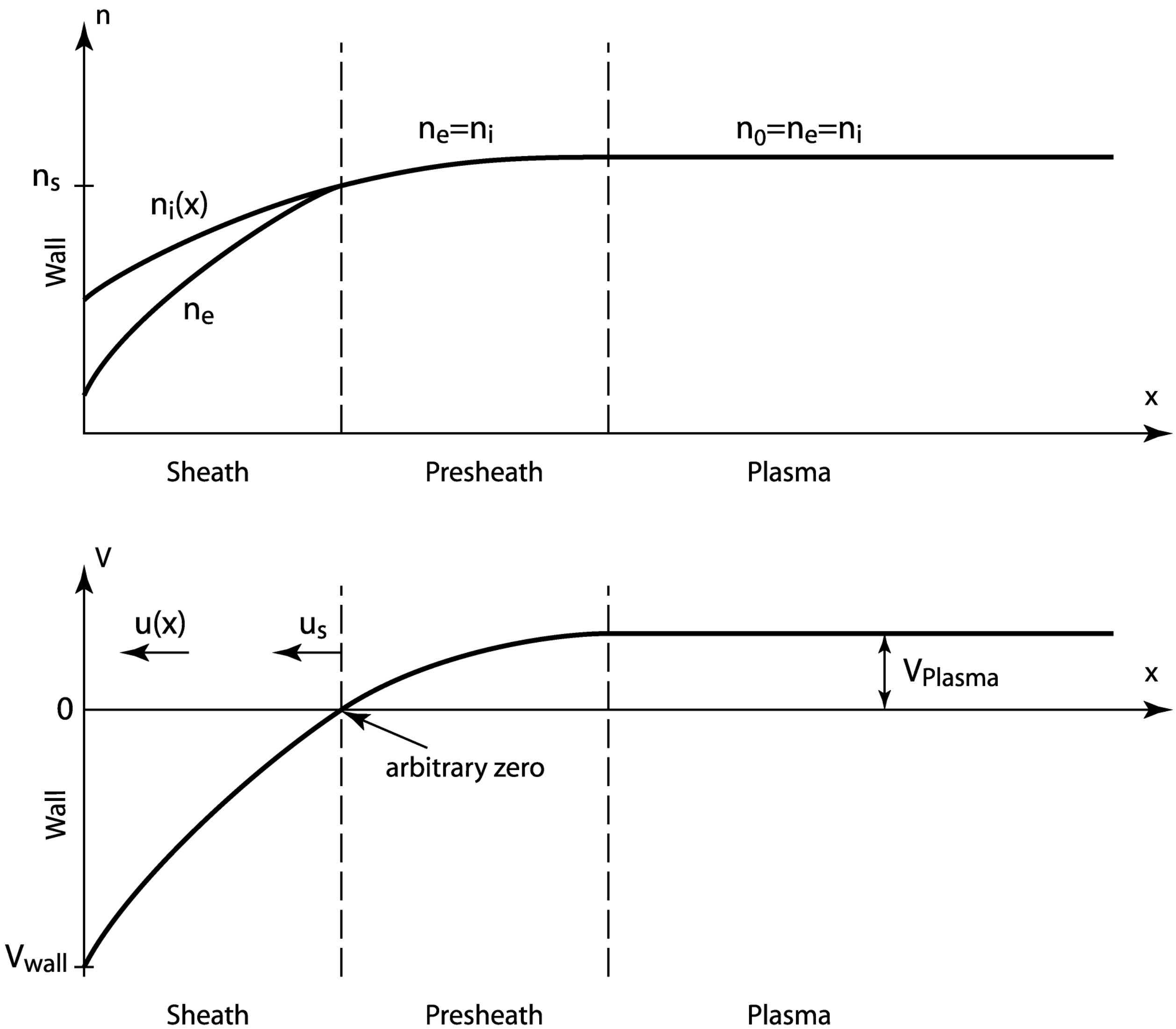

Figure 2.13: Upper: Electron and Ion densities in collisionless plasma near wall. Lower: Plasma potential of a collisionless plasma near wall. Image by Lukas Derendinger under the GNU Free Documentation License.

2.2.5 Plasma Sheath

Whenever a floating or negatively biased solid surface is introduced to the plasma (probe, wall, extraction electrode, etc.), a so called plasma sheath forms between the plasma and the solid surface (henceforth named 'wall'). This is necessary to shield the plasma from the negative potential (with respect to the plasma potential) created by the fact that substantially more electrons than ions hit the wall (due to the difference in mass). Thus there must be a potential drop from the (in general) positive plasma potential Φ_p to the less positive wall potential Φ_w. Figure 2.13 shows the potential and ion/electron densities close to the wall. It can also be seen that between plasma and sheath a pre-sheath with a less pronounced potential drop forms, which accelerates the ions into the sheath. The plasma potential is an important parameter in ECR extraction simulations. In the following we will derive an expression for Φ_p following considerations by P.C. Stangeby et al. [70, 71] for a 1-D plasma sheath. Assuming that the quasi-neutrality of the plasma

$$\sum_i q_i \cdot n_i = n_e \tag{2.69}$$

(with q_i the charge of a certain ion species, n_i its particle density and n_e the electrons' particle density) is conserved, we can calculate the potential difference between wall and plasma ($\Phi_p - \Phi_w$) by setting the electron and ion currents to the wall equal ($j^+ = j^-$). The sheath is very thin, so we can assume the following:

- No ionization or ion collision takes place within the sheath
- Consequently, all ions entering the sheath hit the solid electrode

2.2.5.1 Electron Flux

Inside the plasma we can assume the electrons to be in thermal equilibrium, thus having a Maxwell-Boltzmann velocity distribution

$$f(v_e)dv_e = \left(\frac{m_e}{2\pi k T_e}\right)^{3/2} \cdot e^{-\frac{m_e v_e^2}{2kT_e}} \cdot dv_e \tag{2.70}$$

The particle flux in a given direction $\hat{n}$ is given by

$$\int_V f(\vec{v}_e) \cdot \vec{v}_e \cdot \hat{n} \cdot d^3 v_e \tag{2.71}$$

Let's now consider the random flux through a surface element $\hat{z}dS$ located at the origin and only for particles coming from $z < 0$ (the electrons hit the wall only on the inside of the chamber) of particles with velocities between $\vec{v}$ and $\vec{v} + d\vec{v}$ and an angle of θ to the surface normal. Thus $\vec{v} \cdot \hat{z} = v \cdot \cos\theta$. And in spherical coordinates we have $d^3 v = v^2 \sin\theta \, d\theta \, d\phi \, dv$. Thus the flux is

$$F = \int_0^\infty f(v) v^3 \, dv \int_0^{\pi/2} \sin\theta \cos\theta \, d\theta \int_0^{2\pi} d\phi = \pi \int_0^\infty f(v) v^3 \, dv \tag{2.72}$$

with equation 2.70 as velocity distribution this yields

$$\begin{aligned} F_e &= \pi n_e \left(\frac{m_e}{2\pi k T_e} \right)^{2/3} \int_0^\infty e^{-\frac{m_e v_e^2}{2kT_e}} v_e^3 \, dv_e \\ &= n_e \left(\frac{kT_e}{2\pi m_e} \right)^{1/2} \end{aligned}$$

Knowing that the mean velocity of electrons following a Maxwellian is given by

$$\bar{v}_e = \sqrt{\frac{8kT_e}{\pi m_e}}. \tag{2.73}$$

we can rewrite the above result to

$$F_e = \frac{1}{4} \cdot n_e \cdot \bar{v}_e \tag{2.74}$$

In a repelling, conservative force-field (as the electrons experience in the sheath), only the number density is reduced and the distribution remains Maxwellian, thus we can write the flux of electrons to the wall as

$$F_e = \frac{1}{4} \cdot n_e \cdot \bar{v}_e \cdot e^{\frac{e(\Phi_W - \Phi_P)}{kT_e}} \tag{2.75}$$

2.2.5.2 Ion flux - The Bohm criterion

The shielding effect of the sheath is not perfect and a small portion of the electric field extends into the plasma, causing a pre-sheath acceleration. A physically realistic, steady-state sheath solution requires that the ions enter the sheath with a speed of at least their acoustic speed C_s, while from plasma analysis one finds that no such solution is possible with an ion drift velocity exceeding C_s. Thus (in this simplified case) the ions must enter the sheath with a net drift velocity equal to C_s. This is called the Bohm criterion [70, 71]. For isothermal ($T_i =$ const.) ion flow one finds

$$C_s = \sqrt{\frac{k(T_i + T_e)}{m_i}} \tag{2.76}$$

2.2.5.3 The Plasma Potential

We can now calculate the plasma potential with respect to the wall (on ion source high voltage potential $\Phi_w \approx 20 - 30$ kV). For multiple ion species we cannot simply set the fluxes equal, but have to use the currents because we have to account for k different charge states:

$$j^+ = e \cdot \sum_{j=1}^{k} q_j n_{i,j} \sqrt{\frac{k(T_{i,j} + T_e)}{m_{i,j}}} \tag{2.77}$$

with e the elementary charge, k the number of different species, q_i the respective charge state, $n_{i,j}$ the respective particle density, $T_{i,j}$ the respective temperature and $m_{i,j}$ the respective mass. Setting the currents equal and crossing out e on both sides gives

$$n_e \cdot \sqrt{\frac{kT_e}{2\pi m_e}} \cdot e^{\frac{e(\Phi_w - \Phi_p)}{kT_e}} = \sum_{j=1}^{k} q_j n_{i,j} \sqrt{\frac{k(T_{i,j} + T_e)}{m_{i,j}}} \tag{2.78}$$

thus

$$\frac{e}{kT_e}(\Phi_w - \Phi_p) = \ln\left[\sum_{j=1}^{k} \frac{q_j n_{i,j}}{n_e} \sqrt{\frac{2\pi m_e (T_{i,j} + T_e)}{T_e m_{i,j}}}\right] \tag{2.79}$$

and finally, using equation (2.69) for n_e,

$$\Phi_p = \Phi_w + \frac{kT_e}{e}\left[\ln\sum_{j=1}^{k} q_j n_{i,j} - \ln\left(\sum_{j=1}^{k} q_j n_{i,j} \sqrt{2\pi \frac{m_e}{m_{i,j}}\left(1 + \frac{T_{i,j}}{T_e}\right)}\right)\right] \tag{2.80}$$

The plasma potential difference to the wall $(\Phi_w - \Phi_p)$ is typically some tens of Volts. This has been experimentally observed as well [28]. Typically, both the ion and electron temperatures in the plasma sheath are assumed to be on the order of a few eV. In Section 3.1 I will describe how the plasma density is used in two- and three dimensional self-consistent extraction models for ion sources and ECR ion sources in particular.

2.2.6 Extraction Systems

The extraction system is a series of electrodes with the purpose of accelerating and guiding the ions that come out of the source to the beam line. The minimum number of electrodes is two (*diode system*). This includes the *plasma electrode*, which is in contact with the ion source plasma and has a hole, the *extraction aperture*, through which the beam can exit the source. The plasma electrode is at the same potential as the source itself. The distance between plasma electrode and the next electrode is usually called *extraction gap*. Often a *puller electrode* is added, which is biased negatively with respect to ground potential to keep electrons created further along the beam line from back-streaming into the source. This improves source stability. The simplest system including such a puller electrode consists of three electrodes (plasma-, negative-, ground potential) and is called *accel-decel triode system*. More sophisticated designs exist with even more electrodes on individually adjusted potentials (four electrodes - *tetrode system*, etc.).

2.2.7 Extracted Current

For a planar diode geometry, the maximum current density J that can be extracted from a plasma source is given by the *Child-Langmuir law*:

$$J = 1.67 \cdot 10^{-3} \left(\frac{Q}{mc^2}\right)^{1/2} \frac{V_0^{3/2}}{d^2} \quad [A/m^2] \tag{2.81}$$

with Q the charge, m the mass of the extracted particles, V_0 the extraction voltage (difference between the two electrodes of the diode system), c the speed of light, and d the distance of the two electrodes. However, this is strictly an upper limit imposed on the system by the space-charge of the beam. Two important factors limit this further:

1. The high voltage breakdown in vacuum limits the actual voltage that can be applied to the electrodes.

2. The plasma must be able to provide the necessary current.

In reality, the maximum current from an ECR ion source is limited by the flux of ions leaving the plasma, the ion loss rate (cf. equation 2.77). In [66] Melin et al. also provide an alternate expression depending on the confinement time rather than the ion temperature:

$$I_i^q = \frac{1}{2}\frac{n_i^q qeV_{ex}}{\tau_i^q} \tag{2.82}$$

with n_i^q the density of ion species i in charge state q, τ_i^q the confinement time, and V_{ex} the plasma volume connected to the extraction aperture through magnetic field lines. Both expressions are somewhat academic, because τ_i^q is not really known and must be approximated (which is done in [66]) and V_{ex} is not static, but depends on collision and diffusion processes. Similar problems exist with the ion density n_i. But, let us assume we have a good idea of what the current density at the extraction aperture will be for the ion source in question. Then the extraction system (diode distance and shape) and voltage must be chosen such that the beam is matched well into the subsequent LEBT. This means the focusing at the extraction aperture due to the formation of a *plasma meniscus* should lead to a laminar flow through the extraction system. As shown by R. Geller [14, pp. 293], the shape of the meniscus can to first order be approximated by the switching out J and d in the Child-Langmuir law and modifying it with a geometry factor $\sqrt{1 + e(\pi)}$:

$$d(\pi) = \frac{2}{3}\epsilon_0 \left(\frac{2q}{m}\right)^{1/4} \frac{V_0^{3/4}}{J^{1/2}} \sqrt{1 + e(\pi)} \tag{2.83}$$

where d is the distance from the puller electrode to a point π on the plasma surface. $e(\pi)$ takes into account the actual shape of the electrodes and is 0 for plane electrodes and a homogeneous plasma [14]. The plasma meniscus and extraction of a beam from the plasma surface will be discussed in detail in Chapter 6.

2.2.8 Theoretical Emittance of an ECRIS

Typically, the emittance of an ECR ion source will consist of two contributions [9, 14, 72]:

1. The thermal emittance: ϵ_{th} (due to the transversal temperature the ions acquired while they were inside the plasma)

2. The magnetic emittance: ϵ_{mag} (due to the beam rotation induced by the decreasing axial magnetic field)

Ad 1. The thermal emittance can be estimated by assuming that the velocity distribution of ions inside the plasma is Maxwellian [41, 73]. The normalized rms emittance is then:

$$\epsilon^{th}_{n-rms} = 0.016 \cdot r\sqrt{\frac{k_B T_i}{A}} \tag{2.84}$$

in mm-mrad, with $k_B T_i$ the ion temperature in the plasma in eV, A the mass-number, and r the radius of the extraction aperture in mm. This is for x-x' as well as y-y', assuming a round beam.

Ad 2. Due to the high collisionality of the ions inside the plasma, we assume that they have no 'memory' of the transport processes before reaching the sheath at the extraction aperture. They are thus said to be 'born' close to the aperture, in a region of high magnetic field (up to 3 T for high performance ECRIS). That field rapidly decreases to zero in axial direction thus inducing rotation of the beam (conservation of canonical angular momentum or *Busch's theorem* [41, 74]). A short derivation of the emittance due to this can be found in Geller's book [14] and a paper by W. Krauss-Vogt et al. [75].

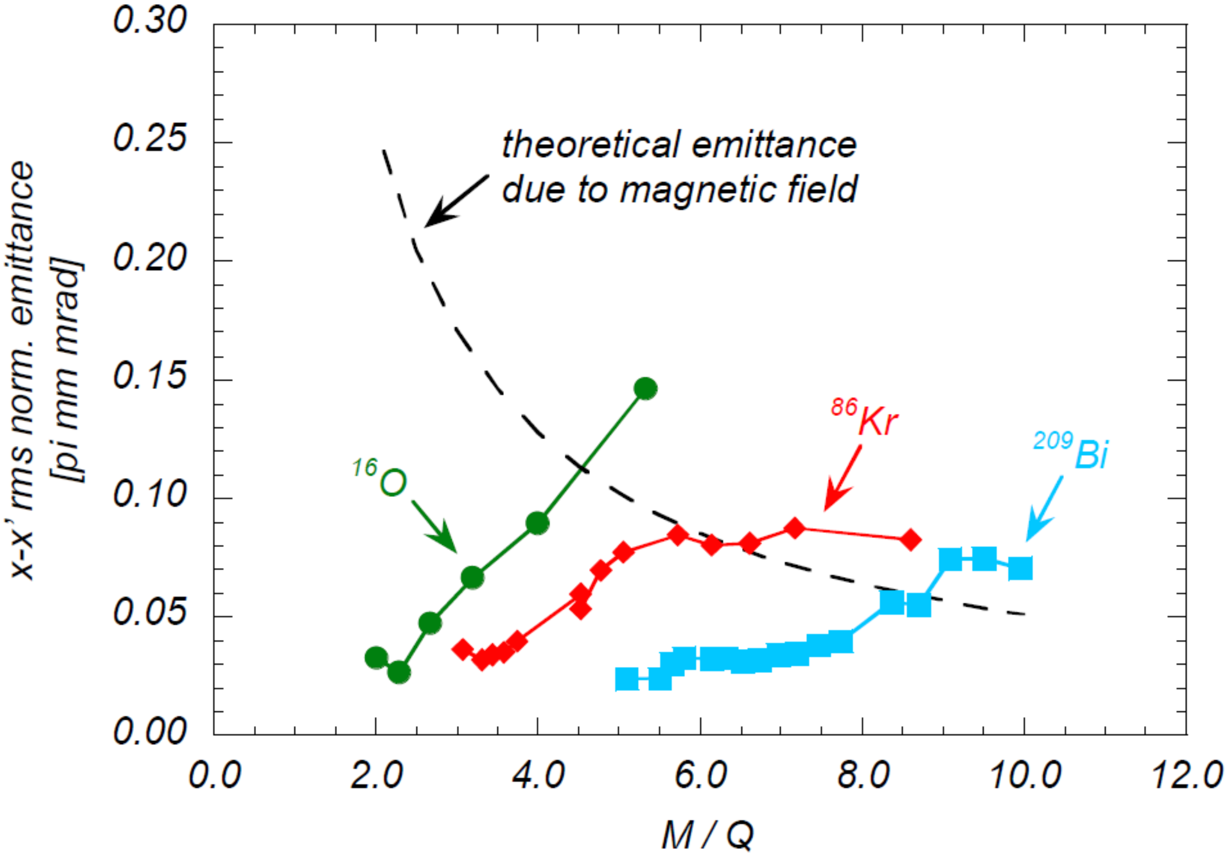

Figure 2.14: Measured emittances of the Lawrence Berkeley National Laboratory AECR-U compared to the theoretical prediction of magnetic emittances. Image taken from [9]

The magnetic emittance can then be written as:

$$\epsilon_{n-rms}^{mag} = 0.032 \cdot r^2 B_0 \frac{1}{A/q} \tag{2.85}$$

in mm-mrad, with B_0 the axial field at the extraction aperture in T, r the radius of the aperture in mm, and A/q the mass-number to charge-state ratio (dimensionless). The total normalized rms emittance is then the sum of the two contributions. However, for typical ECRIS parameters ($T_i \approx$ a few eV [66], $B \approx$ 1-3 T) the magnetic emittance clearly dominates these theoretical values. The theoretical emittance due to equations 2.84 and 2.85 is in contradiction with measured emittances of high performance sources. For instance LBNL's

AECR-U [9]. Figure 2.14 shows the measured emittance values and the prediction for the magnetic emittance. It is assumed that the reason for this discrepancy is the fact that higher charge states are confined closer to the center of the source and the radius r used in the theoretical approach has to be modified appropriately (see [76] for similar results with another ECRIS). This behavior has been observed experimentally as well: (i) It was seen that high charge state ion currents decrease less than lower charge states when the plasma aperture diameter is decreased [77]. (ii) Measurements with a movable faraday cup close to the extraction aperture showed bloated triangular distributions of ions with different charge states with sizes depending on the charge state [78]. From the theoretical emittance ϵ_{th} and the measured emittance ϵ_{act}, an effective plasma aperture, the *virtual aperture*, can be defined [9].

$$r_{eff} = r_{act} \cdot \sqrt{\frac{\epsilon_{act}}{\epsilon_{th}}} \tag{2.86}$$

Such an effective aperture radius can be used in simulations, to better reproduce the measured emittances. Something similar has for example been done in [76].

Chapter 3

Software

In general, the electric and magnetic fields of the complex electrode and magnet geometries in an ion source, beam transport system, or accelerator cannot be solved by hand anymore. Similarly, calculation of the many possible different trajectories of particles making up the ion beam is a non-trivial problem. Especially when including the electrostatic self field interaction between individual beam particles. Consequently, simulations play an important role in the design and study of ion sources, beam transport and accelerators. In this chapter, I will describe the three simulation programs used in the course of this thesis as well as the utility software I programmed.

3.1 Simulation Codes

In this thesis, I mainly used three ion beam simulation codes: SIMION, IGUN and WARP. SIMION and IGUN are commercial software and will only be described briefly in the following Subsections 3.1.1 and 3.1.2. WARP is a particle in cell (PIC) code in ongoing development by Lawrence Livermore National Laboratory (LLNL) and Lawrence Berkeley National Laboratory (LBNL) and was used extensively during this thesis work (simulations in Chapters 6 and 7). It will be described in greater detail in the following Subsection 3.1.3.

3.1.1 SIMION

SIMION 8 [79] is a widely used ion optics simulation program. It provides a graphical user interface, the *ion optics workbench*, that allows the user to create and manipulate (position, rotate, and scale) up to 200 instances of electrostatic and magnetostatic *potential arrays* (PA). PA's can be created either manually in the GUI, or through geometry (*.gem) files written by the user, or through import from CAD data in the *.STL format. Mirror and rotational symmetries can be exploited in the creation of the potential arrays to reduce computation time and memory usage. Once a PA has been created, the potentials between the electrodes are calculated by solving the Laplace equation on a square mesh (*refining* in SIMION jargon) through a finite difference method (*over relaxation*) [79, p 2-2]. Once the solution has been calculated, SIMION can scale the potentials for different voltages applied to the respective electrodes (*fast adjusting*).

Ions can then be flown inside the workbench. In SIMION, a fourth order *Runge-Kutta* method is used for the calculation of the ion trajectories.

A very important feature that was heavily used in this work are *workbench programs* that can be written by the user in the scripting language *Lua*. Through the workbench program, SIMION provides access to certain steps of the ion trajectory calculation letting the user change, e.g., ion positions and velocities, electrode voltages and magnetic fields. Data acquisition and output can be regulated through workbench programs as well.

A new feature of SIMION 8.1 over version 8.0 is the *Poisson Solver* that enables the user to create an arbitrary charge distribution in a PA and solve for the electrostatic field. This was used in Chapter 5 to calculate the space charge potential for various asymmetric beams and obtain secondary ion energy distributions of ions created by beam-residual gas interaction.

3.1.2 IGUN

IGUN [31–33] is a numerical simulation code for ion beam formation at a plasma boundary. IGUN is a 2D code in RZ coordinates, exploiting the fact that most extraction systems are rotationally symmetric and in many cases, the extracted beams are as well. The problem is set up in IGUN by the user through an input file containing the basic parameters (INPUT1), axial values of the magnetic field (INPUT3), boundary points of the electrodes, and runtime variables (INPUT5) [33].

IGUN then solves the problem by iterating multiple times over the following steps until a stable solution has been reached [31]:

1. Solve Poisson's equation for the potential map. This is done on a rectangular mesh using a finite element method and a successive over-relaxation solver (SOR).

2. Solve the equations of motion for the macro-particles using ray-tracing with a fourth order Runge-Kutta procedure.

3. Allocate space charge to the potential map. This is done in two steps: Inside the plasma sheath, the space charge is calculated analytically using a 1D sheath model. Outside the sheath the space charge density is generated from the particle trajectories obtained in step 2 multiplied with a compensation term according to the thermal distribution of electrons.

The magnetic field data (if specified) is given as $\mathrm{B}_z(z)$ at $r = 0$ and the field values for $r > 0$ are calculated through radial expansion up to order 6.

3.1.3 WARP

WARP [36, 80, 81] is a particle-in-cell (PIC) code originally developed for the simulation of intense ion beams used in heavy-ion driven inertial confinement fusion (HIF).

In PIC, macro-particles representing a number of real particles are advanced in time using the Lorentz equation of motion. Electrostatic self-fields of the particles are calculated self-consistently on a mesh. Particles are advanced through a combination of the *Leapfrog* and *isochronous Leapfrog* methods [82].

3.1.3.1 Main Packages (python class name in *italic*)

The main package supervising the simulations is called *top*.

For advancing particles and solving for the electrostatic fields (external plus self-fields) WARP has three different geometry modes:

- WARP3d (particles: *w3d*, field solver: *f3d*). The full three dimensional model.
- WARPxy (particles: *wxy*, field solver: *fxy*). A transverse slice model.
- WARPrz (particles: *wrz*, field solver: *frz*). A cylindrically symmetric model.

The separation of particle pusher and field solver enables the user to combine 3D pusher and RZ field solver for cases where the electrodes are RZ symmetric, but a 3D treatment of the beam is necessary.

In addition to the PIC model, there is also an envelope solver (package: *env*). The envelope solver has not been used in this thesis and will not be described further.

3.1.3.2 Particle Loading

Particles are loaded and injected separately. This is practical since the same initial distribution loaded can be used with different injection methods or in different geometry modes in subsequent simulation runs. WARP provides a variety of built-in initial transversal particle distributions: Gaussian, Semi-Gaussian or K-V (uniform). Longitudinal distributions can be cigar shaped or uniform. WARP also lets the user specify arbitrary transversal and longitudinal particle distributions. The loaded beam can then be injected in one of two ways: *Constant current*, or *space charge limited*.

3.1.3.3 Fields and Lattice Elements

WARP has four built in lattice elements: *quadrupoles, dipoles, bends*, and *acceleration gaps*. Lattice segments can be periodically extended. Special attention should be given to the bend, which is not a lattice element per se, but rather a region of coordinate transformation. In this region, specified by a start point, end point and bending radius, Frenet-Serret coordinates are used to transform the bend into a straight line. These elements are used in superposition with all forms of dipole elements to keep the design trajectory straight.

In addition to the built-in lattice elements, WARP lets the user set electrostatic or magnetostatic external fields in a number of ways:

- Hard-edged multipole description
- Axially varying multipole description
- Gridded elements

For the first two types of descriptions, WARP calculates the fields at the particle position through multipole expansion. Gridded elements are given on a 3D grid and are interpolated to the particle position as needed.

The user can also generate electrode geometries, specify their voltages, and have WARP calculate the electrostatic fields directly.

In addition, there are supplemental python scripts for generating realistic models of common beam optics elements like electrostatic quadrupoles or solenoids.

3.1.3.4 Fieldsolvers

In 3D and in transverse slice mode, the self field of the beam is calculated on a Cartesian mesh. WARP has a variety of field solvers at its disposal (fast Fourier transforms - FFT, capacity matrices, successive over relaxation - SOR, and the multigrid solver - an extension of the SOR solver which utilizes additional coarser grids to speed up the calculations). Because we need to resolve rather complex structures in some of the electrodes, the SOR and multigrid solver are used for the simulations in this thesis. In WARP the variable *fstype* sets the fieldsolver with 3 being the SOR solver and 7 the multigrid solver.

3.1.3.5 Structure of the Simulations

Typically a script written to run a WARP simulation is called a *deck*. A WARP deck consists of the following segments:

- Setting the basic run time parameters. This includes some descriptive strings, size, cell size and boundary conditions.
- A call to **setup()**. This is mandatory and initializes some plotting routines.
- Setting up the lattice elements. This can be done in any of the ways described above.

- Loading the particles and specifying injection of the particles
- Selecting the package. This could e.g. be **package('wxy')** to select the WARPxy PIC package.
- A call to **generate()**. This initializes the PIC simulation, allocates space, transforms lattice arrays into the internal format for faster processing, etc. Note: In general the simulation variables, particles and fields should be set up before the generate. However, there are some convenience functions (e.g. **addparticles()** to load particles) that can be called after the generate() because they can re-allocate the necessary memory.
- Finally, once the problem has been set up (whether in 3D, RZ or XY), the function **step()** is called to run the simulation. Each call to step advances the simulation by either one time step dt (3D, RZ) or one slice dz (XY). Step() can also be called with a number of steps as an argument (e.g. step(100)).

In Chapter 6, I will go into more detail about the WARP packages used for the respective simulations of ion beam extraction and low energy beam transport, how the particles were initialized and loaded, and how the beam optics elements were set up.

3.2 Utility Programs

As mentioned in the previous section, WARP does not provide a graphical user interface (GUI). For IGUN, there exists a suite of programs providing some GUI functionality, but they were developed for Windows XP and are not well supported under Windows 7 and 8. In IGUN, a user generated input file is read in upon start of the program and WARP is run from inside a python script environment. In this section I will briefly describe the utility programs and postprocessors I wrote to simplify the use of IGUN and WARP.

All utility programs are written in python 2.7. The following libraries were used:

- **Numpy** [83]. Numerical library providing a number of array and matrix manipulation functions.
- **cPickle**. A python library for fast and reliable saving and loading of python objects (class instances, arrays, etc.).
- **Matplotlib** [84]. An extensive library for 2D plotting.
- **PyGTK** [85]. GUI development through GTK+2.0 API bindings for python.

In addition, **cxFreeze** [86] was occasionally used to create standalone executables from the python scripts.

3.2.1 Electrode Designer

In both IGUN and WARP, the electrode geometry is provided by the user in form of arrays of vertices and arcs. Without visual feedback, this can be cumbersome, especially if the electrodes have complex shapes. It suggested itself to write a simple GUI to generate the electrodes point-by-point and subsequently export them into IGUN or WARP. The electrode designer provides an easy interface where the user can create and delete electrode objects consisting of vertices and arcs. The state of the program can be saved and re-loaded at any time. The image shown in the preview section can be saved as a *.png image file.

A 1D array containing magnetic field data $B_z(z)$ on axis can be loaded into the program and displayed in the preview windows for WARP and IGUN.

3.2.1.1 IGUN export

In the IGUN preview window, the user can set a number of geometry constraints and specify a set of ion species (m, q, current) to simulate. Exporting for IGUN creates a *.IN file which can directly be run in IGUN. Additional parameters can be set by editing the exported text file.

3.2.1.2 WARP export

Exporting for WARP does not include particles or setting up the whole simulation. This is because WARP is a lot more complex than IGUN and many parameters have to be set appropriately. When the electrode data is exported for WARP, three files are created: A file containing the electrode geometry, a file containing meta data (voltages, id's, and names of the electrodes), and a simple WARP script that can be run immediately called 'main.py'. The script reads in the electrode data, performs a single field solve, and displays the calculated electrostatic field.

3.2.2 WARP Postprocessor

In order to evaluate the results from the WARP simulations, I developed a postprocessor GUI. During the simulations, data is saved depending on the user settings and the type of the simulation. In xy-slice mode, by default, the particle distributions at the start and the end are saved as well as the envelopes (maximum extent and 2-sigma envelopes). Additional locations to save the particle distributions can be specified. In 3D mode, only the particle distributions at the start and the end are saved at this time. All files are written to disk using cPickle. The so obtained data files can then be opened in the postprocessor. The main area of the GUI is a notebook object with several pages:

- Pages 1-5: XY, XX', YY', XY', YX' distributions, respectively.
- Pages 6,7: Horizontal and vertical beam envelopes.
- Page 8: A combination plot of the horizontal and vertical envelopes.
- Page 9: A text window to display the file containing settings and results of the simulation.
- Page 10: A log of the operations performed in the postprocessor since starting the program

Apart from standard graphics operations like changing labels and titles of the plots, zooming, and setting the limits, etc., the postprocessor features the following functionalities:

- Loading multiple data sets for comparison.
- Switching on and off the viewing of individual data sets.
- Calculation of emittances and beam sizes from the particle distributions.

- Loading of lattice description files for display with the beam envelopes.
- Loading of IGUN *.TRJ files. These files contain the results of IGUN RZ symmetric simulations. The postprocessor can calculate a XY particle distribution from the *.TRJ file via a randomization process written by A. Lemut in C and ported to python. This process includes skew angles due to the magnetic field following a procedure described by Chan *et al.* [87].

The postprocessor features the following export options:

- Saving the plots as *.png image files.
- Creating 2D histograms from the cross section and phase space plots to compare to emittance scans and beam viewer images.
- Saving particle data as comma separated value (*.csv) files for import into Excel or other programs.

3.2.3 NeMo Postprocessor

With the GUI foundation already in place, it suggested itself to also create a postprocessor for the neutralization measurements discussed in chapter 5. As in the WARP postprocessor, the main area is a gtk notebook with several tabs which correspond to the different datasets that can be loaded into the postprocessor and manipulated there:

- Pages 1,2: Neutralization spectra obtained with the retarding field analyzer *NeMo* and the simple xy plotter program *ecrtune*.
- Page 3: Charge state distributions (CSD) obtained with the analyzing magnet and *ecrtune*.
- Page 4: Charts obtained by logging the EPICS-channels of the NSCL's control system. These include faraday cup currents, ion gauge readings, and the ion source drain current.
- Page 5: Slit scans of the ion beam cross section obtained with the four-jaw slits discussed in Subsection 4.2.4.
- Page 6: A log of messages from the program to the user.

In all viewports, limits, labels, linewidths, legends, titles, etc. can be set individually. Furthermore, the following options are available for data manipulation:

Ad pages 1,2, and 3: Analysis options for charge state distributions and NeMo spectra include:

- Cutting the data sets individually
- Interpolating.
- Smoothing.
- Normalizing.
- Fitting peaks in the charge state distribution.
- Calculating first and second derivatives of NeMo spectra.
- Calculating preliminary neutralization values from NeMo spectra.

Ad page 4 (the chart viewer): Channels can be scaled individually and deactivated from the view screen. Average and standard deviation of all selected channels can be calculated for the currently displayed time frame (horizontal axis).

Ad page 5 (slit scan viewer): Here, the maximum intensity can be set for the colormap and the slit scan image can be exported to be used as a density map for creating charge distributions and particle distributions in SIMION. The export options include: scaling of the image size, rotating the image, and normalizing it to the correct total current.

Chapter 4

Hardware

4.1 Electron Cyclotron Resonance Ion Sources

4.1.1 LEDA injector ion source

The high current proton source was originally developed at Chalk River Laboratories [88] and subsequently modified for operation as the ion source of the low energy demonstration accelerator (LEDA) at Los Alamos National Laboratory [7, 89, 90]. Of the four ion sources used in this thesis, the LEDA injector ion source is different from the other sources in the requirements and as a consequence in the design of the magentic field. The LEDA injector source was designed to provide very high currents (up to 130 emA) of protons. For single ionization, the required energy of the electrons in the plasma is much lower than in high-charge-state ECRIS. Also, the necessary confinement times for single ionization are short compared to the step-by-step process necessary to achieve medium to high charge states. As a consequence, there is no sextupole for radial confinement. Instead, the two solenoids are close enough together to form a single peak in the longitudinal magnetic field structure. A schematic of the source is shown in Figure 4.1 and the important parameters are listed in Table 4.1. During peak operation under optimal conditions, the beam is composed of 85 - 90% protons and 10 - 15% H_2^+ ions [90].

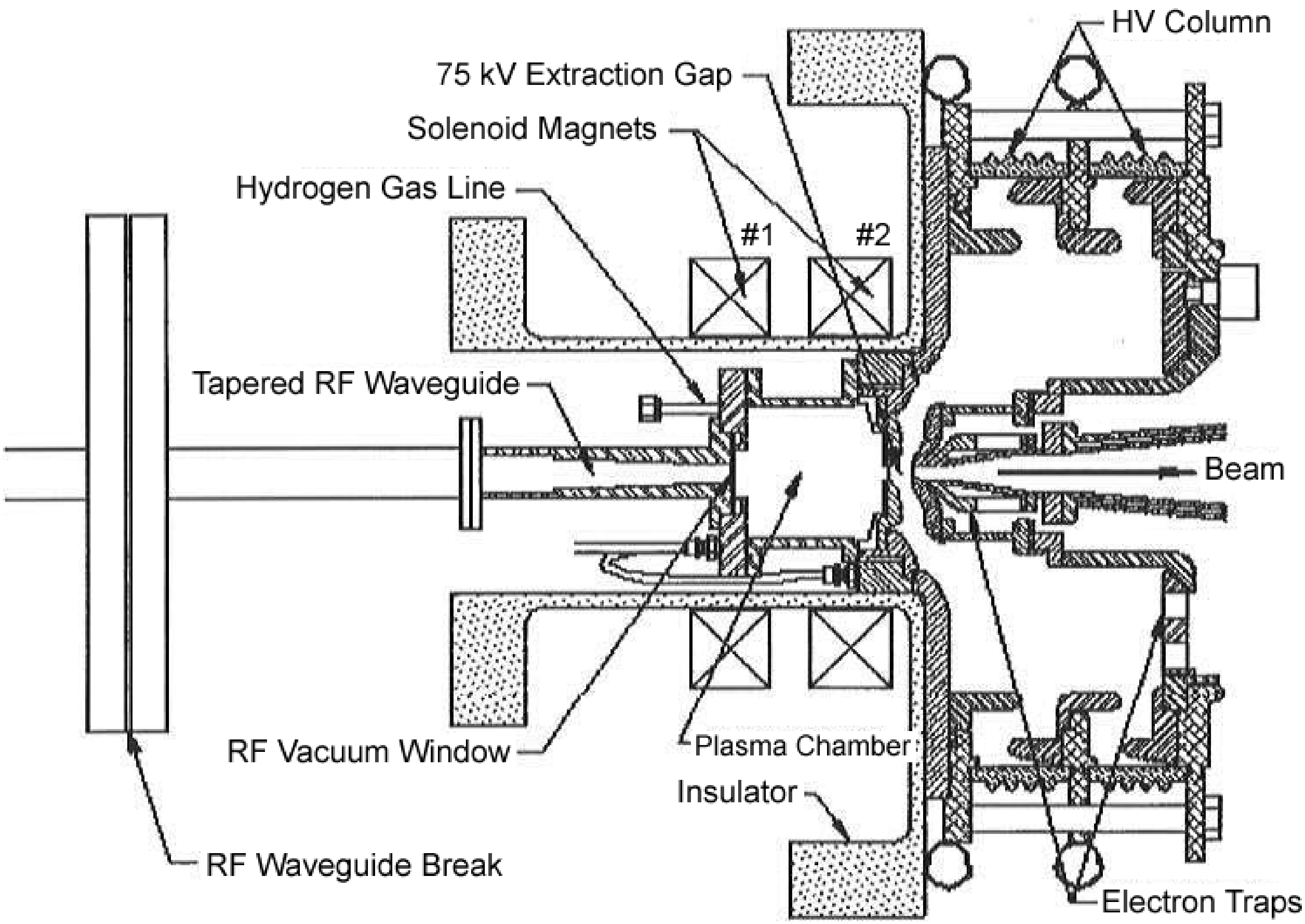

Figure 4.1: Schematic of the LEDA injector ion source. Image taken from [10].

The extraction system as of 1997 is a tetrode accel-decel extraction system. In 2012, the LEDA source was transferred to NSCL for a short time. During this time, neutralization measurements (described in Section 5.3.1) were conducted. It should be noted that during the time at NSCL, the extraction aperture diameter was decreased from 8.6 mm to 3 mm and, consequently, the extracted current was drastically reduced (during the presented measurements it never exceeded 10 emA).

Table 4.1: LEDA - Ion Source Parameters

Parameter	**Value**
Extraction Voltage	max. 75 kV
Proton fraction	85 - 90%
Chamber ∅	90 mm
Chamber length	100 mm
B_{max}	0.0875 T
f_{ecr}	2.45 GHz
MW power	max. 800 W

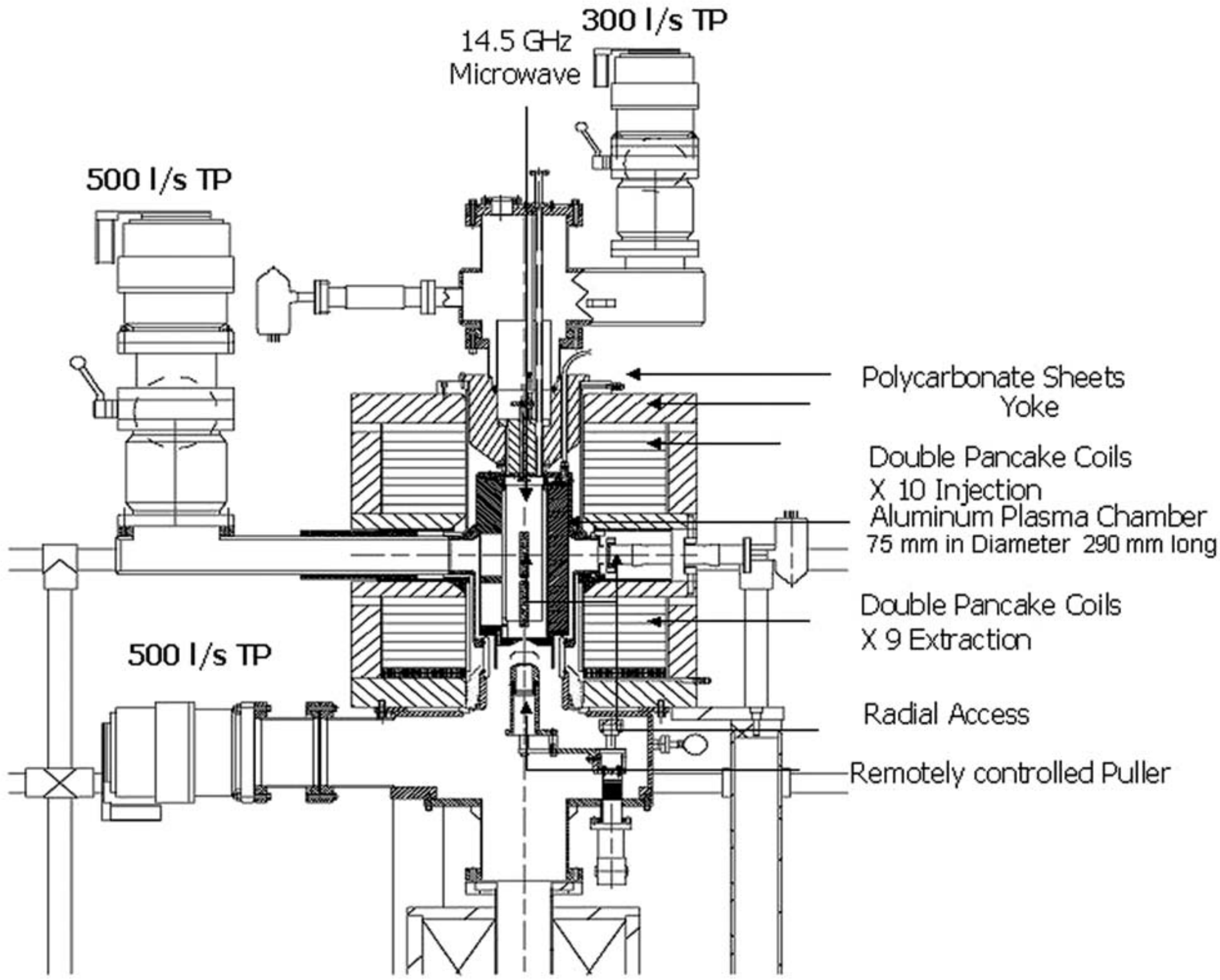

Figure 4.2: Schematic of Artemis B (a duplicate of Artemis A). Image taken from [11]

4.1.2 Artemis A - Room Temperature ECRIS

The Advanced Room TEMperature Ion Source Artemis [11,91,92] is located at the National Superconducting Cyclotron Laboratory (NSCL) at Michigan State University. It is one of the two injector ion sources of the coupled cyclotron facility (CCF). Its design is based on the Advanced ECR (AECR) at LBNL. The longitudinal magnetic field is provided by two room-temperature solenoids and the radial field by a permanent-magnet sextupole. It features a triode accel-decel extraction system with movable puller electrode. The neutral material for ionization is provided either in gaseous form through the gas lines or by evaporation in an oven that is inserted radially between the two solenoid coils. A schematic view of the source is shown in Figure 4.2 and the important operating parameters are listed in Table 4.2. Artemis A was designed to reliably deliver stable DC beams of medium charge state ions over long periods of time (days to weeks).

Table 4.2: Artemis parameters. Magnetic field values are nominal and subject to optimization for each desired ion.

Parameter	**Value**
Extraction Voltage	max. 24 kV
Chamber material	Aluminum
Chamber ∅	75 mm
Chamber length	290 mm
$B_{injection}$	1.8 T
B_{min}	0.2 T
$B_{extraction}$	0.8 T
f_{ecr}	14.5 GHz
MW power	max. 2 kW

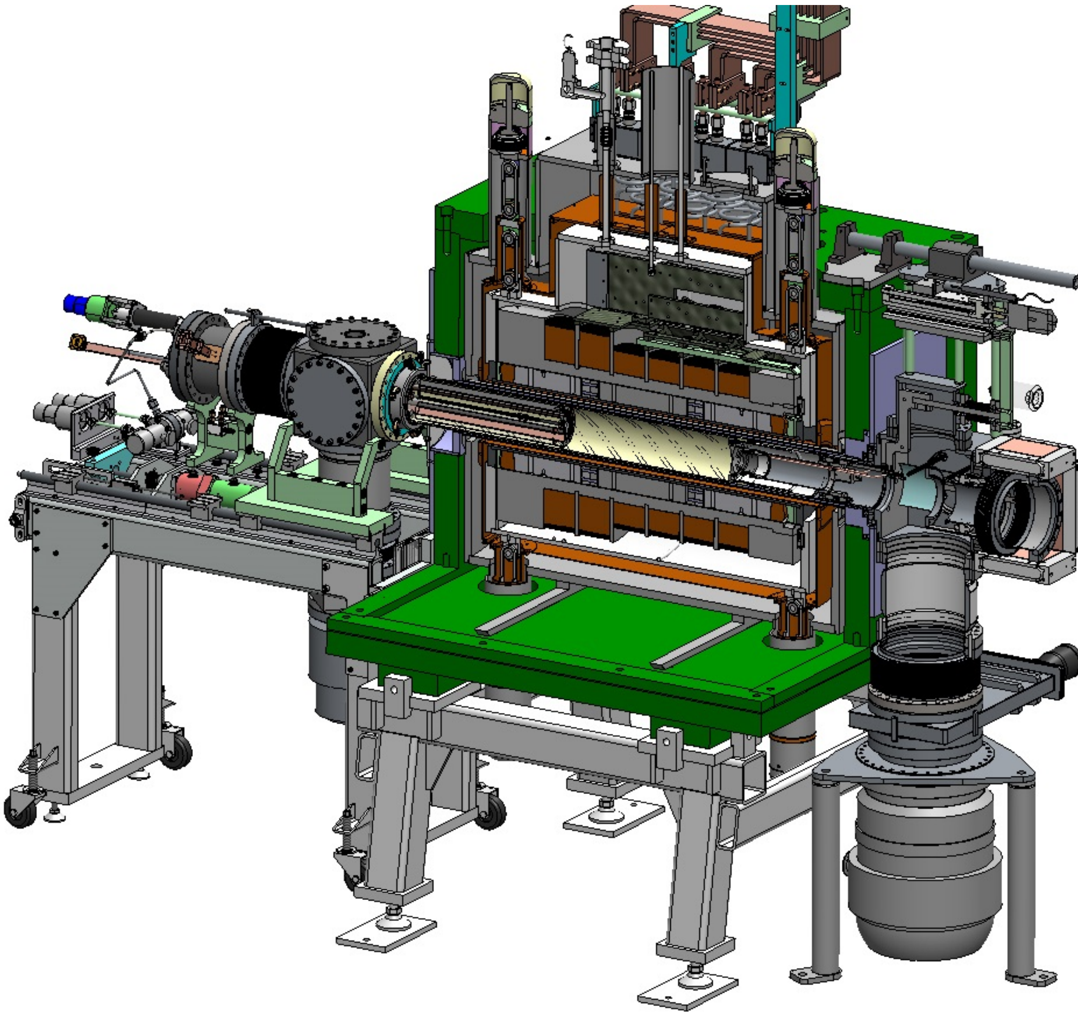

Figure 4.3: 3D CAD model of the SuSI ECRIS. In the center the plasma chamber can be seen, sorrounded by the six solenoid coils. Gas and microwaves are fed from the left, the beam is extracted on the right.

4.1.3 SuSI - Superconducting ECRIS

The SUperconducting Source for Ions (SuSI) [2, 38, 39, 93] is located at the National Superconducting Cyclotron Laboratory (NSCL) at Michigan State University. It is the second of the two injector ion sources of the coupled cyclotron facility (CCF). A 3D CAD model of SuSI can be seen in Figure 4.3. As can be seen in the figure, SuSI features six solenoid coils, which can be adjusted individually, and a sextupole coil structure. All coils are superconducting and inside a cryostat which is kept at a temperature of about 4 K. Liquid nitrogen and liquid helium for cooling are provided by the NSCL cryoplant via fill lines. The injection flange is moveable, allowing the length of the plasma chamber to be adjusted from 400 to 500 mm. On the inside, facing the plasma, a biased disk is mounted on the injection flange. This biased disk is adjustable with respect to the injection flange by 50 mm and can be biased with voltages up to -300 V. The extraction system is a triode accel-decel system with adjustable extraction gap width. The puller is usually biased with voltages between -1 kV and -3 kV. The use of two microwave frequencies can improve the stability of the source and the production of high charge states. In the case of SuSI, the two frequencies are 14 and 18 GHz, but the magnet system is able to provide the necessary fields for 18 + 24 GHz operation and a suitable Gyrotron providing the 24 GHz microwaves is being installed at the moment.

Table 4.3: SuSI parameters. Magnetic field values are nominal and subject to optimization for each desired ion [2].

Parameter	**Value**
Extraction Voltage	max. 24 kV
Chamber material	Aluminum
Chamber ∅	100 mm
Chamber length	400-500 mm
$B_{injection}$	2.4 T
$B_{extraction}$	1.3 T
$B_{rad,wall}$	1.3 T
f_{ecr}	14 + 18 GHz, (24 GHz)
MW power	max. 2 + 2 kW, (10 kW)

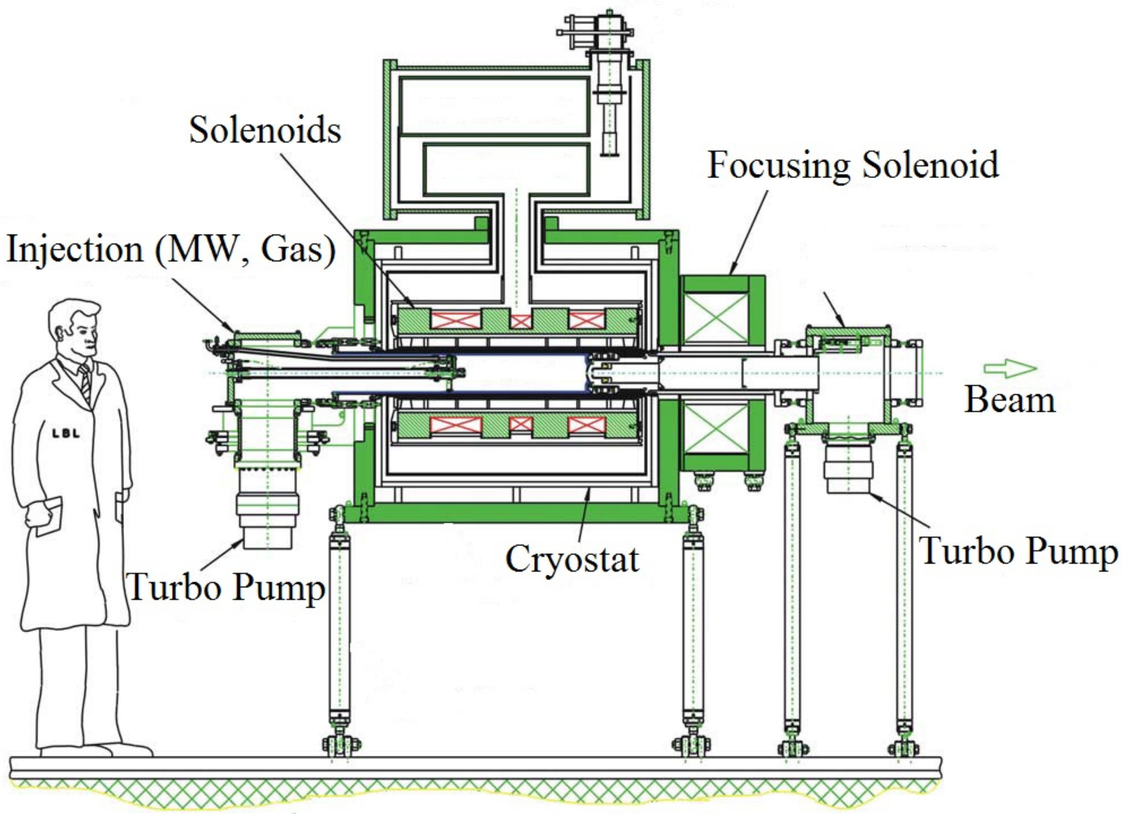

Figure 4.4: Schematic of the VENUS superconducting ion source. Image taken from [3].

4.1.4 VENUS - Superconducting ECRIS

The VENUS ECRIS [3, 8, 37, 94] is located at Lawrence Berkeley National Laboratory. It is one of the injector ion sources of the 88" cyclotron. Unlike SuSI, the VENUS cryosystem operates in a closed loop scheme, using four cryocoolers to keep the working temperature of the liquid helium at 4.2 K. No transfer of helium is necessary during operation. The longitudinal field is provided by three superconducting solenoid coils and the sextupole field by six superconducting race-track coils. The important parameters (like peak magnetic fields) are listed in 4.4.

The extraction system is a triode accel-decel system with adjustable extraction gap width. The puller is usually biased with voltages between -1 kV and -3 kV. VENUS uses double frequency heating (18 + 28 GHz), to improve the stability of the source and the production of high charge states. The 18 GHz microwaves are provided by an oscillator and a klystron amplifier, while the 28 GHz microwaves are provided by a gyrotron system. Inside the chamber, on the injection side, facing the plasma, a biased disk is located which can be biased with a negative voltage up to -300 V.

X-ray production through bremsstrahlung is an important issue in ECR ion sources and more so in superconducting sources, because the produced x-rays can heat the magnet coils and thus lead to quenching, if the cryosystem cannot compensate fast enough. In VENUS, a 2 mm tantalum shield was installed between plasma chamber and cryostat to act as x-ray shielding [95].

Table 4.4: VENUS parameters. Magnetic field values are nominal and subject to optimization for each desired ion [3].

Parameter	**Value**
Extraction Voltage	max. 25 kV
Chamber material	Aluminum
Chamber ∅	140 mm
Chamber length	500 mm
$B_{injection}$	4 T
$B_{extraction}$	3 T
$B_{rad,wall}$	2.4 T
f_{ecr}	18 + 28 GHz
MW power	max. 2 + 10 kW

4.2 Beam Diagnostic Instruments

In this section, I will describe the different diagnostic devices used during the measurements for this thesis. They are:

- Faraday Cup *invasive*
- A/q Analyzer *semi-invasive*
- Beam Viewer *invasive*
- Slit-Scanner *invasive*
- Allison Emittance Scanner *invasive*
- Retarding Field Analyzer *non-invasive*

Devices labeled *invasive* block the beam from travelling on, the A/q analyzer is invasive during the analysis, but is also used to single out the desired species for transport (hence *semi-invasive*) Many of the diagnostic devices have been around for many years and are well known. For these, only the basic principle will be recapitulated, and references will be given to original material.

4.2.1 Faraday Cup

The faraday cup is a basic diagnostic device to measure the total beam current. A schematic of its operating principle is shown in Figure 4.5. A conducting cup is used to collect the positively charged beam ions and a Picoammeter is used to read out the charge per second deposited on the cup. In the case of NSCL, specially designed beam current monitors (BCM), which were designed and built in-house, are used. Because the impact of highly charged ions on a surface leads to the escape of slow (typically 1-50 eV) electrons from the

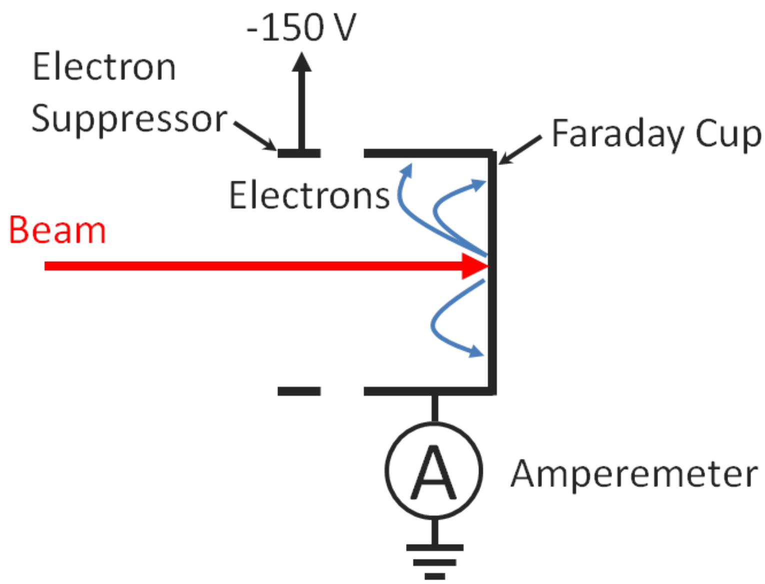

Figure 4.5: Faraday cup schematic. The positive ion beam deposits charge on the cup. Electrons leaving the material due to the ion impact are pushed back onto the cup by a suppressor on a negative potential.

surface material, the current reading of the amperemeter would be artificially high (sum of ions + sum of escaping electrons) for just the cup. To counteract this, an electron suppressor is typically used, which is biased at a negative voltage (up to -300 V). This ring creates a potential barrier that pushes the electrons back onto the cup (as indicated in the figure). Regular faraday cups can withstand a beam power of up to a few hundred watt. Above that, the heat dissipated in the material could destroy the cup. More elaborate designs exist, using special shapes to better distribute the heat load on the cup surface, and cooling systems to transport the heat away from the cup. The beams from the ECR ion sources with sextupole (Artemis, SuSI, VENUS) are below 150 W, and regular faraday cups were used. The LEDA ion source beams reached powers above 700 W. Here the currents were measured with Bergoz current transformers [96] and on a cooled beam stop at the end of the short LEBT, as well as by recording the drain current on the source high voltage power supply.

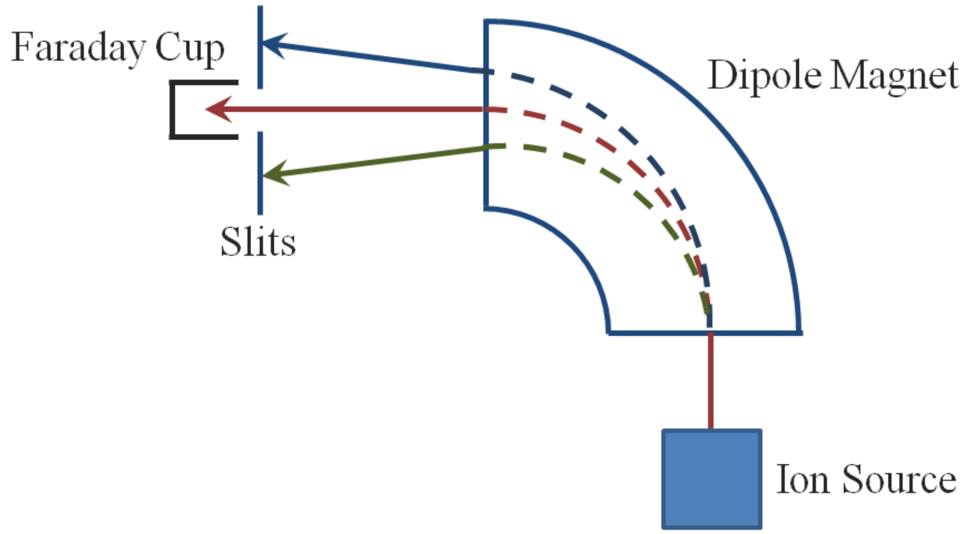

Figure 4.6: Cartoon picture of the A/q analyzer principle.

4.2.2 A/q Analyzer

Assuming the particles move in the horizontal plane, they are bent onto a curved trajectory when transversing a vertical magnetic dipole field. For the non-relativistic case and in absence of an electric field, the radius of curvature of the particle trajectory is given by:

$$r = \frac{mv}{Bqe} \tag{4.1}$$

with B the flux density of the vertical magentic field, v the particle velocity, $m \approx A \cdot amu$ the particle mass, q the charge state, and e the elementary charge. In this context, the magnetic rigidity $[B\rho]$ is often used:

$$[B\rho] = \frac{p}{qe} \tag{4.2}$$

with p the momentum of the beam particle and $\rho = r$ the radius of curvature. This expression is equivalent to equation 4.1. It follows directly from equation 4.1 that particles with different A/q ratios follow different paths inside the dipole field. This can be used to analyze the distribution of different ion species in the beam.

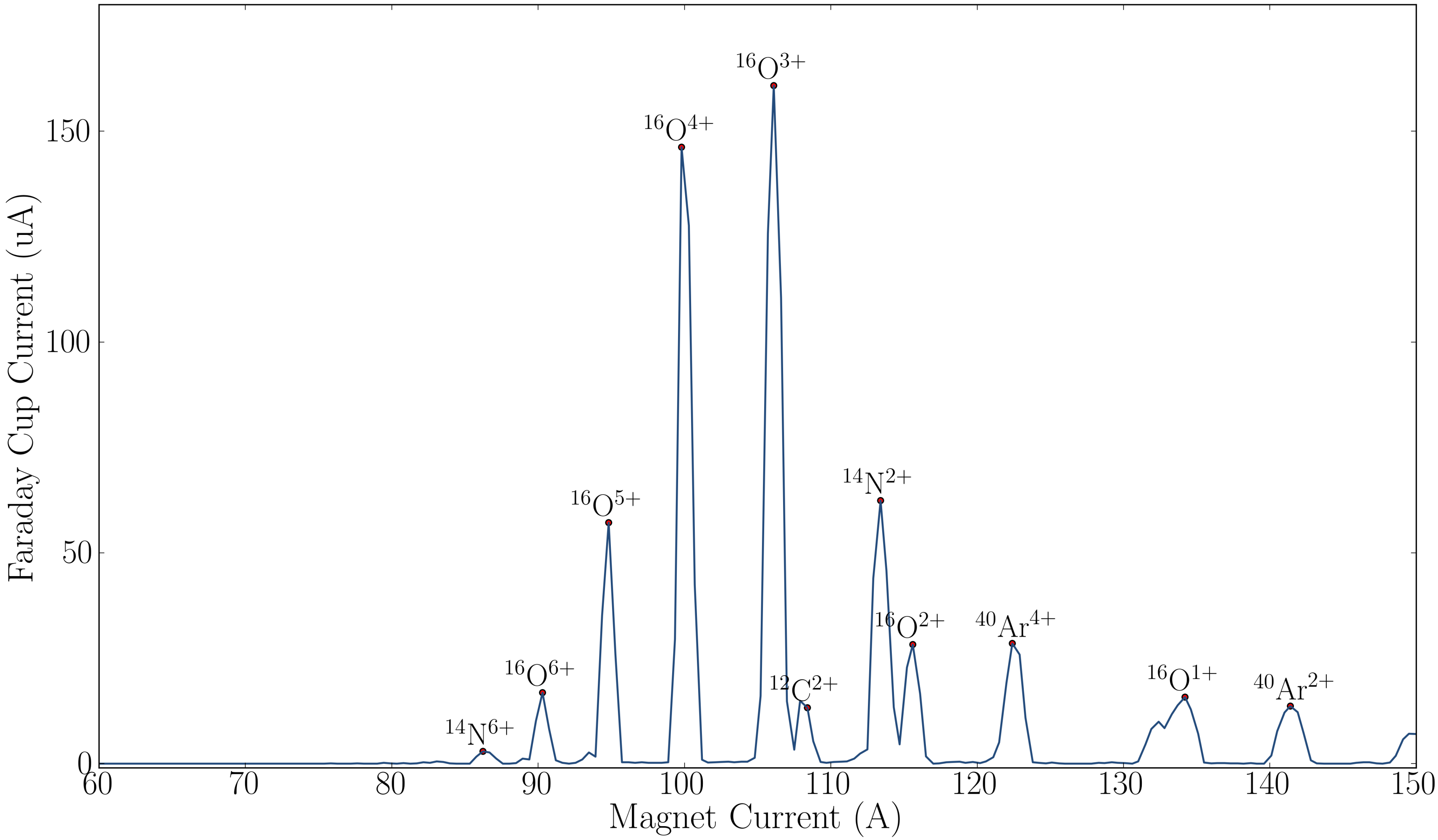

Figure 4.7: Example Charge State Distribution (CSD) of an oxygen beam from the ECRIS SuSI at NSCL. Contamination by argon from a previous experiment can also be seen as well as nitrogen from imperfect vacuum.

In order to do this a dipole magnet is combined with slits at the magnet's image point and a faraday cup right after the slits (see figure 4.6). The magnetic field is then slowly ramped up while recording the ion current in the faraday cup. This leads to a plot commonly referred to as a *charge state distribution* (CSD). An example of a typical CSD is shown in Figure 4.7 for an oxygen beam extracted from the SuSI ion source at NSCL.

4.2.3 Beam Viewer

The beam viewer or viewing screen (sometimes called a *phosphor*) is a simple device that allows us to obtain an image of the beam cross-section. It consists of a viewing plate, made of a scintillator material (like SiO_2 (Quartz), KBr, BaF_2, or YAG) that emits light upon being hit by a beam particle, and a camera to record the picture. Usually, the viewing plate has an angle of 45 degrees with the beam as well as with the camera, to get an undistorted picture of the cross section. Figure 4.8 shows the 3D CAD model of such a beam viewer designed for the AECR-U ion source at Lawrence Berkeley National Laboratory. An example of a beam cross section for an argon beam taken with this beam viewer can be seen in figure 4.9. If the beam particles deposit enough charge on the surface of the scintillator, slow beam ions can be reflected locally by those charge-patches. In order to avoid this, a fine, high-transparency mesh is often used to cover the scintillator. Electrons extracted from the wires by passing ions will then neutralize the deposited charge. The light yield of a scintillator depends on many factors like: material, intensity of the beam, charge state of the beam ions, and the duration of the exposure. One unfortunate property of scintillators is the degradation of light yield with exposure time due to radiation damage [12,97,98]. Because this effect depends on the dose and energy, spots with higher beam intensity and lower charge states will degrade faster, thereby creating a non-homogenous light yield distribution on the scintillator surface.

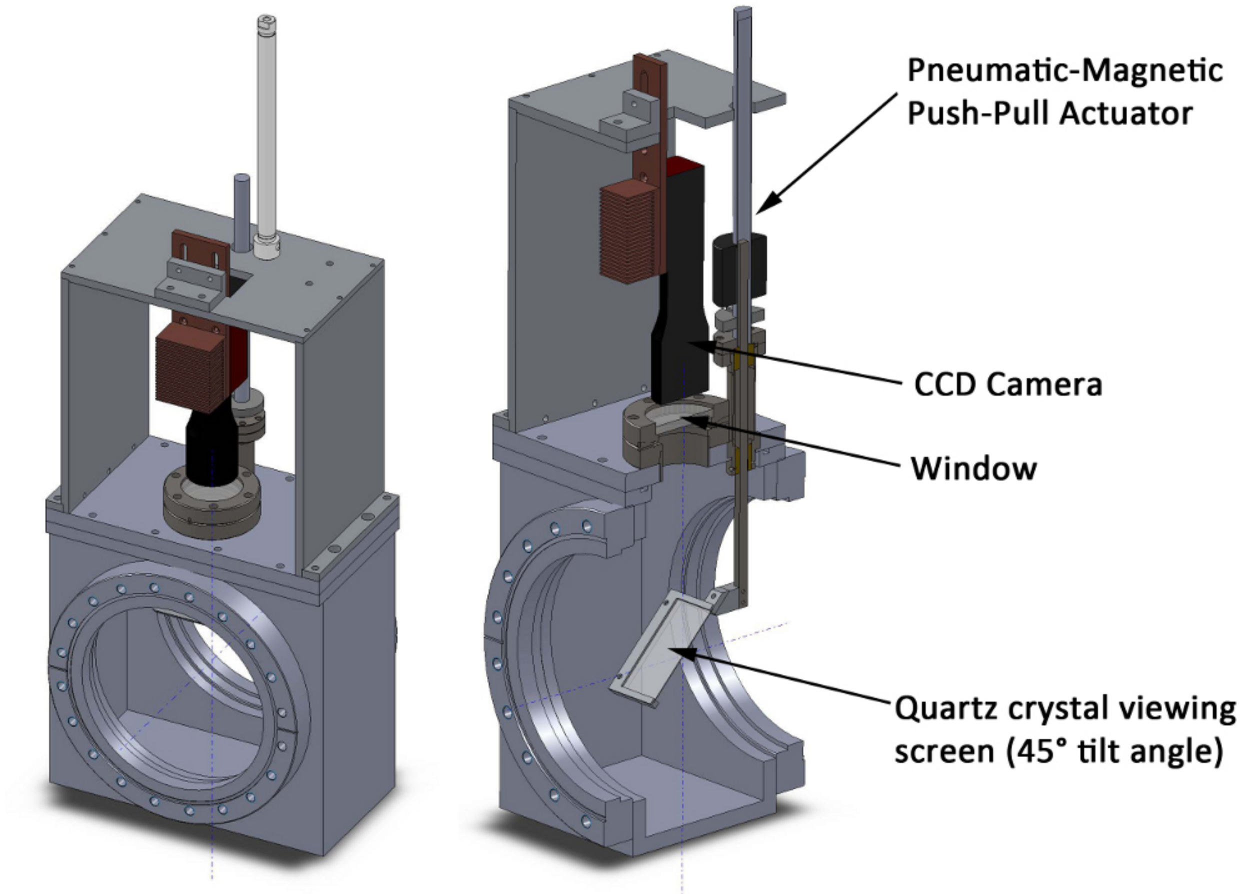

Figure 4.8: 3D CAD model of a beam viewer. This beam viewer was designed for the LEBT of the AECR-U ion source at LBNL.

In order to get quantitative results about the beam intensity distribution, these effects have to be taken into consideration. This is further complicated by the fact that the crystals can regenerate part of their scintillation strength on their own over time. In this thesis, beam viewer images are only used in a qualitative way, to get information about the shape of the beam cross section and compare them with each other and with slit profile scans. In this context the total light yield is not as important.

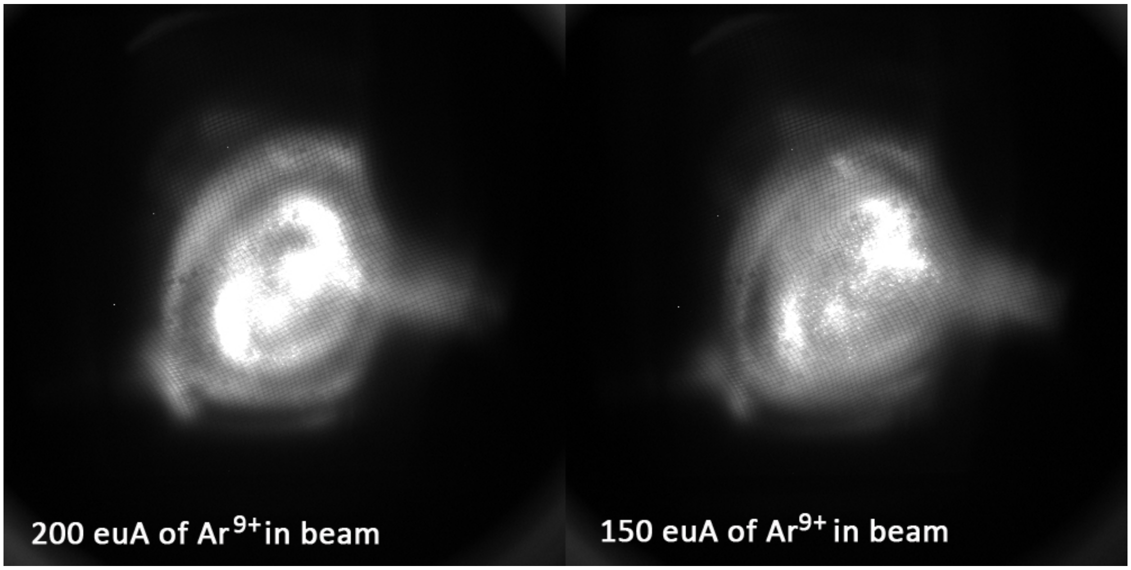

Figure 4.9: Two images taken with a quartz crystal beam viewer. The beam contained mostly argon and oxygen. Different ion species (mass m, charge state q) are focused differently in the extraction region of the source and can be seen as ring-like structures on the viewer. The fine mesh covering the crystal can also be seen.

4.2.4 Slit Profile Scanner

The slit profile scanner is a combination of two slits (horizontal and vertical) and a faraday cup. A schematic of the principle can be seen in Figure 4.10. The variant of a slit scanner used at the NSCL has individually moveable left and right (upper and lower) plates, which earned it the name *4-jaw*. This way, not only the position of the slits can be changed, but also the width. In a slit scan, the slits are moved stepwise to raster the cross sectional area of the beam. At each slit setting, the partial current arriving at the faraday cup placed right behind the slits is recorded. A beam intensity profile is thus obtained. At the NSCL the setting of the slits and readout of the faraday cup current is done with a MATLAB program. In Figures 4.11 and 4.12 two such intensity profiles for beams extracted from SuSI at NSCL are shown with slit widths of 2 mm and bicubic interpolation for a smoother image.

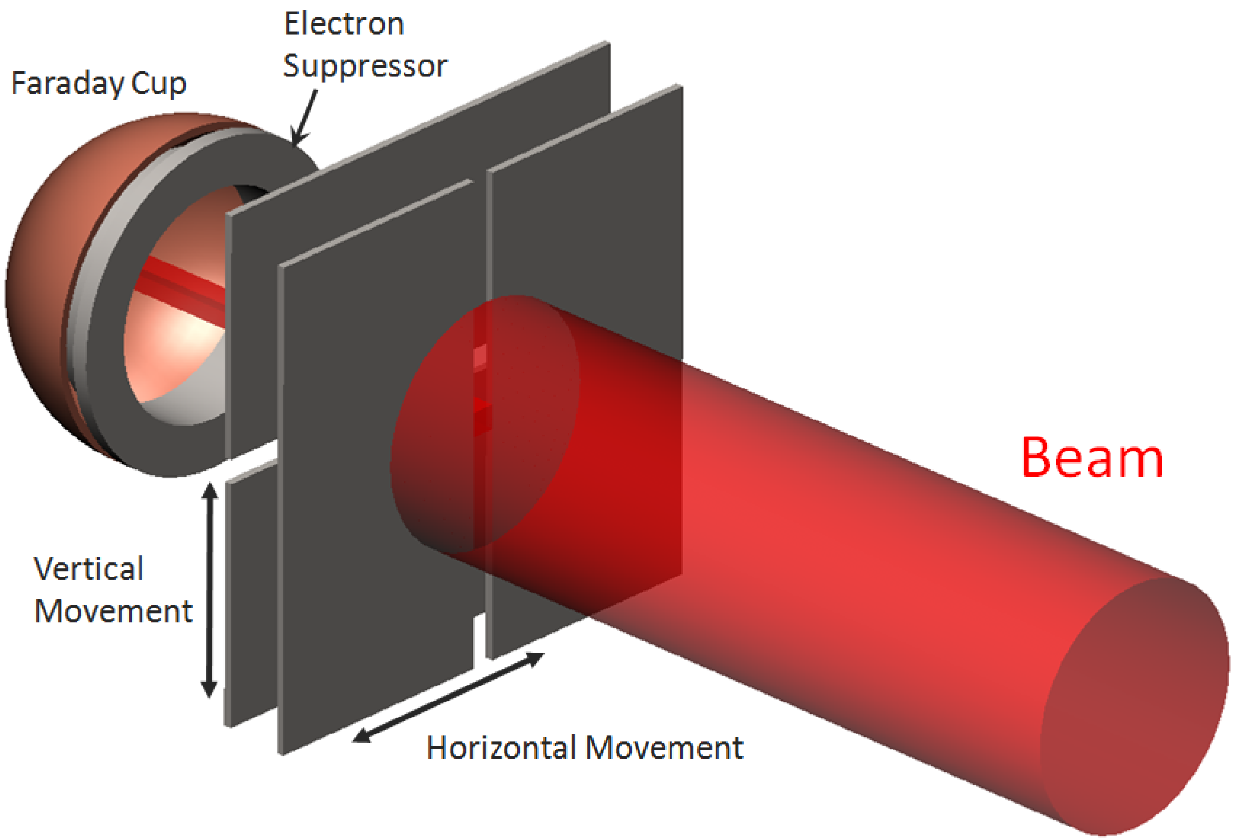

Figure 4.10: Cartoon of the slit profile scanner operating principle. The two slits can move independently. A computer program automatically sets the slits and reads in the faraday cup current. By rastering the area of the beam cross section a transversal beam intensity profile is obtained.

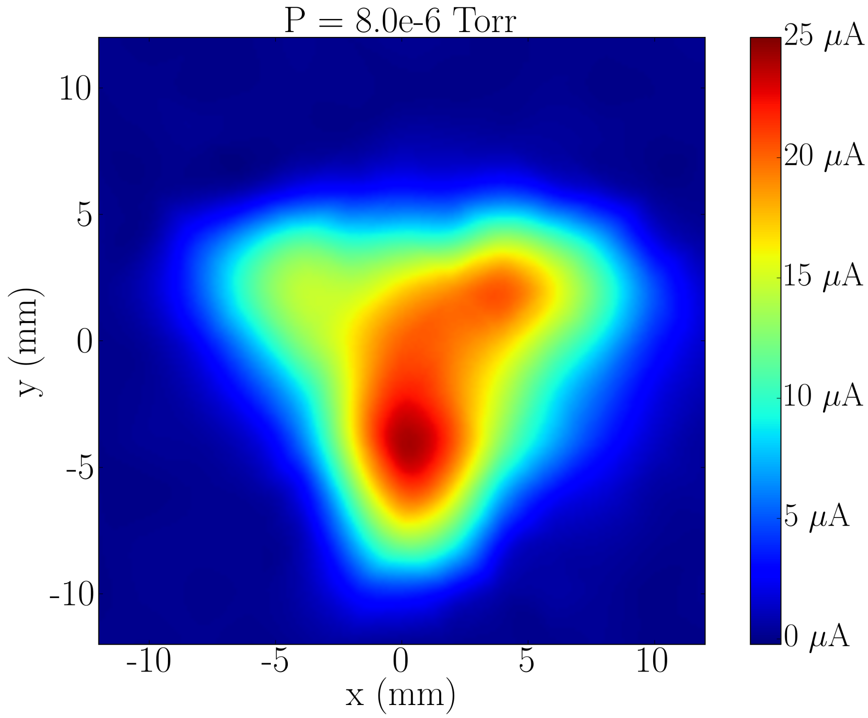

Figure 4.11: Example beam profile of an O^{3+} beam, $\approx$ 235 eμA. The beam exhibits a triangular structure, which is typical for many ECRIS beams.

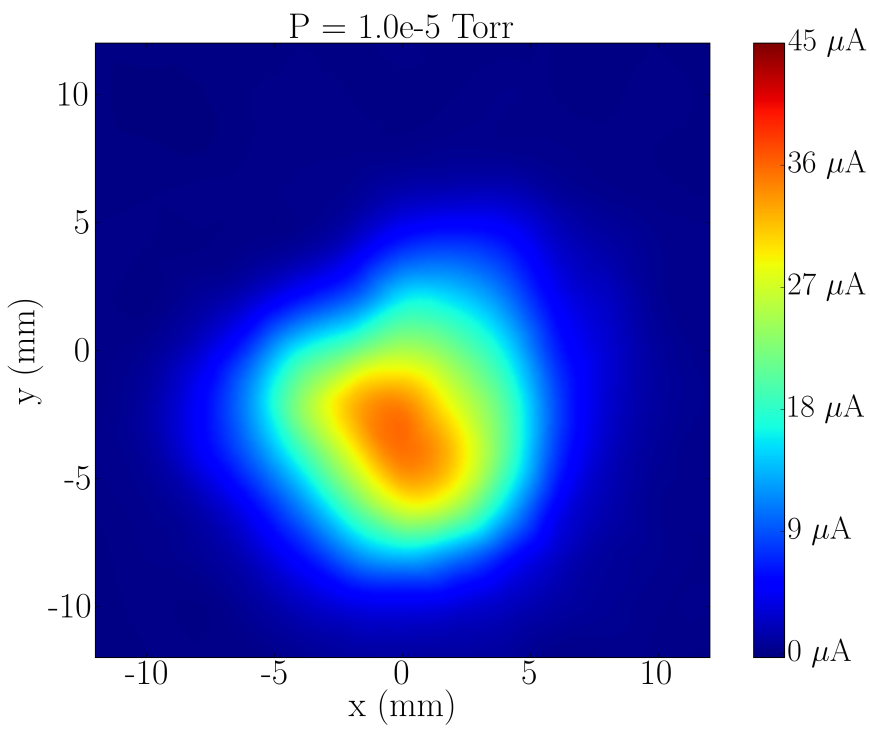

Figure 4.12: Example beam profile of an Ar^{8+} beam, $\approx$ 200 eμA, tuned for 'roundness'.

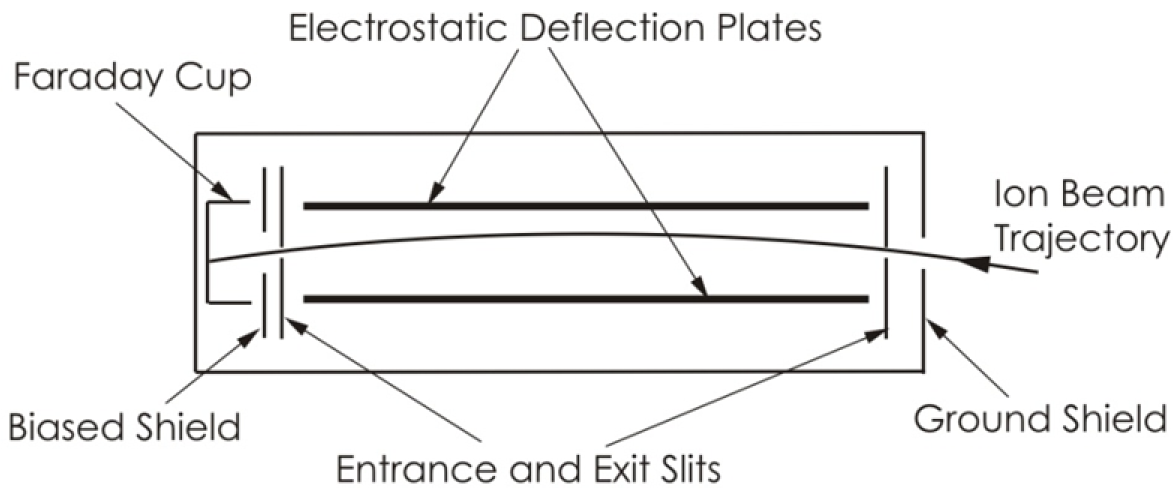

Figure 4.13: Schematic of an Allison-type electrostatic emittance scanner. Image taken from [12].

4.2.5 Allison Emittance Scanner

As discussed in Section 2.1.3, the emittance of the beam is a useful figure of merit to describe its quality. Many methods exist to measure the emittance of a beam. Amongst them are: Slit-wire/harp/slit [99–101] emittance scanners, (*Allison*) electrostatic emittance scanners [102], and Pepperpot emittance scanners [103–105]. The only type of emittance scanner used in this thesis was the Allison scanner. In order to determine the emittance of the beam experimentally, one needs the spatial and angular distribution $f(x, y, x', y')$ of the beam at a longitudinal position z. The Allison scanner can provide this information, albeit only for one of the two transversal directions $f(x, x')$ or $f(y, y')$ while integrating over the other. The scanning box is schematically depicted in figure 4.13. By using two such boxes with perpendicular directions of movement and perpendicular slits, the horizontal $(x - x')$ and vertical $(y - y')$ phase space can be mapped separately. Let us now investigate the example of the horizontal phase-space. The box is positioned with the slits vertical and moved step-by-step in horizontal direction. For each horizontal position, a fraction of the

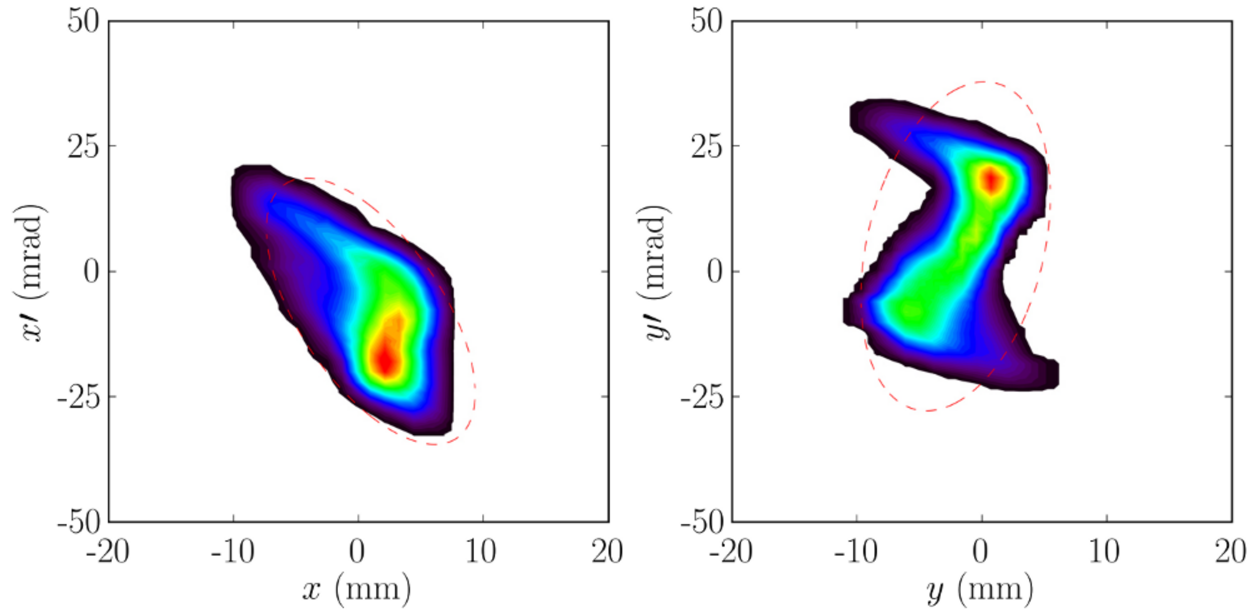

Figure 4.14: Allison emittance scan of a U^{36+} beam. Distortions can be seen that make it hard to determine the 'full' emittance of the beam (cf. discussion in Section 2.1.3) the red ellipses denote the four-rms areas of these two scans.

beam is transmitted through the entrance slit of the scanning box. This is the spatial information. The ions entering through the slit will have different angles with respect to the design trajectory. These angles are scanned by using deflection plates and a second slit (as seen in Figure 4.13). For each horizontal position, the voltage on the plates is swept from some negative value to the corresponding positive one and each time the current in the faraday cup behind the second slit is recorded. Thus a 2 dimensional plot in x and x' is obtained where

$$x' = \frac{V}{E_{kin}} \frac{(D - 2\delta)}{4g}$$

with V the plate voltage in V, E_{kin} the beam energy in eV, D the distance between entry and exit slit, g the gap between the deflection plates, and δ the small gap between the slits and the deflection plates [102]. By weighting each x/x' pair with the current in the cup, the rms emittance is then obtained. Because the x'-voltage relation depends on the beam

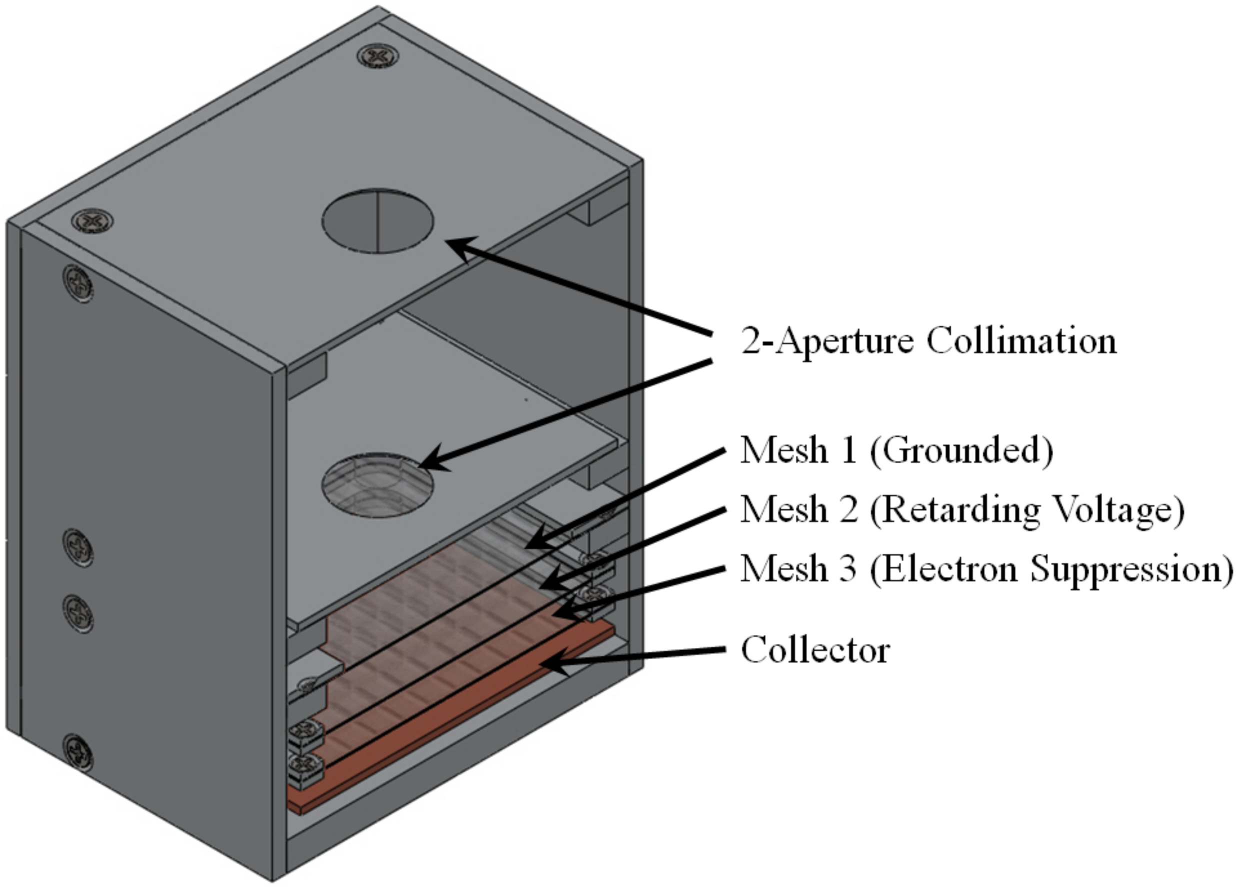

Figure 4.15: 3D CAD model of the retarding field analyzer. The measured ions enter from the top and are repelled by grid 2 if their energy in eV is lower than the grid voltage in V. The current measured with a picoammeter connected to the collector is proportional to the number of ions reaching the collector.

energy, the maximum analyzable angle is a function of the scanner geometry (D, g, δ). The resolution of the detector is a matter of entry- and exit-slit width. Both, geometry and resolution have to be chosen for the respective application. As an example, a scan with the LBNL Allison emittance scanner is shown in Figure 4.14 for a U^{36+} beam.

4.2.6 Retarding Field Analyzer

A retarding field analyzer (RFA) is a device used to measure the energy distribution of incoming ions by sweeping the voltage on a retarding field grid while measuring the number of ions still penetrating the grid. The RFA built in this thesis is a three-grid device with two entry apertures (a 3D CAD drawing can be seen in Figure 4.15). The measured ions enter through an aperture system, pass through the grounded grid 1 and are repelled by grid 2 if their energy in eV is lower than the grid voltage in V. The current measured with a picoammeter connected to the collector is proportional to the number of ions reaching the collector.

The current measurement works exactly like in the case of a faraday cup and electron suppression is necessary to push back secondary electrons onto the collector plate. This is the function of grid 3, which is negatively biased. Grid 3 also serves a second purpose: To keep electrons from outside the detector from reaching the collector and contaminating the measurement of the ion currents. A cartoon picture of the process is shown in figure 4.16. In the presented case, the current readout was done with a Keithley 6485 Picoammeter or a beam current monitor (BCM) built in-house at the NSCL and routinely used for measuring very low beam currents with faraday cups. The voltage on the retarding field grid was set with a Kepco BOP-1000 bipolar power supply. Both BCM and Kepco were connected to the laboratory's EPICS system and a computer program was used to set the voltages and read the corresponding collector current. In order to obtain a spectrum, the voltage on the retarding grid is increased in small steps from 0 V to an upper limit depending on the ion energies. At each step the collector current is measured. An example spectrum is shown in Figure 4.17.

The measurement setup of the RFA at the different locations in the beam lines of the ion sources used for these experiments and the interpretation of the spectra and data analysis will be treated in detail in Chapter 5.

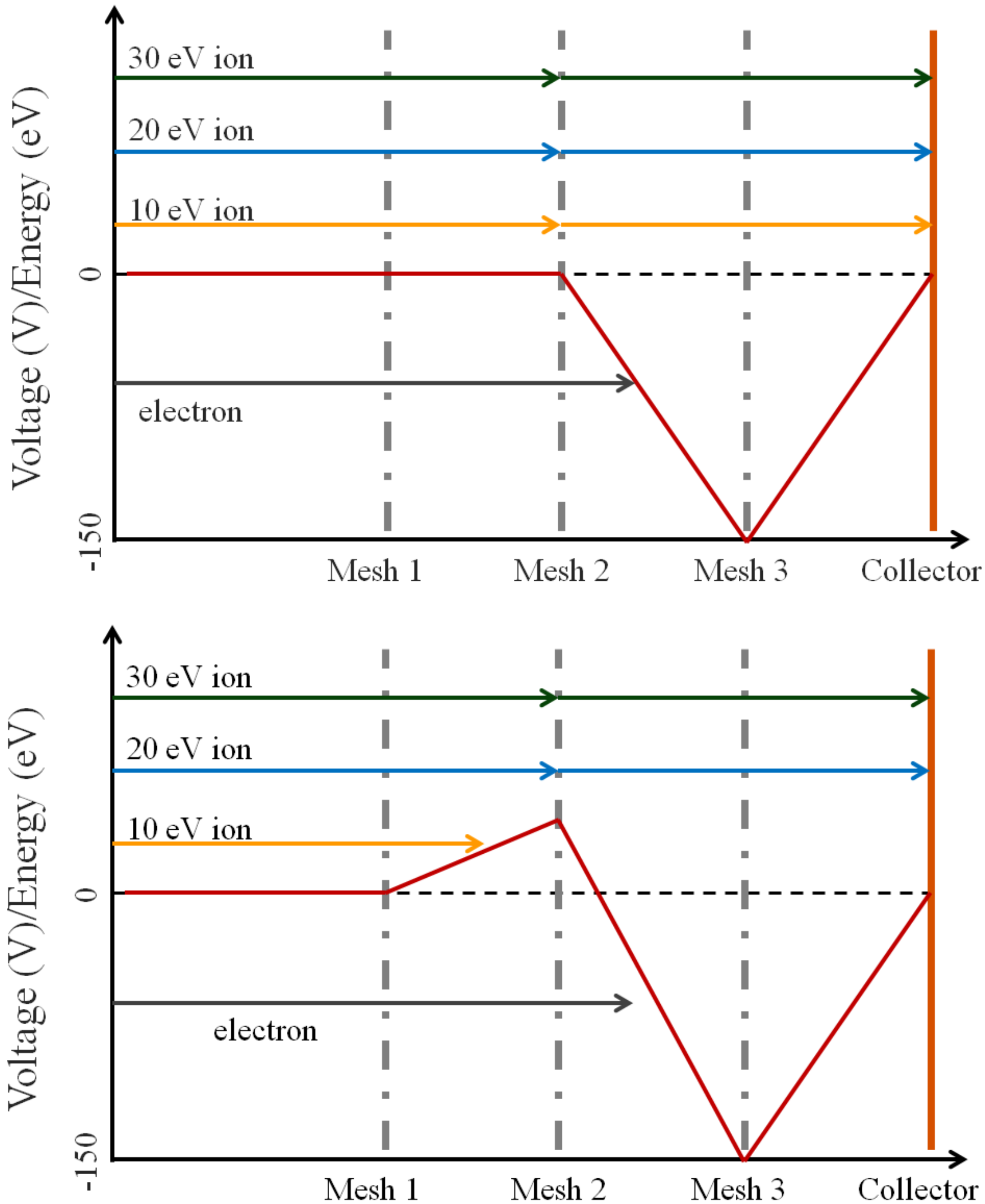

Figure 4.16: Cartoon demonstrating the working principle of a retarding field analyzer. Upper image: Retarding grid ('Mesh 2') at 0 V. All ions make it to the collector. Lower image: Retarding grid at 15 V. Ions with less energy (e.g. 10 eV) are repelled. In both cases electrons from the outside are repelled by the electron suppressor ('Mesh 3').

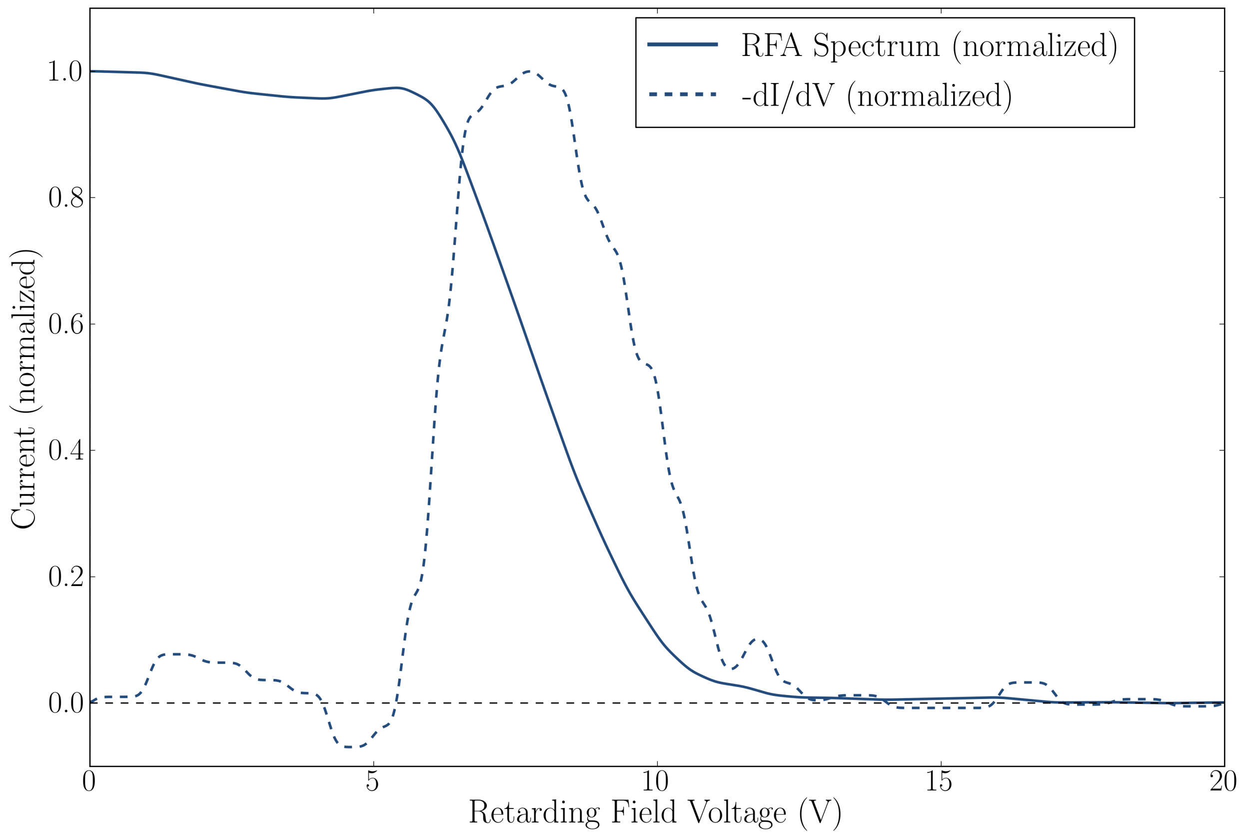

Figure 4.17: Example RFA spectrum. The directly obtained spectrum (solid line) and the first derivative -dI/dV (dashed line) are both normalized to one for better visibility. The first derivative of the obtained spectrum represents the ion energy distribution.

Chapter 5

Space-Charge Compensation Measurements

In ion source and accelerator design, one important topic are space-charge forces. These usually become important for higher intensity beams, but can also already be an issue if one wants to focus even a lower intensity beam into a very small beam spot. Especially in the framework of ECR ion sources and the corresponding low energy beam transport lines, with the ever growing demand for higher beam currents, space charge is a factor that has to be included in any simulation effort that claims to be accurate. The compensation process reducing the space charge through ionization of residual gas molecules and subsequent trapping of slow free electrons inside the beam envelope has already been discussed in theory in chapter 2.1.5. However, the model presented there is rather simplified and so far only confirmed for highly compensated beams. Very little data exists for the type of beams produced in ECR ion sources and the ECRIS LEBTs where the neutralization can be $\ll 100$ %. In this chapter, I will report on measurements conducted at the NSCL in four different locations in the beam lines of various ECR ion sources using a retarding field analyzer (RFA). Several problems arise with using such a device in the current and beam line pressure regimes associated with ECR ion sources which will be discussed in detail as part of the data analysis.

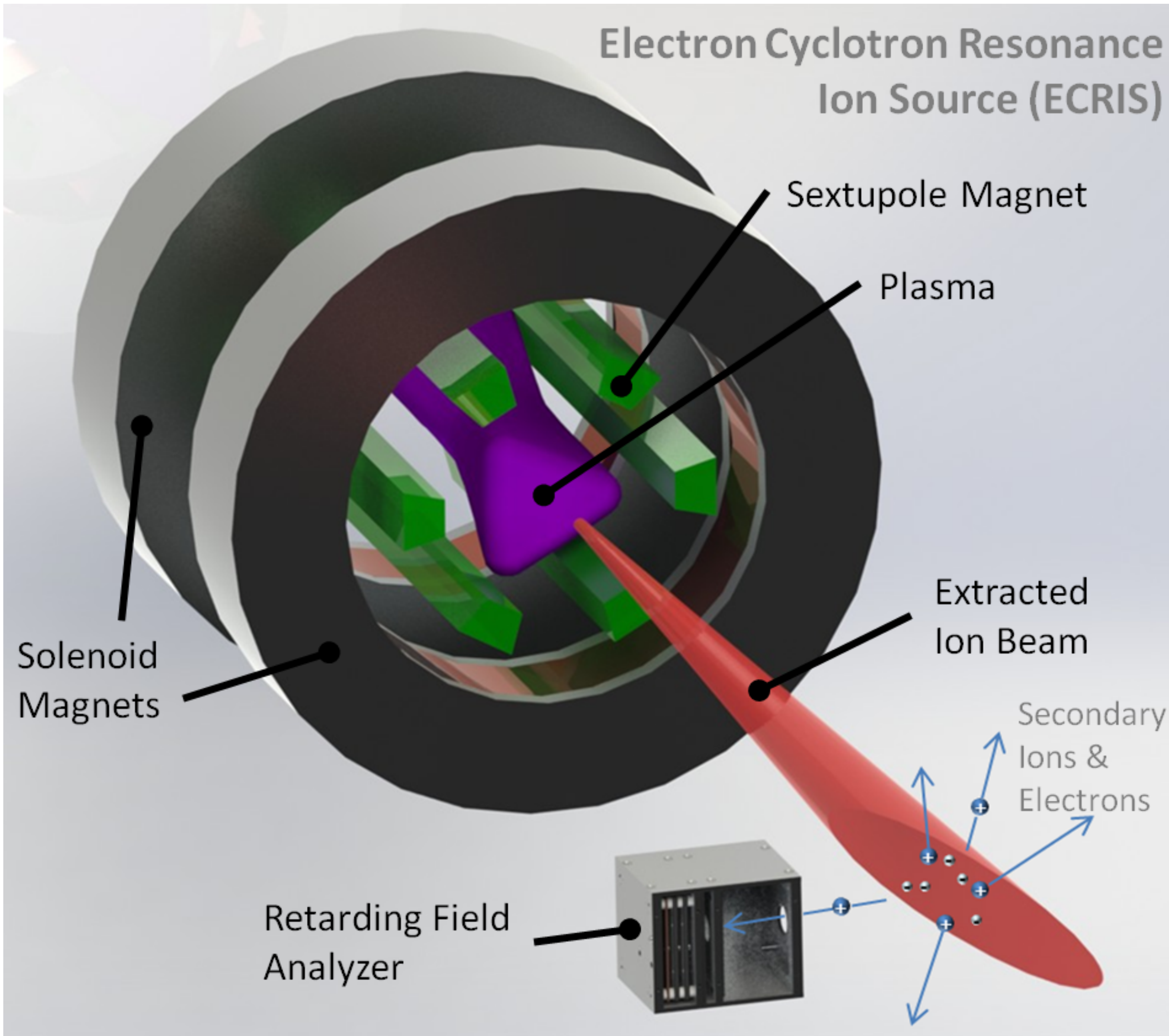

Figure 5.1: Cartoon of space-charge compensation through secondary electrons and measurement of the energy distribution of the secondary ions with the retarding field analyzer 'NeMo'. Electrons and ions are created inside the beam by ionization and charge-exchange of the beam with the residual gas. Electrons are captured and lower the beam space charge potential. ions are expelled and can be measured with NeMo.

5.1 Preliminary Considerations

As a reminder of the processes involved in space charge compensation and neutralization measurement, Figure 5.1 shows a cartoon picture of an ECR ion source with beam and the retarding field analyzer 'NeMo' (Neutralization Monitor). Before going into the details of the measurements, I will discuss a few general topics and issues related to RFA measurements.

5.1.1 Saturation Current

The current arriving on the collector plate with the retarding field grid (Grid 2) grounded is called *saturation current* I_{sat}. In theory, the saturation current are all the ions produced by the beam and emitted into the solid angle of the detector aperture. Inside the detector, positive ions are not repelled as long as the retarding field grid is at 0 V. If we go back to our simple view of a round uniform beam, we can estimate I_{sat}. The total production of ions per unit time inside a beam volume of length ℓ is:

$$\frac{dn_i}{dt} = \ell r_b^2 \pi n_b v_b \sum n_g \sigma_{i,g} \tag{5.1}$$

with n_i the number of secondary ions, r_b the beam radius, n_b the primary ion beam density, n_g the partial densities of the residual gas species and $\sigma_{i,g}$ the total secondary ion production cross sections for those residual gas species interacting with the primary ion beam. Using the beam current $I_b = qer_b^2 \pi v_b nb$ and the solid angle of emission into the detector aperture, we can write down the saturation current as a function of beam current and residual gas densities:

$$I_{sat} \approx \frac{r_a \arctan \frac{r_a}{d} I_b \sum n_g \sigma_{i,g}}{2q} \tag{5.2}$$

and for small angles (small r_a, large d):

$$I_{sat} \approx \frac{r_a^2 I_b T \sum n_g \sigma_{i,g}}{2dq} \tag{5.3}$$

with q the primary ion charge state, r_a the radius of the detector's entry aperture, and d the distance of this aperture from the beam center. In addition, a transmission factor T was added, to account for the losses on the three grids. In our case each grid has a (theoretical) transmission of 90%. This leads to an estimation of $T \approx 73\%$ for all grids combined. Because of ion optical effects due to the finite mesh sizes of the grids and the fact that we apply a negative voltage on grid 3, the transmission is not constant but actually a function of grid 3 voltage, grid 2 voltage, and ion energy and angle of incidence. This will be explained in more detail in the next subsection (5.1.2). The situation is further complicated in the presence of (even weak) magnetic fields. The lower the beam potential (be it due to low beam currents or high neutralization), the lower the secondary ion energy. For secondary ions with only a few eV energy, even very low magnetic fields (< 10 Gauss) can change the beam trajectories enough to keep the ions from entering through the aperture system (the two aperture collimation system can be seen in Figure 4.15). The secondary ion energies for our ECRIS beams are expected to be below 10 eV. As we will see, this effect actually acts as a *high pass filter* because higher energy ions are more likely to make it through the collimator system. This problem will be discussed in Subsection 5.1.3. Both, mesh effects and magnetic fields have to be included in the data analysis.

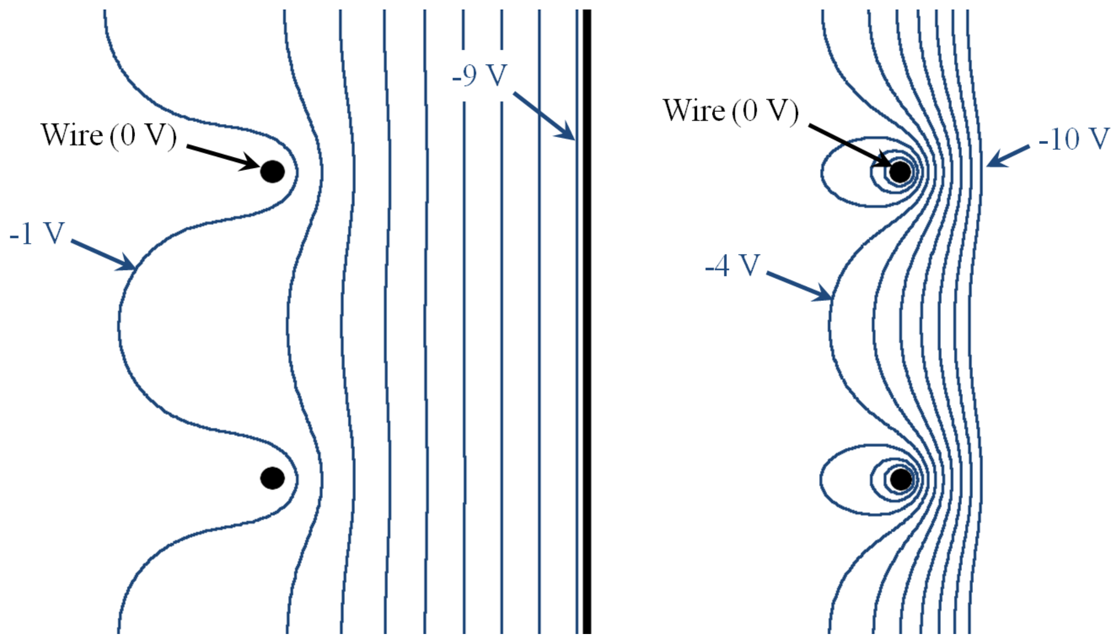

Figure 5.2: Equipotential lines close to the mesh wires of Grid 2 calculated with SIMION 8.1. Grids 1 and 3 are not shown as the distances from grid to grid (6mm) are much larger than the wire spacing. Left: Grid 3 at -150 V. Right: Grid 3 at -500 V. Grid 1 and 2 at 0 V in both cases. It can be seen that the holes between the wires have a lower potential than the wires and that this depends on the setting of Grid 3.

5.1.2 Realistic Mesh Effects

As mentioned earlier, the retarding field analyzer designed and used for the presented measurements is a three-grid device. Each grid is made of a copper wire mesh held by an aluminum frame. The mesh was produced by Precision Eforming LLC. (Part #: MC-17) and the details of the mesh are listed in Table 5.1. Each mesh has a maximum transmission of 90 % due to the fact that wires block the path of the incoming ions. The theoretical transmission of the three meshes combined would then be $0.9 \cdot 0.9 \cdot 0.9 \approx 0.73$ or 73 %. However, in reality the situation is more complicated. Due to the finite size of the wires and the openings and the fact that there are neighbouring grids at different potentials (Grid 1 = 0 V, Grid 3 = -150 V to -500 V), the equipotential lines close to Grid 2 are not straight lines. An example is shown in Figure 5.2. The implications for RFA measurements have already been pointed out by, e.g., Hanson *et al.* [106, 107] and Sakai and Katsumata [108] and are:

1. Formation of an *effective potential* between the wires of the mesh, which is lower than the applied voltage and depends on the distances and voltages of the neighbouring meshes [106].

2. A *lens effect* from the potential depressions between the wires that changes the measured ions' trajectories and thereby the transmission and introduces an energy spread that leads to a finite detector resolution [108].

3. *Reflected ions.* Depending on the potentials on grid 2 and 3, the ion energies, and whether or not a bias is applied to the collector ('faraday cup') plate, ions can be reflected back from the collector after making it past the retarding field grid.

These three problems will now be discussed in more detail and will be included in the data analysis 5.2 and the error estimation 5.2.4.

Table 5.1: NeMo - Copper mesh parameters.

Parameter	**Value**
Wires per mm	2.756
(Wires per inch)	70
Space	0.34417 mm
Wire ∅	0.018542 mm
Max. Transmission	90 %
Material	Copper

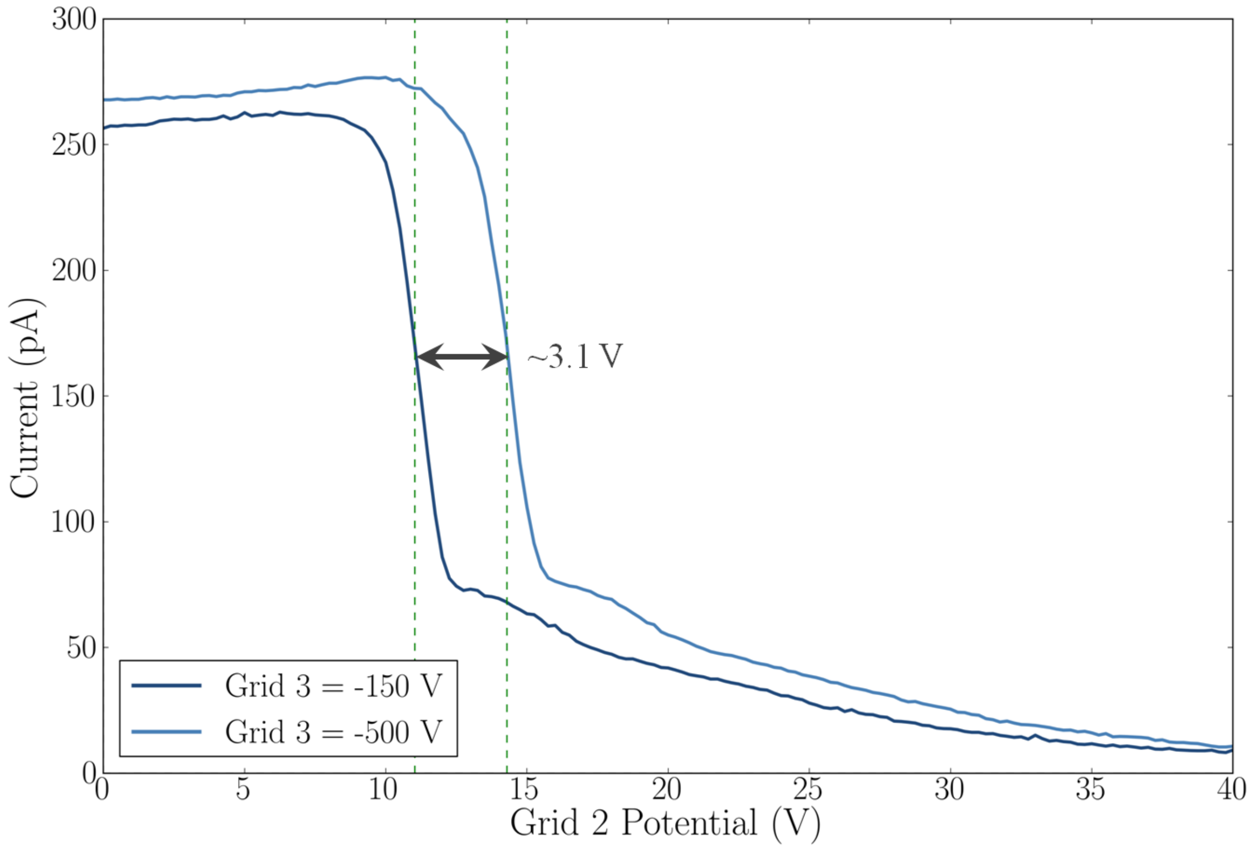

Figure 5.3: Two measured RFA curves exhibiting a shift towards higher potential with increasing voltage on Grid 3 due to the formation of an effective potential lower than the applied voltage in the space between mesh wires. Left curve with grid 3 at -150 V, right curve with grid 3 at -500 V.

5.1.2.1 Effective Potential

The shift due to the effective potential and its dependence on the voltage applied to Grid 3 (V_3) was observed in all the measurements with the RFA. An example spectrum with V_3 = -150 V and -500 V is shown in Figure 5.3. In their paper, Hanson *et al.* present a formula to calulate the shift in dependence on the applied voltages and the mesh parameters (wire thickness, wire distance, inter-grid distances). Here, simulations of the mesh with very high resolution (0.0037 mm/grid unit) in SIMION 8.1 were conducted in order to compare the semi-empirical formulae of Hanson *et al.* and Sakai and Katsumata with simulations and to better understand the ion optical effects inside the detector. The observed shift between

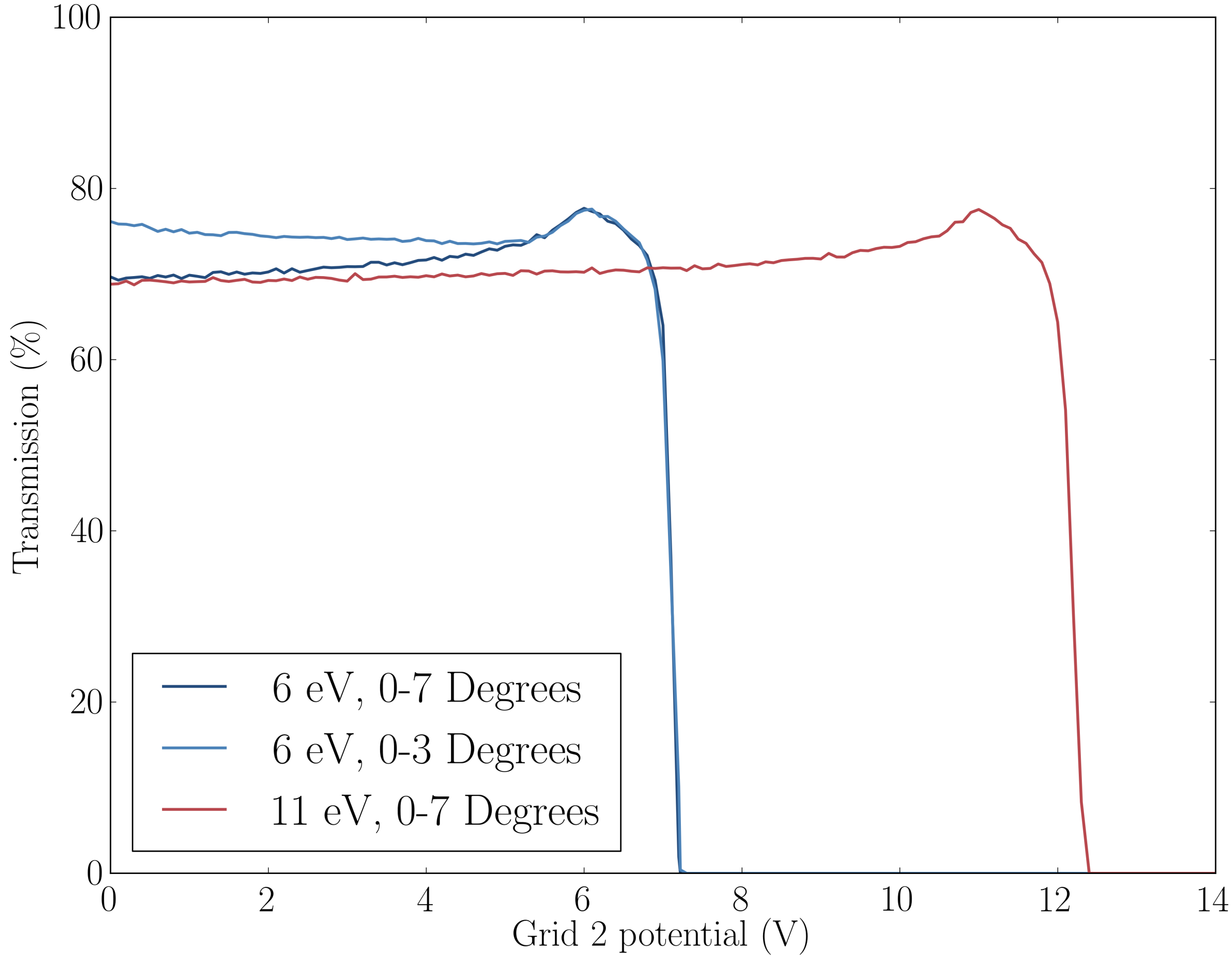

Figure 5.4: Effects of realistic mesh for three different types of initial particles. The rightmost curve is for 11 eV ions, the other two for 6 eV with the one starting higher having smaller incident angles. All three are with grid 3 on -150 V as during the measurements in the SuSI LEBT. A bump is clearly noticeable in all three curves. This is due to the fact that for grid 2 voltages close to the particle energy, incident ions that would otherwise collide with mesh wires are now bent around the wires. Changing the angle of incident changes the saturation current, but not the horizontal shift and the finite width of the dropoff (ΔV).

V_3 = -150 V and V_3 = -500 V during the RFA measurements was $\Delta V_{exp} \approx 3.1$ V. With the mesh parameters given in Table 5.1, the shift calculated with Hansons procedure [106] is $\Delta V_{calc} = 2.78$ V. The SIMION simulations suggest an even lower value of $\Delta V_{sim} = 2.25$ V.

5.1.2.2 Voltage Dependent Transmission

Using the same SIMION simulation as in Subsection 5.1.2.1, it is possible to obtain simulated detector signals for arbitrary secondary ion energies and angles of incidence in the detector. In figure 5.4 three such curves are shown for 6 and 11 eV incident particles with angles between 0 and 7 degrees. Characteristic of these curves is that, in accordance with the prediction of Sakai *et al.* the curves exhibit a bump at grid 2 voltage close to the particles' energy [108] and a falloff that is not infinitely steep as one would expect from a monoenergetic beam, but has a finite slope that depends on the particle energy and adds to the RFA's uncertainty. That is to say the meshes act as a high pass filter (cf. Hanson *et al.* [106]). The similarities of the curves for constant grid 3 (electron suppressor) voltage are such that we can use the simulations to obtain a set of detector resolution curves for each voltage on grid 3 (i.e. -150 V for SuSI measurements and -450 V for LEDA measurements) which are scalable with ion energy and can thus be used in the data analysis in a least squares fit model (cf. Section 5.2.2).

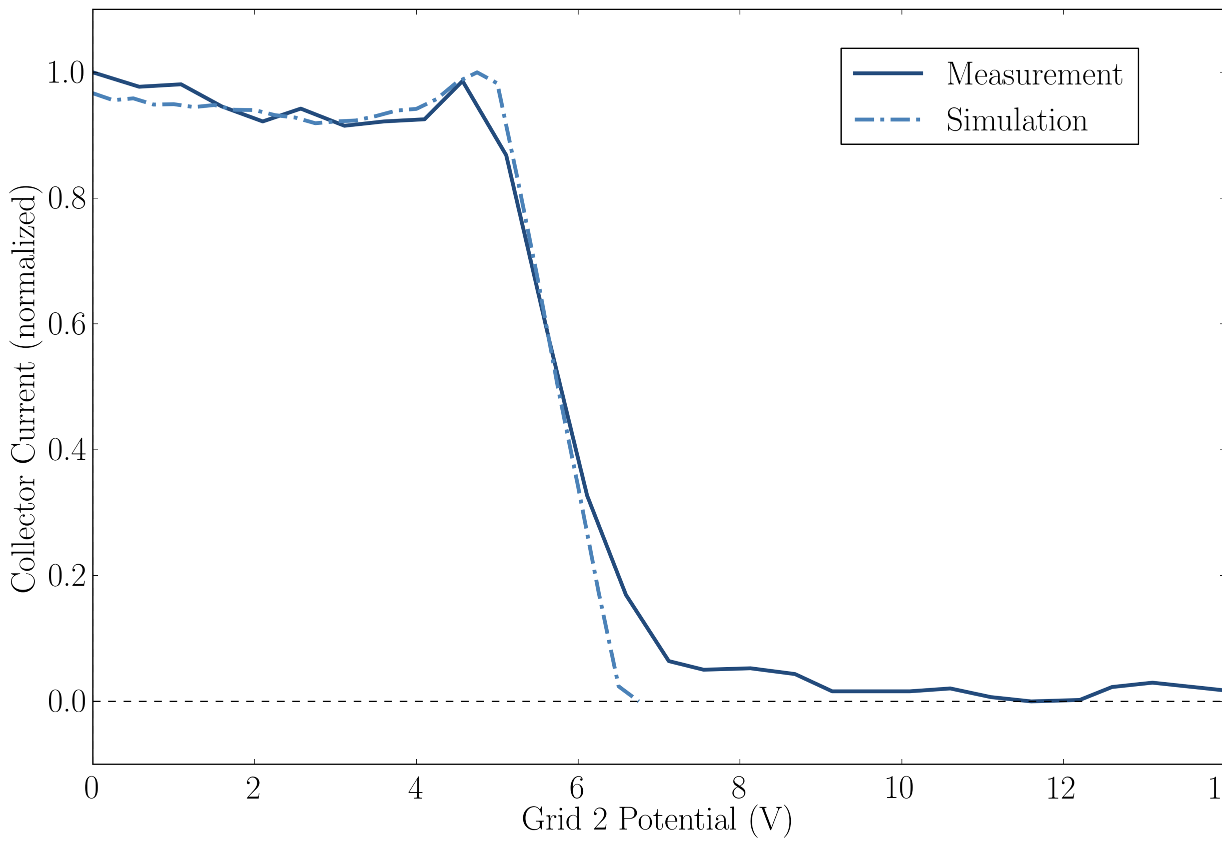

Figure 5.5: Comparison of slow ion reflections as seen for the lowest secondary ion energies in the LEDA injector source measurements and simulations under similar conditions (i.e. similar ion energies, same voltage of -450 V on grid 3). This simulation did not include magnetic field effects.

5.1.2.3 Reflections

The third effect of the meshes is the partial reflection or even oscillation of the slow ions between the collector and the retarding field grid 2 around the electron suppressor grid 3. This only happens if the collector plate is grounded and can be avoided by biasing it at a negative voltage (e.g. -50 V). This effect leads to a significantly lower collector current halfway between 0 V on grid 2 and the secondary ion energy. An example is shown in figure 5.5. As can be seen, the dip effect is well reproduced in the simulation which was performed modelling a high resolution mesh in SIMION and applying similar voltages.

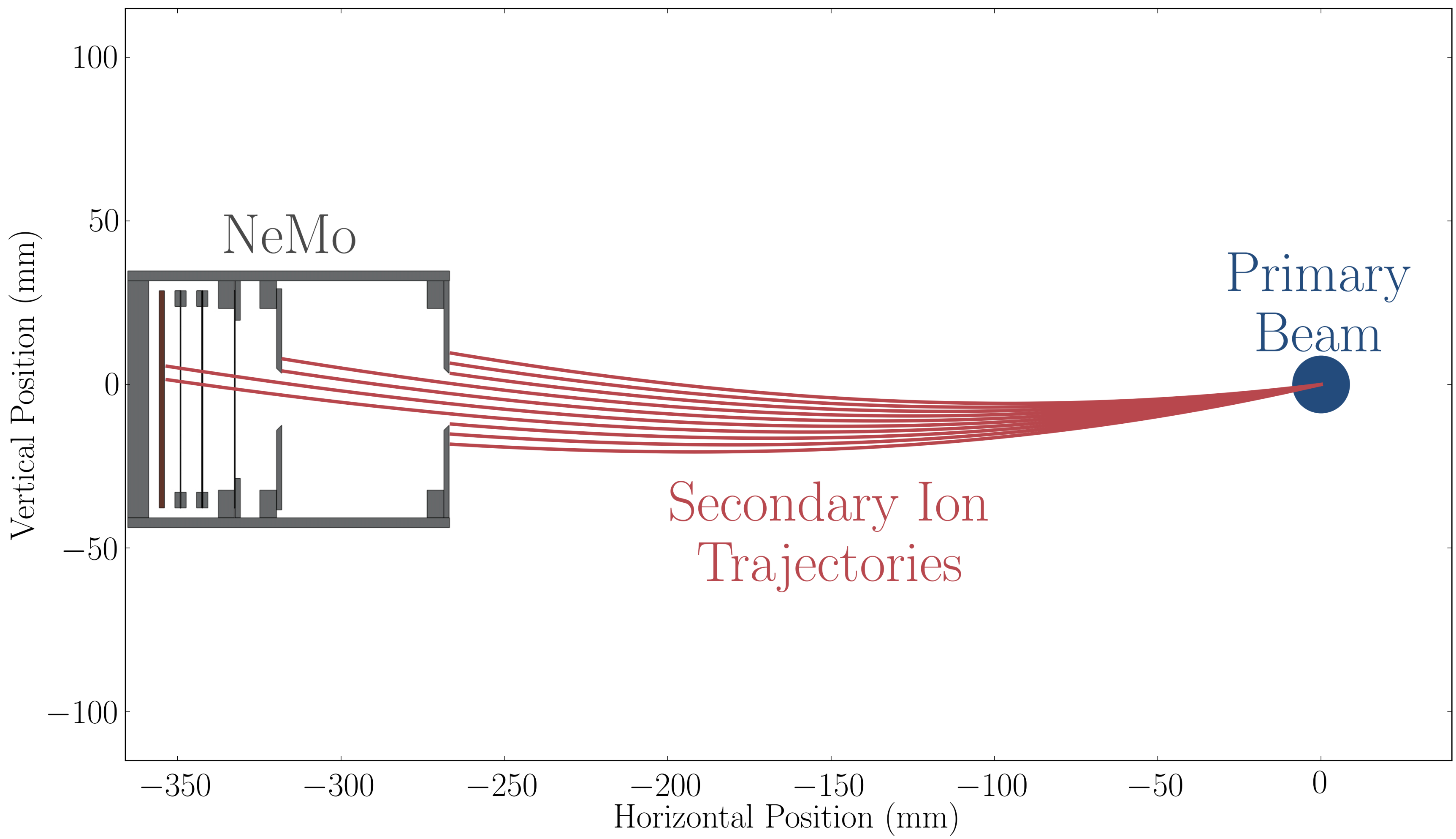

Figure 5.6: Example trajectories of secondary H_2^+ ions in the residual longitudinal magnetic field of the two solenoid magnets of the LEDA injector ion source. Trajectories were calculated with SIMION 8.1 for 5 eV ions.

5.1.3 Magnetic Fields

As mentioned before, the presence of a magnetic field at the location of the neutralization measurement can have severe consequences for the outcome of said measurement. Unfortunately, when dealing with ECR ion sources, magnetic fields can not be avoided at all locations. Of the four different measurement locations, two were very close to the source itself: SuSI/Q001 and the LEDA injector ion source (cf. Subsection 5.3.1). In both cases, there are residual fields of the solenoid magnets of the sources' confinement fields, and the influence of these fields can be observed in the measurements. At the second SuSI measurement location further downstream in the beam line (SuSI/Q014, cf. Subsection 5.3.2) a focusing solenoid is close enough to the measurement location to potentially create similar problems, but for the highest solenoid current setting of 170 A, the residual field at the measurement location is only ≈ 3 Gauss and the secondary ions are mostly N_2^+ which has a much higher magnetic rigidity than the H_2^+ of the LEDA source and thus the magnet does not pose a problem here. In the measurement in the beam line of Artemis B, no magnetic field was present distorting the particle trajectories. The measured or calculated residual magnetic fields of the four measurement locations are listed in Table 5.2. In the two cases with magnetic field presence, the influence of the field may be taken into account, but naturally imposes additional errors on the results. In the LEDA case, a POISSON Superfish calculation revealed a field of only approximately 6 Gauss on axis, but as shown in Figure 5.6 this small magnetic field is enough to bend ions onto curved trajectories. In this case, the residual gas was mostly H_2 and thus the secondary ions have a small magnetic rigidity. In earlier experiments with a retarding field analyzer and the same source (e.g. [7]), this might not have been a problem, as the device had only one entrance aperture. In our case we have a two-aperture collimation system and, as is illustrated in Figure 5.6, some of the ions cannot pass through the second aperture.

This leads to a *collimator transmission* depending on:

1. Secondary ion mass
2. Secondary ion energy
3. Magnetic field strength
4. Geometry (aperture size, detector distance from beam center)

With the help of SIMION, the collimator transmission of a given geometry, for a set of secondary ion energies can be calculated. Such a curve is shown in Figure 5.7 for the case of the LEDA injector source. As can be seen, H_2^+ ions experience strong deflection, whereas the heavier H_2O^+ seems rather unperturbed. Similar curves have been calculated for the two locations in the SuSI beamline. In Section 5.2 I will discuss how the transmission curves are used to correct the saturation currents and fit the neutralization curves.

Table 5.2: Residual magnetic field $B_z(z)$ on axis at the different neutralization measurement locations.

Location	$B_z(z)$	**Method**
LEDA Box 1	≈ 6 Gauss	Superfish calculation
Artemis A	≈ 0 Gauss	No Magnet
SuSI Q001	≈ 60 Gauss	Measured
SuSI Q014	≈ 3 Gauss	Superfish calculation

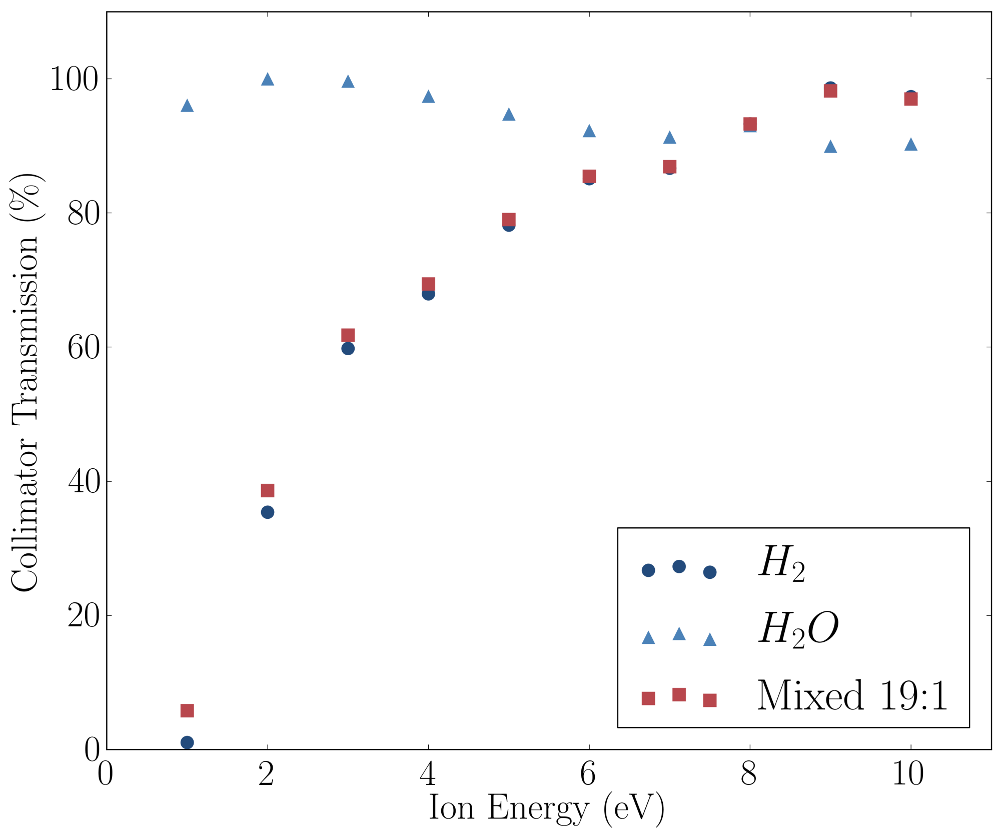

Figure 5.7: Collimator transmission curves for the case of the LEDA injector ion source. The two secondary ion species H_2^+ and H_2O^+ are the two biggest contributors to the residual gas pressure (as measured with a residual gas analyzer (RGA) and have a ratio of $\approx$ 19:1.

5.2 Data Analysis

In order to be consistent for the different measurement locations and pressure and current variations, the same procedure has been applied to all the data:

1. The saturation current for each series was plotted and checked against the theoretical prediction with equation 5.3 with a transmission factor T modified for mesh effects and magnetic fields (cf. Subsection 5.2.1).

2. Neutralization spectra were fitted with a least squares method including the various transmission factors and mesh effects (cf. Section 5.2.2).

3. The errors imposed on the results by the various approximations and uncertainties in the data acquisition were estimated and added as errorbars to the results (cf. Section 5.2.4.

5.2.1 Calculating Saturation Currents

As discussed in Subsection 5.1.1, the saturation current I_{sat} on the collector plate while grid 2 is at 0 V, should to first order be directly proportional to the number of secondary ions created by the interaction of the primary beam with the residual gas:

$$I_{sat} \approx \frac{r_a^2 I_b T \sum n_g \sigma_{i,g}}{2dq} \tag{5.4}$$

It should grow linearly with the residual gas pressure and the primary beam current. Consequently the saturation current is a good first check whether or not the measurements make sense. Unfortunately, as discussed in Subsection 5.1.2, the transmission through the meshes of the three grids, and as discussed in subsection 5.1.3, the transmission through the two-aperture system in the presence of a magnetic field can greatly depend on the ion energy and the setting of the negatively biased electron suppression grid and thus the saturation currents do not necessarily exhibit the expected linear behaviour. However, as mentioned in Sections 5.1.2 and 5.1.3, it is possible to calculate transmission curves through the collimation system and the meshes with grid 2 at 0 V. Thus the transmission factor T in equation 5.3 is no longer constant, but instead a function of magnetic field, secondary ion energy, mass, and grid 3 voltage (m, B and V_3 voltage are discrete parameters rather than free variables).

$$T = T(E, m, B, V_3) = T_{coll}(E, m, B) \cdot T_{mesh}(E, V_3) \tag{5.5}$$

Here we have identified the two main contributions to T as the collimator transmission depending on energy, mass and magnetic field and the mesh transmission depending on energy and grid 3 voltage.

In order to calculate T_{coll} we first have to determine the presence and strength of a magnetic field at the location of measurement. This was done either by directly measuring with a Gauss meter or by calculating the magnetic field with POISSON Superfish. Secondly, a transmission curve has to be calculated for each secondary ion species (this can be generalized into the two categories H_2^+ and heavier ions). The free parameter in these transmission curves is the secondary ion energy. The transmissions are determined by starting a large number of particles from the center of the primary ion beam and plotting the ratio of secondary ions making it through the first aperture to those reaching the collector plate.

The second part is to calculate T_{mesh}. This is done using SIMION as well by modeling the meshes realistically in very high resolution and sending ions of different initial energies and angles through the meshes. This accounts for the three mesh effects discussed in Section 5.1.2.

Examples of T_{coll} and T_{mesh} for the LEDA injector source are shown in Figure 5.15. There H_2 is the light ion and H_2O is representative for all heavier ions.

From the RFA curves obtained with NeMo, we can now determine an estimate of the secondary ion energies by shifting the spectrum using the empirical formula for the effective potential presented in [106] and discussed in Section 5.1.2. Then we can use $T = T_{coll} \cdot T_{mesh}$ in formula 5.3 to calculate the theoretical I_{sat} and compare them to the measured ones. Examples are shown in Section 5 (e.g. Figure 5.16).

5.2.2 Least Squares Fitting

In general, all NeMo spectra were fitted with a least squares method using python scripts. The *lmfit* library provided by the University of Chicago [109] was used, which is a wrapper around pythons scipy.minimize method, which in turn uses *MINPACK*. The least squares method requires an objective function to minimize. In our case this is

$$f_{obj} = \frac{I_{col,theo}(V_2) - I_{col,meas}(V_2)}{\sigma_I(V_2)} \tag{5.6}$$

with $I_{col,theo}$ the theoretical collector current, $I_{col,meas}$ the measured collector current and σ_I the measured standard deviation of the collector current, all functions of the voltage V_2 on grid 2 (retarding field). Note: The minimizer automatically squares the objective function. Before the fitting, a calibration curve is applied to the voltages of grid 2 (V_2) corresponding to the data points $I_{col,meas}$. This measured calibration curve shows that the KEPCO power supply has an offset of $\approx$ -0.75 V.

The theoretical collector current $I_{col,theo}(V_2)$ is calculated in a two step process:

1. Generation of the theoretical secondary ion energy distribution f(E)
2. Folding of this distribution with the transmission functions T_{coll} and T_{mesh}.

5.2.2.1 Secondary Ion Distribution Function

We have two options for generating the secondary ion distribution function f(E).

The first method (and the one used for the LEDA injection source) is to assume an axially symmetric beam distribution (e.g. uniform or Gaussian) and calculate the theoretical beam potential $\Phi(r)$. We can then generate an ensemble of ions with density according to the distribution and beam radius r_b (or σ_b), and determine their kinetic energy from their place of birth inside the beam envelope. For the case of the uniform cylindrical beam the energy distribution can also be calculated and is simply:

$$f(E) = \begin{cases} 0 & \text{for } E < e \cdot \Phi_{edge} \\ \text{const.} & \text{for } e \cdot \Phi_{edge} \leq E \leq e \cdot \Phi_{cent} \\ 0 & \text{for } E > e \cdot \Phi_{cent} \end{cases} \tag{5.7}$$

Generating particle ensembles is more versatile, though, and multiple beamlets with different radii and different ion species can be used.

The second method is to measure the ion beam distribution at the location of the RFA measurement (e.g. with a slit scanner or with a beam viewer) and use this measurement to determine the energy distribution. This was done for the measurement in the SuSI beam line at diagnostic box Q014. For each set of measurements (except one, because the image acquisition was unavailable) a slit scan and a beam viewer image were obtained. The slit scan using the 4-jaw slits gives a well resolved ion distribution, but is located $\approx$ 20 cm before NeMo (Q013). There (Q014), a beam viewer with a quartz (and later a KBr) plate and a CCD camera are available. The resolution of the viewing plates is not good enough to determine the intensity distribution, but by comparing slit scans and beam imaging at the NeMo location, it is possible to determine the rotation of the beam due to the solenoid, and the change in beam size. The process of obtaining f(E) is then as follows:

- The slit scan and beam viewer image are compared and rotation and scaling of the beam from Q013 to Q014 are determined.
- The density distribution from the slit scan is scaled and rotated accordingly and saved into a file.
- This file is now loaded into a SIMION simulation of diagnostic box Q013/Q014 to provide the charge density distribution of the primary beam.
- SIMION's poisson solver is used to calculate the beam potential for an unneutralized beam.
- Particles are initialized with a small random thermal energy (0.2 eV) at positions according to the beam density profile and experience the space charge field of the beam.
- Particles entering the aperture of NeMo are registered and their energy is saved to a file, yielding f(E).

In both cases, the secondary ion energy distribution

$$f(E) = f(E, v_b, r_b, I_b, f_e, r_p)$$

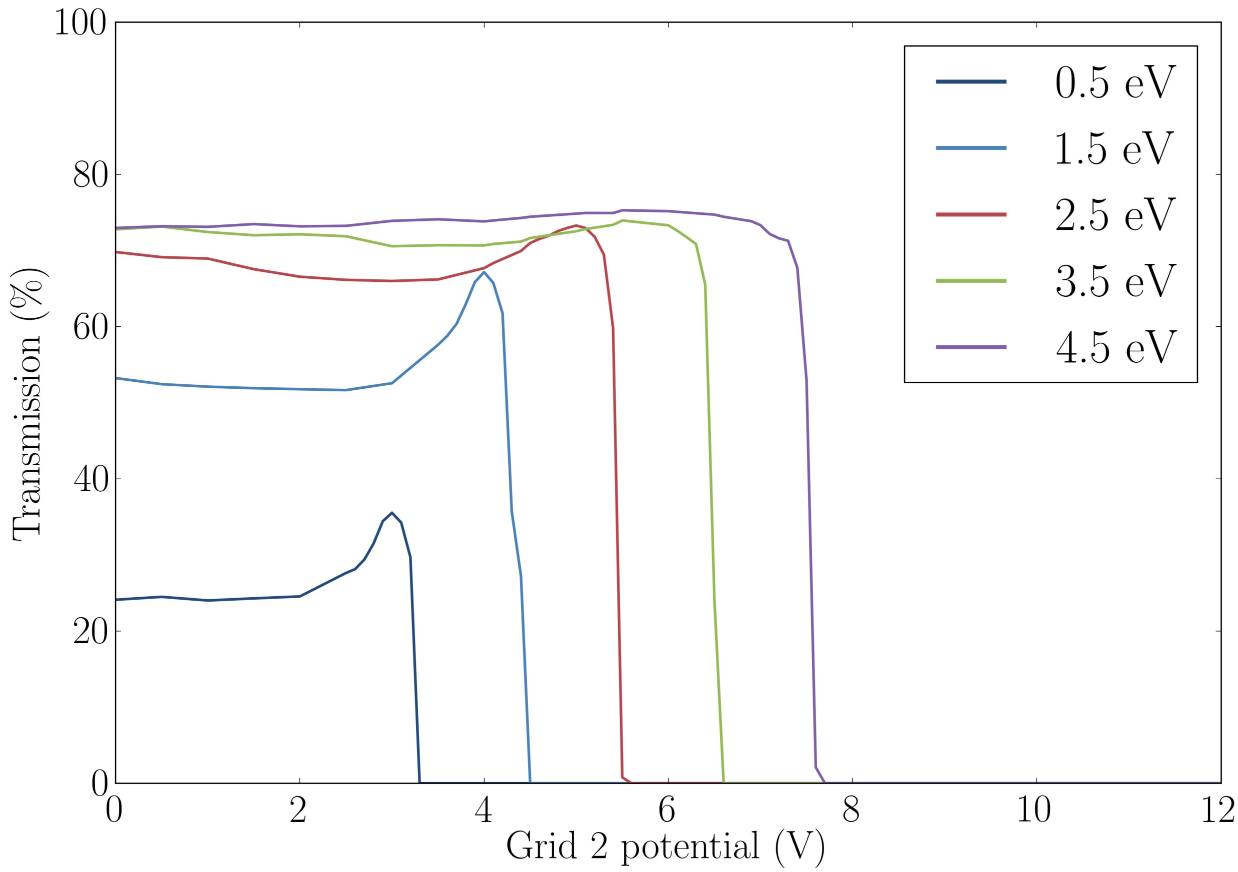

Figure 5.8: Mesh transmission curves for -450 V on grid 3. The ion energy increases from left to right. A drop in transmission as well as the formation of a peak can be seen towards the lowest energies. At higher energies ($>$ 5 eV) the transmission curve only shifts further to the right without changing its shape.

is a function of E, but depends also on the following parameters: beam velocity v_b, beam radius r_b, beam current I_b, neutralization factor f_e, and the pipe radius r_p. For r_p it should be noted that in the case where f(E) is calculated with SIMION, the actual shape of the box is taken into account, and in the analytical approach an effective wall radius is approximated.

5.2.2.2 Detector Transmission Function

In order to include the mesh effects and transmission into the data analysis, the high resolution SIMION model of the three grid system was used to to generate mesh transmission curves for different monoenergetic ions and linear interpolation was used to obtain the cor-

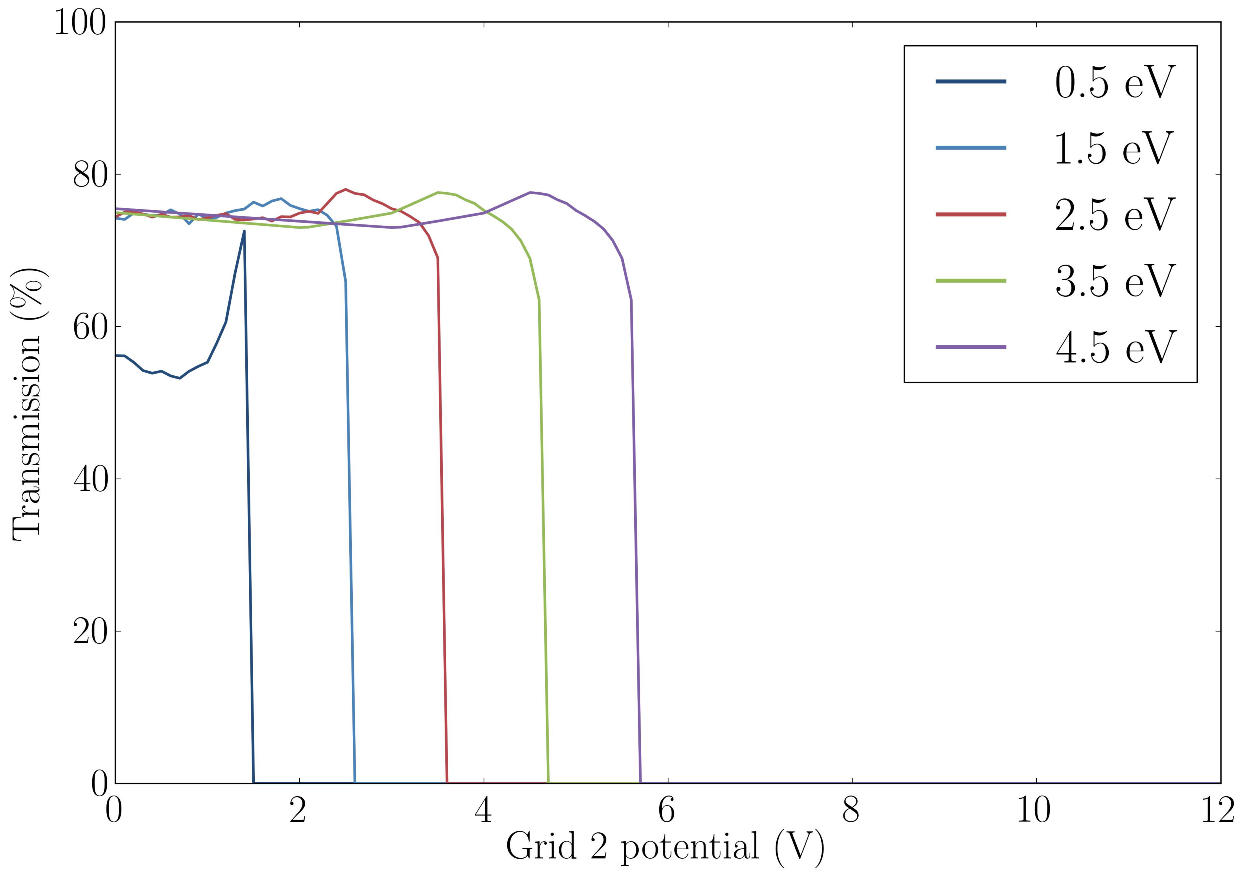

Figure 5.9: Mesh transmission curves for -150 V on grid 3. The ion energy increases from left to right. A drop in transmission as well as the formation of a peak can be seen towards the lowest energies. At higher energies ($>$ 5 eV) the transmission curve only shifts further to the right without changing its shape.

responding curves for intermediate energies. Selected curves for the $V_3 = -450$ V case (LEDA source) are shown in Figure 5.8 and for the $V_3 = -150$ V case (SuSI/Q014) in Figure 5.9. With $f(E)$, T_{coll}, and T_{mesh}, the theoretical collector current $I_{col,theo}(V_2)$ used in the objective function 5.6 can be expressed as:

$$I_{col,theo}(V_2) = A \cdot \sum_{E_i=E_{min}}^{E_{max}} f(E_i) \cdot T_{coll}(E_i) \cdot T_{mesh}(E_i, V_2) \tag{5.8}$$

assuming a discrete set of energies, as is usually the case in numerical treatments. A is a scaling factor that contains the normalization and I_{sat}.

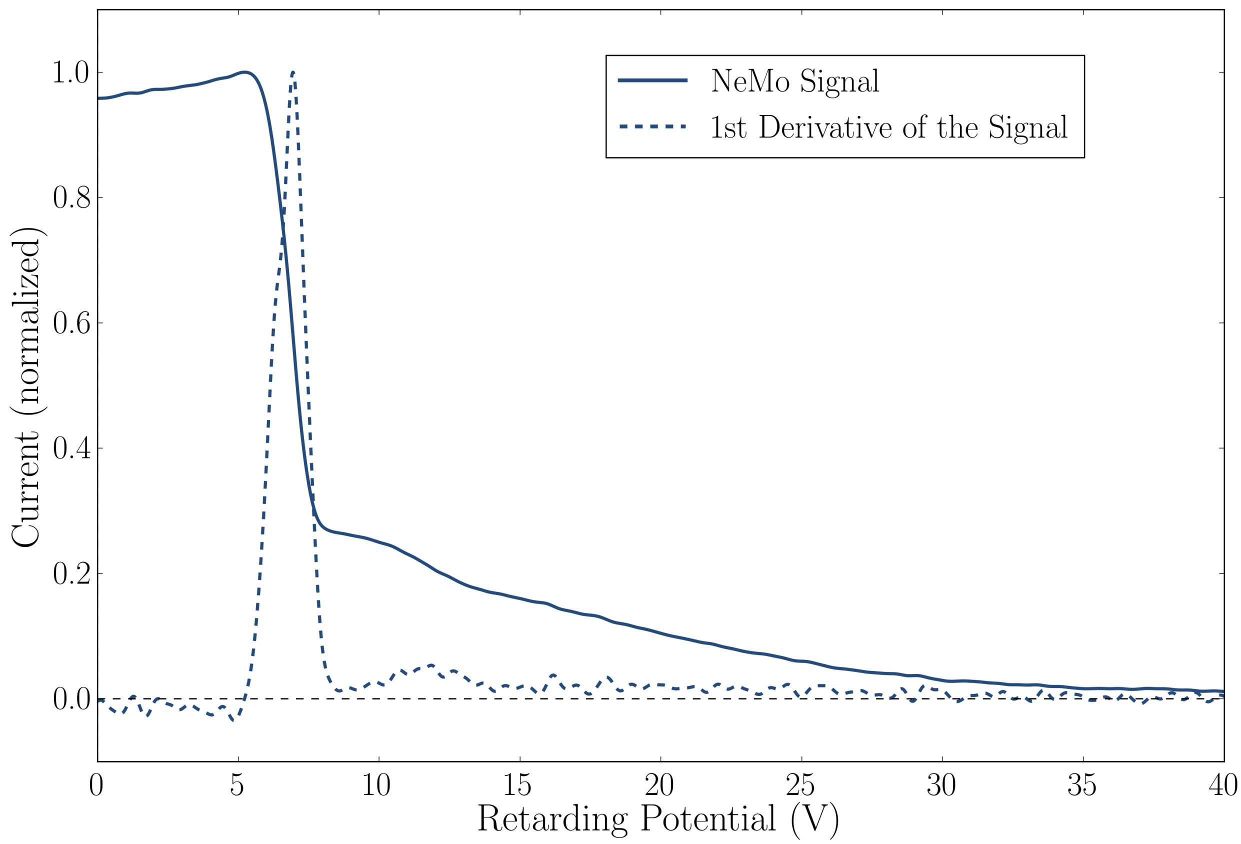

Figure 5.10: Example of a high energy tail. This spectrum was taken with a 180 μA Ar^{8+} beam at SuSI/Q014. The long tail can clearly be seen. The tail contributes approximately 25 % to the saturation current. The first derivative corresponds to the energy distribution of the secondary ions. Both, signal and derivative are normalized to a maximum of one for better visibility.

5.2.3 High Energy Tail

Many of the RFA spectra exhibit features that diverge from the simple linear drop one would expect from the energy distribution of a uniform round beam. Some of these features can be explained by the transmission through the three grids of the RFA or reflection from the collector plate (a dip in the low energy part, a bump before the steep dropoff of the actual ion distribution). These have been discussed in Section 5.1.2. In addition, non-uniform distributions (e.g. Gaussian) or beam halo can lead to a significant rounding of the low-energy edge of the spectrum. However, the high energy edge of the spectrum should, in theory, be relatively sharp. But most of the spectra taken with the RFA at the LEDA source show a rounding also of the high energy side, and in all of the spectra taken with the RFA in the SuSI beam line, a tail towards higher energies is observed. An example of such a tail is shown in Figure 5.10 for the case of a 180 μA Ar^{8+} beam at SuSI/Q014. A long tail as well as a pronounced bump can be seen, which, in the first derivative, looks like an additional separate ion population peaking at $\approx$ 12 V and linear falloff to 0 between 35 and 40 V. Other authors have observed similar behaviour of their retarding field analyzer spectra (albeit not with such a pronounced tail) and have, depending on the respective situation, found different explanations:

1. Dissociative ionzation. A diatomic molecule can be excited by ion- or electron impact and subsequently dissociate into ions with energies peaking around 8-10 eV [7, 110].

2. Beam halo. In [111] Sherman *et al.*, found that depending on the aspect ratio of the beam they sometimes saw mostly the beam halo consisting of H_2^+ and possibly H_3^+, and observed the actual beam contribution as the high energy tail. However, the energy range of this tail was never as wide as the tail observed in this work.

3. Residual gas temperature. The gas molecules have a Boltzmann-distributed energy with maximum around 0.2 eV. This is not much, but can contribute a little to the rounding off of the edges.

4. Rapid oscillation of the beam between two space charge compensation levels due to collective oscillations in the beam plasma [7, 48].

5. Ion beam oscillations. Recently, Toivanen *et al.* have published a paper on their measurements of fast beam current oscillations in the ECR LEBT of the University

of Jyväskylä [112]. These oscillations are too fast to be seen with a standard faraday cup setup and might offer an explanation for the long tail in the RFA spectra in the SuSI diagnostic box Q013/Q014. The observed oscillations are in the hundreds of Hertz to kHz regime. They depend on the ion source parameters like strength of the solenoid fields and microwave power. 2σ oscillation amplitudes up to 80% relative to the observed average beam current have been seen, although 10 - 20 % seem more typical. If the beam intensity suddenly and for a short time increases, so does the beam potential, and a few ions with higher energy might enter the detector (before the beam goes back to steady state), leading to a tail.

6. Insulating layers building up on the grid surfaces. Sherman *et al.* [113] observed that it was necessary to heat their RFA to $\approx 350^\circ$ in order to prevent the buildup of material on the grids and obtain consistent resolution and calibration. They cite a study by Poole *et al.* [114] in which electron impingement on deposited layers of organic material creates radicals and subsequently polymerizes them, thereby forming high resistance films. The main source for the initially deposited material was claimed to be vacuum grease used in combination with rubber O-rings. In the SuSI set-ups presented here only copper gaskets were used for sealing of vacuum components and thus heating was considered, but deemed not feasible. However, with the appearance of the high energy tails, heating might be considered as part of a future upgrade of the detector system.

7. Charge-exchange of two electrons. According to the Müller-Salzborn empirical scaling law, the cross-sections for the exchange of two electrons is not negligible. If secondary ions are in the q = 2+ state and pick up an electron on the way to the detector, their energy could be up to twice $e\Phi_{center}$.

5.2.4 Error Estimation

Because this measurement can not be considered a precision measurement, and because of the rather large errors associated with the cross sections in the theoretical prediction I will not attempt a detailed error analysis, but instead estimate in a broad way the largest contributions to the errors associated with the presented measurements, thereby providing only constraints to the maximum errors.

5.2.4.1 Statistical Errors in the Measurements

In the LEDA data sets, the collector current for each voltage step was calculated as the average of a sample of 200 data points. The σ of each data point was used as individual error in the least squares fit. During the SuSI measurements, the signal on the collector plate was monitored continuously and the σ of the data point with the lowest current in each measurement was calculated from ≈ 100 samples and used as error for all data points in the set (the largest error is associated with the lowest currents measured by the beam current monitor). The absolute statistical errors on the grid voltage (V_2) of ± 0.05 V are considered negligible (systematic errors of the grid voltage are corrected with a calibration curve). The relative errors Δf_e of the neutralization factor resulting from including statistical errors of the collector current are between 1% and 4%.

5.2.4.2 Systematic Errors in the Measurements

The main sources of systematic errors in the measurements are the uncertainty of the total beam current, the beam line pressure, and the contribution of the high energy tail.

LEDA injector source

In the LEDA case, the beam current can conservatively be said to be known to ± 0.75 mA (this is the difference of drain current, and the higher Bergoz 1 reading, cf. Subsection 5.3.1). This introduces a relative error from Δf_e of -1.4% to + 1.0% for the highest current (where $\Delta I_{beam} = \pm 8\%$) to -13% to + 6% for the lowest beam current (where $\Delta I_{beam} = \pm 26\%$). The high energy tail can make up 5 - 20% of the saturation currents measured in the LEDA injector source beam line. Fitting the tail with an underlying Gaussian energy distribution gave good fit results and only changed the neutralization factor by +1 to +2%. As a conservative approximation, I will assume a systematic error of ±5% due to the tail. The errors in f_e due to tail and beam current are added in quadrature to the statistical error for the errorbars in the plots.

SuSI/Q014

In the SuSI beam line at Q014, a faraday cup was used to measure the beam current ≈ 20 cm upstream of NeMo. In combination with the beam current monitors (BCM) produced in-house at the NSCL, a conservative estimate of the accuracy of the beam current is ±10%. The ion gauge used to measure the pressure of the residual gas was calibrated for N_2 (which is also the gas used in the experiments to raise the pressure in the beam line). Both, the ion gauge and the leak valve for raising the pressure are located in the same diagnostic box as NeMo. I am assuming an accuracy of the pressure values of better than ±10% as well. The tail can account for up to 35% of the saturation current. Fitting with different background functions revealed an absolute error in neutralization factor f_e of 5% to 10%. As a conservative approximation, I will assume an absolute systematic error of ±10% due to the tail. Compared to this error, the statistical error and the error due to the beam current uncertainty are small. Added in quadrature, the total error is estimated to be ±11%. This will be used as vertical error bars in all SuSI plots.

5.2.4.3 Systematic Errors in the Theoretical Predictions

Uncertainties in the theoretical calculations will be indicated by a shaded area in the plots.

LEDA saturation current. During the LEDA measurements, an ion gauge and a residual gas analyzer were available. Both were uncalibrated and showed a large discrepancy. Using the average of both readings as value for the pressure, and being very conservative, this means the relative error on the pressure reading was ±75%! The ion creation cross sections $\sigma_{i,g}$ are only known to ±30% as well. As mentioned before, the ion beam currents are known to ±0.75 mA (±8% to ±26% error in this current regime). Assuming that the transmission factors calculated with SIMION are correct to ±10%, this leads to a total systematic error for the theoretical saturation current of ±82 to ±85%.

LEDA neutralization. Müller and Salzborn claim that 2/3 of the measured charge exchange cross sections are within ±35% of their empirical formula [1]. Ionization cross sections are available for protons in the energy range of the LEDA source, and are cited with similar uncertainties. In the following I will assume that the cross sections for ionization and charge exchange are known with ±35% accuracy for the LEDA source. Uncertainties in beam current (±8% to ±26%) and beam line pressure (±75%) have to be considered as well.

SuSI saturation current and neutralization. Unfortunately, the typical energies of ECRIS beams are below the validity of the Kaganovich fit for ion-atom impact ionization [59]. However, at lower energies, charge exchange processes are dominating over ionization and we can use the Müller-Salzborn fit for σ_i. I assume that additional processes like single ionization, dissociative ionization, etc. will not increase the cross section by more than 50%. σ_e is approximated as a quarter of σ_i.

5.3 Measurements

Space charge compensation measurements have been attempted at four different locations:

1. LEDA injector source, diagnostic box 1.

2. Artemis A, vertical beam line before the first dipole.

3. SuSI, first diagnostic box (Q001).

4. SuSI, diagnostic box after the dipole (Q013/Q014).

Detailed analysis has so far been carried out for the two locations LEDA injector source and SuSI Q014 and will be presented in the following sections. Unfortunately, the beam current measurements in the Artemis beam line are not reliable due to a faulty faraday cup. Since knowledge of the total beam current is integral in the analysis of the RFA data, the Artemis measurement will not be reported here. The analysis of the data in the SuSI diagnostic box Q001 is more complex than LEDA and SuSI/Q014 because of the multitude of present species in the ion beam (Q001 is before the first analyzing magnet), which have different charge states and beam radii. In addition, the residual solenoid field (≈ 60 Gauss) of SuSI at Q001 further complicates the analysis. No results from this location will be reported in this thesis, pending future thorough analysis of the data.

5.3.1 LEDA injector ion source

5.3.1.1 Overview

When the LEDA ion source was moved to the NSCL in 2012, an opportunity presented itself to try and measure neutralization of high intensity proton beams and compare the results

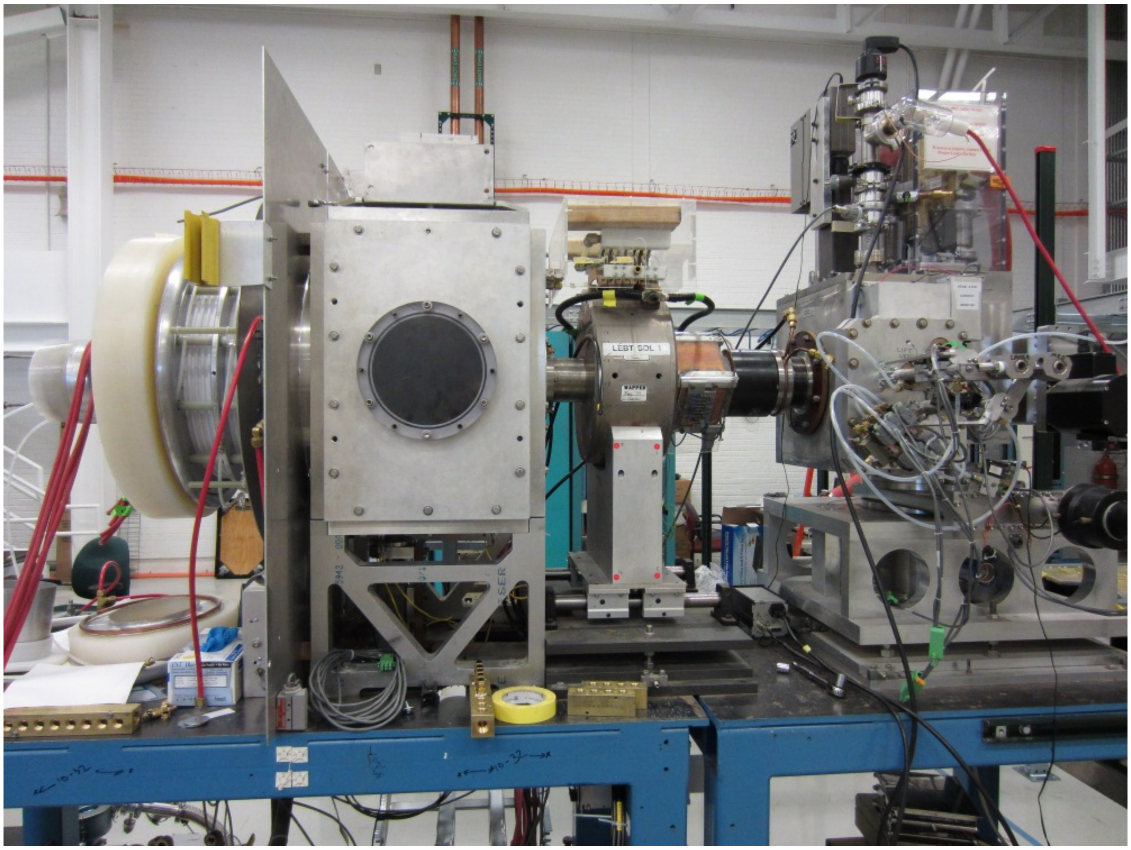

Figure 5.11: Foto of the LEDA injector source at NSCL. The source is located on the left, followed by diagnostic box 1 (the large box in the middle of the image). NeMo was mounted where a transparent flange can be seen in the center of diagnostic box 1. Courtesy of Felix Marti.

to previous measurements on the same source, albeit under different operating conditions. Previous measurements were reported in 1998 by Ferdinand *et al.* [7] with a four-grid energy analyzer developed in 1988 by Sherman *et al.* for H^- beams [111, 113, 115]. The LEDA injector ion source itself is described briefly in section 4.1.1. Beside the design differences in the retarding field analyzer (three grids instead of four, not heated, two-aperture collimation instead of one entry aperture), one major difference to the previous measurements is the current regime. The measurements presented by Ferdinand *et al.* were obtained with beam currents from 50 mA to 130 mA, whereas the results presented here are for much lower currents from 5 mA to 10 mA; a result of the drastically reduced diameter of the extraction

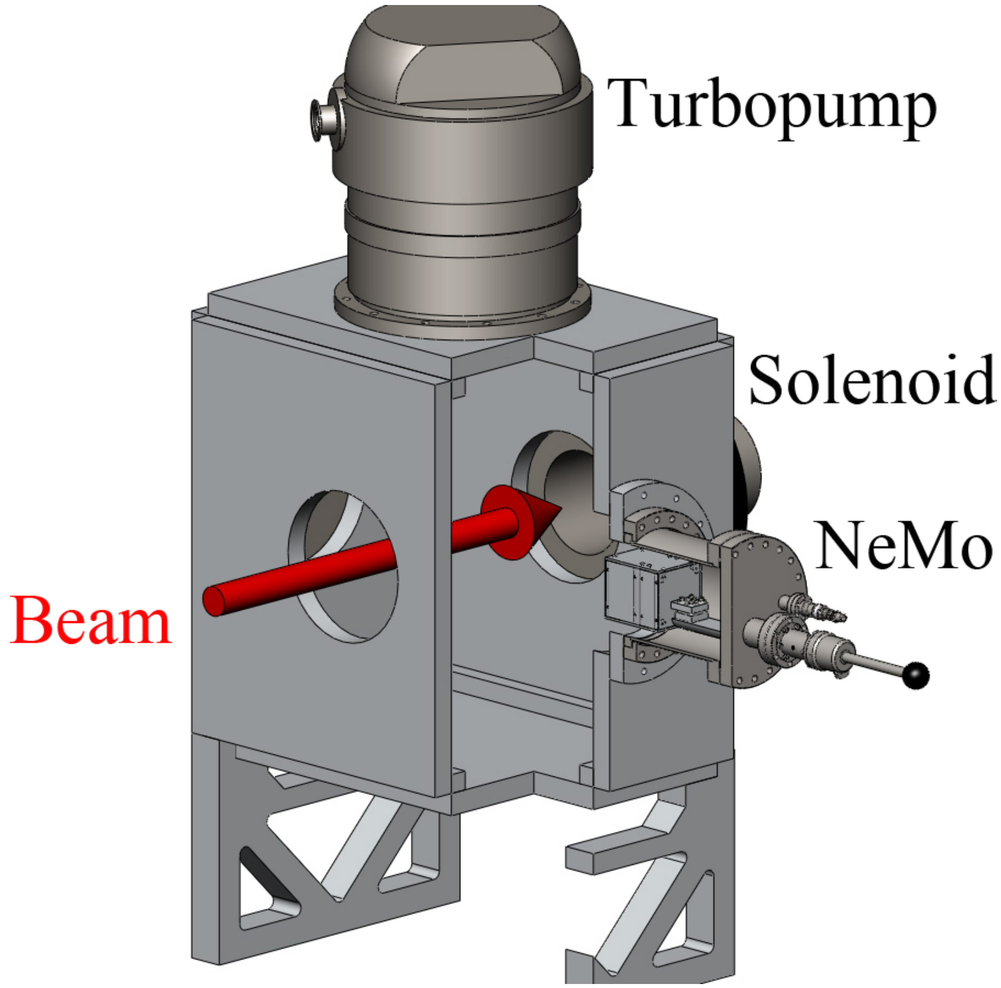

Figure 5.12: 3D CAD drawing of diagnostic box 1 and the NeMo retarding field analyzer in the LEDA injector source beamline. The source itself is to the left and not shown.

aperture. This was done in order to decrease the beam emittance for another experiment. The NeMo detector was mounted on the side of diagnostic box 1 which is shown in the photograph in Figure 5.11 and as a CAD drawing in figure 5.12.

5.3.1.2 Data Acquisition

In contrast to the other measurements, and due to the location of the LEDA injector source in a remote area of the laboratory, the data acquisition had to be a stand-alone system. This was realized with LabView 2010 on a laptop computer communicating with a Keithley

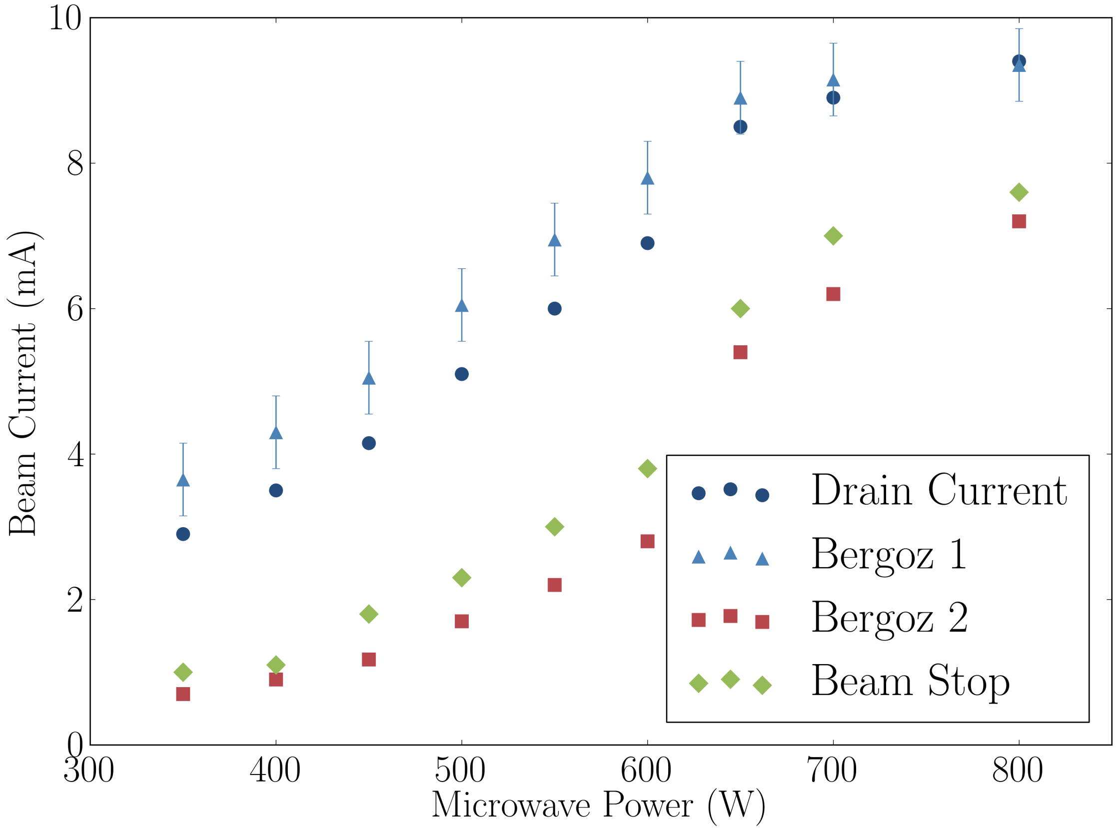

Figure 5.13: NeMo - LEDA injector source: Beam currents versus microwave power. Bergoz 1 and the drain current are representative of the total beam current at the location of the neutralization measurements. It can be seen that the extracted current behaves linearly with microwave power up to 600 W and then flattens out. This could be because not enough gas is supplied to sustain the higher currents or because the source is outgassing, thereby contaminating the plasma.

6485 Picoammeter for the collector current readout and a KEPCO BOP-500M bipolar power supply for the retarding field voltage via USB-to-serial port converters. The voltage on grid 2 (the retardign field) provided by the KEPCO BOP-500M was changed manually. Each time a data point was taken, the LabView program would read out the power supply's voltage and average over 200 picoammeter readings.

5.3.1.3 Diagnostics

The total beam current was measured at four different locations in the beam line:

1. As drain current on the ion source high voltage power supply after subtracting the dark current of ≈ 0.1 mA which was recorded each day at the beginning of the measurements and frequently re-checked.
2. Shortly after the extraction system by means of a Bergoz DC current transformer (Bergoz 1).
3. Shortly after the solenoid at the exit of diagnostic box 1 by means of another Bergoz DC current transformer (Bergoz 2)
4. At the end of the short beamline on a copper beam stop.

Both Bergoz current transformers showed large fluctuations during the measurements even when drain current and beam stop current, as well as visual imaging of the beam would suggest good beam stability. The most accurate account of the actual beam current in diagnostic box 1 was thus given by the power supply drain current. A measurement of beam current versus the microwave power is shown in Figure 5.13. For demonstration of the high uncertainty of the current transformers, the errorbars on Bergoz 1 are shown. The errobars on the drain current are smaller than the markers. It can be seen that the extracted current behaves linearly with microwave power up to 600 W and then flattens out. This could be because not enough gas is supplied to sustain the higher currents or, more likely, because the source is outgassing, thereby contaminating the plasma. Before and during the measurements, the beam line had to be opened several times, leaving little time to condition the source properly.

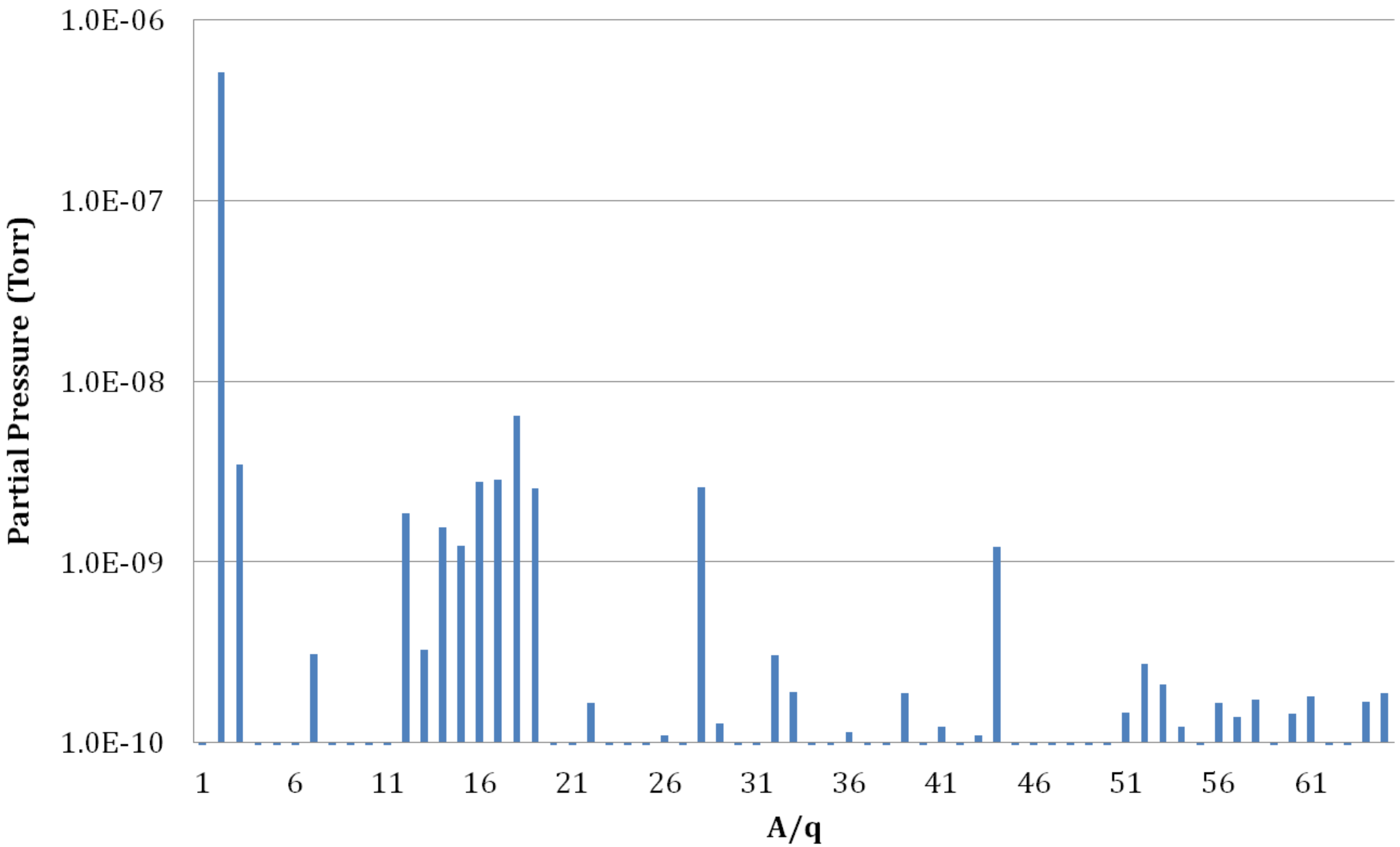

Figure 5.14: A typical residual gas analyzer spectrum during a neutralization measurement. The data suggests a ratio of roughly 19:1 of molecular hydrogen (H_2) to heavier species. Note the logarithmic scale for the pressure.

The beam line pressure was measured with a hot cathode ion gauge close to the end of the beam line and in parallel monitored with a residual gas analyzer (RGA). Both devices were not calibrated and thus, unfortunately, can give only a ballpark idea of the correct pressure in the beamline. However, the RGA can at least give us an idea of the composition of the residual gas. A typical histogram plot of the RGA is shown in Figure 5.14. It can be seen that the main contribution to the residual gas is hydrogen, which was to be expected because hydrogen is the source gas and leaks into the beamline. The RGA data suggests a total pressure of $\approx 5 \cdot 10^{-7}$ Torr of H_2 versus $\approx 2.6 \cdot 10^{-8}$ Torr for the rest of the gas species (mostly H_2O, N_2, N and O) which is a ratio of 19:1. The corresponding ion gauge readings are in the regime of $4.25 \cdot 10^{-6}$ Torr - almost an order of magnitude higher. This, of course imposes a very large error on the entire measurement.

5.3.1.4 Measurements

Due to time constraints and difficulties setting up the data acquisition, only one dataset was finally obtained with the LEDA injector source: A measurement where the total beam

Table 5.3: Parameters for the neutralization measurement in the LEDA injector ion source low energy beam transport line.

Parameter	**Value**
Beam current	2.9 - 9.4 mA
Primary beam	protons
Total RGA pressure	$5.26 \cdot 10^{-7}$ Torr
Ion gauge pressure	$4.25 \cdot 10^{-6}$ Torr
Residual gas	95% hydrogen
NeMo grid 3	-450 V

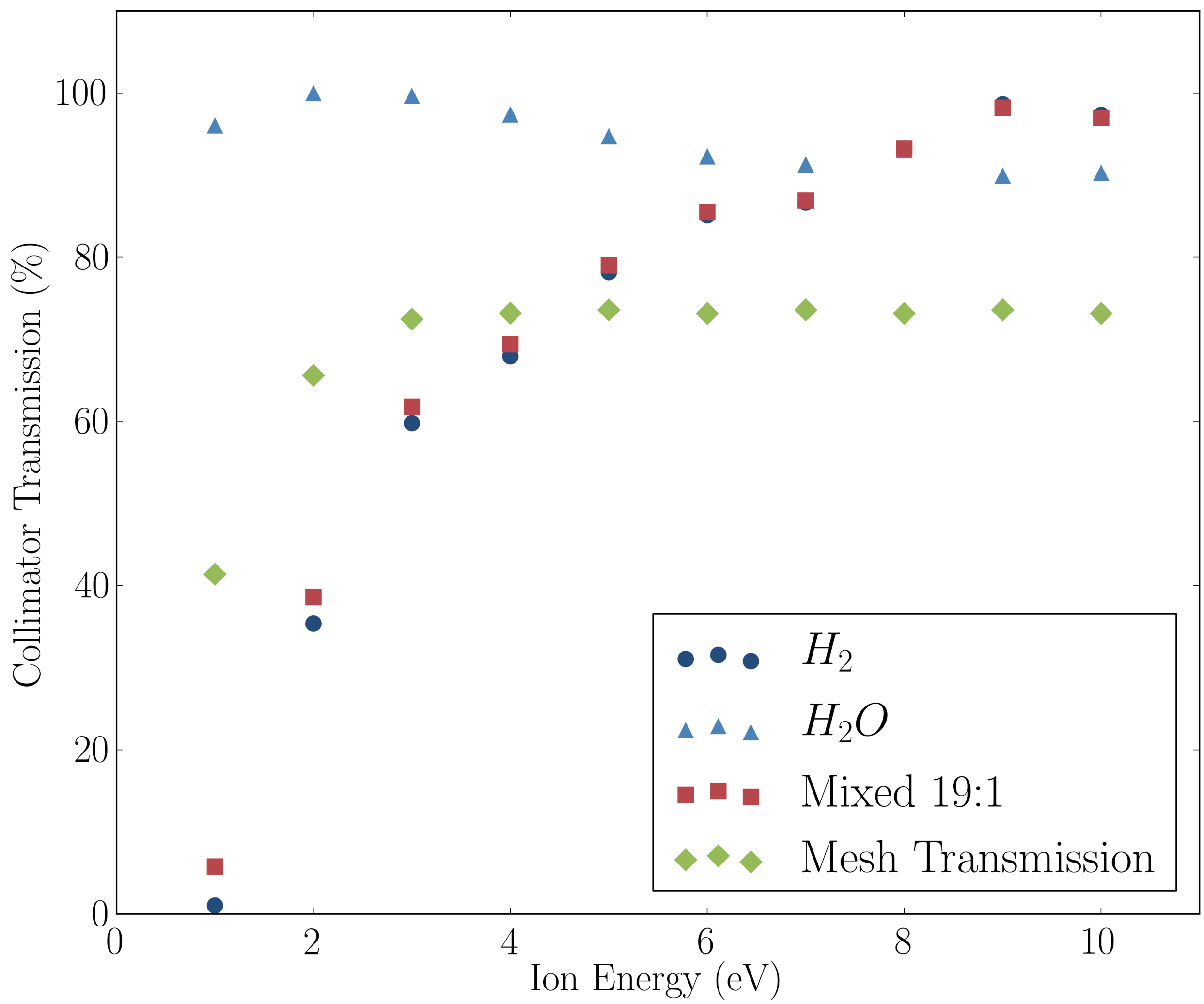

Figure 5.15: Transmission curves for H_2 and H_2O as well as a mix of the two with ratio 19:1 as observed in the RGA spectra. It is evident that for heavier ions the magentic field does not have a very big effect, thus H_2O is representative of all ion species heavier than ^{14}N. It can also be seen that the mesh transmission is around 73% (as expected) down to ion energies of about 2.5 eV where it rapidly drops towards lower energies due to reflection.

current was varied while the pressure was kept constant. The parameters of the series are listed in Table 5.3.

As suggested in Section 5.2, we begin our analysis by plotting the saturation currents and comparing them with the theoretical prediction. During this measurement a residual magnetic field of ≈ 6 Gauss was present along the beam axis at the location of the measurement. The residual gas molecules according to the RGA data were mostly H_2. As discussed earlier, this warrants the use of a collimator transmission curve in order to correct the saturation currents for losses in the collimation system and a grid transmission curve to account for losses through reflections and focus effects (the voltage on grid 3 was -450 V, hence the reflection of ions is more pronounced in these measurements). The transmission curves as calculated with SIMION are shown in figure 5.15. For lack of a better approximation, the pressure was assumed to be halfway between the total RGA pressure and the ion gauge pressure reading, with a ratio of residual gases as given by the RGA. The necessary cross-sections for ionization were calculated with the empirical formula provided by Kaganovich *et al.* [59], the contribution from charge exchange was estimated by scaling a measured cross-section curve at higher energies with the low-energy values obtained by using the Müller-Salzborn scaling law [1]. The cross-sections are listed in Table 5.4.

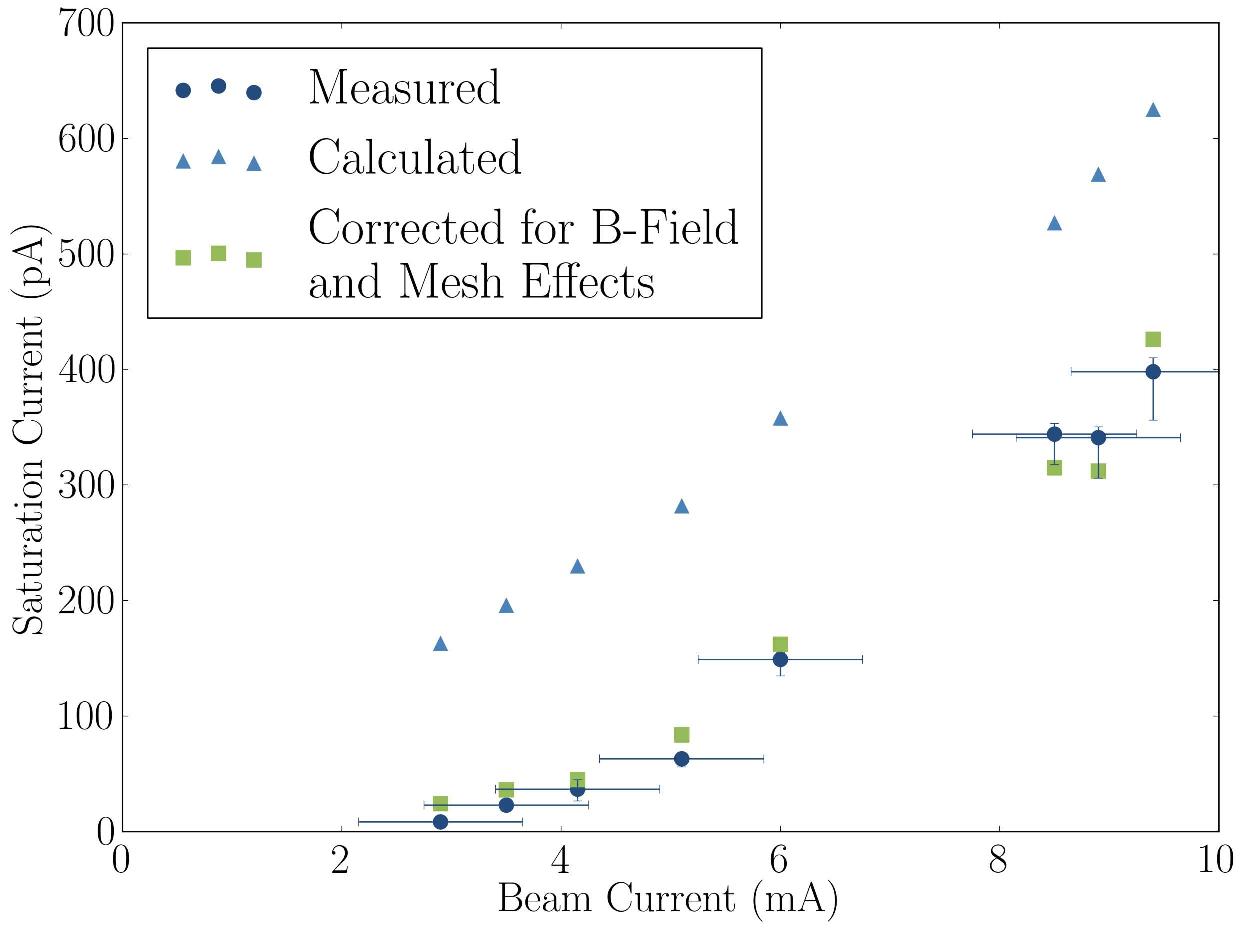

Figure 5.16: Corrected saturation currents. Note that the three data points at the highest beam currents actually have lower secondary ion energies, either due to a larger beam radius or higher space charge compensation. As discussed in Section 5.2.4 the systematic error bars on the theoretical prediction are $\approx 82 - 85\%$. This is very large and makes an absolute comparison mute. However, the relative change of saturation current with beam current can be examined and reproduced by applying transmission factors (cf. text).

Table 5.4: Cross-sections for creation of slow secondary ions calculated for 70 keV proton beams in different residual gases. Note: Only includes single ionization and charge-exchange.

Gas molecule	$\sigma_{i,g}$ (m^2)
H_2	$2.98 \cdot 10^{-20}$
N_2	$6.92 \cdot 10^{-20}$
H_2O	$1.28 \cdot 10^{-19}$
Ar	$7.29 \cdot 10^{-20}$

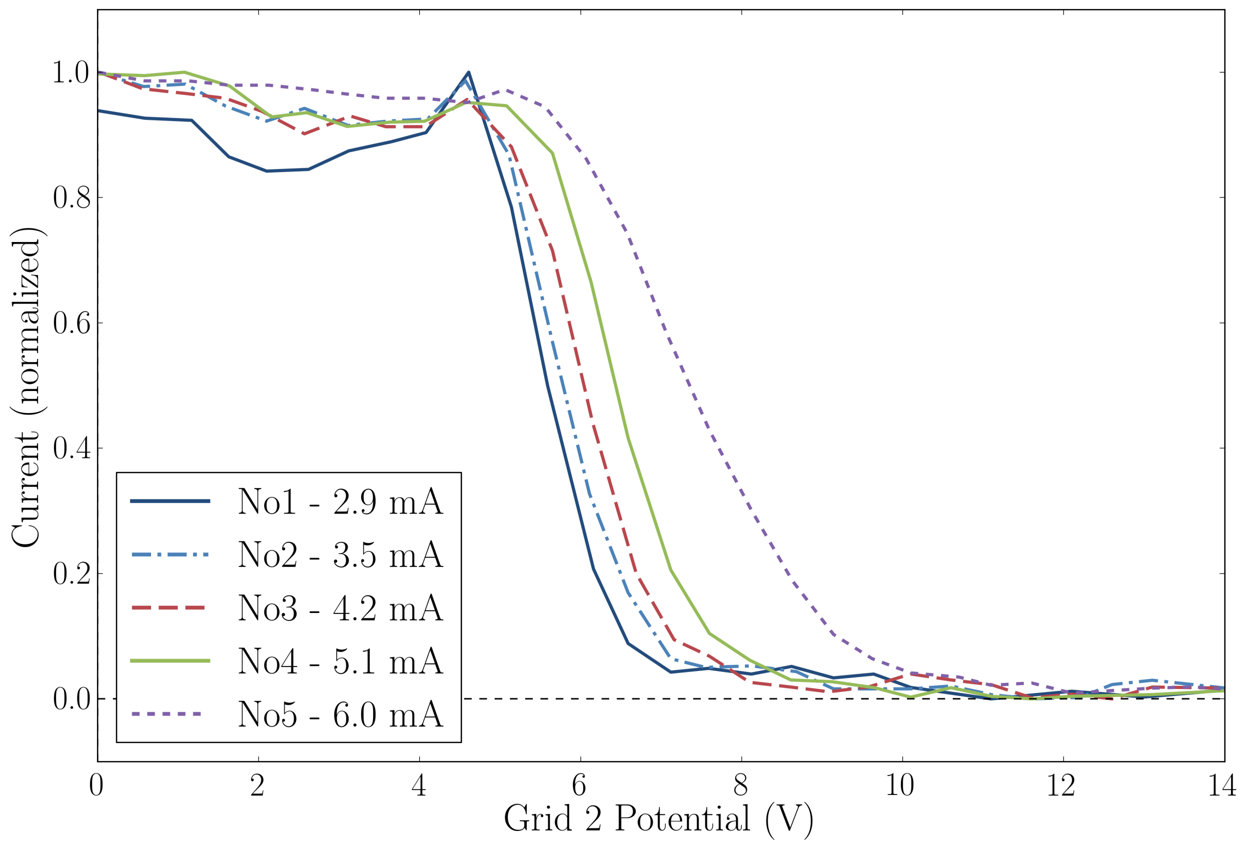

Figure 5.17: NeMo neutralization Spectra for 5 different beam currents in the LEDA injector ion source beam line diagnostic box 1. The voltages have not yet been corrected for the effective potential inside the meshes. The curves increase in current from left to right.

The corrected theoretical saturation currents for the given beam currents and pressures alongside the uncorrected predictions and the measured currents are shown in Figure 5.16. It can be seen that the corrected calculated saturation currents are aligning quite well with the measured ones.

The next step in order to obtain the neutralization values is to analyze the NeMo spectra. The first 5 spectra of the current variation series (i.e. beam currents of 2.9 mA to 6.0 mA) are plotted in figure 5.17. All of them have been normalized so they are easier to compare. For the lowest beam current (2.9 mA) we observe a pronounced dip in the collector current due to the reflection of ions discussed earlier (cf. 5.1.2). It is also seen for the next two

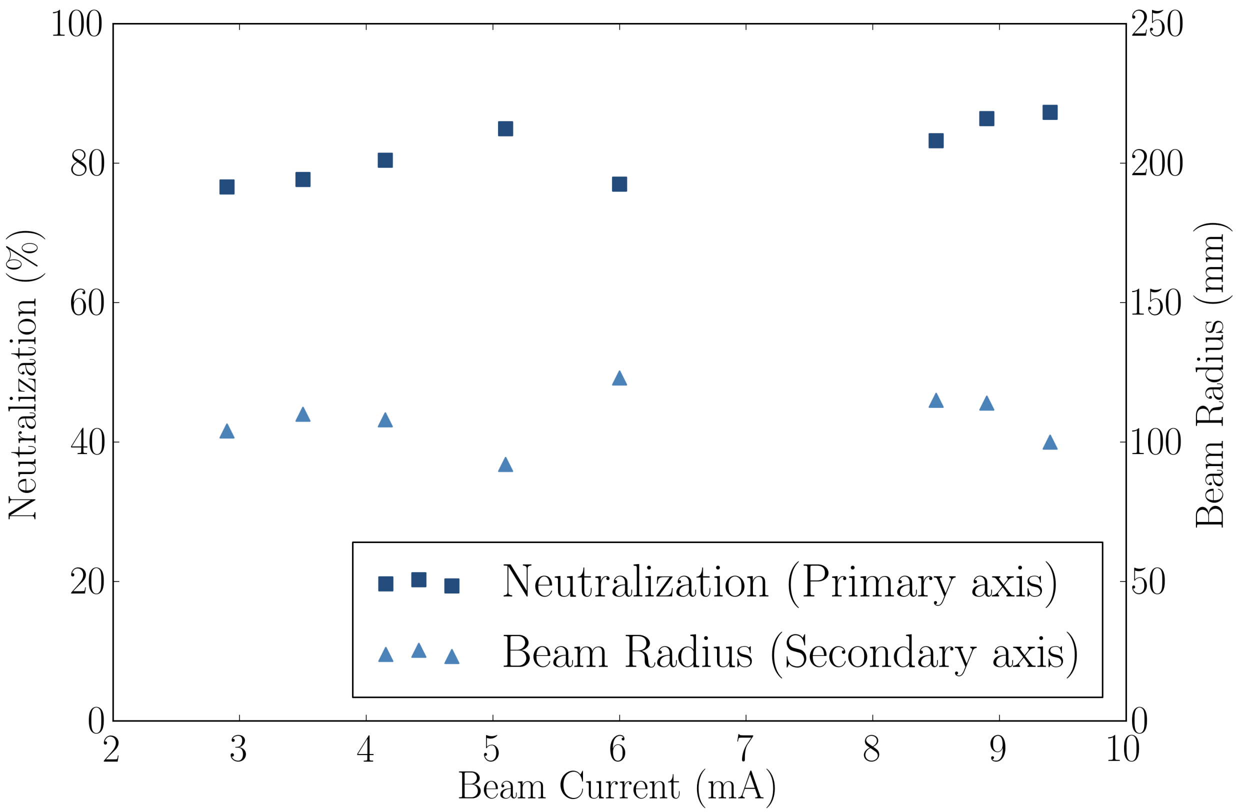

Figure 5.18: Results of the current variation with the LEDA injector ion source: Neutralization and Beam sizes. It can clearly be seen that although the overall beam radii are much too large, they reflect the observed variations in neutralization. Note that changing the beam radius in the analysis only changes the center potential of the beam (shifts the spectrum left-right) and not the slope of the curve (i.e. the neutralization).

currents, albeit not as strong because the overall beam potential increases with current and the secondary ions have slightly higher energies. Following the procedure described in Section 5.2.2, we calculate the mesh transmission curves for the given setup (cf. figure 5.8) and use the least squares fitting method to calculate neutralization and beam radius for the measured curves.

It should be mentioned that the obtained neutralization f_e is independent of beam and beam pipe radii (as we saw in chapter 2.1.5), the overall potential, however, is not. The obtained value for the beam radius is highly dependent on the ion density distribution of the beam and the sorrounding walls (in this case of diagnostic box 1). We have assumed a uniform

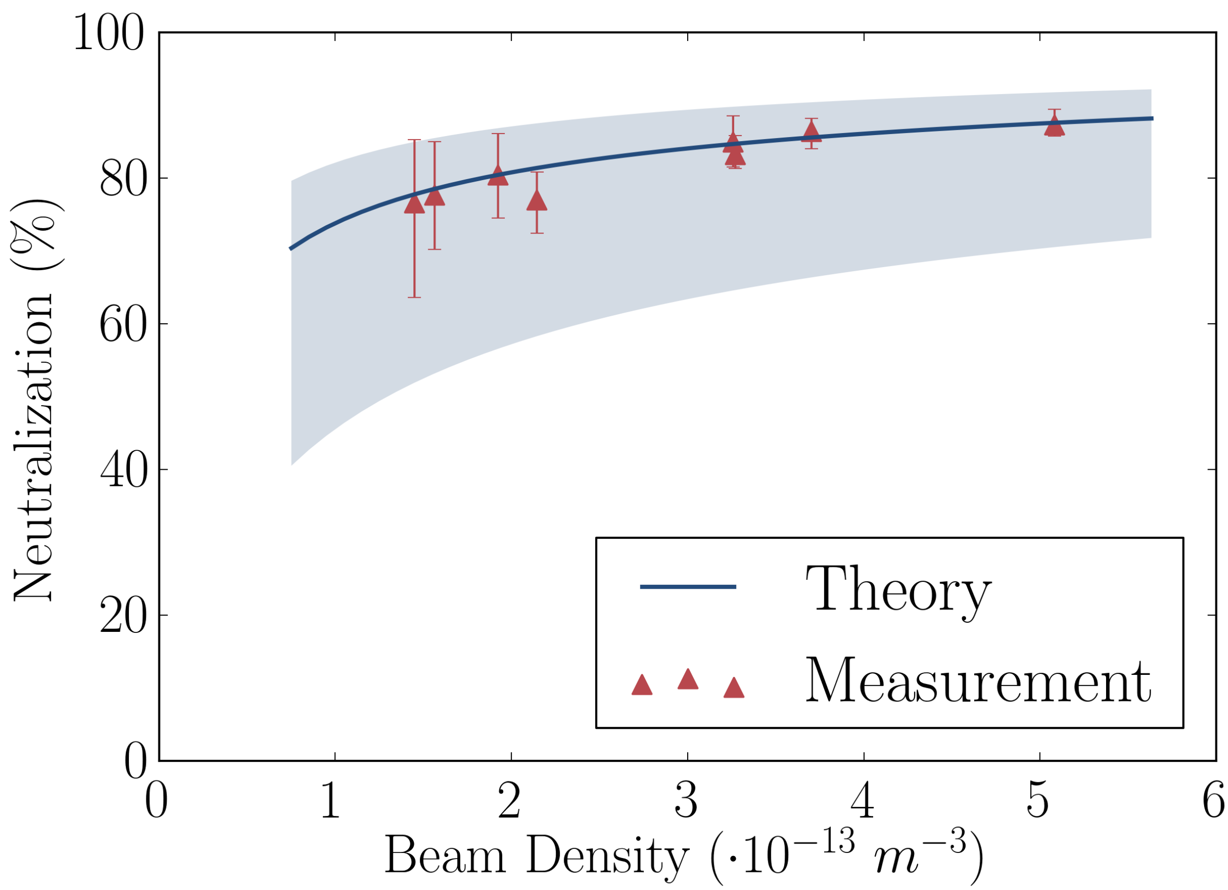

Figure 5.19: Measured neutralization as a function of ion beam density. The solid line is the theoretical prediction following the model described in 2.1.5, the shaded area includes the uncertainties in pressure and cross sections.

distribution, which is a good approximation for determining the neutralization, but may not be ideal to give realistic beam radii just from neutralization spectra. In addition, SIMION simulations revealed that the potential calculated from a round pipe corresponding to the size of the square box is actually much too high and a smaller *effective beam pipe radius* r_p of 175 mm should be used (as opposed to the 280 mm half-width) this is because the half-length of the box is only 190 mm and beam pipes with diameters of only $\approx 100mm$ lead away on both sides. That being said, the obtained beam radii are consistently an order of magnitude too large (they are shown in Figure 5.18 alongside the neutralization results). This could have several reasons:

- The effective wall radius of 175 mm is still overestimated. Other objects in diagnostic box 1 (e.g. cooling water pipes, cables) could further change the beam potential offset.

- The Mesh transmission curves are overestimating the shift towards higher effective potentials.

- The beam distribution is not uniform.

Another possibility, though unlikely, should be pointed out: In case of a misalignment of the detector and offcentered beam, it is possible that mostly ions created in the beam halo enter the detector and only at the highest beam currents, a contribution from the actual beam is seen as tail in the spectrum (similar to item 2 in Subsection 5.2.3). The ions making up this tail would have a higher energy, corresponding to a tighter beam. However, comparison with previous work by Ferdinand *et al.* [7] shows that beam radii calculated from their presented RFA data are also much too large (although this is not discussed in the paper).

Regardless of the overall mismatch of the beam radii which were expected to be between 10 and 20 mm, the obtained values can be used to calculate a beam density by scaling them all with a factor 10 in order to compare the results with formula 2.50 derived in section 2.1.5. The result can be seen in figure 5.19. The same cross sections for ion and electron production as in the saturation current calculations were used as well as the same pressure of $2.4 \cdot 10^{-6}$ Torr lying halfway between the ion gauge reading and the RGA total pressure. It can be seen that the results match well to the theoretical prediction and that the neutralization increases with beam density, as was expected.

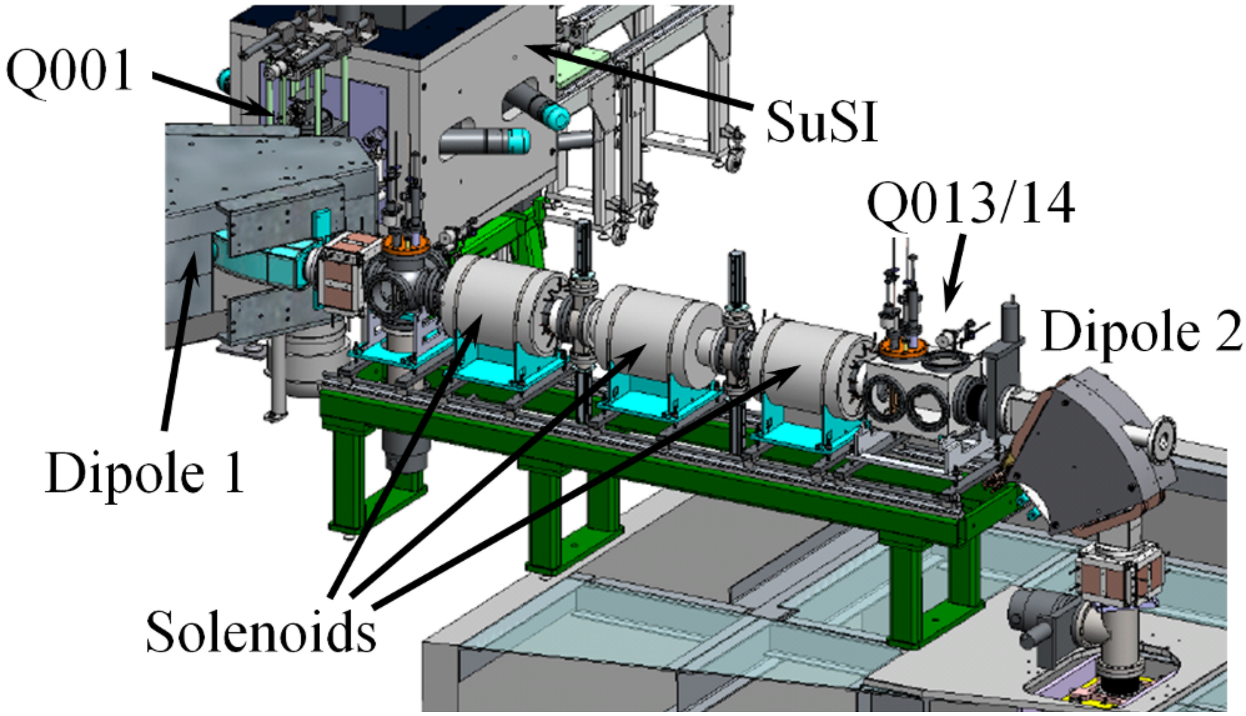

Figure 5.20: Schematic of the SuSI LEBT system up to the second dipole magent. Between the first dipole and the location of NeMo (in the diagnostic box Q013/14) there is a focusing and collimation channel consisting of 3 solenoids, apertures, and slits.

5.3.2 SuSI Superconducting ECRIS

5.3.2.1 Overview

The second location where space charge compensation measurements were performed is the diagnostic box Q013/14 in the LEBT of the superconducting ECRIS SuSI. The location of the diagnostic box in the SuSI LEBT system is shown in Figure 5.20. The beam optics elements in the LEBT system between extraction and measurement location in order of distance from the source are:

- **Q002EL** - Einzel lens directly after the extraction system
- **Q003DH/DV** - Horizontal and vertical steering magnets.
- **Q005DS** - Dipole magnet for selection of desired ion species by A/q.

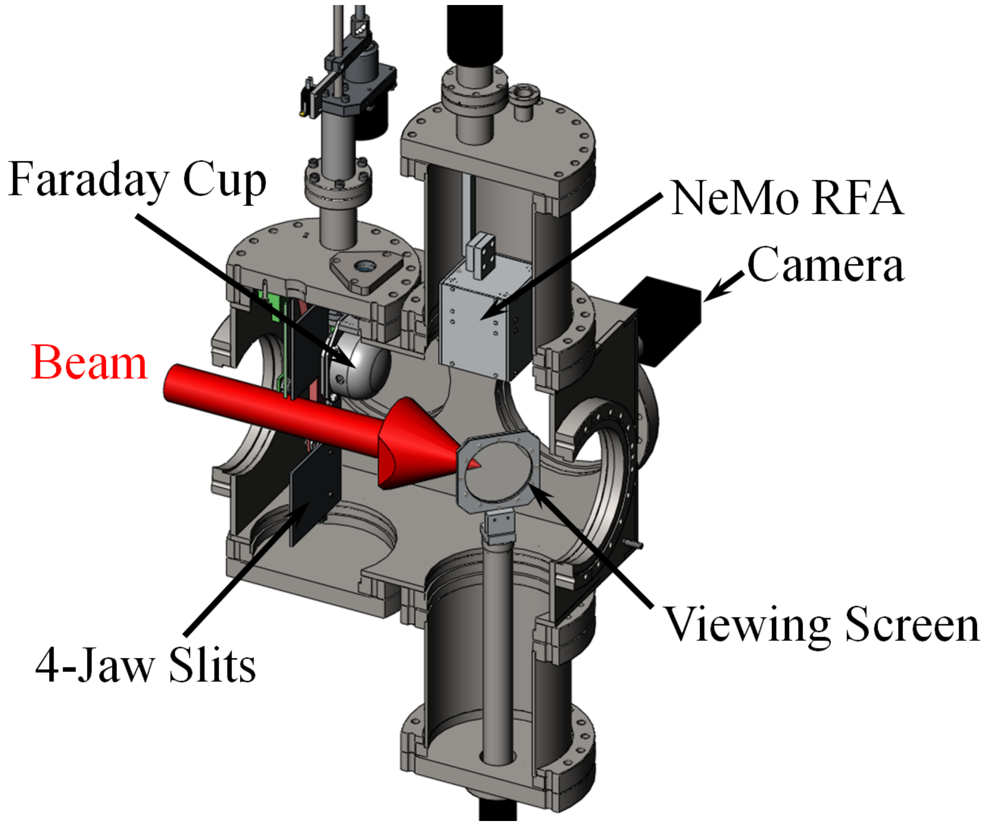

Figure 5.21: 3D CAD schematic of diagnostic box Q014 in the SuSI LEBT.

- **Q006DH/DV** - Horizontal and vertical steering magnets.
- **Q008SN** - First collimation channel solenoid.
- **Q010SN** - Second collimation channel solenoid.
- **Q012SN** - Third collimation channel solenoid.

In between, there are various apertures and 4-jaw type slits (cf. section 4.2.4). One important fact to notice is that this measurement was carried out after the analyzing magnet (Q005DS). Hence the beam was composed mostly of one ion species and a small fraction of the charge state below $(q - 1)$ created by charge exchange processes.

5.3.2.2 Data Acquisition

The collector current of NeMo was measured with a *beam current monitor* (BCM) built in-house at the NSCL. BCM and collector plate were connected by a double-shielded BNC cable to decrease noise. Communication with the BCM was established via the laboratory's EPICS system. A simple x/y plotter program (*ECR-tune*) was used to set the voltage on grid 2 (V_2) with a remotely (EPICS) controlled KEPCO BOP-1000 power supply and read the BCM current after a user defined delay.

5.3.2.3 Diagnostics

The diagnostic box Q013/14 with NeMo and other diagnostic devices is shown in Figure 5.21. The box contains the following:

- Faraday cup (Q013).
- 4-jaw type slit (Q013).
- Hot cathode ion gauge (Q013).
- Leak valve connected to a N_2 feed line (Q013).
- Viewing screen (exchangeable material: SiO_2 or KBr coated metal screen) (Q014).
- NeMo retarding field analyzer (Q014).

5.3.2.4 Measurements

The following six cases were measured at Q014 and will be discussed in detail:

1. O^{3+} Pressure $1.1 \cdot 10^{-5}$ to $1.1 \cdot 10^{-6}$ Torr, current approximately constant at 235 eμA.

2. O^{3+} Current 125 eμA to 298 eμA, pressure approximately constant at $5.0 \cdot 10^{-6}$ Torr.

3. O^{6+} Pressure $1.0 \cdot 10^{-5}$ to $1.0 \cdot 10^{-6}$ Torr, current approximately constant at 700 eμA.

4. O^{6+} Current 194 eμA to 604 eμA, pressure approximately constant at $5.0 \cdot 10^{-6}$ Torr.

5. Ar^{8+} Pressure $1.0 \cdot 10^{-5}$ to $1.0 \cdot 10^{-6}$ Torr, current approximately constant at 200 eμA.

6. Ar^{8+} Current 110 eμA to 331 eμA, pressure approximately constant at $5.0 \cdot 10^{-6}$ Torr.

Pressure Series

Let us begin the examination by looking at the pressure variations. For each set of measurements (except for the O^{6+} pressure series number 3), a corresponding set of slit scans has been made in order to approximate beam size and shape at the location of the RFA. For the O^{3+} and for the Ar^{8+} series, these are shown in Figures 5.22 to 5.25 and figures 5.26 to 5.30, respectively. All slit scans were obtained using a 2 mm by 2 mm opening and the images were interpolated afterward, using a bicubic algorithm. Unfortunately the MatLab library for image acquisition was unavailable during the O^{6+} series. For O^{3+} we can observe a triangular structure which is not uncommon in ECR ion sources. The beam seems to get a bit more focussed with higher pressures. The Ar^{8+} appears to be better tuned for roundness. The slight fading of the beam with higher pressure stems from a slight decrease in beam current from 701 μA to 686 μA. The beam diameter increases slightly from lower to higher pressure, hinting at a change in focussing of the beam, which in turn hints at a change in space charge potential (i.e. higher neutralization).

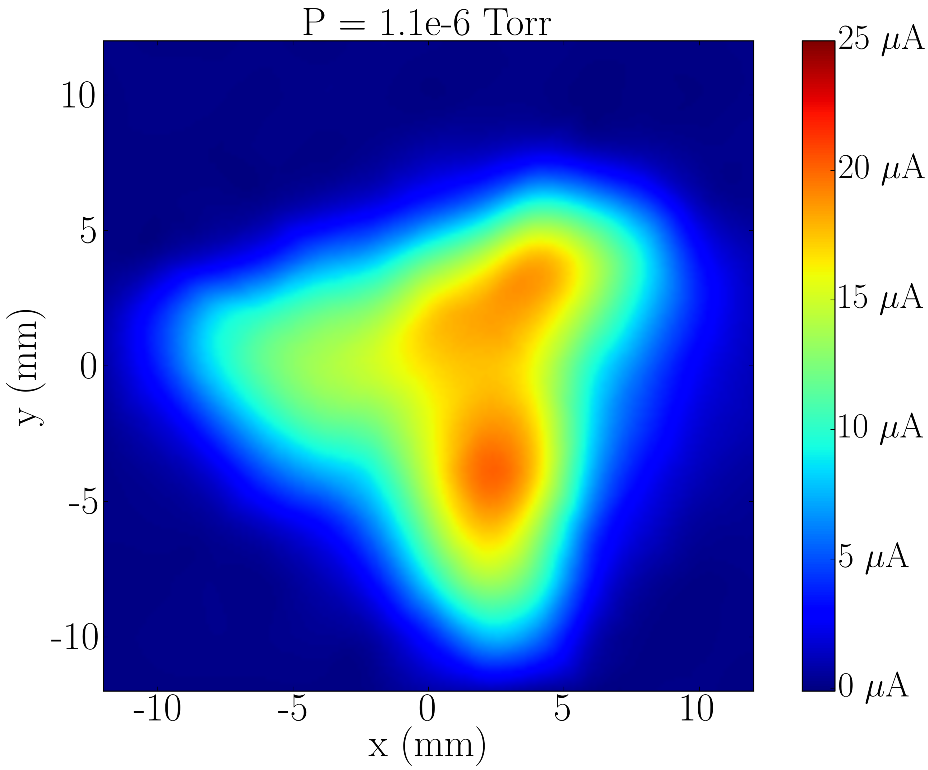

Figure 5.22: Beam profile of O^{3+}, $1.1 \cdot 10^{-6}$ Torr

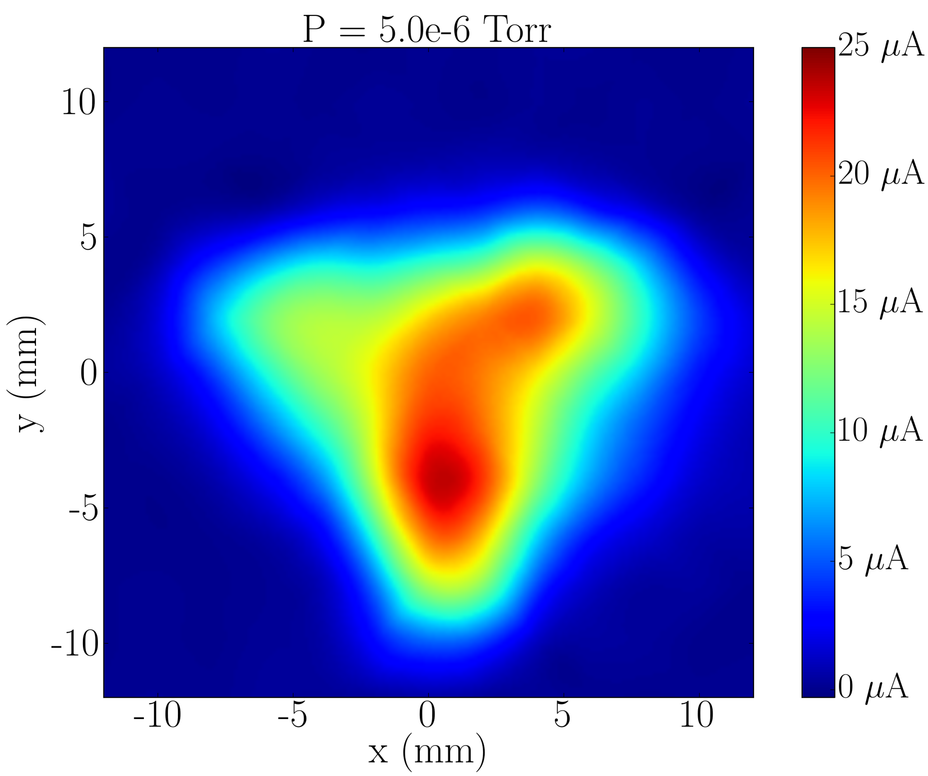

Figure 5.23: Beam profile of O^{3+}, $5.0 \cdot 10^{-6}$ Torr

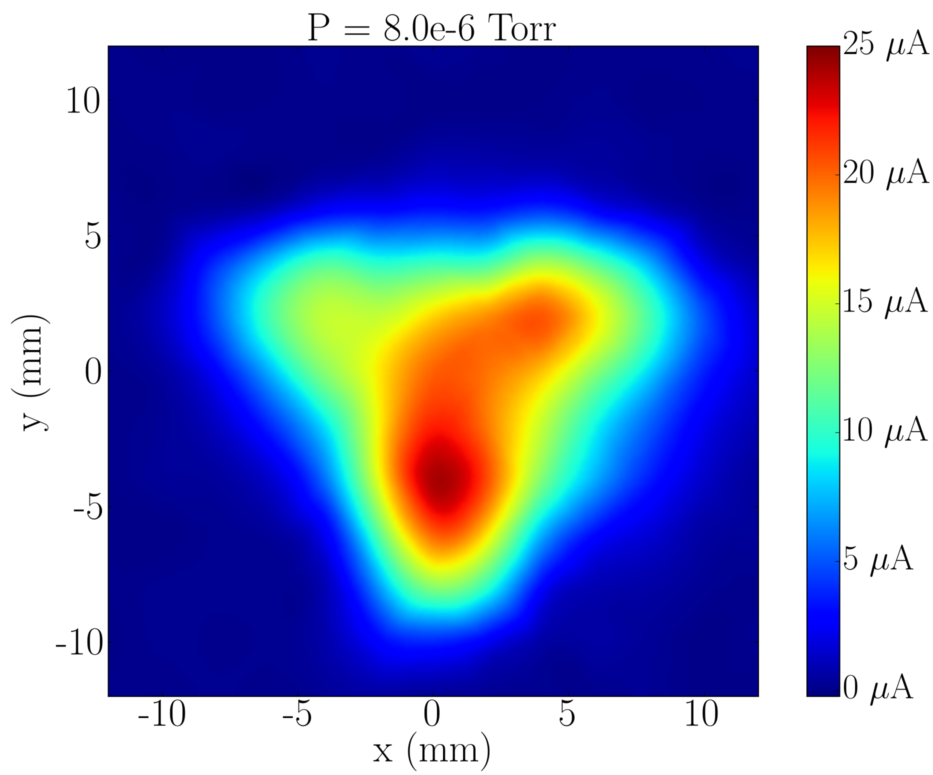

Figure 5.24: Beam profile of O^{3+}, $8.0 \cdot 10^{-6}$ Torr

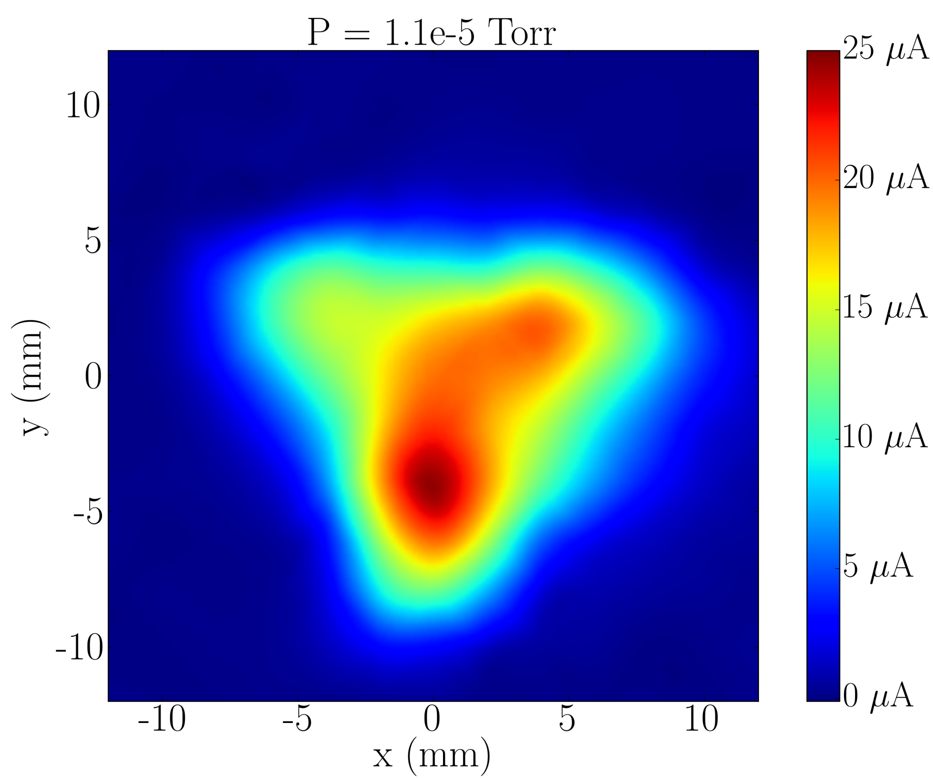

Figure 5.25: Beam profile of O^{3+}, $1.1 \cdot 10^{-5}$ Torr

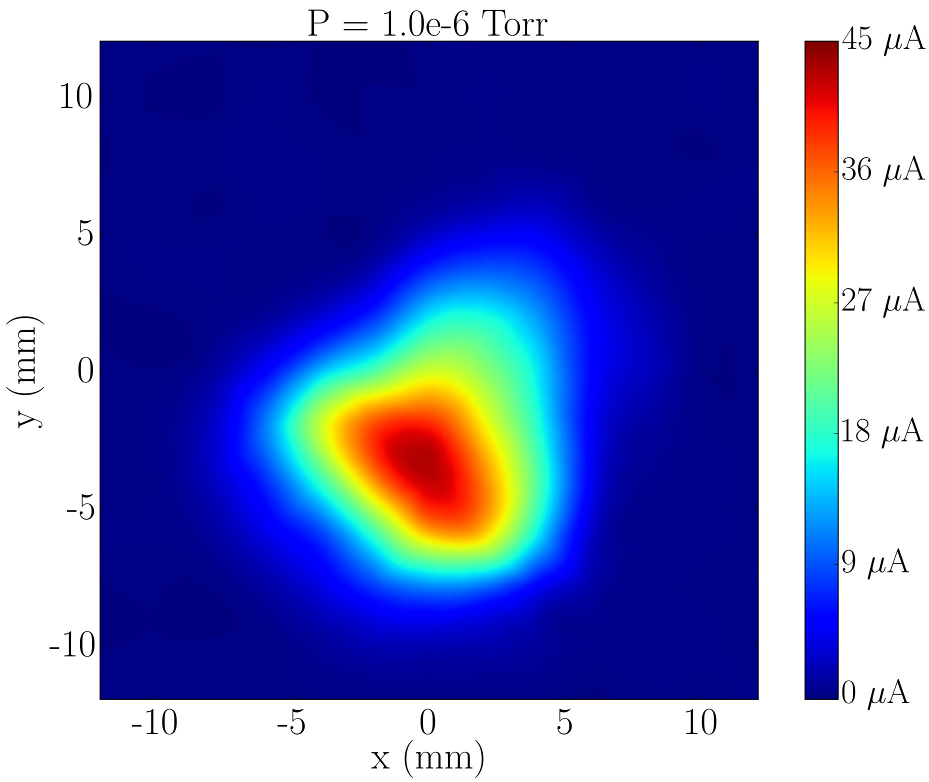

Figure 5.26: Beam profile of Ar^{8+}, $1.0 \cdot 10^{-6}$ Torr

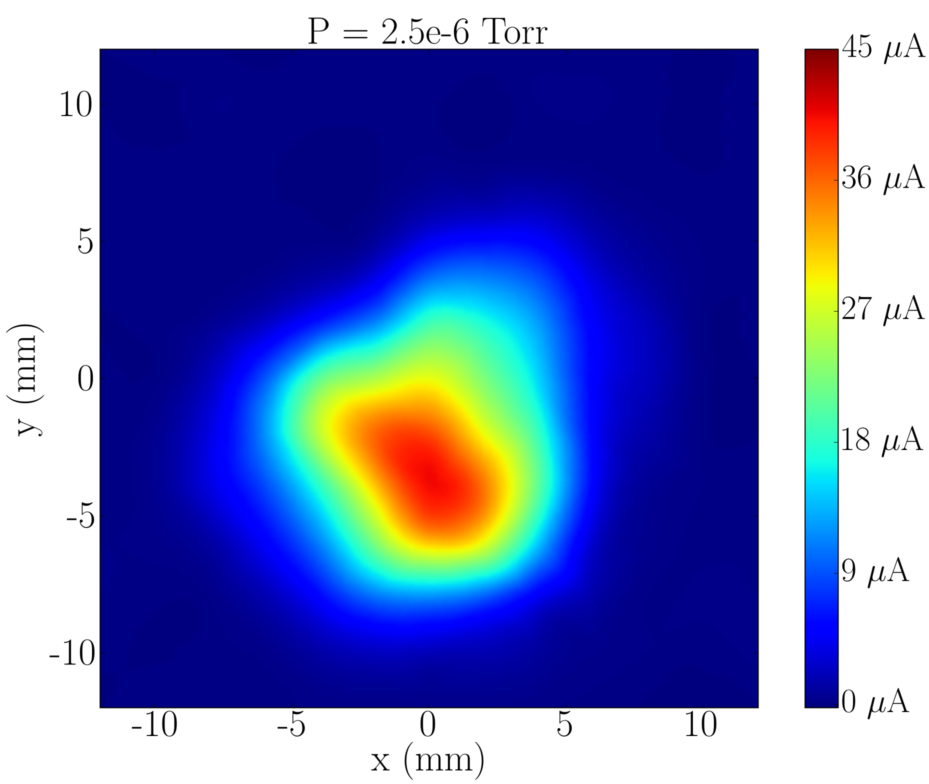

Figure 5.27: Beam profile of Ar^{8+}, $2.5 \cdot 10^{-6}$ Torr

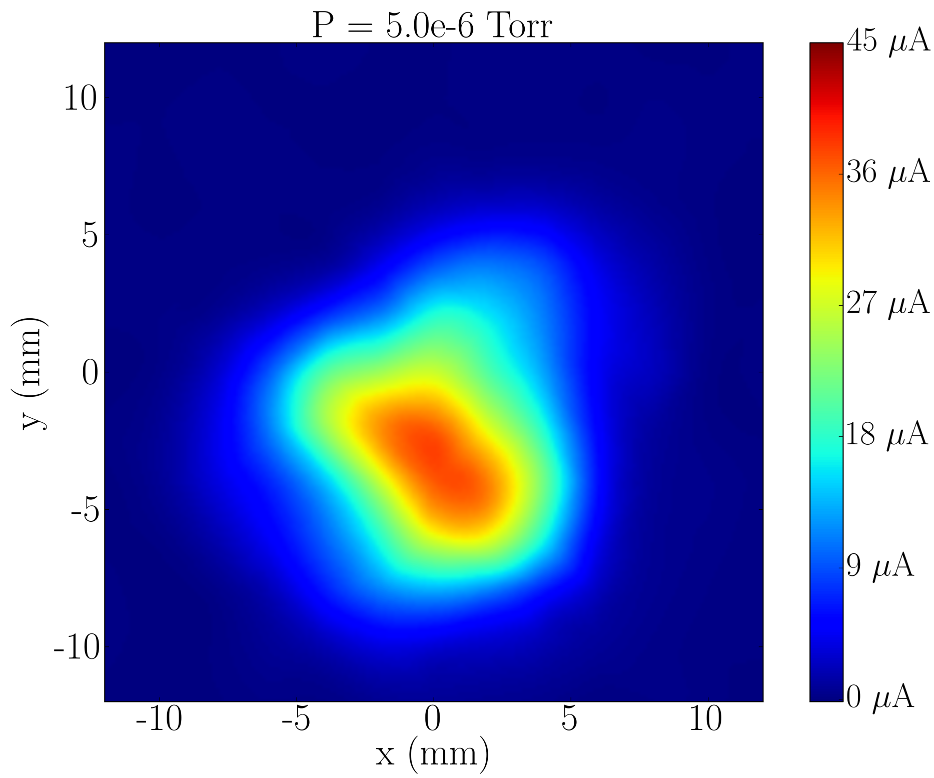

Figure 5.28: Beam profile of Ar^{8+}, $5.0 \cdot 10^{-6}$ Torr

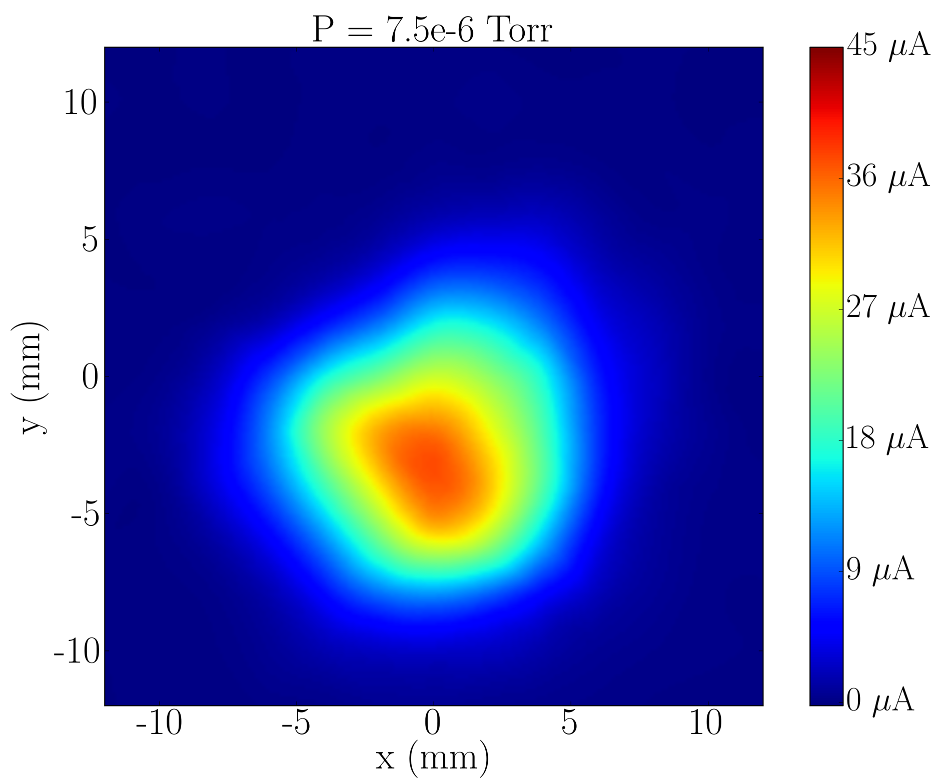

Figure 5.29: Beam profile of Ar^{8+}, $7.5 \cdot 10^{-6}$ Torr

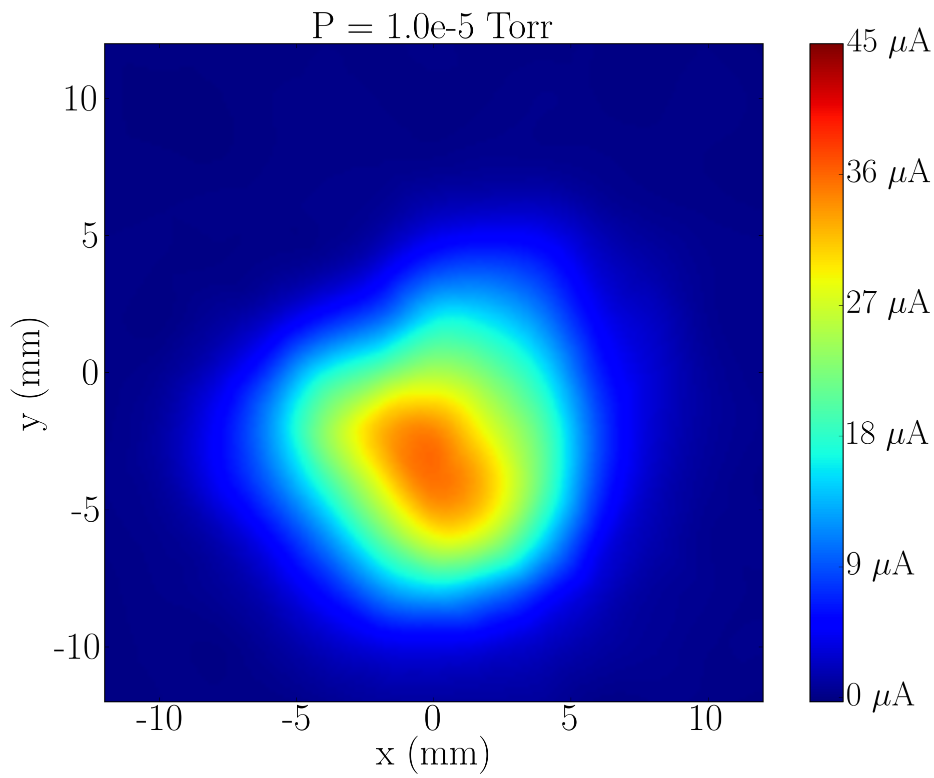

Figure 5.30: Beam profile of Ar^{8+}, $1.0 \cdot 10^{-5}$ Torr

As with the LEDA measurement, the first analysis step is to examine the saturation currents I_{sat}, which are plotted in figure 5.31. The last solenoid of the collimation channel which is close to the diagnostic box, was at a low setting $< 100A$, leading to a residual magnetic field on axis at the measurement location of < 2 Gauss. This combined with the fact that the background gas is mostly N_2, which is much heavier than H_2 lets us expect a linear dependence of I_{sat} on the beam line pressure, which we indeed observe. The theoretical values were calculated according to equation 5.3 with a transmission factor $T = 0.65$ and cross-sections according to the Müller-Salzborn empirical formula for charge-exchange [1]. At these energies, charge-exchange is the dominating contribution to σ_i. The mesh transmission T depends slightly on the ion energy and on the angle of incidence, hence we expect it to be less than the optimal value of 0.73 discussed earlier. Overall, considering the large

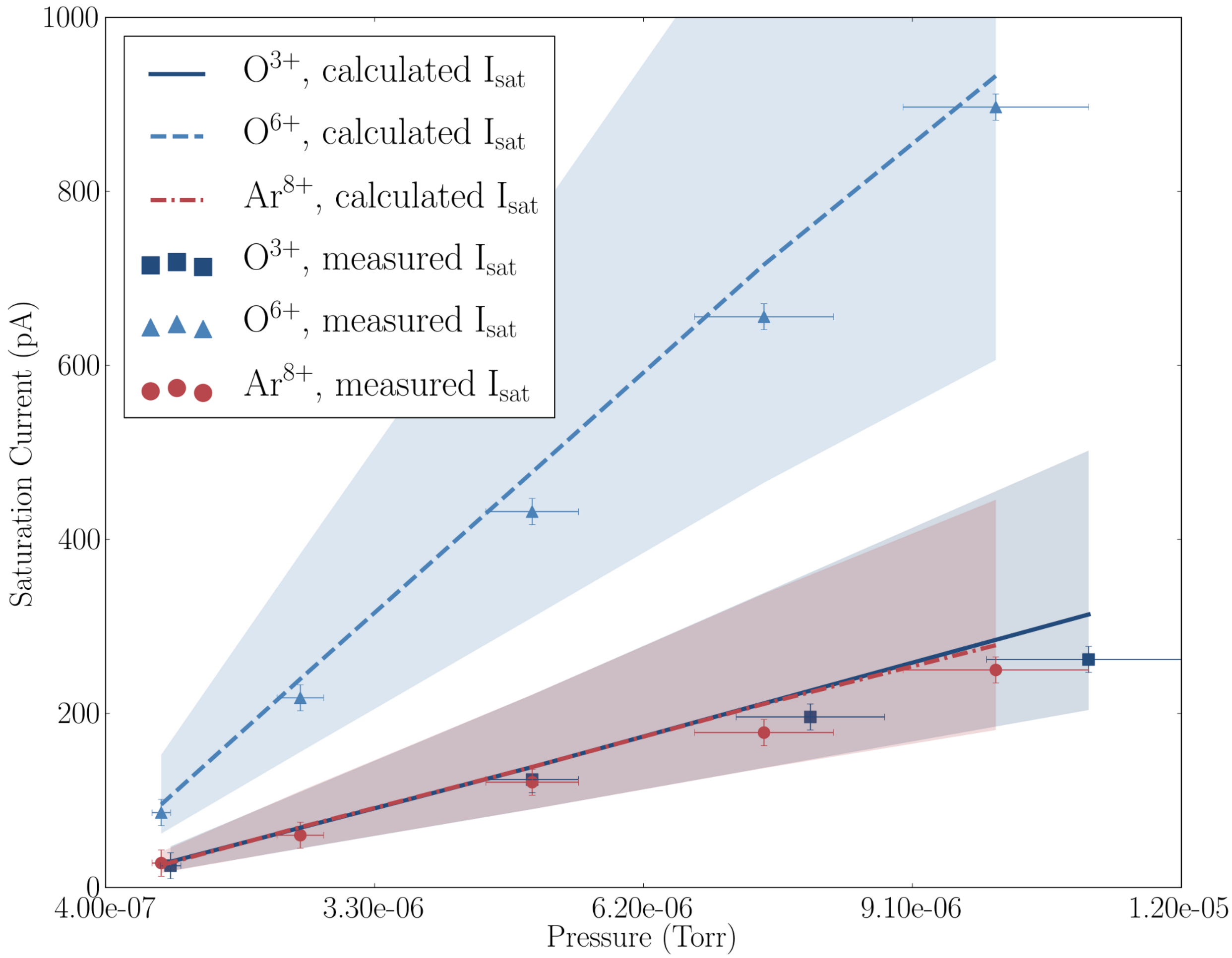

Figure 5.31: Saturation currents for three pressure variations in the SuSI LEBT at Q014. The theoretical predictions are according to equation 5.3 with T = 0.65 and cross-section according to the Müller-Salzborn empirical formula [1]. The transmission T depends slightly on the ion energy and on the angle of incidence.

uncertainties on the cross-sections given by Müller and Salzborn, prediction and experiment are in good agreement. Fitting the RFA spectra with the least squares method described in section 5.2.2 yields the neutralization values plotted in figures 5.32 and 5.33. It should be mentioned that in some cases the contribution from the background in form of a Gaussian energy distribution is considerable (up to 45 %). Because the reason for the high energy tail (approximated by the Gaussian energy distribution) is unclear at the moment, this consequently has to add significantly to the estimated errors (cf. Section 5.2.4).

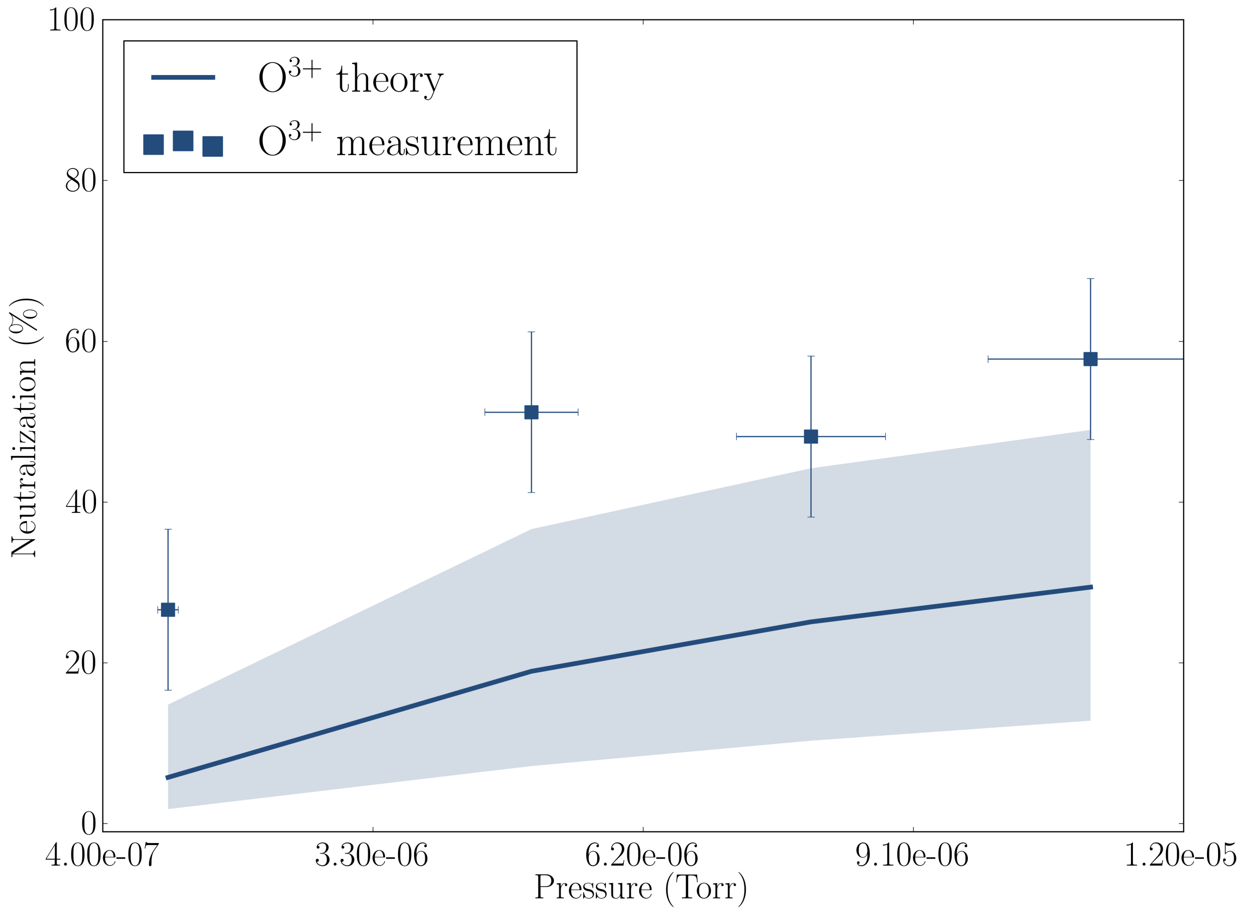

Figure 5.32: Pressure variation of O^{3+}, neutralization measured and theory. It can be seen that the theoretical prediction is significantly lower than the measured values.

In Figure 5.32 we can see that the measured values are significantly higher than the theoretical prediction. The only explanation at this point is that the cross sections for ion and electron production σ_i and σ_e are estimated falsly. Especially if the ratio of σ_e to σ_i is increased, we quickly obtain much better agreement. On the other hand, the theoretical prediction is not very sensitive to the absolute magnitude of the two cross sections if they are changed by the same factor. In Figure 5.33, the measured and predicted values for Ar^{8+} and O^{6+} agree rather well.

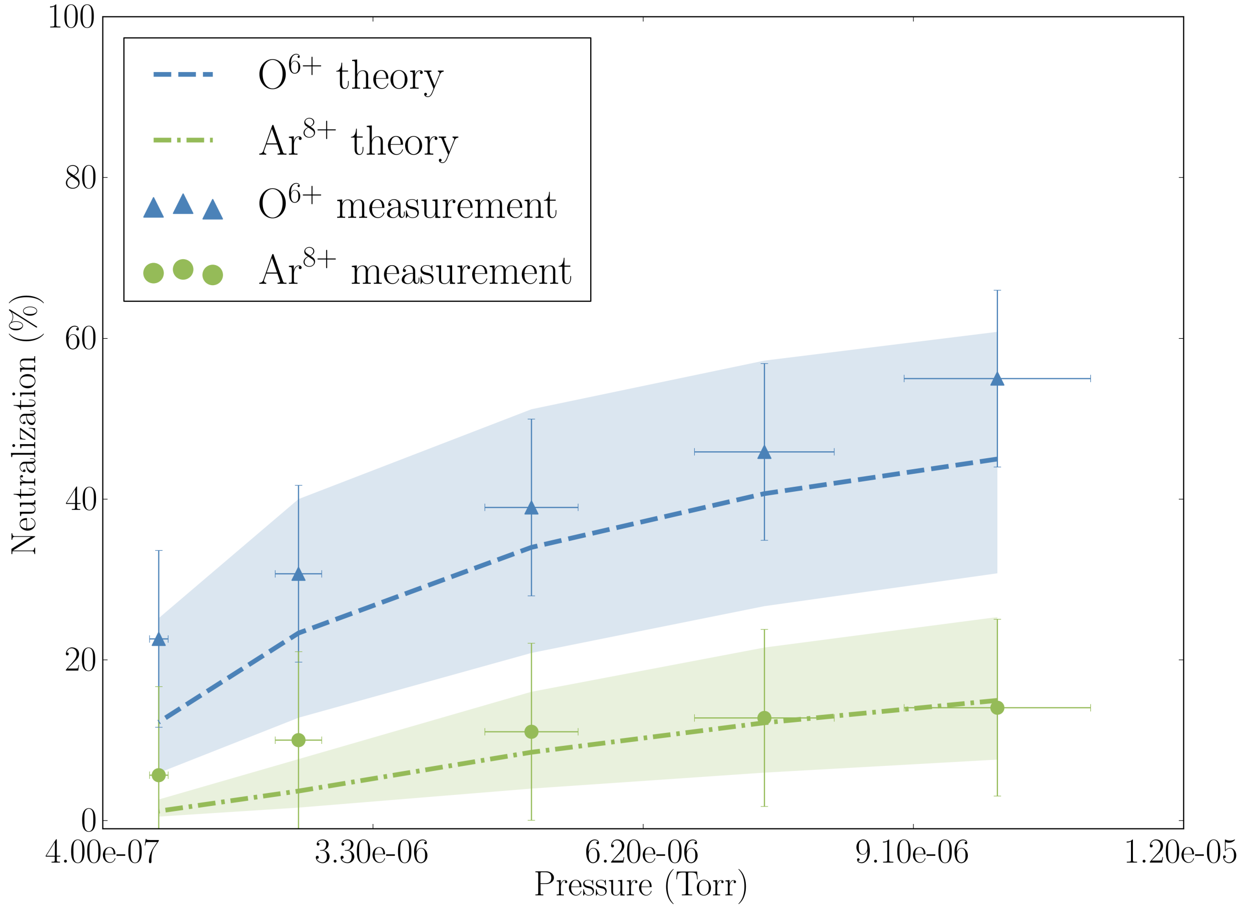

Figure 5.33: Pressure variations of O^{6+} and Ar^{8+}, neutralization measured and theory.

Current Series

Let us now examine the current variations. Here we have a set of slit scans for each measurement. They are shown for O^{3+}, O^{6+}, and Ar^{8+} in Figures 5.34 to 5.36, Figures 5.37 to 5.41, and figures 5.42 to 5.46, respectively. Immediately, we see that in the O^{3+} current series, the beam changes its shape and size quite drastically. This is due to the fact that the biased disk in the source shut down from the first (Figure 5.36, 298 μA) to the second measurement (Figure 5.35, 203 μA). Consequently, the plasma conditions changed, and with them the beam shape and extracted current. I kept the series for completeness, but the results should be viewed with caution. The O^{6+} series exhibits a slight asymmetry in the beginning, and a round, almost uniform beam shape for higher currents. Ar^{8+} shows a triangular structure and especially towards the higher currents a clear vertical asymmetry.

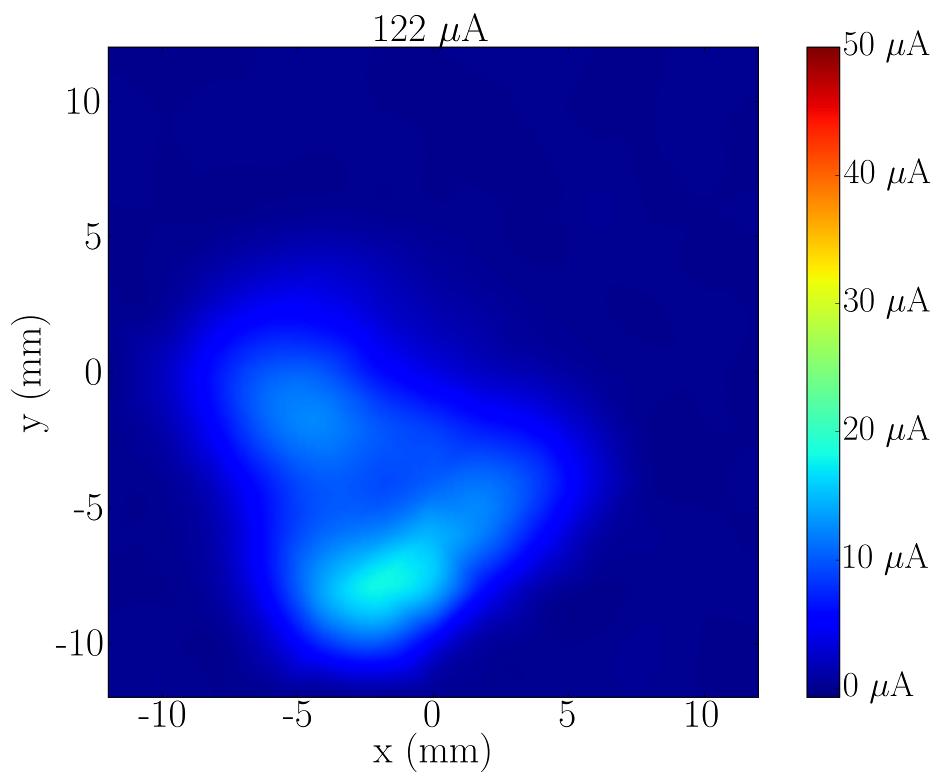

Figure 5.34: Beam profile of O^{3+}, 122 μA.

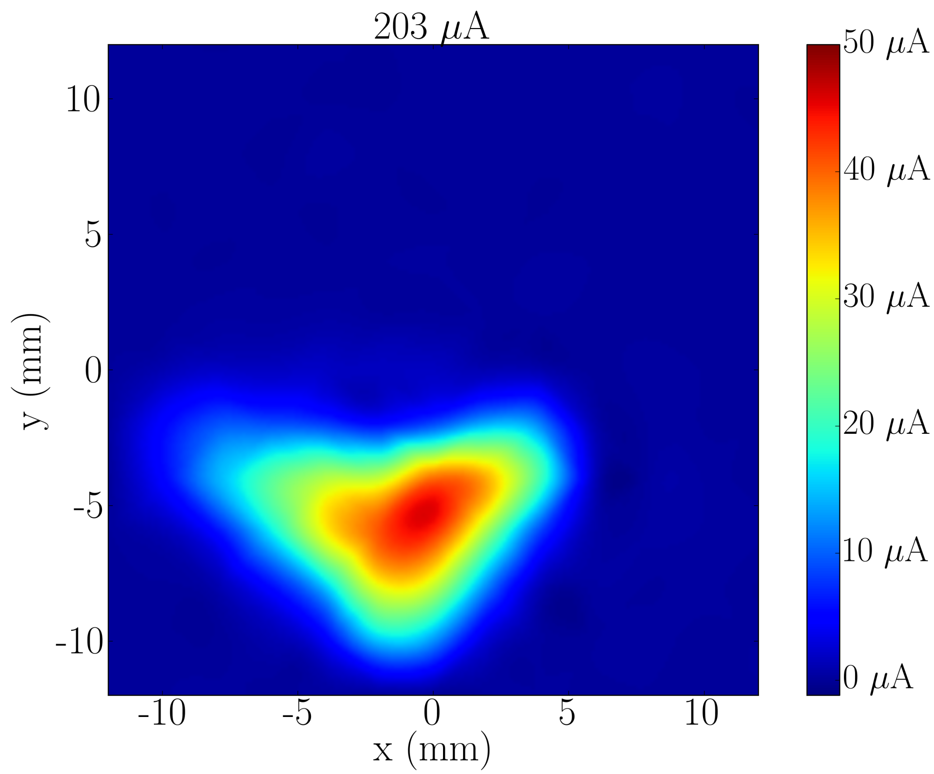

Figure 5.35: Beam profile of O^{3+}, 203 μA.

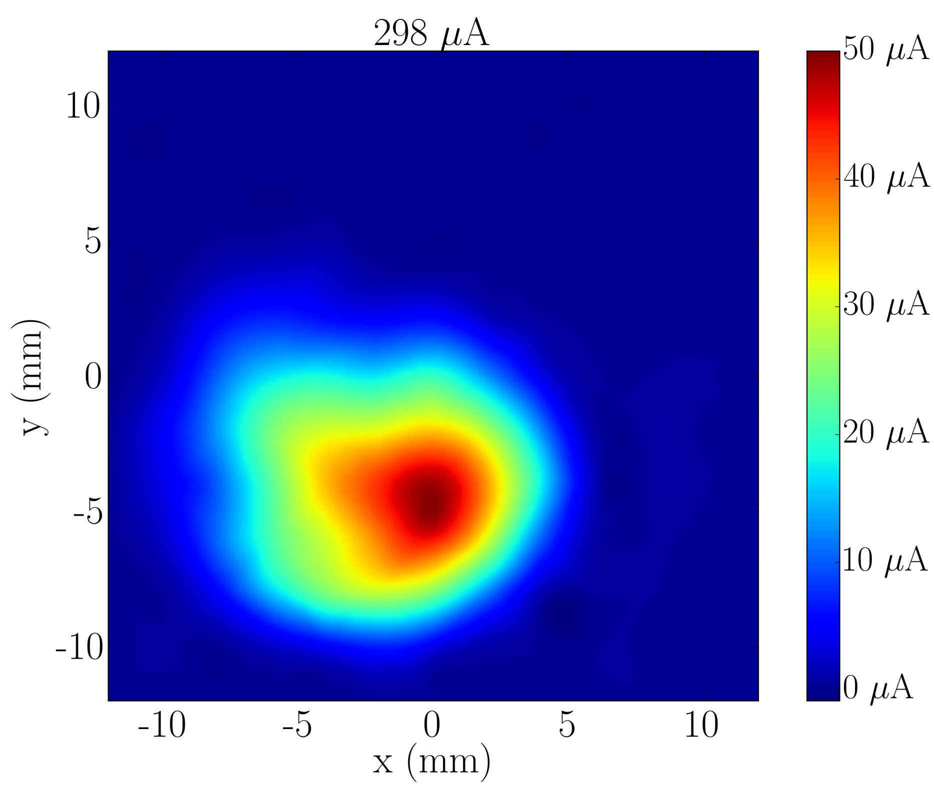

Figure 5.36: Beam profile of O^{3+}, 298 μA.

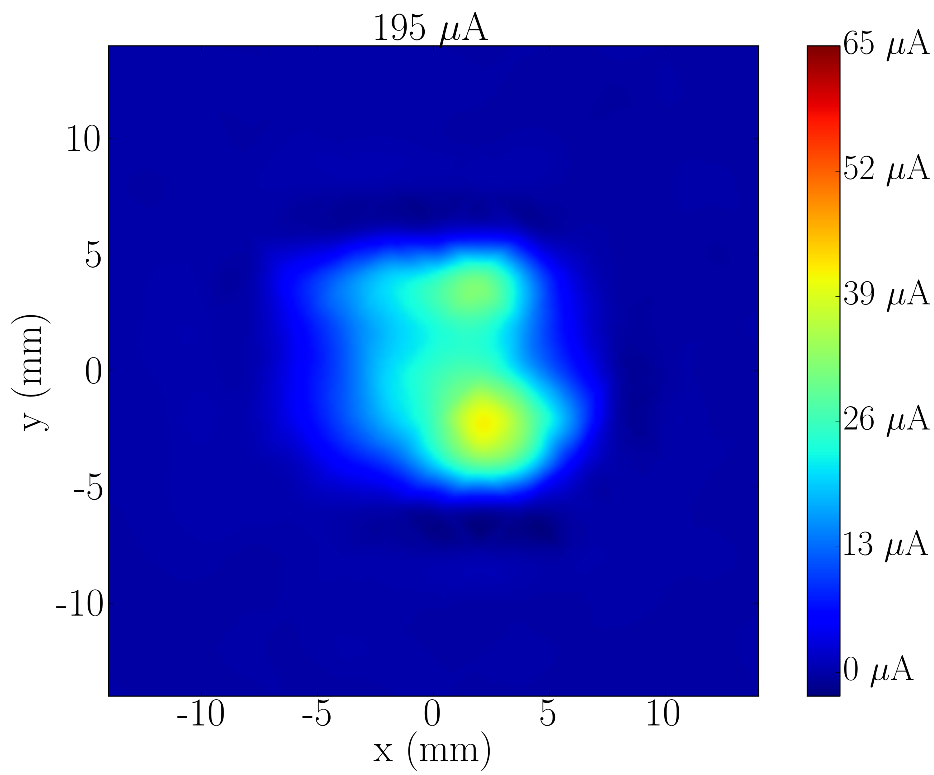

Figure 5.37: Beam profile of O^{6+}, 195 μA.

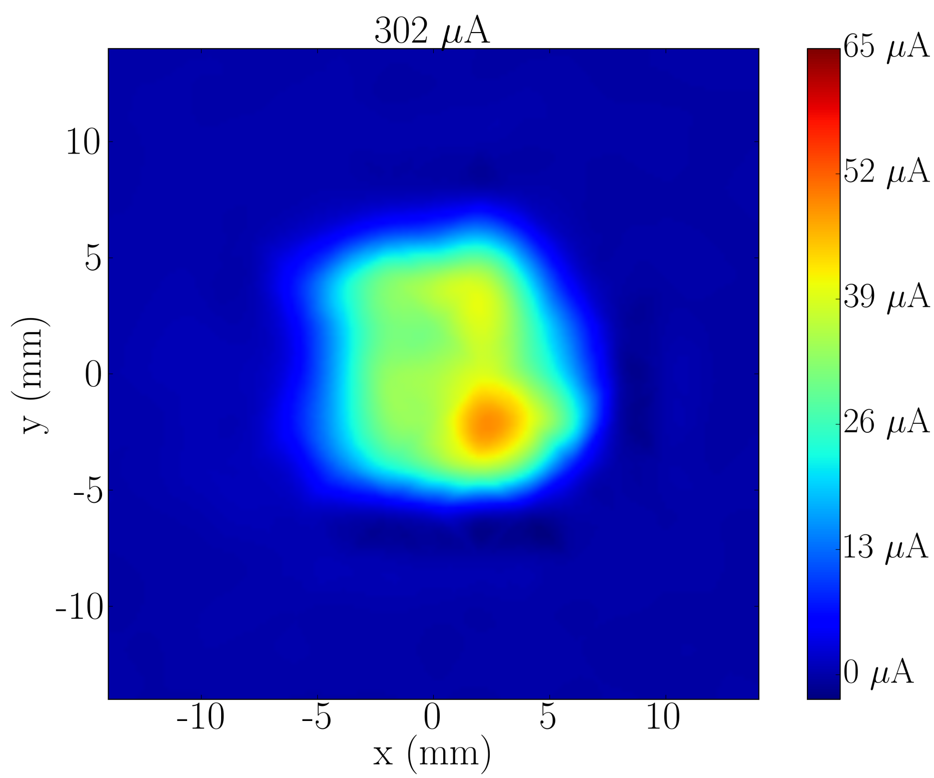

Figure 5.38: Beam profile of O^{6+}, 302 μA.

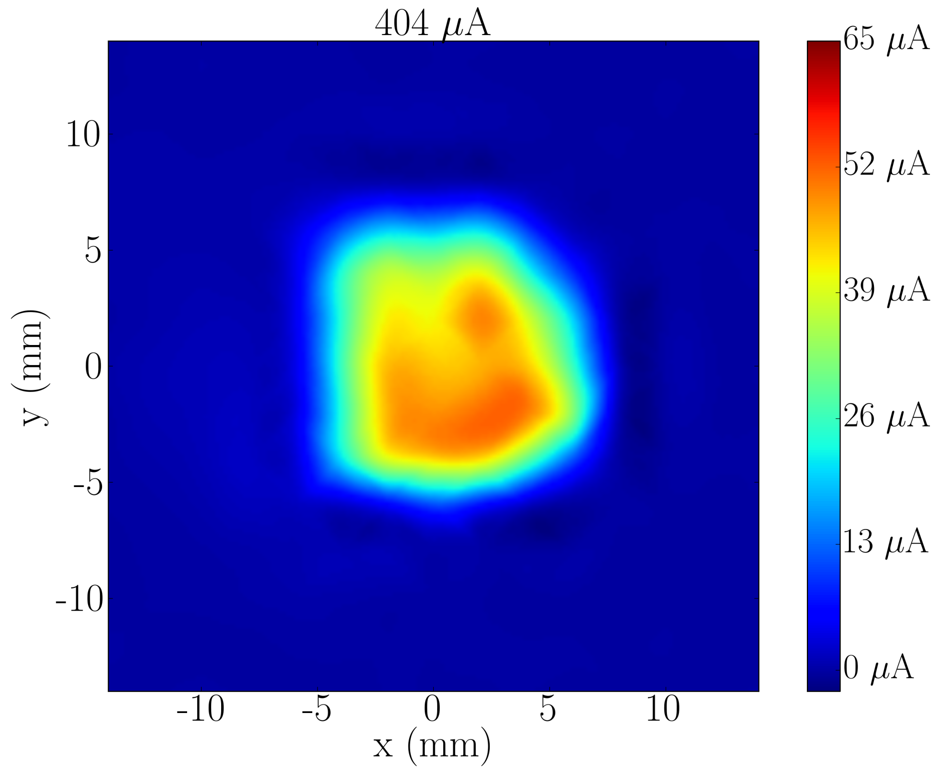

Figure 5.39: Beam profile of O^{6+}, 404 μA.

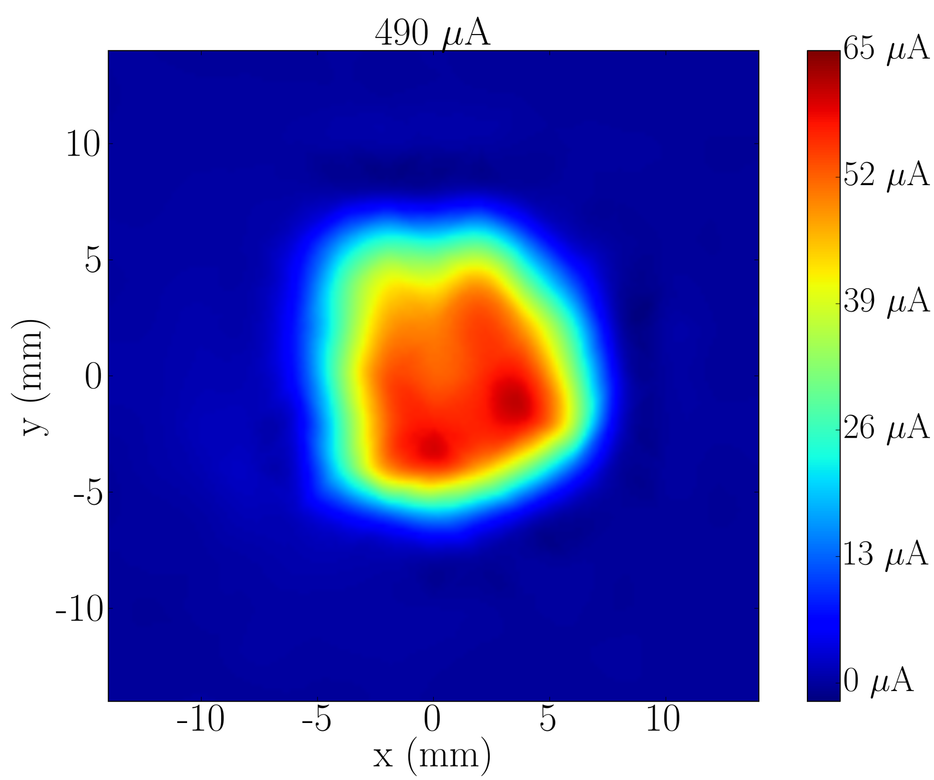

Figure 5.40: Beam profile of O^{6+}, 490 μA.

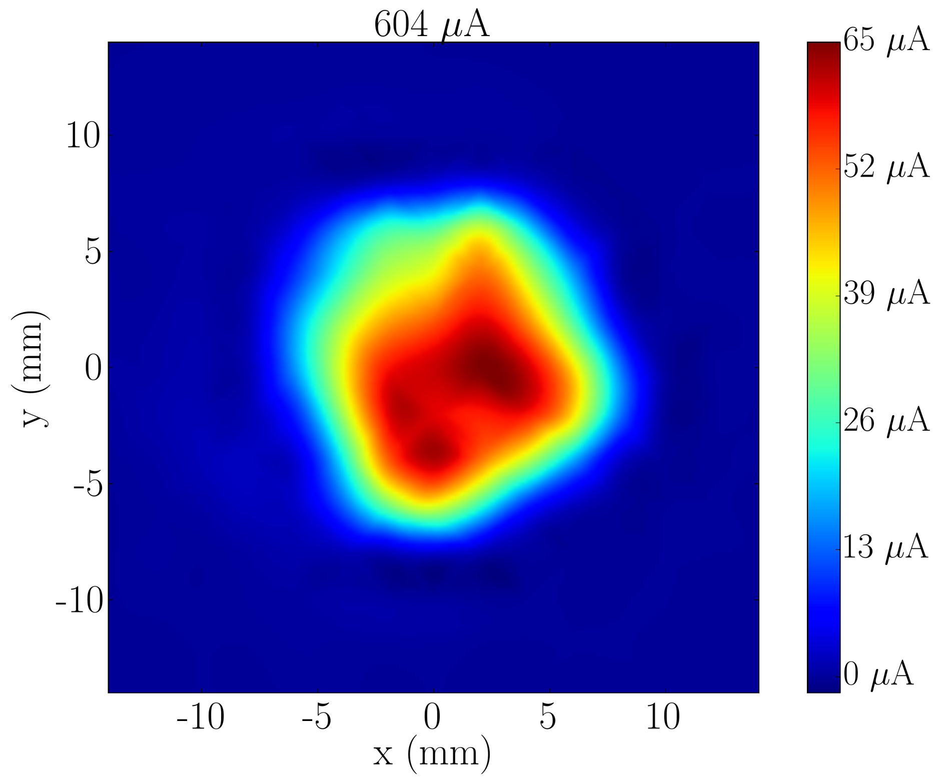

Figure 5.41: Beam profile of O^{6+}, 604 μA.

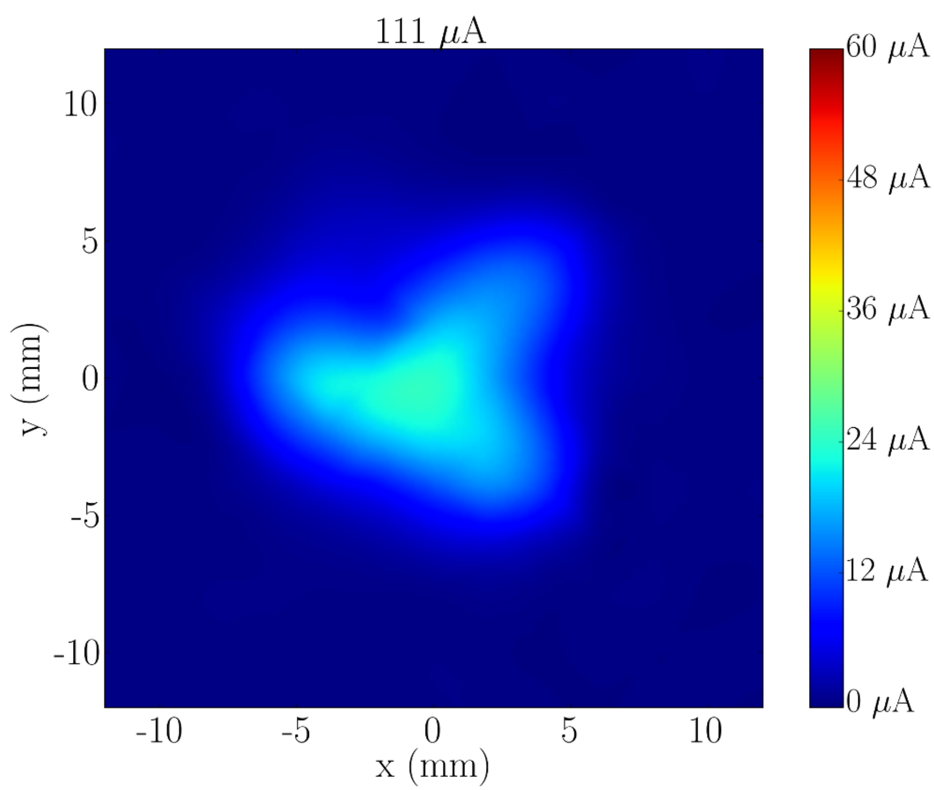

Figure 5.42: Beam profile of Ar^{8+}, 111 μA.

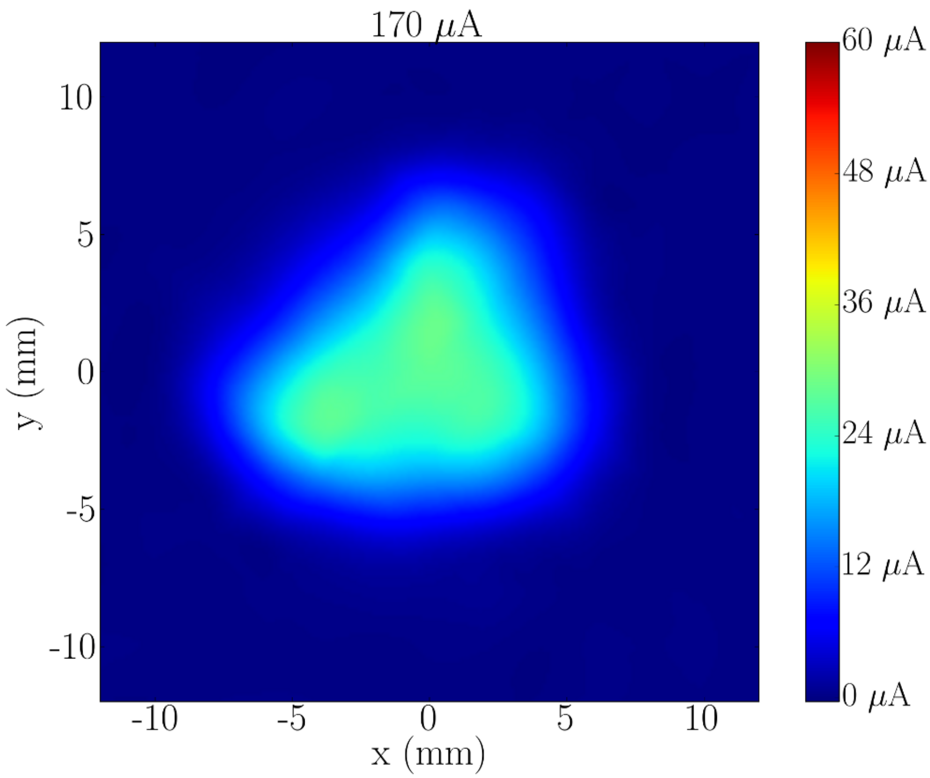

Figure 5.43: Beam profile of Ar^{8+}, 170 μA.

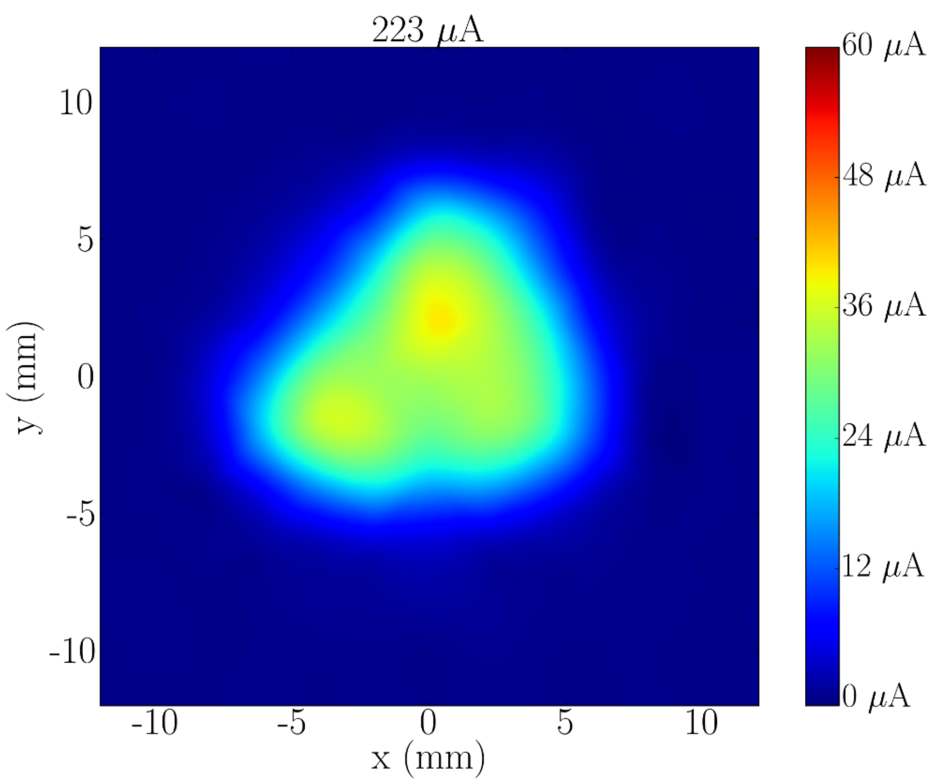

Figure 5.44: Beam profile of Ar^{8+}, 223 μA.

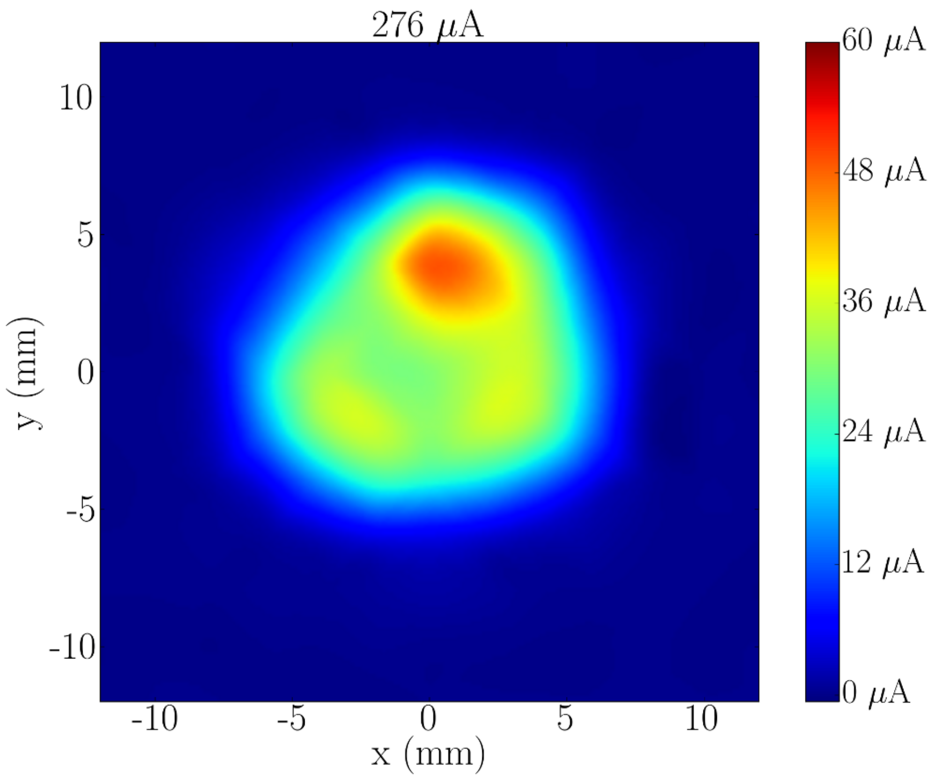

Figure 5.45: Beam profile of Ar^{8+}, 276 μA.

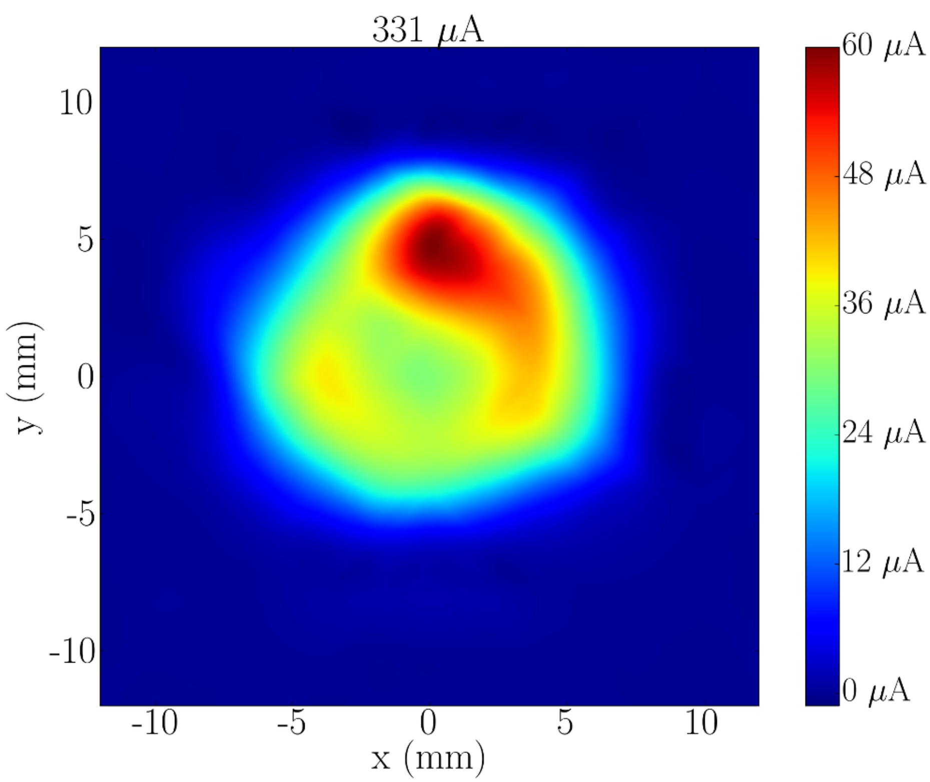

Figure 5.46: Beam profile of Ar^{8+}, 331 μA.

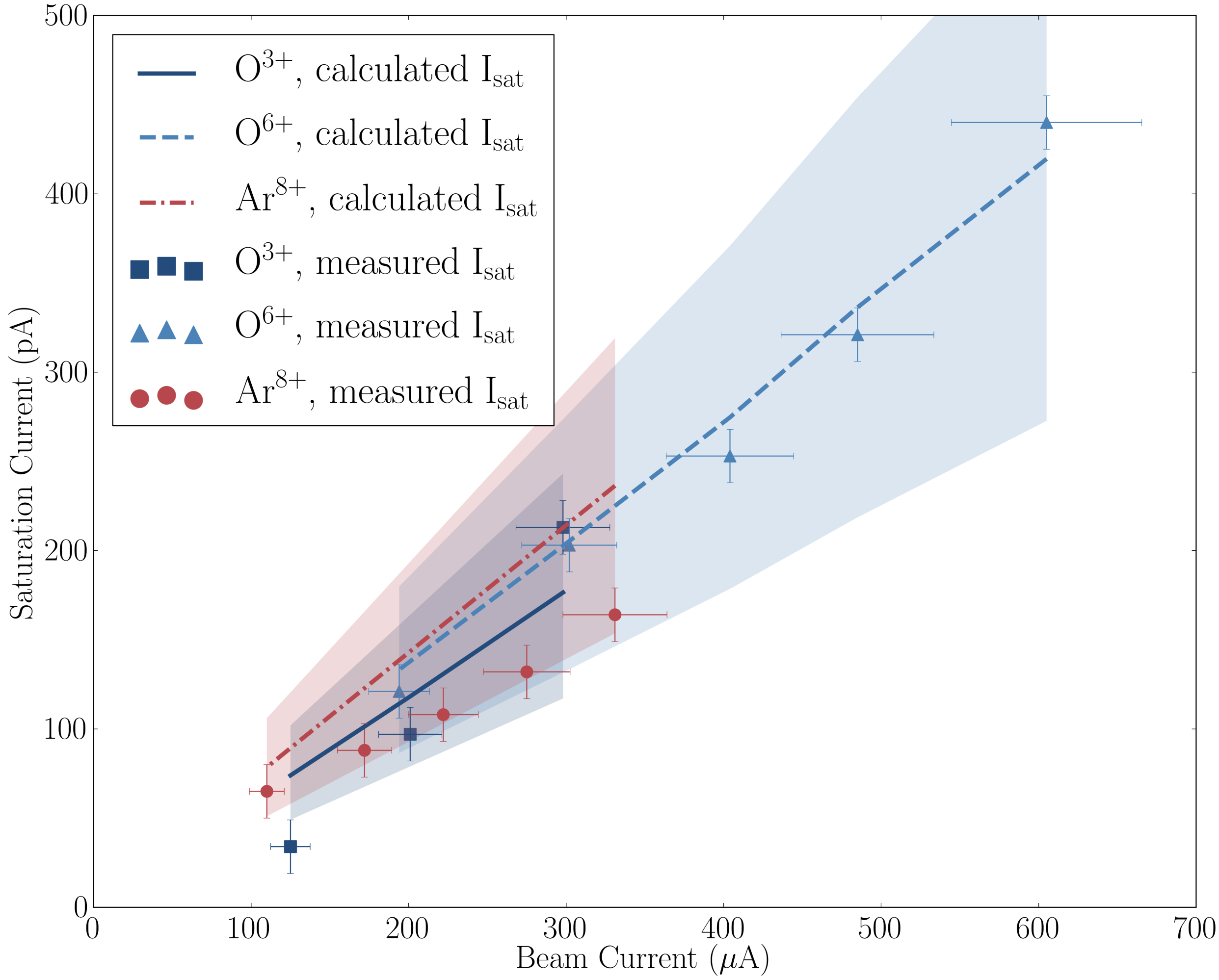

Figure 5.47: Saturation currents for three beam current variations in the SuSI LEBT at Q014. A transmission factor of T = 0.65 was used. The lower measured saturation current for the Ar^{8+} series could be due to the vertical asymmetry.

In Figure 5.47 the saturation currents are plotted versus the beam currents. It can be seen that for O^{6+}, the measured values agree well with the theoretical prediction. The measured saturation currents for Ar^{8+} are consistently lower than the predicted ones, but more so for higher beam currents. This could be attributed to the vertical beam asymmetry. The values for O^{3+} are in the right regime, but the intercept of the measurement is not at 0 as would be expected. As stated earlier, this measurement was under very unstable source conditions and is only shown for completeness.

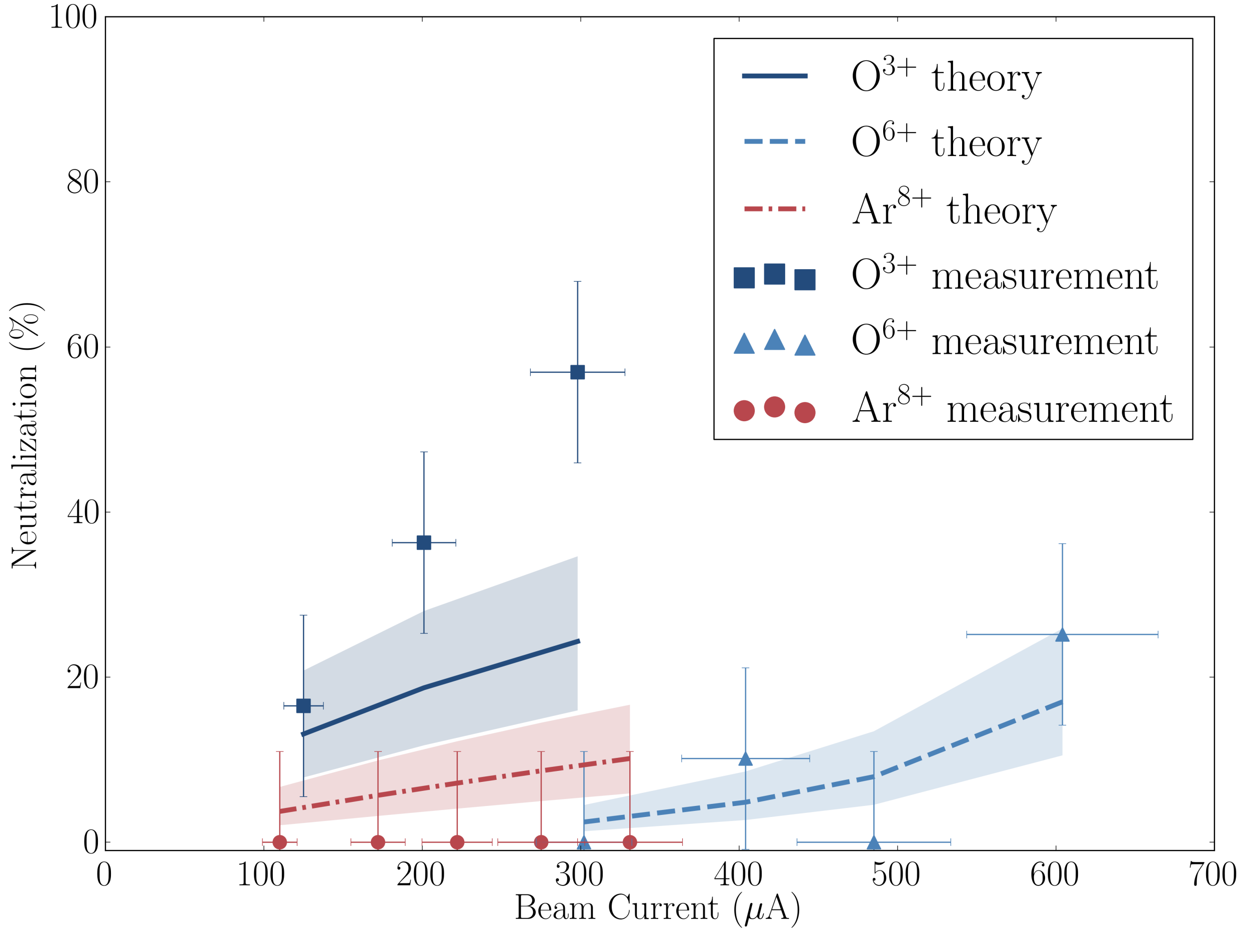

Figure 5.48: Neutralization for three current variations.

In Figure 5.48 the neutralization factor f_e is plotted versus the ion beam currents for the three series. It can be seen that O^{6+} and Ar^{8+} agree reasonably well with the theoretical prediction, while the calculation for O^{3+} underestimates the neutralization factor. Considering a similar result from the pressure series, we must assume a systematic error that was not taken into account.

5.4 Conclusion

5.4.1 Summary

In this chapter, I presented neutralization measurements at two different locations: in the beam line of the LEDA injector source and in the beam line of the SuSI superconducting ECRIS.

The LEDA measurements agree with previous measurements at the same source with a similar detector and show neutralization values around 80-90 %, which depend on beam intensity. It is possible to calculate the beam radius from the RFA spectra alongside the neutralization. In case of the LEDA source this yielded very large beam radii which could not be explained. A similar discrepancy showed up in previous measurements at the same source. Theoretical calculations using reasonable beam radii compared well with the measured neutralization, however.

The measurements in the beam line of SuSI suggest overall low neutralization factors (0% - 50%) which compare reasonably well with the theoretical model introduced by Gabovich [51] and discussed in detail in Chapter 2. They follow the prediction of higher neutralization with higher residual gas pressure, larger beam radii and higher beam density. For typical ECRIS LEBT settings, where the beam line pressure is kept as low as possible to prevent losses due to charge exchange, this means very low neutralization factors and beam lines should be designed accordingly. The reasonable agreement of the model with the measurements suggests incorporating the simple theoretical treatment into the simulation of low energy beam transport. This will be presented in chapter 6.

5.4.2 Outlook

The datasets taken at the two additional locations (Artemis beam line, SuSI diagnostic box Q001) may still yield useful results upon further investigation. The analysis methods presented in this chapter can be extended to accomodate multispecies ion beams and similar collimator transmission curves as used in the LEDA injector source analysis can be obtained for SuSI Q001. Preliminary analysis of data from the two locations suggests similar findings as at the other locations (neutralization of 0% to 50% depending on beam size, beam current, and residual gas pressure).

In order to settle questions of beam aspect ratio and to improve the statistics of the measurement by increasing the total measured current, a second identical detector put perpendicular or under 45°to the existing detector might prove useful. The beam current monitors used at the NSCL already provide two input channels and electron suppressor (V_3) as well as retarding field (V_2) could be provided in parallel by the same power supplies. Q014 in the SuSI beam line with the perpendicular ports for the Allison emittance scanners would be an ideal starting point.

The RFA setup as it is is certainly improvable as well. Possible changes that could benefit the setup are

- Applying a bias to the collector plate to suppress oscillations.
- Exploring the option of heating the detector in order to suppress insulating film deposition on the grids.
- Trying different combinations of apertures in the collimation system (e.g. taking out the inner aperture, using smaller apertures).

Chapter 6

3D ECR Extraction Model

6.1 Overview

In this chapter I will describe in detail a semi-empirical model for extracting ion beams from an ECRIS using the PIC code WARP. This model was developed in collaboration between the 88" Cyclotron's Ion Source group at Lawrence Berkeley National Laboratory and the *Heavy Ion Fusion Science (HIF) Virtual National Laboratory* (a collaboration of Lawrence Berkeley National Laboratory and Lawrence Livermore National Laboratory) as an alternative to existing extraction simulation models (IGUN [32], PBGUNS [116], KOBRA-INP [35]). The success of WARP with intense heavy ion beams, its 3D capability and non- commercial approach suggested expanding the code's functionality with a 3D plasma extraction model similar to IGUN's 2D model. In addition, as discussed in Section 3.1.3 WARP has powerful capabilities for multispecies beam transport simulations including space charge and so makes end-to-end simulations of ion source and LEBT relatively easy. All simulations presented in this chapter (from the source to the respective targets) were thus performed in WARP.

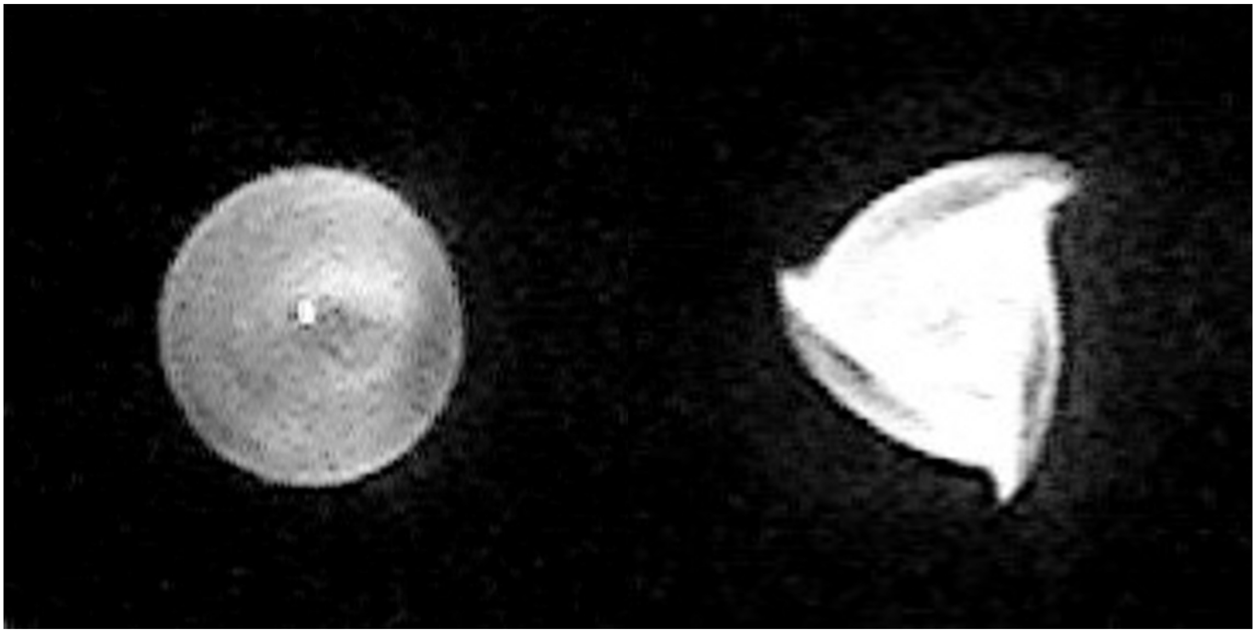

Figure 6.1: Two helium beams extracted from VENUS. Left: without the radial confinement sextupole, right: under normal operating conditions with the sextupole. The beam line layout can be seen in Figure 6.5. The solenoid was set to 400 A in both cases.

6.2 The Extraction Model

6.2.1 Initial Conditions with WARPxy

One of the challenges with extracting ion beams from ECR ion sources is the triangular beam structure coming from the sextupole confinement field. In Figure 6.1 two beam images are shown for a helium beam extracted from VENUS. One without the use of the sextupole magnet, which is clearly round, and one under normal operating conditions with the use of the sextupole, which is clearly triangular (the position of the viewing screen can be seen in Figure 6.5). In both cases, the focusing solenoid directly after extraction was set to 400 A to focus the beam onto the viewing plate. The question is now: How to create the initial (triangular) distributions $f_i(x, y, z, vx, vy, vz)$ for each species to be extracted from the ECRIS in the extraction simulation? Ideally, the plasma processes, rf-heating, and electron impact ionization inside the source should be simulated self-consistently. And indeed, there

Figure 6.2: Plasma sputter marks inside VENUS. Left: The biased disk exhibits a large star structure and a smaller clear triangle of about 5 mm height etched into the plate. Right: The same (now rotated) discolorations are seen, however the triangle would be inside the extraction aperture.

are several groups trying to model the plasma processes inside the source [21, 117, 118]. This theoretically yields the desired ion distributions and one of the most recent results for an ECRIS at KVI Groningen looks very promising [20, 119]. However, these simulations take a long time and are still highly specialized. In this work, I am using a simple semi-empirical approach proposed by D. Todd and D. Leitner [120]. In this approach, the plasma markings on the biased disk (shown e.g. for the VENUS source in Figure 6.2, left) are used as reference to initialize the particles on the injection side of the source, give them a Boltzmann distributed velocity and track them through the magnetic field of the source to the extraction aperture. In Figure 6.2 the discolorations and sputter marks on the biased disk (left) and inside the plasma electrode with the extraction aperture (right) of the ECRIS VENUS are shown. The 5 mm high triangle etched deeply into the bised disk is used as reference for starting the particles.

In WARPxy the particle tracking to obtain the initial conditions is implemented in the following way:

- The magnetic field of the source is modeled in a program capable of calculating 3D magnetic fields for coils and permanent magnets in the presence of other magnetic materials like iron. In this thesis, the VENUS field was calculated using *VectorFields Opera 3D* [121] and the SuSI field was calculated in a similar manner with *Lorentz-EM* [122].

- This field is loaded into WARP as a gridded magnetic element (full 3D) via the convenience function:

  addnewbgrd(zs, ze, xs, ys, sf, sc, dx, dy, bx, by, bz, nx, ny, nz)

  with zs and ze the start and end coordinates in z direction in m, xs and ys the starting coordinates in x and y in m. sf and sc are scaling factors and the field will be scaled by (sc + sf). dx, dy are the field's x and y grid cell sizes and nx, ny, nz are the number of cells in the three respective directions. The field data is stored in bx, by, bz which each are three dimensional matrices with x the first index, y the second, and z the third. This function has to be called before the generate().

- Particles are initialized at the location of the biased disk inside the ECRIS with a triangular spatial distribution and a Boltzmann velocity distribution of peak energy between 2 and 5 eV. This is the energy regime of ions in an ECRIS and an adjustable parameter in the simulations.

- Particles are then tracked through the source's magnetic field with a very small step size (10^{-5} m) to resolve the spiraling motion.

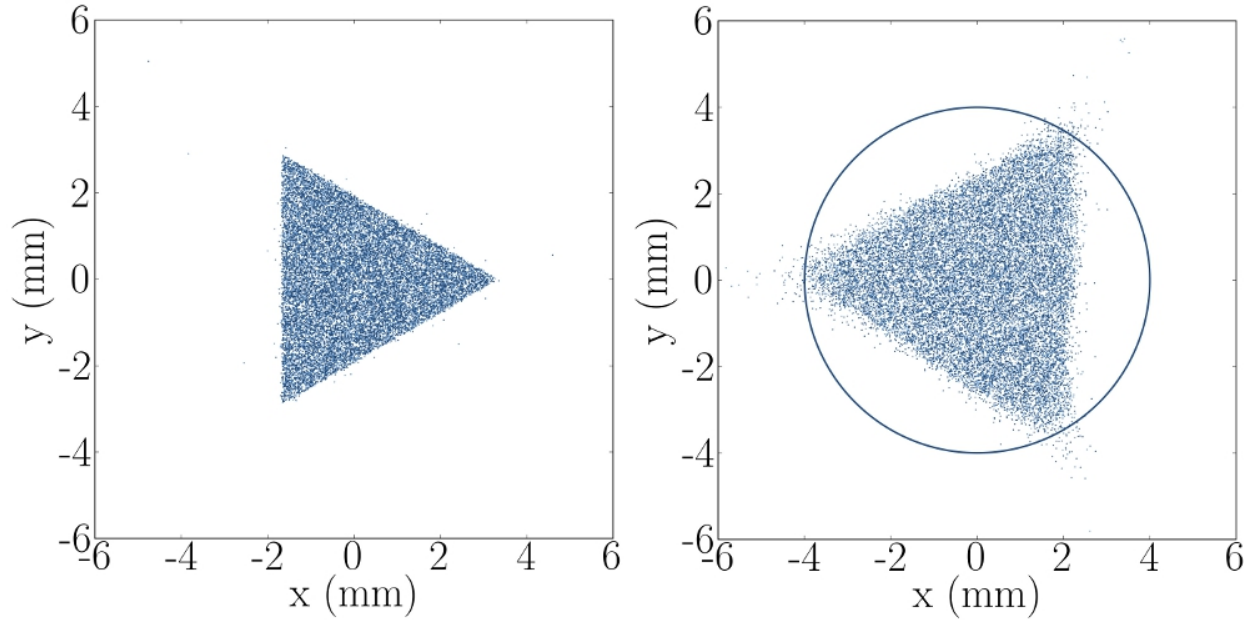

Figure 6.3: Obtaining the initial conditions for a helium beam from the VENUS ECRIS. Left: Particle distribution at the biased disk. Right: After tracking through the sources magnetic field. The circle represents the extraction aperture.

- The final particle distributions $f_i(x, y, z, vx, vy, vz)$ are saved at a location a few mm before the extraction aperture to leave some space for the subsequent extraction simulation to develop a plasma sheath.

An example of particle distributions for He^{1+} and He^{2+} at the VENUS biased disk and the corresponding distribution at the extraction aperture after tracking through the sources magnetic field are shown in figure 6.3. Note the horizontal mirroring from injection to extraction. The circle represents the extraction aperture of 4 mm radius.

6.2.2 2D+ Extraction with WARP3d

Recently, WARP was updated with a 2D (RZ) plasma extraction model similar to IGUN and a 3D plasma extraction model using the same principles but on a 3D grid.

In these models, a plasma surface inside the source is defined which is at *plasma potential*. The plasma potential is usually 10 to 30 V higher than the wall potential (which, in the case of ECR ion sources is typically between 20 and 30 kV).

From there, ions are tracked through the extraction aperture and the extraction system. From the trajectories, the charge distribution of the beam is determined and accumulated on the mesh. The poisson equation is solved for the combined external and beam space charge potentials. In order to account for the plasma electrons, the so calculated potential is updated with electrons distributed proportional to

$$\propto \exp \frac{e(V(\vec{r}) - V_{plasma})}{kT_e}$$

with $V(\vec{r})$ the potential determined from the external and space charge potentials and T_e the electron temperature.

The updated potential map is then used as an applied field in the next run. This process is repeated until a steady state solution has been reached. This is called a *relaxation method*.

It should be noted that in IGUN the potential distribution between the plasma surface and the ion source wall (and extraction aperture) is calculated analytically using a one dimensional plasma sheath model [31], rather than through ray-tracing. Outside the aperture, the process is the same as in WARP.

An (optional) magnetic field can be added to the simulation in WARP as well as in IGUN. This field changes the trajectories of the extracted ions and thus the space charge map. It is crucial to include the field if it is present in the real ion source.

The two WARP models (RZ and 3D) were benchmarked against each other [123] and it was found, that agreement between the 3D and the RZ model was only good if the mesh size in the 3D simulation was much smaller than in RZ mode. This leads to excessive memory usage and so Todd *et al.* proposed the *2D+ model* which essentially runs in RZ mode until a steady state solution has been reached, saves the potential array containing external potential and space charge potential in a file and reloads that file for a subsequent single run in 3D mode. This 2D+ method was benchmarked against the full 3D model, a pure 2D model, and IGUN by Todd *et al.* and showed reasonably good agreement [123]. The 2D+ model has been used in all the extraction simulations presented in this chapter.

The 2D+ model is implemented in the WARP deck in a way that the same script can be used for the RZ run to obtain the relaxed solution and also for the subsequent 3D run to track the actual triangular distribution by just setting an initial flag. The RZ run consists of these major steps:

- The particle data from the particle tracking to obtain the initial conditions is read in and ion species data (masses, charge states) is set.

- RZ injection is switched on. The variables **w3d.l_inj_rz** and **w3d.l_inj_regular** are set to **True** to ensure RZ injection and a higher particle density in the center to ensure having particles there (the weights are adjusted accordingly, so the current distribution is still uniform). The initial velocity in z direction is calculated from equation 2.76 (Bohm criterion).

- The plasma variables are set. The most important ones are:

  - **w3d.plasmapotential**. The plasmapotential (in V) is calculated from equation

2.80.

  - **w3d.iondensity**. The density of the extracted ions inside the plasma. Calculated from the extracted current and the initial velocity.
  - **w3d.electrontemperature**. The temperature of the Boltzmann electrons (eV).
  - **w3d.xbemin**, **w3d.xbemax**, **w3d.zbemin**, **w3d.zbemax**. The extent over which the Boltzmann distributed electrons are included (in m)

- The conductors geometry and the voltages are loaded from a file.
- Then the simulation is carried out in subsequent runs until a stable solution has been reached (*relaxation*):
  - **gun()** is called 4 times to obtain a preliminary solution.
  - **gun()** is then called 6 more times with the *current* option. WARP will adjust the particle weights in subsequent runs so that the total current at a location specified by *currentiz* (usually near the end of the simulation) is the total current desired by the user (e.g. the measured beam current).
  - Finally, **gun()** is called 8 more times (still with the *current* option) with *rhoparam* set to 0.5 which mixes in the last run's potential array to finalize and smoothen the solution.
- After this, the 3D potential map (external fields + space charge) is saved to a file for the 3D run.

The number of calls to **gun()** and how much of the potential array of the last run should be mixed in with the new one are, of course, parameters that the user can set. The ones listed above are the ones that gave good results.

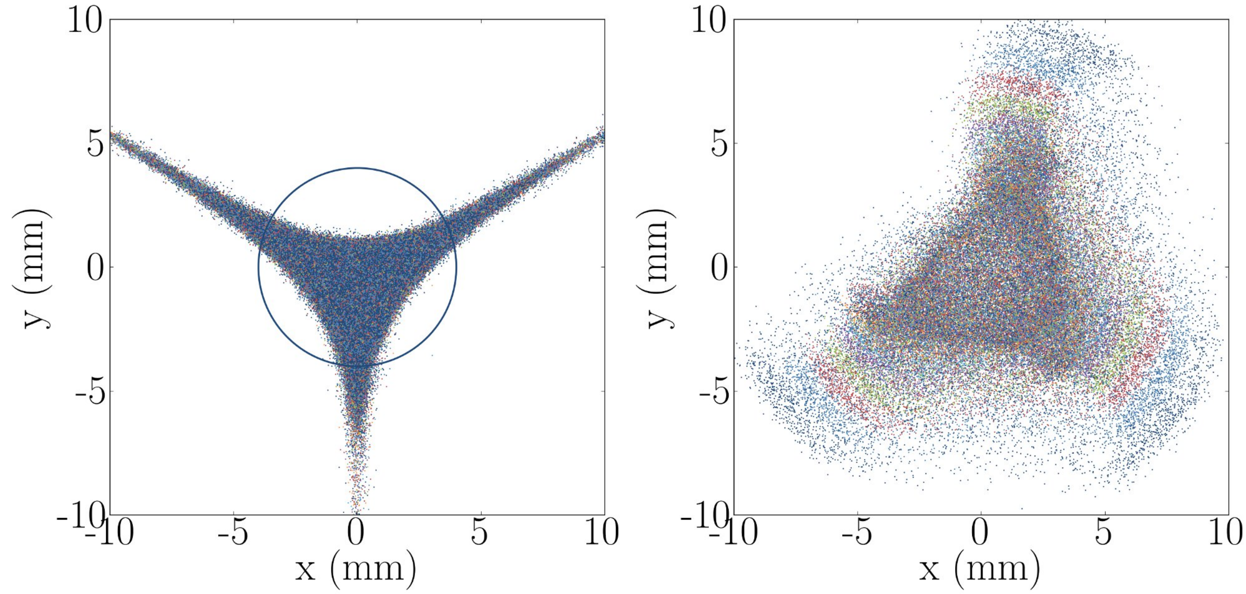

Figure 6.4: Example of start and end distribution in an extraction simulation. Shown is an argon beam with 4.6 mA extracted from SuSI. Left: initial distribution. Note the slight vertical offset due to a hole in the source's iron yoke. Right distribution after 15 cm. The rotation is induced by the residual solenoid field.

In the 3D run, no field calculation is done, instead the field from the RZ run is loaded from the file. Most of the parameters are exactly the same, with the exeption, of course, of the initial particle distributions $f_i(x, y, z, vx, vy, vz)$, which are loaded from a file. After all the parameters have been set, **gun()** is called once to track the particles through the simulation and obtain the ion distributions $f_e(x, y, z, vx, vy, vz)$ at the end of the extraction system (0.25 m in the VENUS simulations, 0.15 m in the SuSI simulations). Examples of the initial and final ion distributions for the extraction of an argon beam from the SuSI ECRIS are shown in Figure 6.4.

6.3 Beam Transport with WARPxy

After successfully extracting ions from the ECRIS with the 2D+ extraction method in WARP, it is necessary to simulate the beam transport to the locations of the beam diagnostic devices (for comparison of the simulations with measurements) or to the accelerator (for design purposes). This can be done with a xy slice simulation in WARP as well, because ECRIS beams are usually DC beams, thus the longitudinal space charge forces are negligible. At the same time, the beams are non-relativistic, so relativistic corrections of the fields are not necessary and the self magnetic field is negligible as well. As already discussed in Subsection 3.1.3, lattice elements can be included in WARP simulations in a number of different ways (as hard-edged multipole elements, axially varying multipole elements, gridded elements, electrodes which are solved with the SOR solver, and as one of the four built in elements: quad, bend, dipo, and accl).

6.3.1 Electrostatic Elements

In order to include fringe field effects as accurate as possible in the beam transport simulations, but save computation time, the following approach was taken to include electrostatic elements like einzel lenses or acceleration gaps:

- The element in question is given a unique filename including the applied voltages (e.g.: "SuSI_EL-21000V-v1.0_HR.wrp").
- The main deck looks for a field file with this name. If it exists, it loads the field as a gridded element from file.
- If it doesn't exist, it calls another WARP script to load the geometry, apply the new

voltages and solve for the electrostatic field. This is a fully separate run of WARP.

- The solved field is now saved into the file with the filename above and the second WARP run is terminated.

- The field is reloaded into the main WARP deck as a gridded element.

This way, fields are only calculated when a new voltage is applied, but not if e.g. only the particle distribution changes from run to run. Note that the geometry loaded in the second WARP deck can be generated with the electrode designer utility presented in Section 3.2.

6.3.2 Automatic Space Charge Compensation

Because of the reasonably good agreement between measurements presented in Chapter 5 and the theoretical prediction with the extended formula originally developed by Gabovich et al. (cf. Subsection 2.1.5), it suggested itself to include the option of automatically calculating the neutralization factor from a set of cross sections σ_i and σ_e, and a beam line pressure specified by the user and the beam currents, and species used in the simulation.
This is done in the following way:

- After each step, all the particles still alive are gathered in an array.

- An average 2σ beam radius is calculated for all species together. This is of course a simplification, but necessary for the multispecies extension of the Gabovich formula to work. Anyway, multiple species are only present in the section between source and analyzing magnet, which is usually very short.

- The beam velocities are calculated for each individual species.

- A function is called to calculate the neutralization according to the multispecies expression presented in equations 2.62 and 2.65. Only ion species with a number of particles still alive > 0 are considered.

- The species currents and weights are then modified with the new neutralization factor f_e.

Note: This procedure was implemented after the measurement of the space charge compensation and has only been used with the latest simulations of the transport through the SuSI LEBT.

Examples of extraction and beam transport simulations using the models described above will be presented in the following sections.

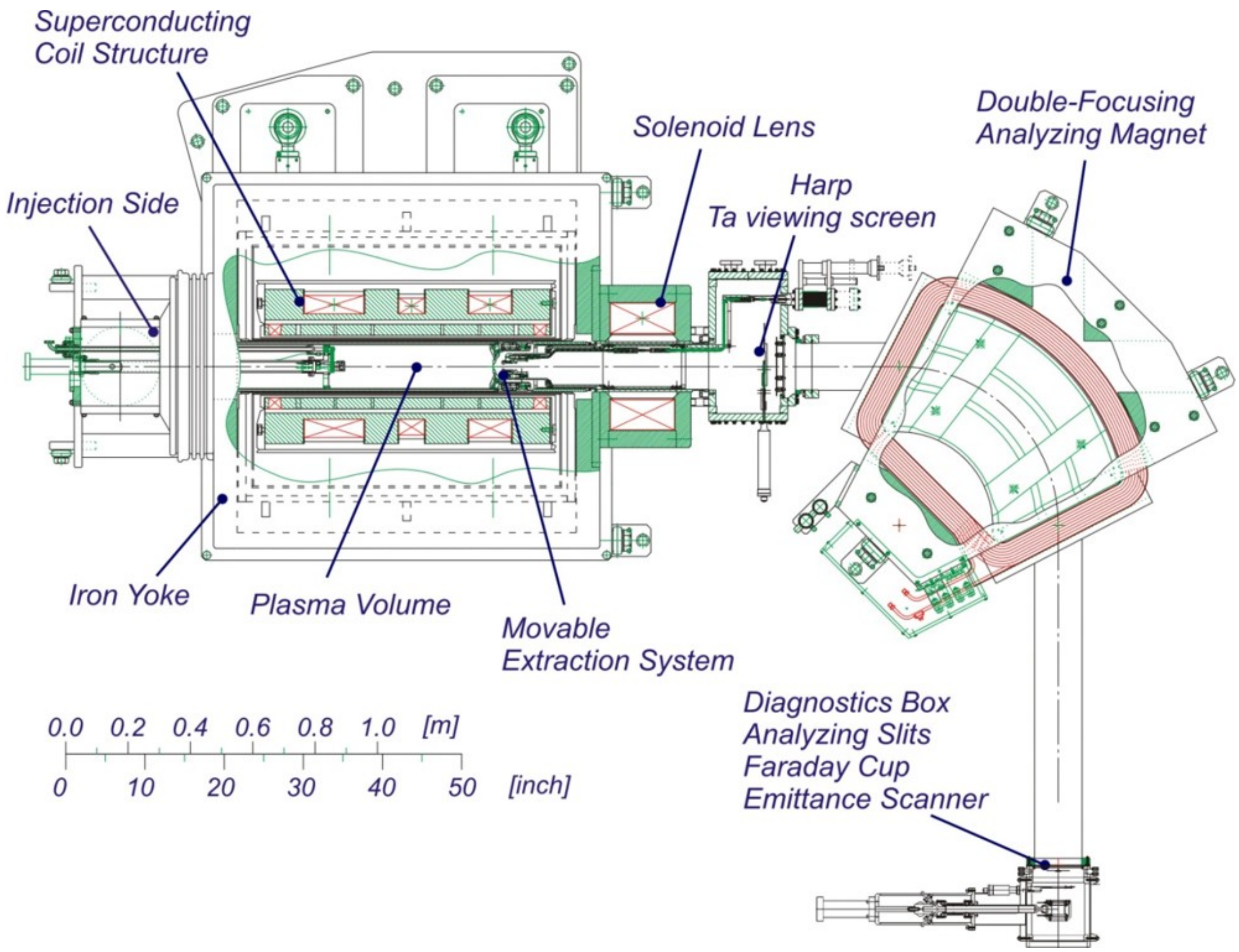

Figure 6.5: VENUS - Source and LEBT.

6.4 VENUS Simulations

The layout of the VENUS LEBT is shown in Figure 6.5. The beam optics elements can be seen in the figure and are:

- Solenoid lens (center 0.4 m after extraction).
- Dipole magnet (90°, 1m radius, 26.5°face angles).

The beam diagnostic elements are:

- Quartz viewing screen (0.8 m after extraction).

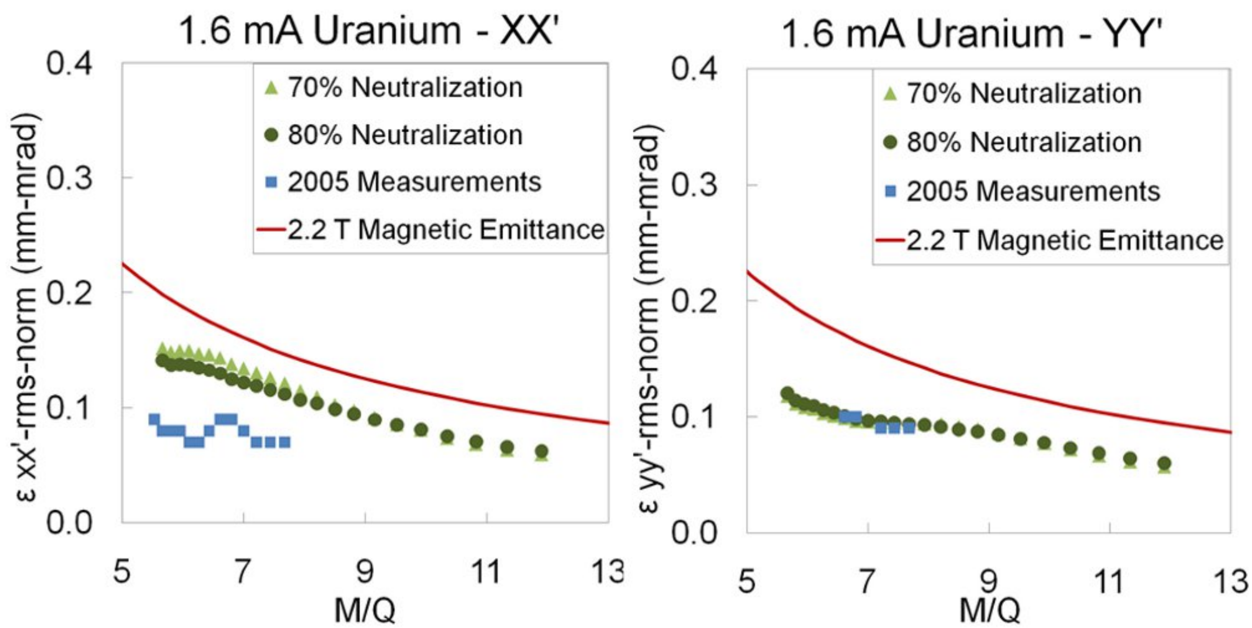

Figure 6.6: Simulation of a 1.6 mA uranium beam extracted from VENUS.

- Allison emittance scanner (3.3 m after extraction).
- Faraday cup (3.3 m after extraction).

6.4.1 Heavy Ions

The first test of the simulation model was performed for uranium ions (mass 238 and charge states from q = 20+ to q = 42+) extracted from VENUS in a measurement in 2005. Oxygen was used as support gas, so oxygen ions were mixed in with the uranium (m = 16, q = 2+ to 6+). The simulation parameters are listed in Table 6.1 and the emittances are plotted in Figure 6.6 for two different fixed neutralization values (70% and 80%). It can be seen, that the vertical emittance agrees very well while the simulation overestimates the horizontal emittance by a factor of 1.5. This could be due to the formation of a virtual aperture (cf. Section 2.2.8) which was not taken into account at that time (initial triangles were the same size for all species) in combination with an overestimated neutralization factor.

6.4.2 Light Ions

In order to test the simulation method on a more fundamental level, a simple beam was chosen next: helium, high pressure, without support gas. Thus the extracted beam consisted mostly of He^{1+}. Here, the source was run in two different ways: Without the radial confinement sextupole and in regular mode using the sextupole. Emittances measured with the allison scanners compared to simulations with the model described above are shown in Figure 6.7. It can be seen that the vertical emittances agree very well and the horizontal emittances are still in the same regime.

In Figure 6.8 a variation of the puller distance with solenoid fixed at 100 A under regular operating conditions of the source (sextupole energized) is shown. It can be seen that the measured and simulated emittances show similar trends with the puller variation, but the simulated emittance is about a factor 2 smaller than the measured one. This behavior can be explained by looking at the beam viewer right after the solenoid magnet (Figures 6.9 and 6.10). For the case with sextupole ON, the simulated beam is much smaller than the

Table 6.1: VENUS - Uranium simulation parameters

Parameter	**Value**
Total extracted current	1.6 emA
Source Voltage	20 kV
Puller Voltage	-2 kV
B_{max} at extraction	2.1 T
Extraction Aperture $\leftrightarrow$ Puller	31.5 mm
T_e	5 eV
T_i	2 eV

measured one. It is possible that it is only transported through the good field region of the dipole magnet, thereby not undergoing significant emittance growth.

It can be concluded that the semi empirical model does not work well for less confined singly charged ions, such as helium, which are created in a single ionization step.

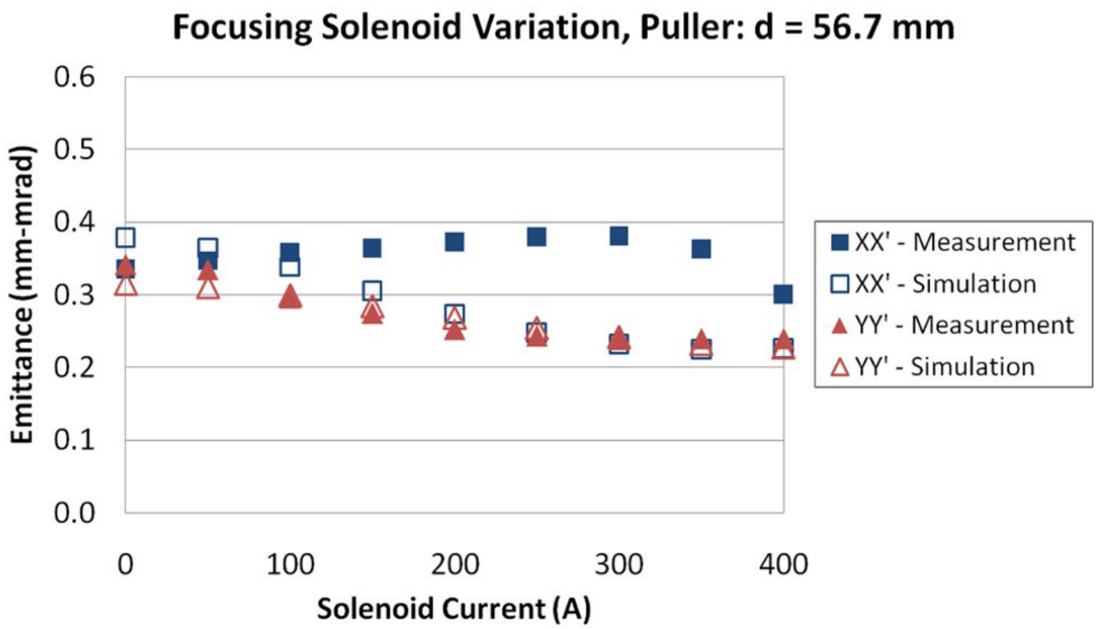

Figure 6.7: VENUS simulation of a helium beam without the sextupole for radial confinement. The simlations agree reasonably well with the measurements.

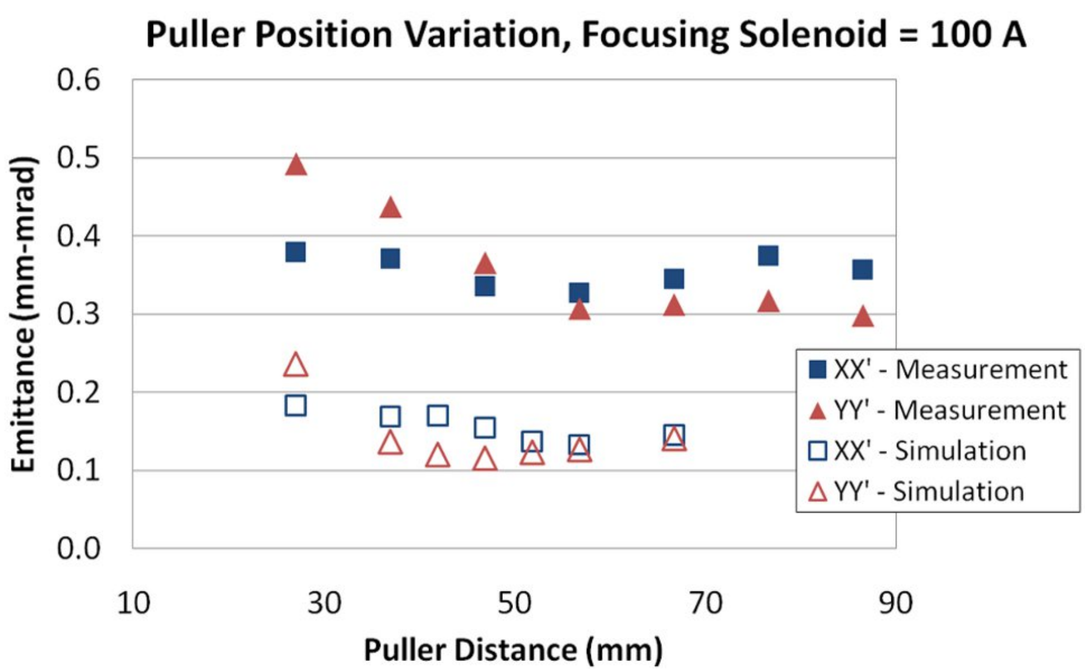

Figure 6.8: VENUS simulation of a helium beam with the sextupole for radial confinement energized, compared to measurements. Simulation and measurement disagree by a factor of 2.

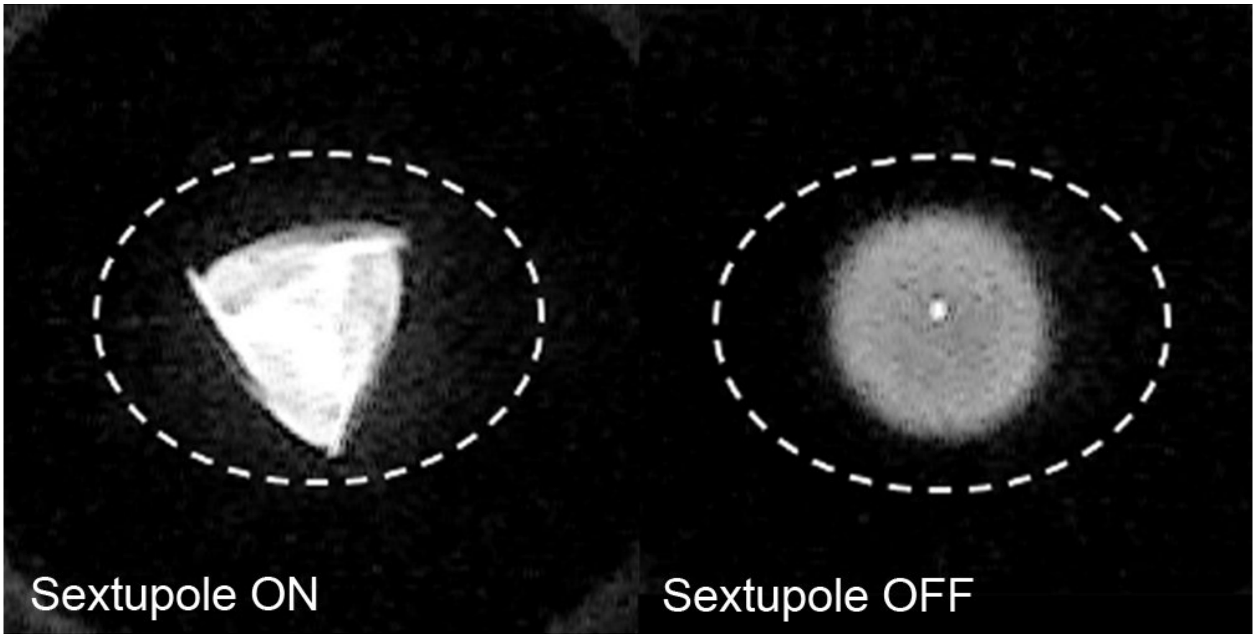

Figure 6.9: Two images from the beam viewer. Both were taken with the same settings: Solenoid lens current = 400 A, Puller position = 50 mm. Left: Sextupole magnet on, right: sextupole magnet off. Due to the confining qualities of the sextupole, the extracted beam current in the off case was lower (1.3 mA vs. 2 mA).

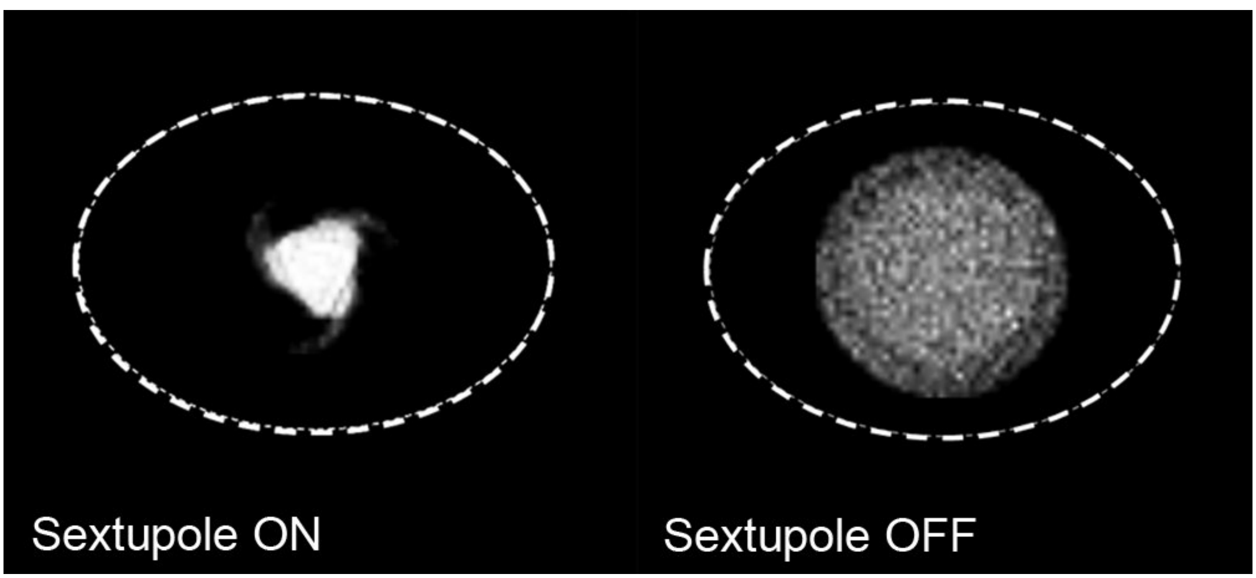

Figure 6.10: Simulation results 825 mm after extraction (position of the beam viewer). Both were simulated with the same settings: Solenoid lens current = 400 A, Puller position = 50 mm. Left: Sextupole magnet on, right: sextupole magnet off. The simulated currents were matched to the measurements (left: 2.0 mA, right: 1.3 mA).

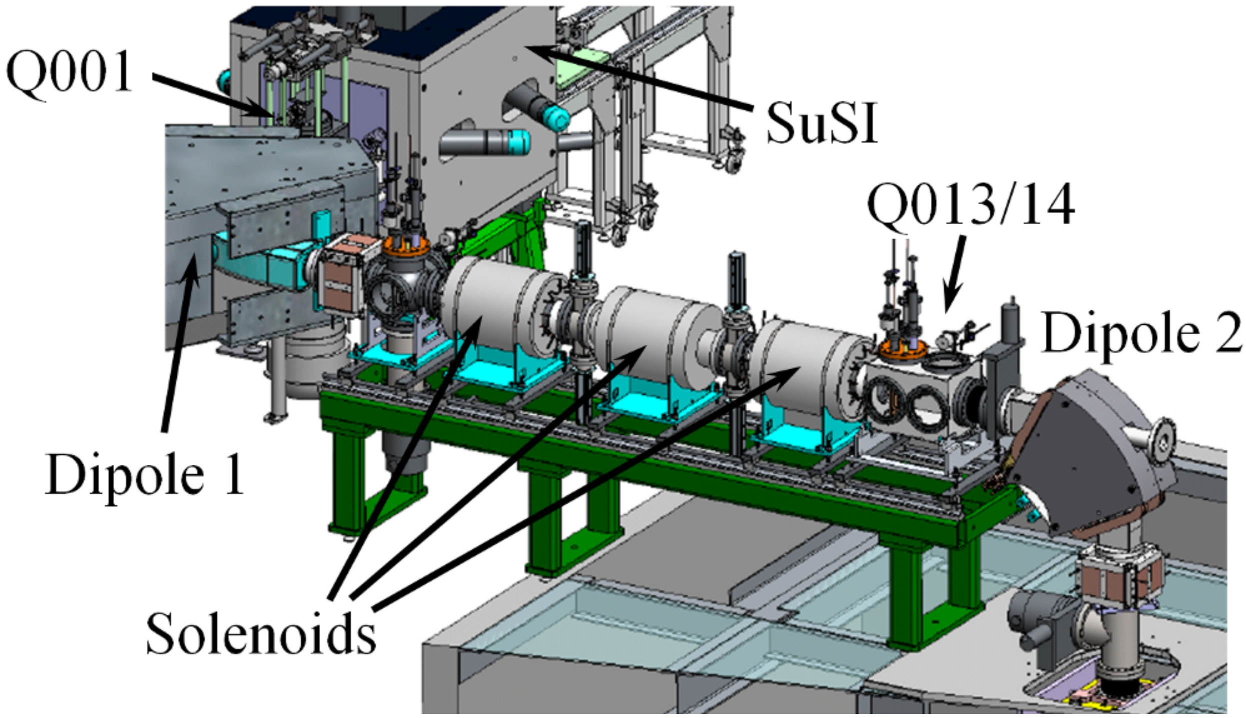

Figure 6.11: Schematic of the SuSI LEBT system up to the second dipole magent. Between the first dipole and the location of NeMo (in the diagnostic box Q013/14) there is a focusing and collimation channel consisting of 3 solenoids, apertures, and slits.

6.5 SuSI Simulations

As a first test of the automatic calculation of the neutralization factor in the LEBT beam transport simulations, simulations were performed for the two pressure series O^{3+} and Ar^{8+} presented in chapter 5.3.2 to go along with the space charge compensation measurements. This includes obtaining the initial conditions, extracting the beam from the ECRIS and transporting it through the LEBT using the automatic calculation of neutralization presented in Subsection 6.3.2. Unfortunately, no emittance scanners were available in this setup, so I can compare the simulations only to the slit scans and beam images obtained during the neutralization measurements. Figure 6.11 shows again the SuSI LEBT. Simulations were terminated at Q014. An example of argon extracted from SuSI was shown in figure 6.4. The cross sections for oxygen so close to the extraction aperture look very similar, so I will not show more beam distributions directly after extraction, instead I will focus on the results at Q014 and the beam envelopes through the LEBT. The following beam optics elements were present in the LEBT and were included in the simulation as well:

- **Q001EL** - Einzel lens directly after the extraction system. Field calculated from electrode data.
- **Q003DH/DV** - Horizontal and vertical steering magnets. In this model, a simple thin kicker was used.
- **Q005DS** - Dipole magnet for selection of desired ion species by A/q. In this simulation, the built-in hard edge model of WARP was used.
- **Q006DH/DV** - Horizontal and vertical steering magnets. In this model, a simple thin kicker was used.
- **Q007** - 4-jaw slits.
- **Q008SN** - First collimation channel solenoid. The field was calculated in POISSON superfish and imported into WARP.
- **Q009AP** - 25 mm aperture.
- **Q010SN** - Second collimation channel solenoid. The field was calculated in POISSON superfish and imported into WARP.
- **Q011AP** - 25 mm aperture.
- **Q012SN** - Third collimation channel solenoid. The field was calculated in POISSON superfish and imported into WARP.

- **Q013** - 4-jaw slits.

These are the two measurement series that will be presented:

1. O^{3+} Pressure $1.1 \cdot 10^{-5}$ to $1.1 \cdot 10^{-6}$ Torr, current approximately constant at 235 eμA.

2. Ar^{8+} Pressure $1.0 \cdot 10^{-5}$ to $1.0 \cdot 10^{-6}$ Torr, current approximately constant at 200 eμA.

As an example of the beam envelopes obtained from the beam transport simulations, the envelopes for O^{3+} at $1.1 \cdot 10^{-5}$ Torr are shown in Figure 6.12. It was necessary to use the vertical steerers a little bit to compensate for an initial vertical angle due to the asymmetry in the source's iron housing where the magnet leads are entering the source through the cryostat.

In Figures 6.13 to 6.18 the beam cross sections of the three highest pressures of the O^{3+} pressure series are compared to the measured slit scans. It can be seen, that shape and size as well as a relative rotation with increasing pressure are reproduced. However, there is a mismatch in absolute rotation.

Note that the only variable changed in this simulations was the pressure, which is only used to calculate the neutralization factor. The argon pressure series (not shown) exhibits similar tendencies the beam cross sections are round (compare to Figures 5.26 - 5.30) and have the correct size. However, they appear more uniform in the simulations than in the measurements.

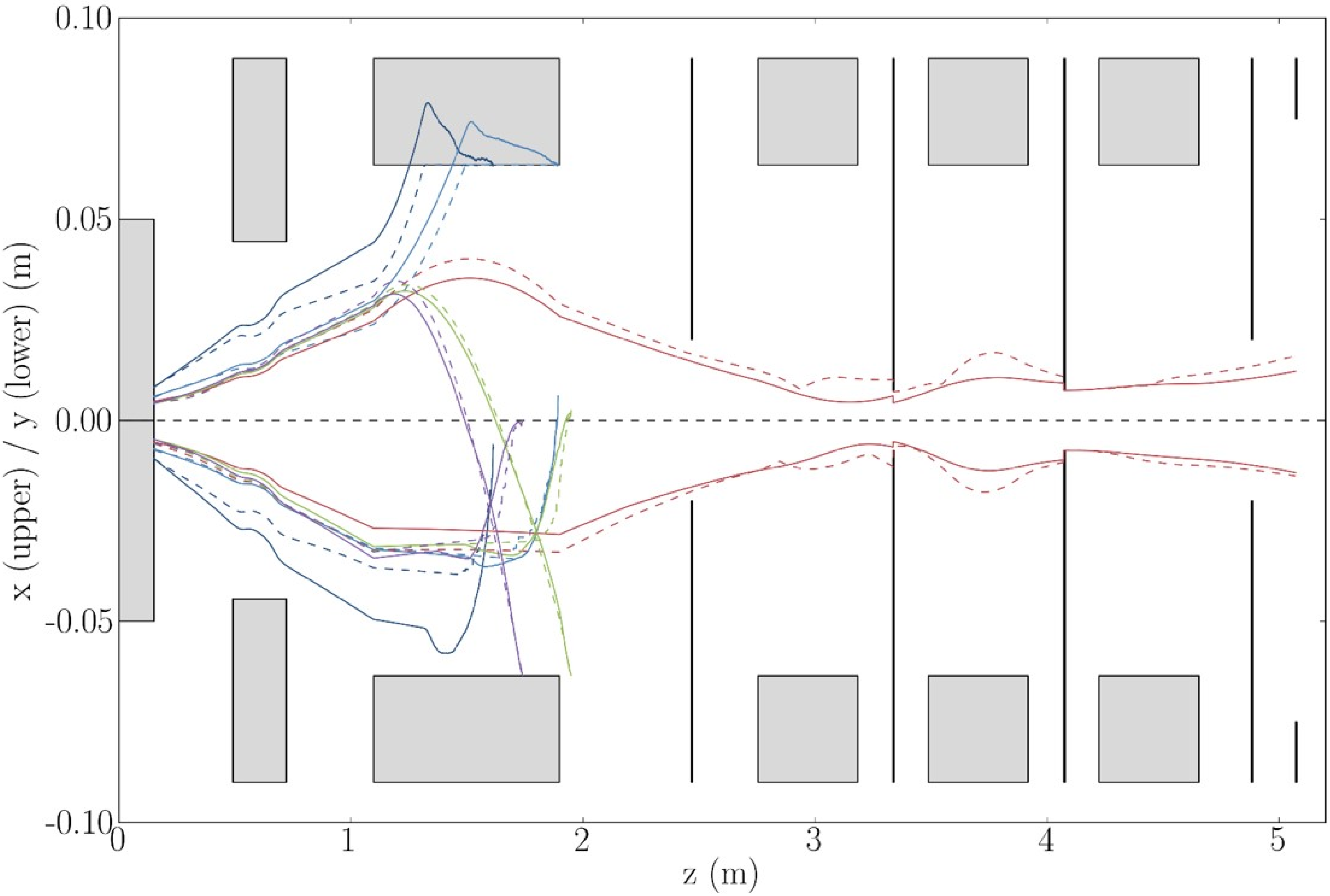

Figure 6.12: Envelopes of a O^{3+} beam in the SuSI beamline with a pressure of $1.1 \cdot 10^{-5}$ Torr. The upper envelope is the horizontal one and the lower envelope the vertical one. From left to right, the grey boxes are: Source, einzel lens, analyzing magnet, and the three solenoids of the collimation channel.

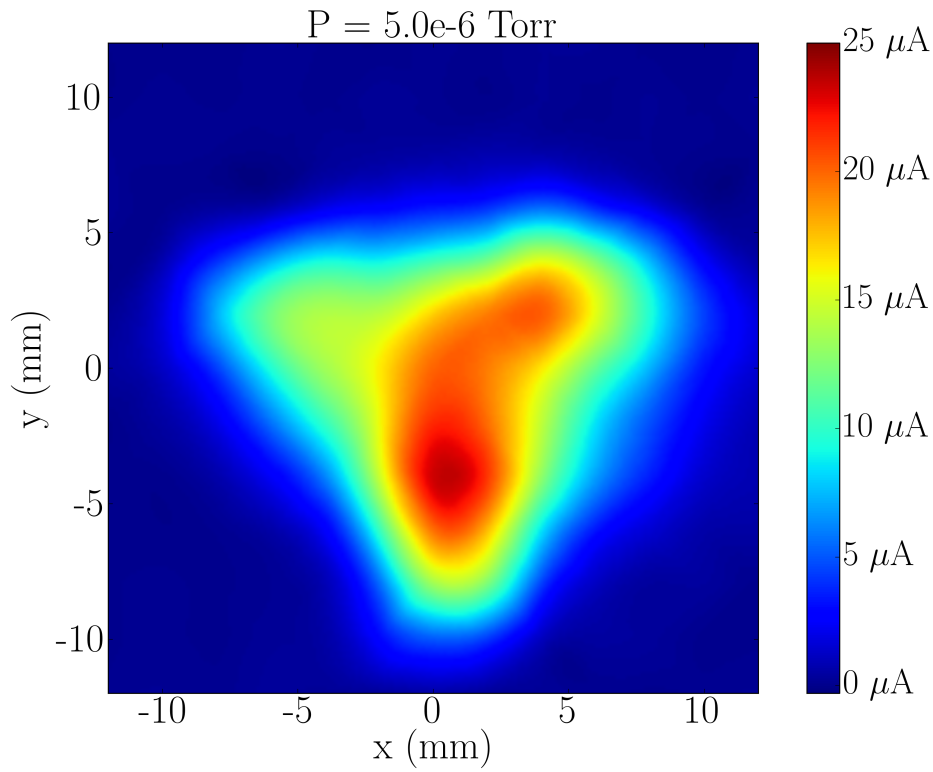

Figure 6.13: Measured beam profile of O^{3+}, $5.0 \cdot 10^{-6}$ Torr

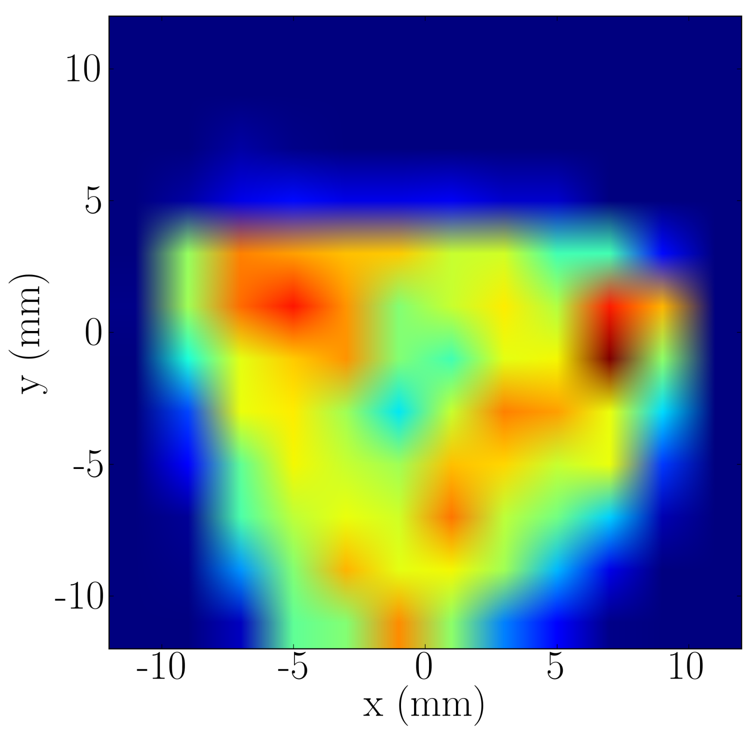

Figure 6.14: Simulated beam profile of O^{3+}, $5.0 \cdot 10^{-6}$ Torr

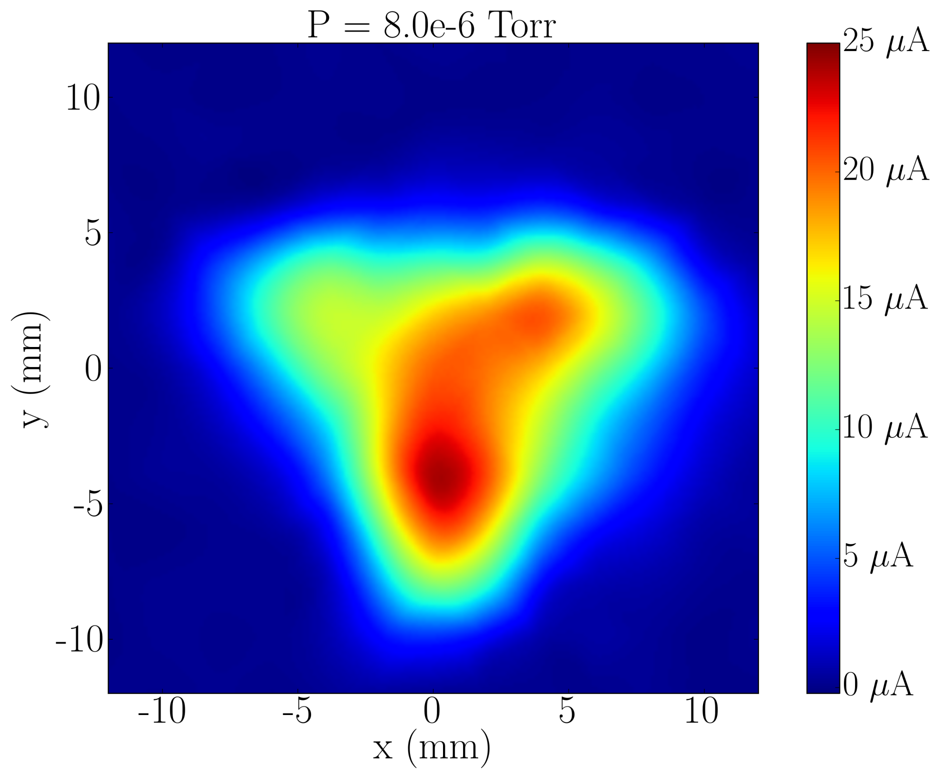

Figure 6.15: Measured beam profile of O^{3+}, $8.0 \cdot 10^{-6}$ Torr

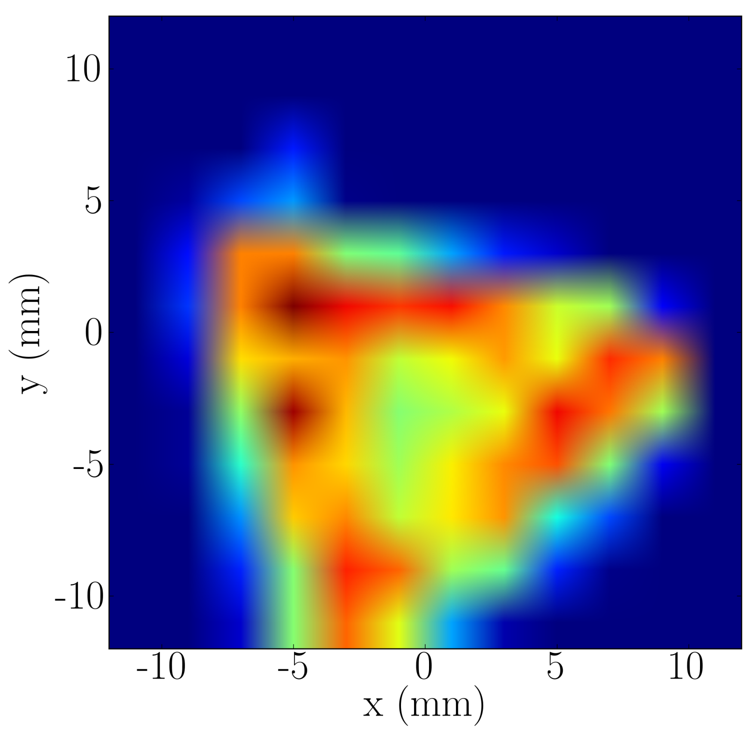

Figure 6.16: Simulated beam profile of O^{3+}, $8.0 \cdot 10^{-6}$ Torr

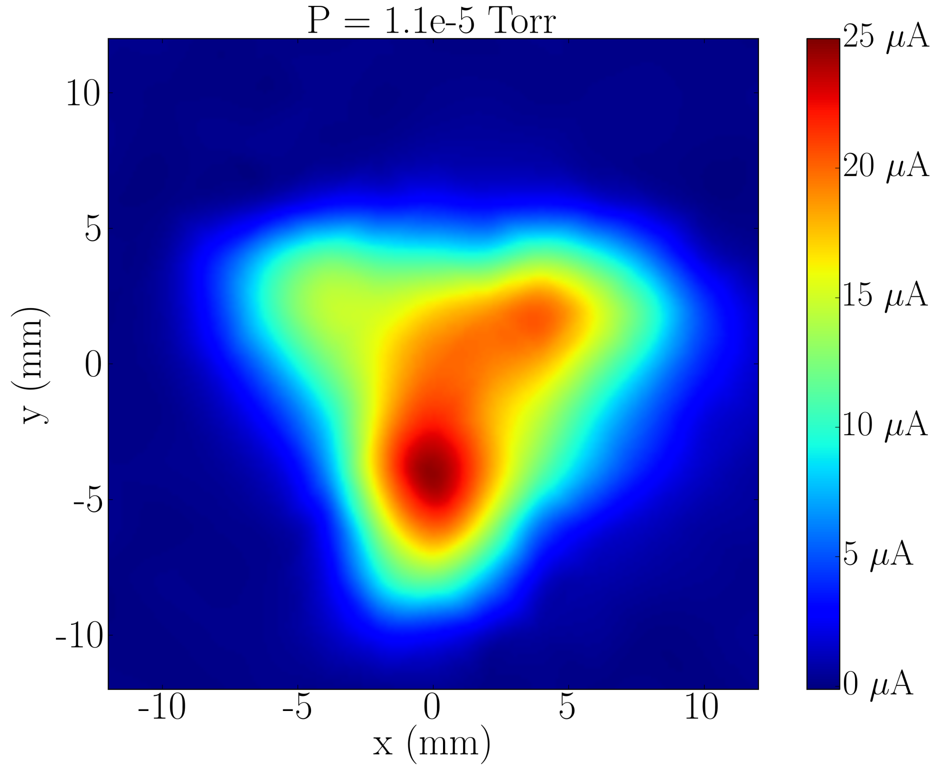

Figure 6.17: Measured beam profile of O^{3+}, $1.1 \cdot 10^{-5}$ Torr

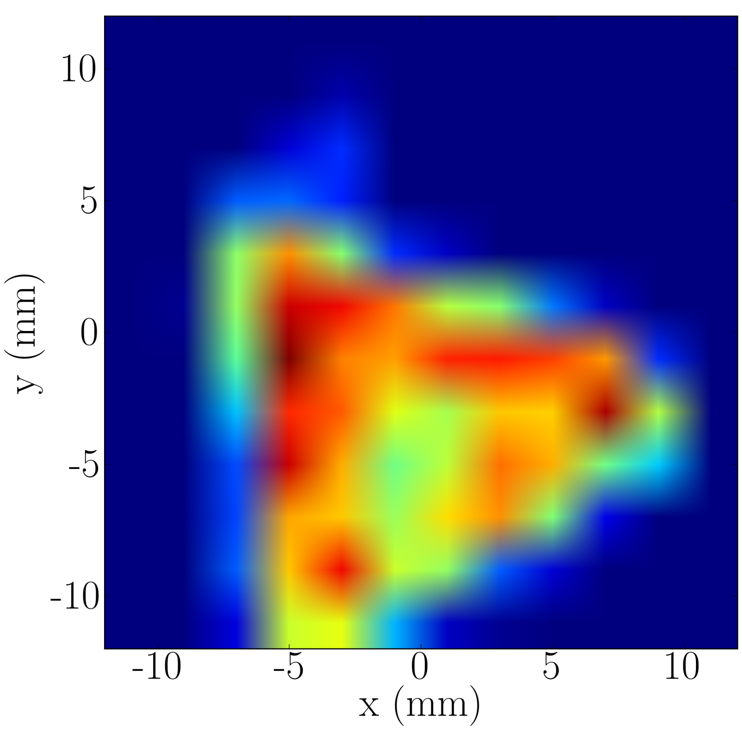

Figure 6.18: Simulated beam profile of O^{3+}, $1.1 \cdot 10^{-5}$ Torr

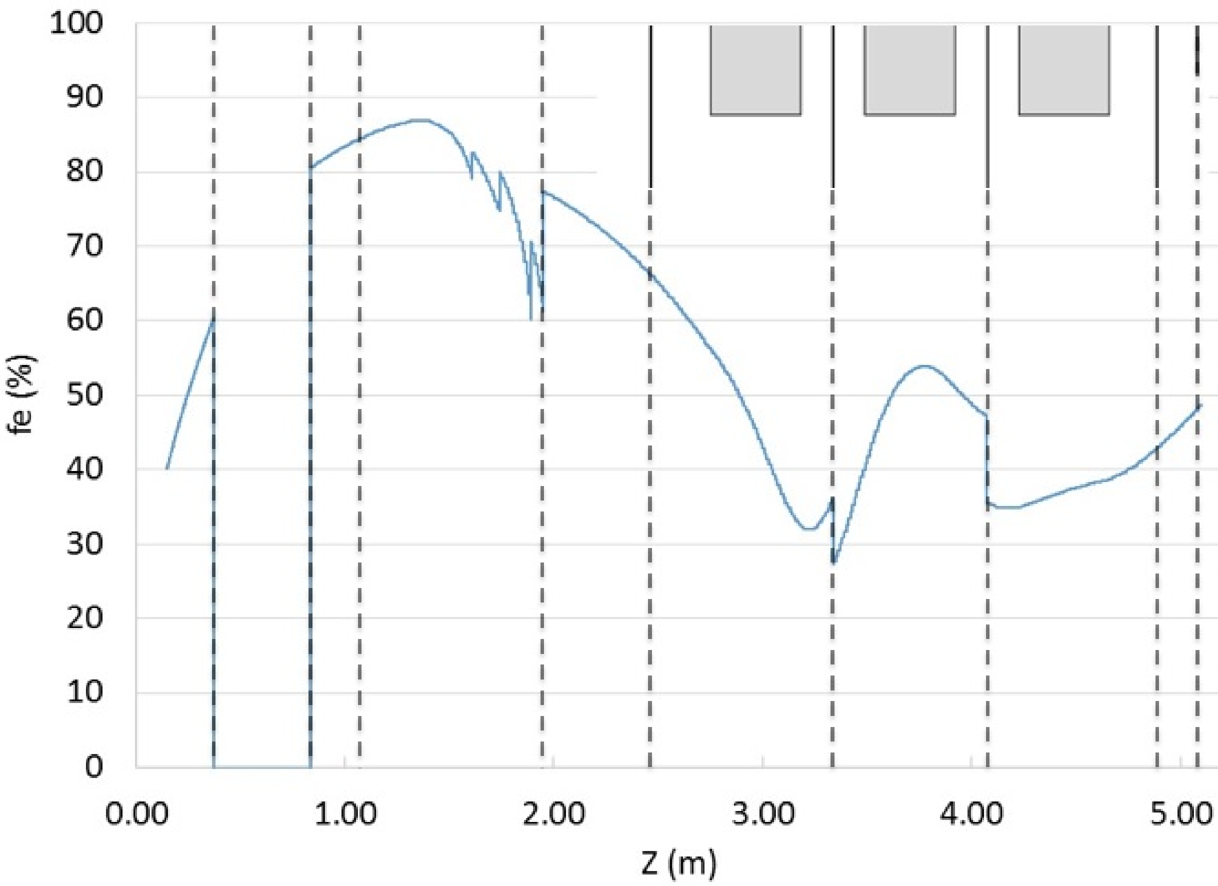

Figure 6.19: Neutralization along the beam line in the SuSI LEBT for a O^{3+} beam in $1.1 \cdot 10^{-5}$ Torr residual gas pressure. The center line represents the simulation run with the charge exchange cross section obtained by using the Müller-Salzborn formula. The three boxes correspond to the solenoids in the collimation channel. The dashed lines are element boundaries and apertures. Inside the einzel lens (0.4 - 0.8 m), the neutralization is zero, inside the dipole (1.1 - 1.9 m) the beam contaminants are filtered out.

In Figure 6.19 the neutralization factor according to the automatic calculation presented in Section 6.3.2 along the SuSI beamline is shown. The part with zero neutralization in the beginning is the einzel lens, where the presence of an electrode prohibits the accumulation of electrons inside the beam envelope. It looks like neutralization can reach very high values in the region before the bending magnet, where the beam current is still high (due to the many species in the beam) and the beam radius is large.

6.6 Conclusion

In this chapter, I presented the three parts of the ECRIS extraction suite using the particle in cell code WARP. The initial conditions are obtained semi-empirically from plasma markings inside the source. The particles are then extracted from the plasma by means of a relaxation process in which the steady state solution and the plasma meniscus form self-consistently. The hybrid RZ-3D model called 2D+ saves computation time and space and compares reasonably well with full 3D simulations. The use of the same simulation code (WARP) for the two parts of the ion source simulation and the beam transport together with a number of python utility programs and GUI's lets the user seamlessly go from one step to the next thereby obtaining an end-to-end simulation of an ECRIS driven accelerator front-end. As will be shown in Chapter 7, it is even possible to include the accelerator into the simulation. First tests of the extraction simulations with uranium and helium beams extracted from VENUS suggest the simulation model can be used for medium to heavy ions of medium to high charge states, but the approach to obtain the initial conditions breaks down for very light singly ionized ions. A more self-consistent model of the plasma as suggested by Mironov *et al.* [20] might help obtain more realistic initial distributions for the subsequent extraction simulation.

The implementation of the multispecies extension of the formula derived by Gabovich *et al.* [51] as part of the LEBT beam transport simulation yielded promising first results and gave interesting insights in the distribution of space charge compensation along the beam line. It might be possible that in the region before the analyzing magnet, space charge compensation is as high as 90% due to the high beam current and large average beam radius. This has to be confirmed by future measurements, though.

Chapter 7

An Example Application: DIANA

7.1 Introduction

During the course of the presented thesis work, several simulation codes were used to simulate extraction from Electron Cyclotron Resonance Ion Sources (ECRIS) and beam transport through Low Energy Beam Transport (LEBT) systems. Utility programs were developed in python to simplify the creation of the necessary input files for the simulations as well as the post processing of the results. The Dual Ion Accelerators for Nuclear Astrophysics (DIANA) [124–127] presented an interesting opportunity to apply some of the simulation codes and utility programs, as well as know-how, to a new project. DIANA is a proposed underground laboratory for nuclear astrophysics experiments currently being designed by a collaboration of the University of Notre Dame, the University of North Carolina, Western Michigan University, Michigan State University, Lawrence Berkeley National Laboratory, and the Colorado School of Mines.

The scientific goal of DIANA is to measure charged particle nuclear cross- sections in low energy regimes, corresponding to stellar burning processes. These cross-sections are important for determining the rates of nucleosynthesis processes from the Big Bang, through the early development of the universe, up to the current stars, thereby shedding light on the abundance of elements [128]. The charged particle nuclear cross- sections present a major uncertainty in the stellar model simulations and, so far, for most of the reactions, low-energy data are only available through extrapolation from higher energies. One of the challenges in measuring these cross-sections is the fact that most of them are very small (pico- to femto-barn range) at the desired energies. Background from cosmic rays in the detectors is therefore a major problem. The two paths taken in DIANA to enable measuring these cross-sections are:

1. Minimize the background by going to an underground location and benefit from the natural shielding of the rock,

2. Design the accelerators for significantly higher luminosity as compared to existing facilities (e.g. LUNA [129]).

DIANA will consist of two accelerators: A low energy (50 - 400 keV) machine and a higher energy (300 - 3000 keV) machine (the energies are quoted for q = 1+ charge-states and will be higher for multiply charged ions). While the 400 kV accelerator certainly also presents very interesting possibilities for the application of programs and results presented earlier in this thesis, the focus of this chapter lies on the 3 MV machine. This accelerator includes an ECRIS, a LEBT system, an electrostatic acceleration column, and aims to provide 1 mA of beam current (regime of non-negligible space-charge effects) and is therefore an ideal application of the software described in Chapter 3. Detailed simulations were carried out for the base design of the accelerator and modifications were proposed and discussed with the prospective vendor. In this chapter the base design will be described, the modifications will be explained, and simulations will be presented to demonstrate the improvement and feasibility of the final design.

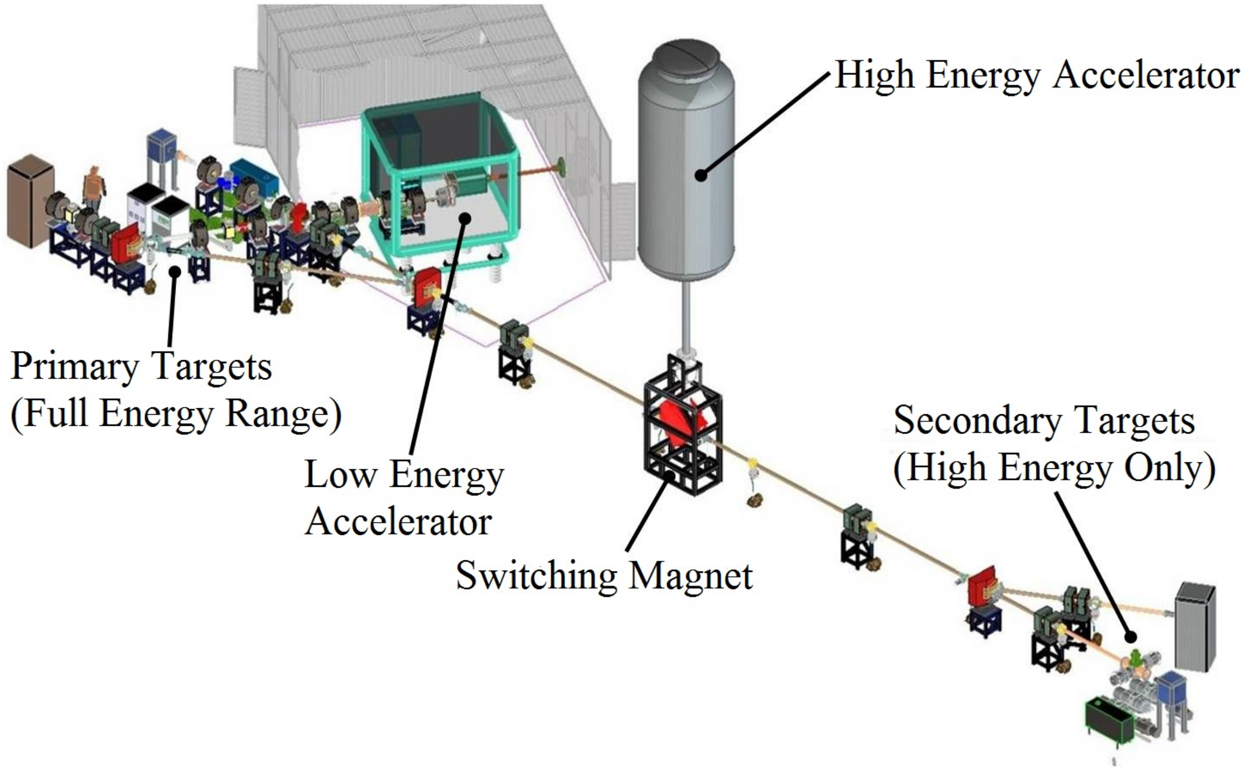

Figure 7.1: DIANA - Facility layout. Courtesy of the DIANA collaboration.

7.2 Layout

A general layout of the planned DIANA facility can be seen in figure 7.1. The most important features are:

- **Low energy accelerator.** A flat-field (no multipole for radial confinement) ECR ion source placed on a high voltage platform, capable of delivering up to 100 emA of $^{4}He^{1+}$ with an energy range of 50 keV to 300 keV.

- **High energy accelerator.** A Pelletron electrostatic accelerator with a small permanent magnet ECR ion source inside the high voltage terminal, capable of delivering a minimum of 850 eμA of $^{4}He^{1+}$ with an energy range of 300 keV to 3000 keV.

- **Primary target stations.** A solid target and a gas-jet target can both receive beam from both accelerators to provide consistent data over a wide energy range.

- **Secondary target stations.** In a later phase of the project, a second set of targets is envisioned to allow for individual operation of both accelerators at the same time.

As mentioned in the introduction to this chapter, the focus of the presented work lies on the high energy accelerator. More precisely on the simulation of the ion extraction from the small all-permanent-magnet ECR ion source and the transport through the electrostatic acclerator. Therefore the other parts of the DIANA facility will not be discussed further. The high energy accelerator is envisioned to be an off-the-shelf Pelletron by the National Electrostatics Corporation (NEC) [130] with custom modifications to achieve the desired beam intensity and quality over the full energy range. A Pelletron is similar to a Van de Graaff generator [131], but instead of a rubber band, charges are transferred to the high voltage terminal by means of pellet chains. This particular system will have a set of 10 chains capable of delivering 150 eμA of current each, to provide the necessary charge to extract a 1 emA beam. The whole system is typically enclosed in an SF_6 vessel to minimize high voltage breakdown, while the beam pipe in the center is evacuated.

The criteria necessary to reach DIANA performance level are listed in table 7.1. As can be seen, the DIANA high energy accelerator features a wide energy range of 300 keV - 3 MeV throughout which a constant beam current with consistent beam quality is desired. This was the motivation for doing extensive simulations and add custom modifications to the standard design.

Figure 7.2 shows a more detailed schematic of the high energy accelerator system, loosely divided into the three parts (cf. also figure 7.10):

- **Front end.** Ion production, species separation, and transport of the beam to the accelerator. This section ends at the entrance of the accelerator.

- **Accelerator column.** Acceleration of the ions to the final energy. This section contains the electrostatic acceleration column and an electrostatic quadrupole triplet (ESQ1) [41, pp. 98]. It ends at the exit of the column.

- **Bending section.** Bending of the beam from the vertical direction into the horizontal plane. This part consists of an electrostatic quadrupole triplet (ESQ2) after the exit of the column, and a $90°$ bending magnet. This section ends at the image point of the magnet.

These three parts will now be discussed in more detail, followed by a list of the custom modifications (Section 7.3) and simulation results (7.4).

Table 7.1: DIANA - High energy experiment performance criteria.

Parameter	**Performance Criteria**	**Comment**
Output Energy (min)	300 keV	*ion charge state
Output Energy (max)	3000 keV	*ion charge state
Beam Currents:		(by species)
^{1}H	$\sim$ 1 mA	
^{3}He,^{4}He	$\sim$ 1 mA	
Heavy Ions (A $\leq$ 22)	$>$ 50 pμA	
Maximum magnetic rigidity	1.44 Tm	
Energy spread	0.05 %	
Energy stability	0.01 %/h	

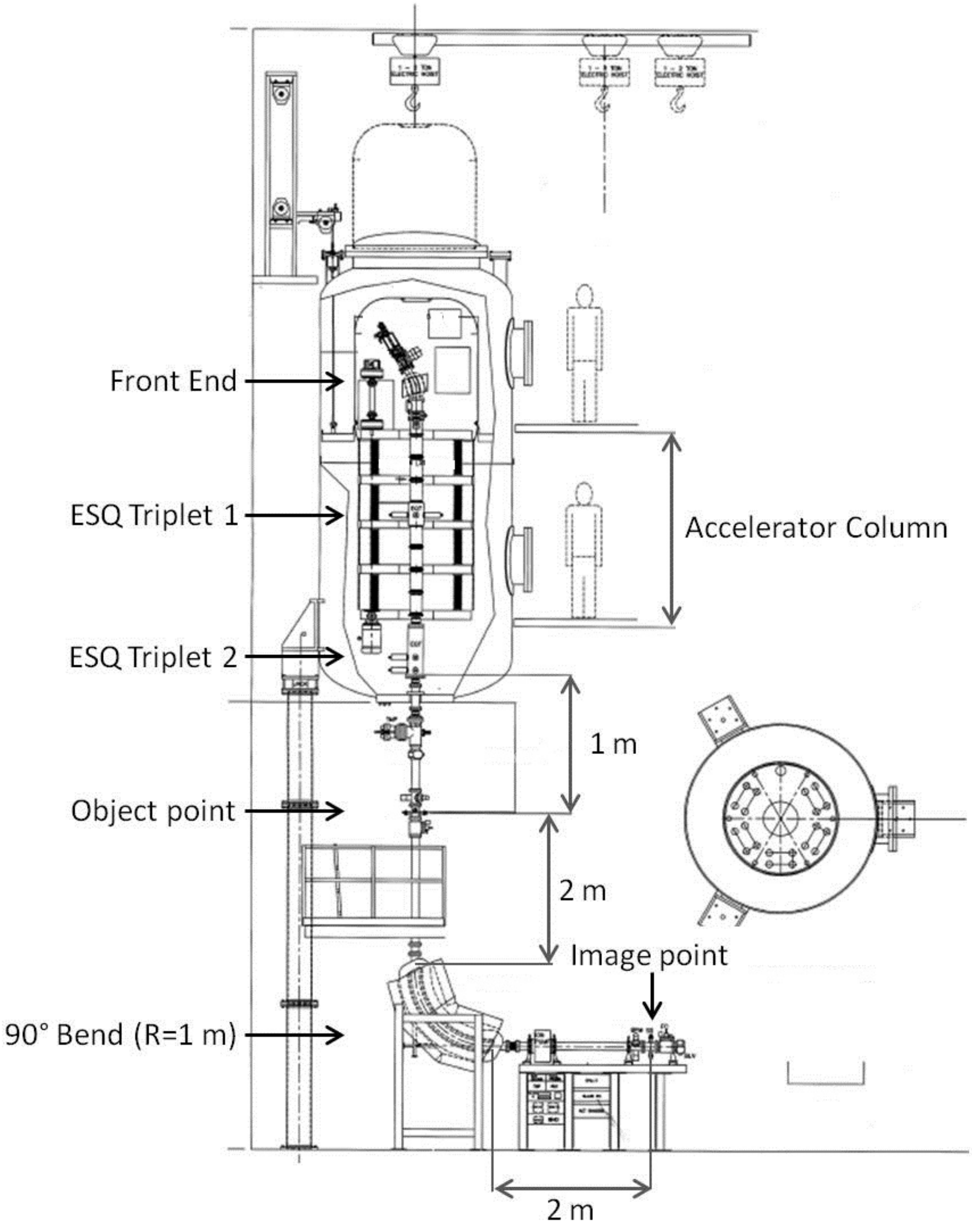

Figure 7.2: High energy accelerator layout. From the top: Front end with ion source and species separation. Accelerator column including an electrostatic quadrupole triplet (ESQ1). Bending section including an electrostatic quadrupole triplet (ESQ2) and a 90°bending magnet. Courtesy of NEC.

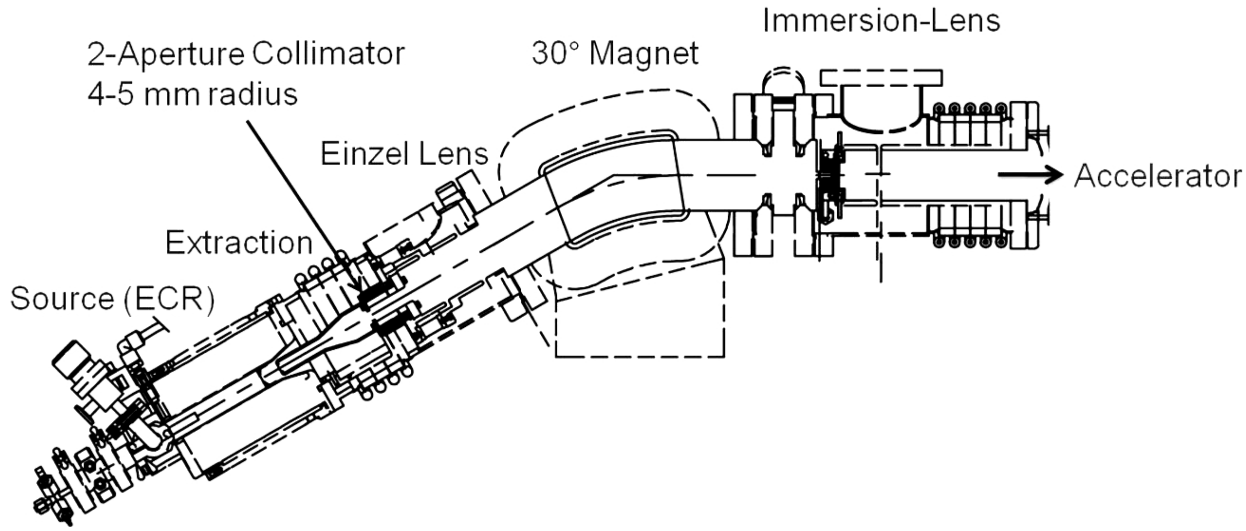

Figure 7.3: Front end layout. From the left: ECR ion source, extraction system, collimator, einzel lens 30°, bending magnet, immersion lens. Courtesy of NEC.

7.2.1 Front End

A detailed layout of the front end inside the high voltage terminal of the accelerator is shown in Figure 7.3. The relevant elements are:

- **ECR ion source.** A small, all-permanent-magnet Electron Cyclotron Resonance Ion Source (ECRIS). See Subsection 7.2.2.

- **Extraction system.** The standard extraction system of Nano-PK is a diode system (see Figure 7.7 top). In Subsection 7.3.1, an improved extraction system will be introduced.

- **Collimator.** This collimator is part of the standard design and proves helpful in restricting the beam size for low energies. It consists of two apertures with a center distance of 50 mm and a diameter of 6-8 mm.

- **Einzel lens.** Unipotential electrostatic lens (see [41, pp. 78]). The maximum voltage on the center element is +20 kV.

- **30° bending magnet.** A double-focusing dipole magnet to separate ion species by different $\frac{m}{q}$ (mass [amu] to charge-state [e] ratios). The magnet specifications are listed in Table 7.2.

- **Immersion lens.** Bipotential electrostatic lens (see [41, pp. 78]). This lens accelerates and focuses the beam into the entrance of the accelerator column. The maximum voltage difference of the two elements as specified by NEC is 50 kV.

Table 7.2: 30°dipole specifications. For more information about Rogowski pole tips see [4,5]

Parameter	**Value**
Type	double focusing
Bending radius	300 mm
Bending angle	30°
Face angles	8.8°
Air gap	30 mm
Focal length	600 mm
Pole tip shape	Rogowski-type

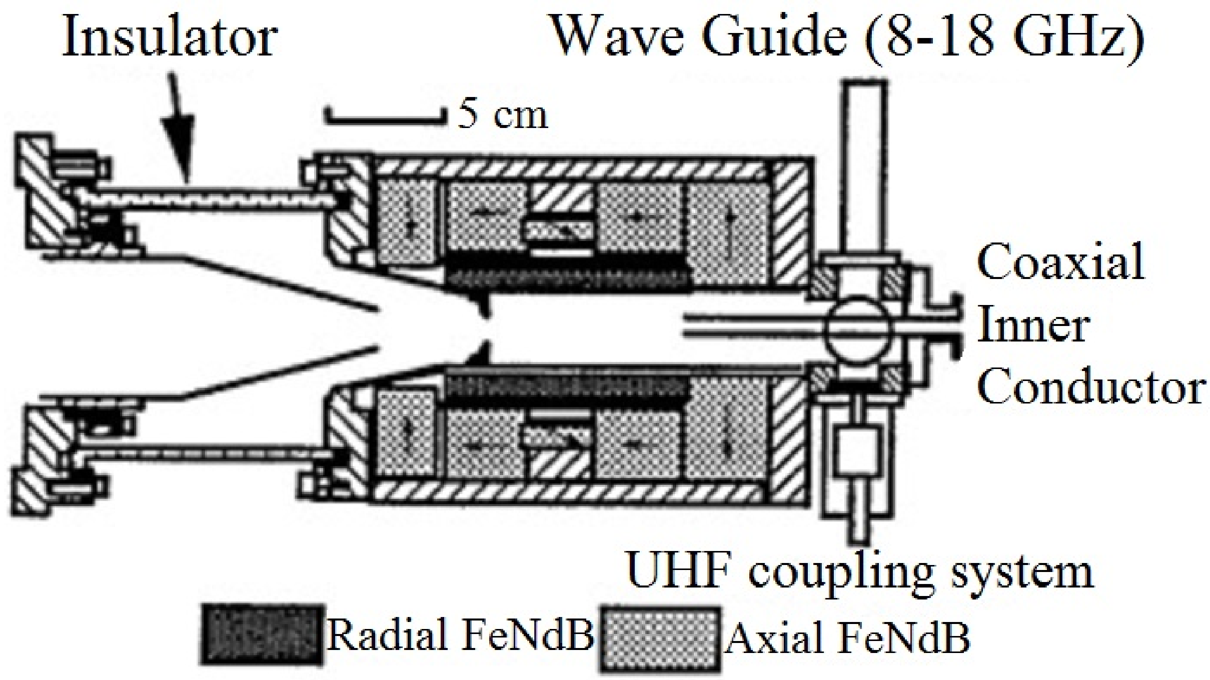

Figure 7.4: NANOGAN Sectional view. The beam is extracted from right to left. This image shows the standard diode extraction system. 'Axial FeNdB' denotes the permanent magnets creating the solenoid field, 'radial FeNdB' the permanent magnet sextupole. Image adapted from [13].

7.2.2 Ion Source

The Electron Cyclotron Resonance Ion Source is of the type Nano-PK (former NANOGAN [13, 132]), produced by the company Pantechnik in France [6]. A section-view is shown in Figure 7.4. The principles are the same as described in Sections 2.2 and 4.1 for larger ECRIS with the exception that now all magnets are FeNdB permanent magnets.

Table 7.3: DIANA - NANOGAN parameters.

Parameter	**Value**
Chamber ∅	26 mm
Mirror length	100 mm
B_{max}	0.80 T
B_{min}	0.25 T
$B_{extraction}$	0.58 T
f_{ecr}	10 GHz
MW power	<100 W

Table 7.3 lists the important source parameters and table 7.4 the ion beam currents guaranteed for NANOGAN/NanoPK by the company on their webpage. This does not include any information about beam size, diameter of the extraction aperture, and beam emittance. A little more information can be found in several conference proceedings and review papers [13, 132, 133]. For DIANA the main focus lies on singly charged H and He. In [133] A. Villari shows measurements of 99% emittances for a NANOGAN-II (which is similar to NANOGAN) of 125 π-mm-mrad and 175 π-mm -mrad at 15 kV extraction voltage for He^{1+} and He^{2+}, respectively. Assuming $\epsilon_{99\%} \sim 4 \times \epsilon_{RMS}$ this would correspond to normalized RMS emittances of 0.089 mm-mrad and 0.175 mm-mrad, respectively. These values will be important in Subsection 7.4.1 for comparison of simulations with actual measurements. Improvements of the extraction system leading to better beam quality and matching into the accelerator column will be discussed in subsections 7.3.1 and 7.4.1.

Table 7.4: Company guaranteed ion beam currents for NANOGAN. Vertical: Ion species, Horizontal: Charge-state. Currents in eμA. From [6].

	1+	**2+**	**4+**	**6+**	**8+**	**9+**	**10+**	**11+**	**12+**	**13+**	**14+**	**15+**	**16+**
H	1000												
He	1000	100											
Ar	300		100	45	40	10		1					
Xe										8	7		5
Ta									10		5		
Au			10	9	8	6	6			5	2	1	

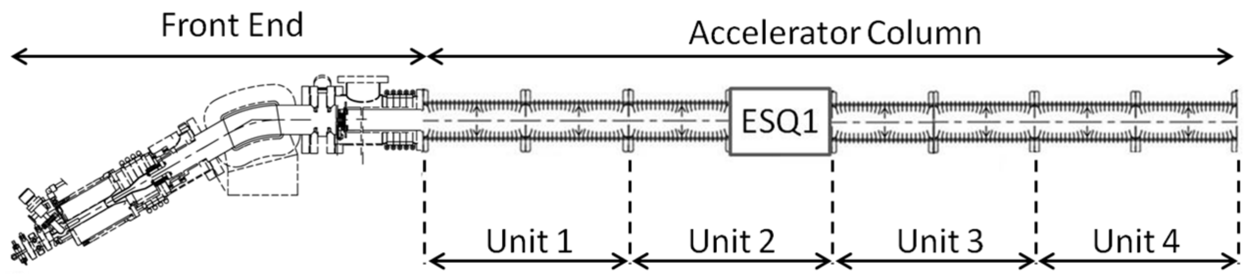

Figure 7.5: Electrostatic accelerator column layout. The column consists of 4 units, each unit is composed of 2 segments á 23 rings (except unit 2 which holds the electrostatic quadrupole). Courtesy of NEC.

7.2.3 Accelerator Column

The accelerator column consists of 4 units, each of which houses two electrostatic acceleration segments. Each segment consists of 23 concentric rings which are shaped to minimize secondary electron emission. The layout of the column including the injector can be seen in figure 7.5. The voltage grading of the immersion lens and the rings is realized by a resistor chain parallel to the column (as depicted schematically in Figure 7.6). The standard gradient through the column is a linear voltage gradient. This corresponds to all the resistors R having the same resistance (immersion lens excluded). Improvement of beam matching into the column by using a custom, adjusted voltage gradient in unit one (by adjusting the resistor values individually), and the NEC standard technique of using a shorting rod will be discussed in Subsection 7.3.2. In unit two, the second segment was replaced by an electrostatic quadrupole triplet (ESQ1) for focusing the beam at lower energies, thereby providing additional tuning flexibility. The quadrupole triplet has an aperture radius of 19 mm, and an electrode rod radius of 21.9 mm. The lengths of 1$^{\text{st}}$, 2$^{\text{nd}}$ and 3$^{\text{rd}}$ element are 63.5 mm, 127.0 mm and 63.5 mm, respectively, with gaps of 19 mm in between the three elements.

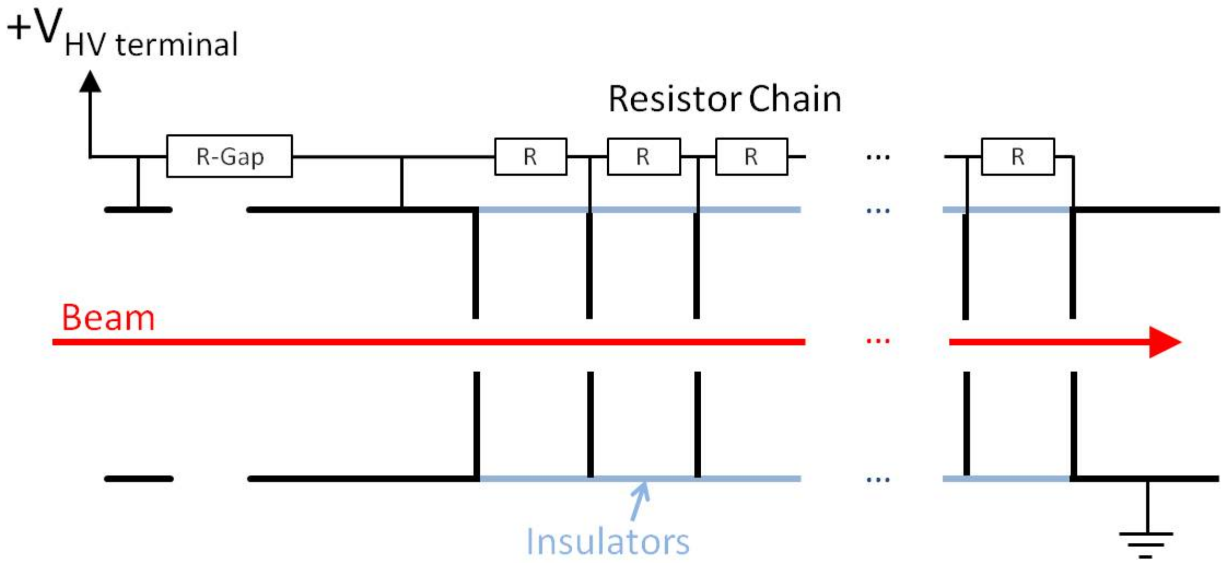

Figure 7.6: Cartoon picture of the NEC Pelletron accelerator tube including resistor chain. The resistor chain acts as a voltage divider. The HV terminal voltage can be set from 300 kV to 3 MV. The Gap voltage as well as the voltages on the respective rings is then determined by the ratio of the resistors to each other. In the simplest case, all ring resistors R are equal and thus the voltage difference between each ring as well.

7.2.4 Bending Section

After reaching its final energy at the exit of the column, the beam is transported through the bending section where it is bent into the horizontal plane. The bending section consists of a second electrostatic quadrupole triplet (ESQ2), and a double-focusing 90° dipole magnet. ESQ2 is necessary to focus the beam into the object point of the dipole. The bending section ends at the image point of the dipole, which is assumed at 2× the bending radius from the exit of the dipole. At this point, the present design and simulation effort is considered concluded. A simplified layout including the bending section can be seen in Figure 7.10. The resulting particle distributions are used in beam transport simulations to the two (four) target stations by another group in the DIANA collaboration.

7.3 Custom Modifications

Preliminary simulations of the off-the-shelf design of the NEC Pelletron described in the previous section showed that the beam quality and size could not be preserved through the whole system mainly for two reasons:

- **Strongly divergent beam out of the source.** The diode system proposed for NANOGAN/NanoPK by Pantechnik and NEC is insufficient to achieve laminar flow of the beam through the extraction region which leads to a strongly divergent beam. In the rest of the system, the inner diameter of most elements is too small to avoid particle loss and emittance growth due to aberrations from fringe field effects (stronger at larger radii).

- **Strong focusing effect at the entrance of the column.** Due to the sharp change in voltage gradient at the entrance of the column, the still rather low energy beam ($\sim$ 50 - 65 keV) experiences a strong focusing force which matches the beam poorly into the column.

7.3.1 Ion Source Extraction System

There are several ways to remedy the divergent beam from the source (negative effects in parentheses): Smaller extraction aperture (less beam), collimate the beam (less beam), increase the aperture sizes of the the rest of the system (more space required), add more focusing elements (more space required). Instead, the extraction system was modified from a simple diode system to a more complex tetrode system in order to improve the beam size and beam quality from the source. The original diode system and the proposed tetrode system are compared side-by-side in Figure 7.7, the results are discussed in Section 7.4.1.

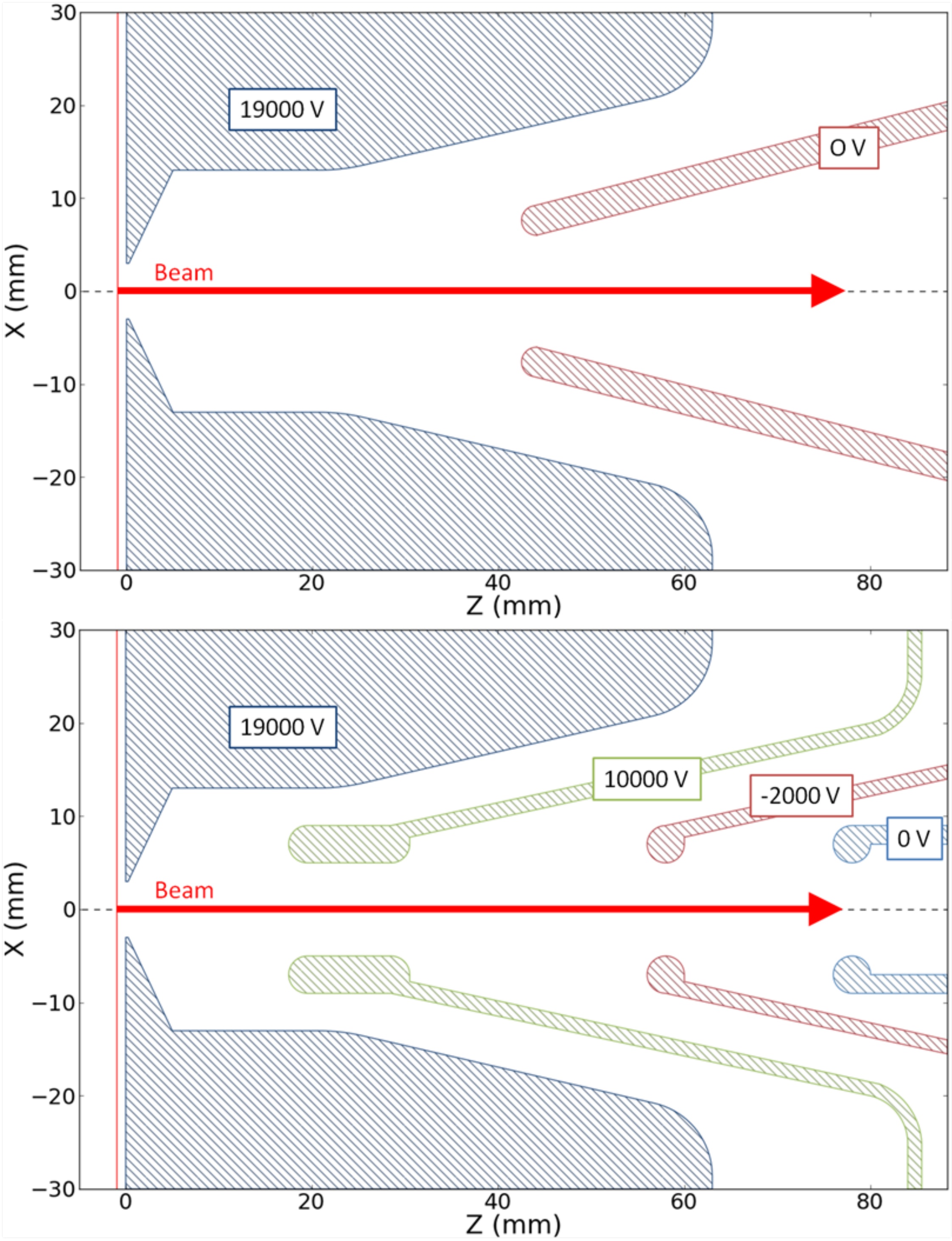

Figure 7.7: Side-by-side comparison of the two different extraction systems proposed for the Nano-PK ECR ion source. Diode system (top); Tetrode system (bottom). Note that the final beam energy (19 keV for singly charged ions) is the same for both systems. The tetrode system gives more tuning flexibility by adjusting the voltage of the '10000 V' electrode (green).

7.3.2 Adjusted Voltage Gradient

In order to improve the beam matching into the accelerator column, the grading of the ring voltages in unit 1 (cf. Figure 7.5) was adjusted to be non-linear. The voltage distribution in unit 1 now follows equation 7.1 with $V_0 = 2941$ kV (3000 kV - 19 kV source - 40 kV immersion lens), $V_{VG} = 300$ kV, and $L = 0.717$ m.

$$V(z) = V_0 - V_{VG}\left(\frac{z}{L}\right)^{\frac{4}{3}} \tag{7.1}$$

Here L is the optimal length of the adjusted part in order to achieve a voltage drop of V_{VG}. This would lead to a perfect matching of adjusted gradient and linear gradient thereafter (the remaining 2641 kV). Unfortunately, this would also mean a much longer column. Instead, the adjusted voltage gradient part is terminated after 0.52 m (physical length of unit 1) and the linear voltage gradient part is shortened a bit as well (to fit in units 2-4), leading to a slightly higher gradient there. This procedure keeps the focusing at the entrance minimal, thereby matching the beam well into the column. Although, due to this compromise, the original focusing effect is now shifted to the transition from unit 1 to unit 2, it is also weakened a little and the beam has a higher energy and is thus less influenced by the effect. As a matter of fact, the focusing is actually helpful now, as will be seen in Section 7.4.2 (simulation results). In Figure 7.8 a comparison between a purely linear voltage gradient and the adjusted voltage gradient is shown for the full 3 MV case, in order to illustrate the points made above. In practice, it is not feasible to set all resistors of unit 1 individually. Each one is custom made and it would be expensive to produce 41 different resistors and stock as many spares. Instead, the adjusted voltage gradient in unit 1 was approximated piecewise linearly using only 5 different resistor values. In appendix the ideal resistor values

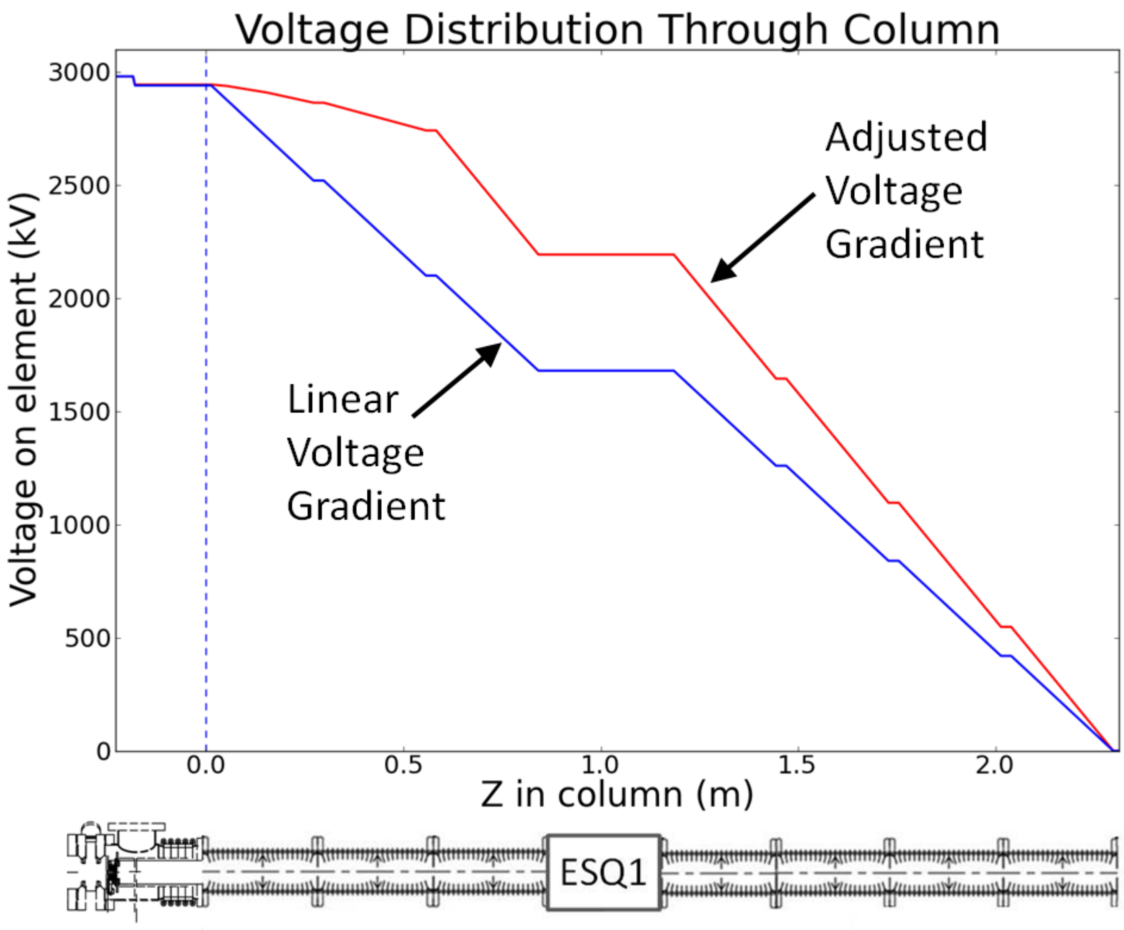

Figure 7.8: Comparison of linear voltage gradient and adjusted voltage gradient. The voltage on each element of the column is shown versus the position along the accelerator axis. The horizontal axis corresponds to the picture of the column below the figure.

(normalized to a total of 1) are listed together with the practical values (in MΩ). This includes also the resistor parallel to the immersion lens. Thus, the gap voltage scales with the total acceleration voltage (HV terminal voltage).

The second technique that will be employed in the column is the well- established *shorting rod technique*, which is part of many of NEC's electrostatic accelerators. This is independent of the grading of the rings and adds three connectors to the accelerator at which the column can be grounded (see Figure 7.9, bottom) by inserting a shorting rod from the exit of the column. This means that the rings coming afterwards are all at ground potential as well,

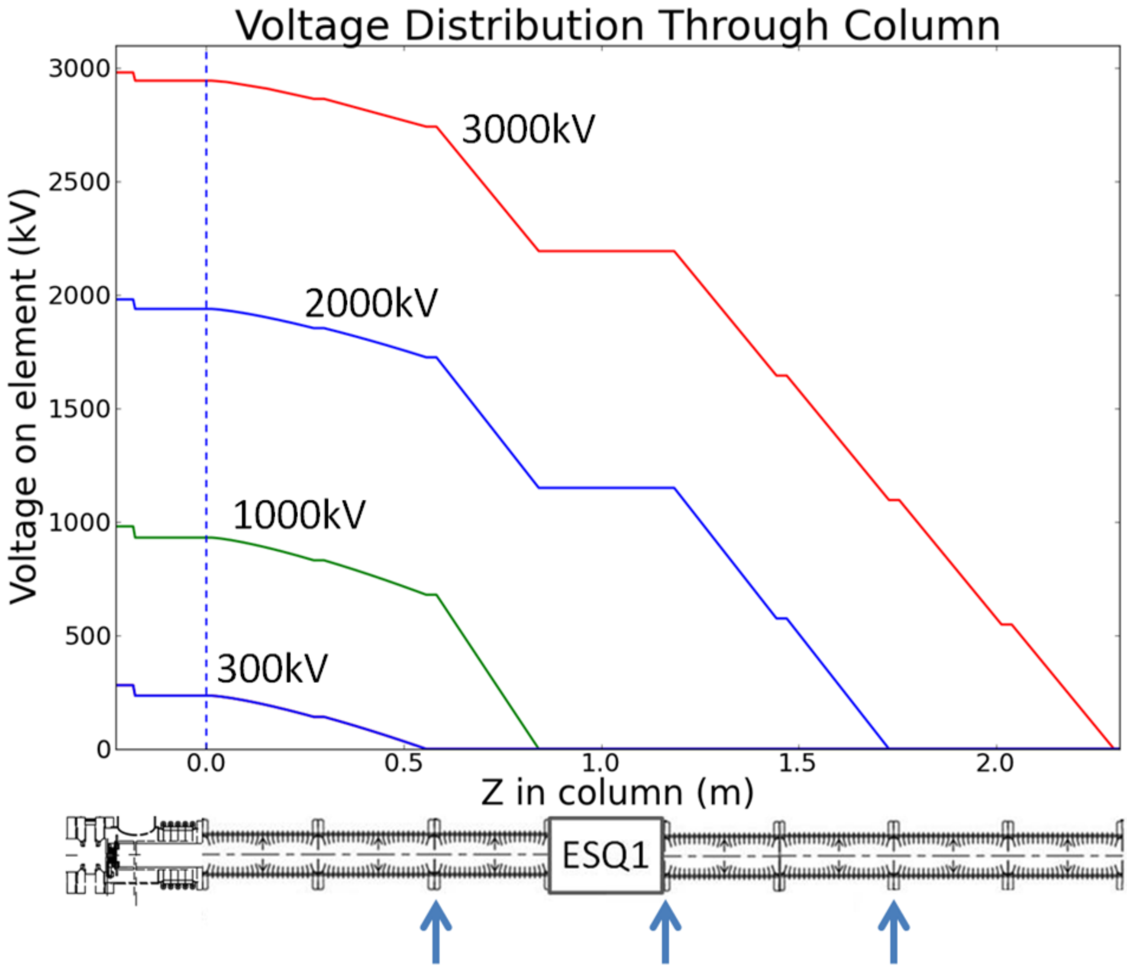

Figure 7.9: Comparison of different total voltages using the adjusted voltage gradient and the shorting rod technique. The voltage on each element of the column is shown versus the position along the accelerator axis. The horizontal axis corresponds to the picture of the column below the figure, The vertical arrows denote the shorting positions.

thereby effectively shortening the column and keeping the gradients (and the immersion lens gap-voltage) in the beginning of the column the same for different HV terminal voltages. The voltage distributions for a few HV terminal voltages are plotted in 7.9. Another beneficial effect of grounding part of the accelerator for lower energies is that in the grounded section, the beam will experience space-charge-compensation (which cannot occur in the presence of strong electric fields).

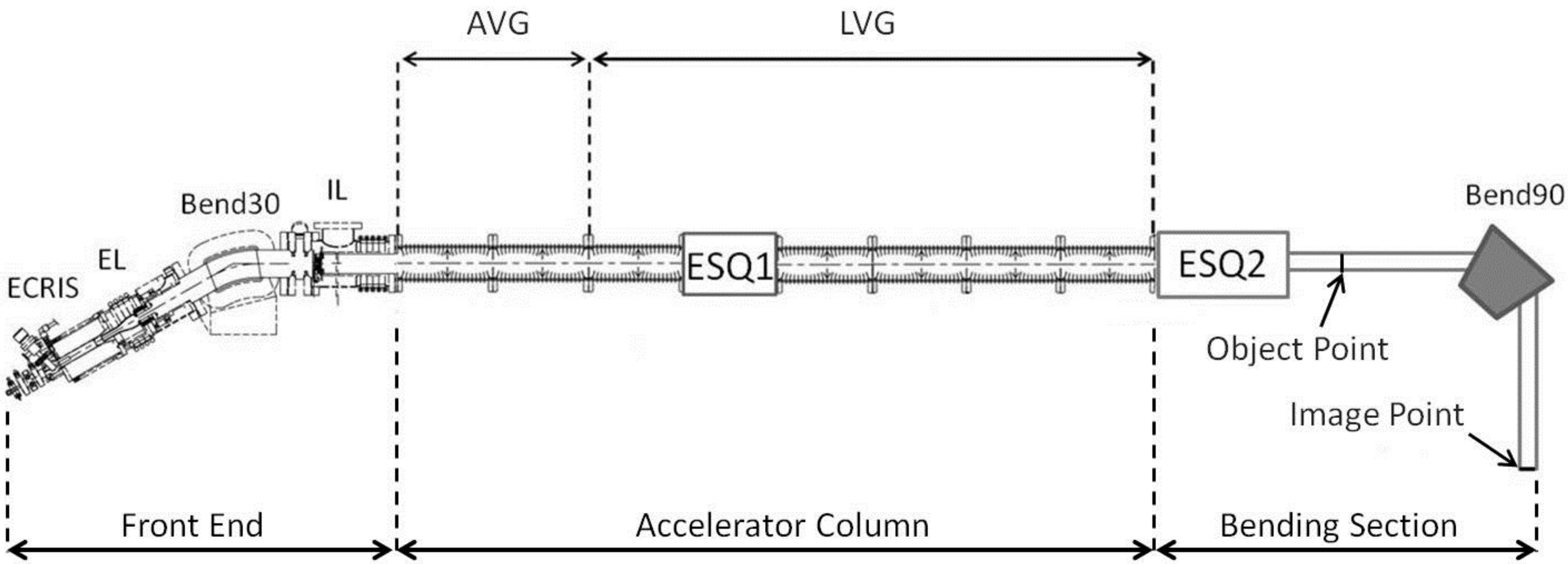

Figure 7.10: Simplified layout of the simulated high energy accelerator and beamline. The ion source extraction simulation ends 88.25 mm after the plasma aperture of the source. This is where the WARP simulation starts, which covers the rest of the system in one continuous simulation.

7.4 Simulations

In this section, the simulations carried out for the DIANA high energy accelerator are described and results are presented. There are two different parts: The ion source extraction simulation and the subsequent simulation of front end, accelerator, and bending section (all in one simulation). A layout overview can be found in Figure 7.10. The z = 0 point for all the simulations is at the plasma aperture. Details to software (simulation codes and utility programs) used in the two parts can be found in the respective subsections.

7.4.1 Ion Source Extraction

The electrode geometry of the tetrode extraction system was designed in the ElectrodeDesigner presented in Section 3.2.1, which includes an import function for simple magnetic fields and an option to export IGUN [31–33] input (*.IN) files. The magnetic field of NANOGAN was calculated in RZ geometry in PANDIRA, which is part of the Poisson -Superfish suit of software [134, 135]. This calculation did not include the sextupole magnet (because it is not RZ symmetric), but the contribution of the sextupole to the longitudinal B-field on axis ($B_z(z)$) is very small. Figure 7.11 shows the field calculated by PANDIRA and Figure 7.12 the interpolated field $B_z(z)$ on the center axis using Poissons SF7 interpolator. This field was imported into the ElectrodeDesigner and an *.IN file was created which was then used to simulate extraction from the source with IGUN.

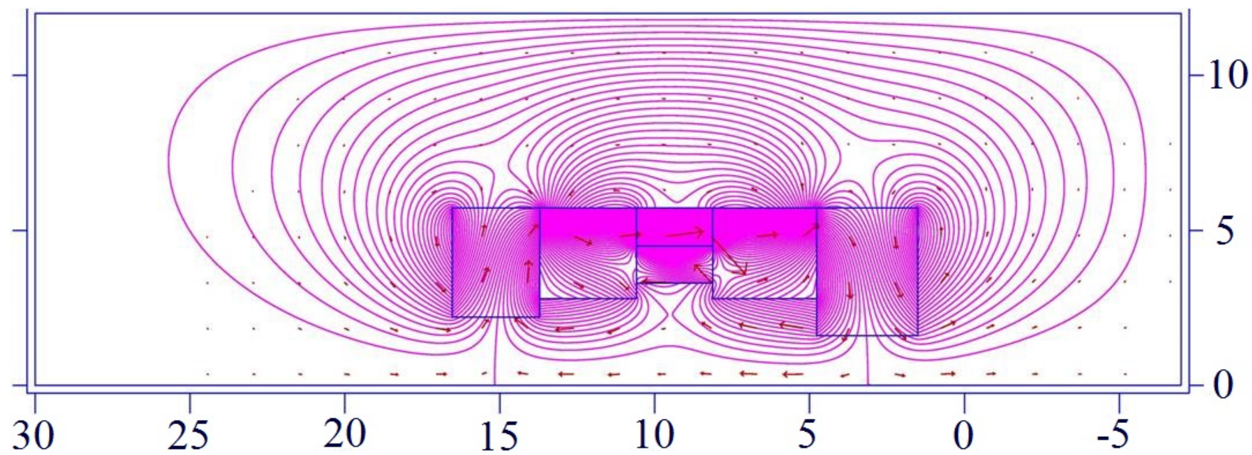

Figure 7.11: RZ-symmetric PANDIRA model of the permanent magnet structure of NANOGAN. Dimensions are in cm, horizontal axis is Z, vertical is R. Sextupole magnet not included.

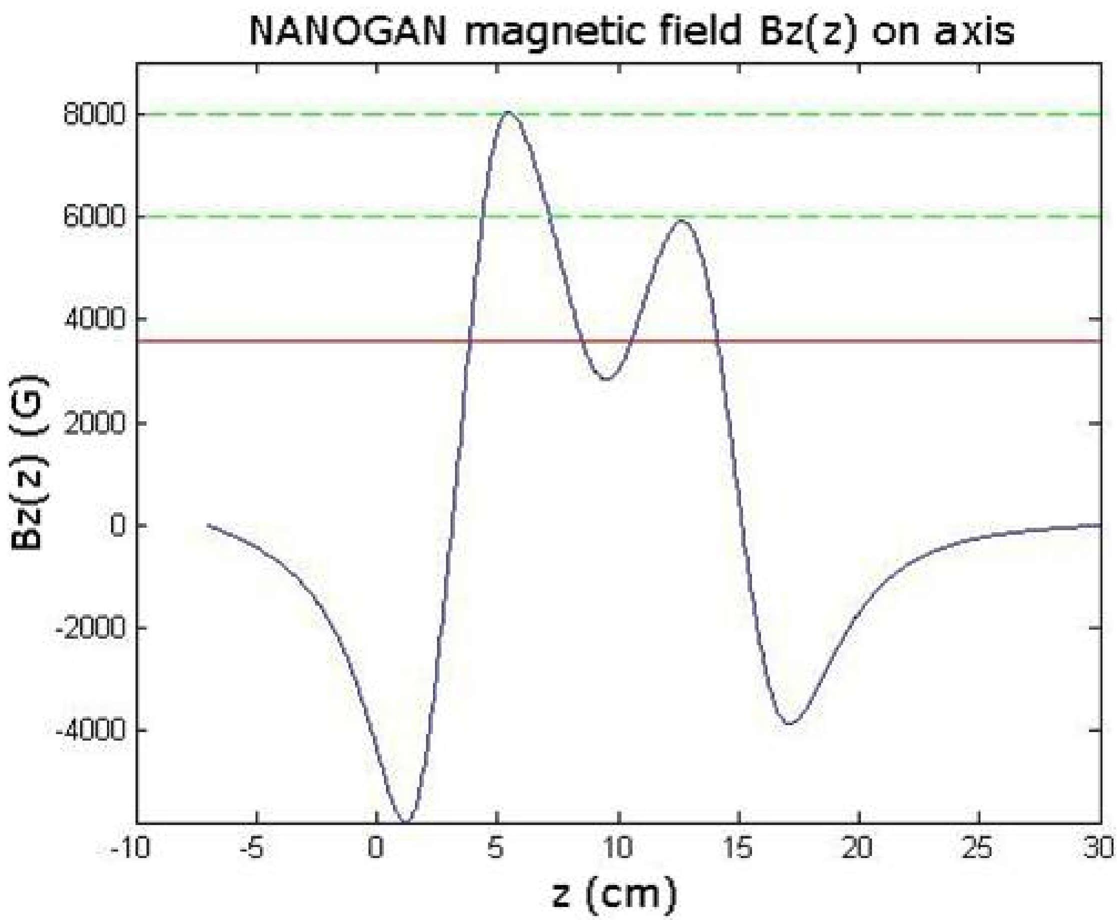

Figure 7.12: NANOGAN - $B_z(z)$ on axis. As is typical for permanent magnets, the field (here in Gauss) becomes negative, before going to zero. The plasma volume is located between the two peaks in the middle.

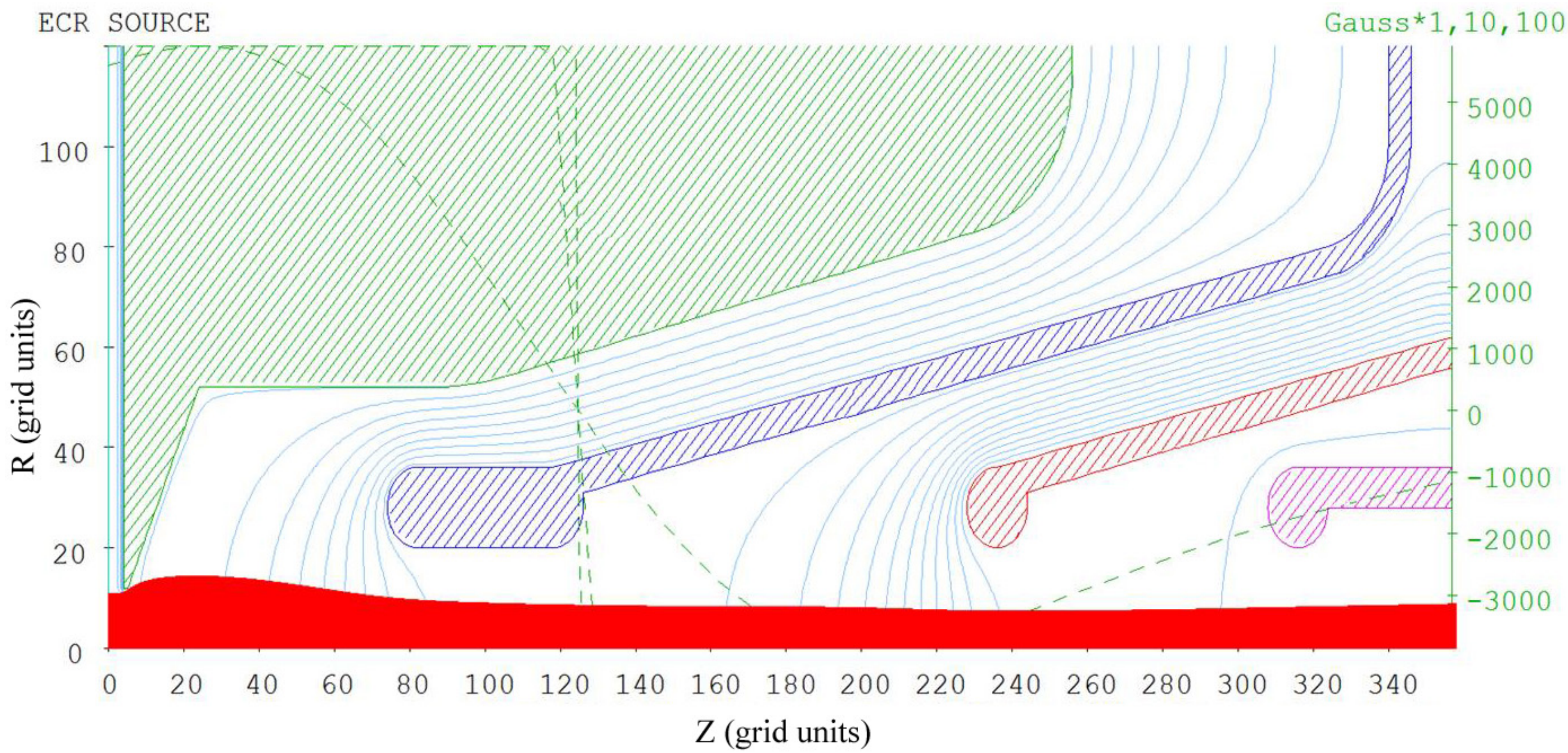

Figure 7.13: IGUN simulation - Trajectory plot. The electrode voltages (from left to right) are: Plasma electrode = 19 kV, puller electrode = 10 kV, electron repeller = -2 kV, ground electrode = 0 kV. The axes are in grid units (1 gu = 0.25 mm). The magnetic field (secondary axis) is shown as a green dashed line.

As a first step, the original diode system (see figure 7.7, top) was simulated for a plasma aperture diameter of 7 mm and extracted current of 1.5 mA (He^{1+} + He^{2+} combined) as found in literature to NANOGAN. The obtained normalized RMS emittance of 0.067 mm-mrad compares reasonably well with the 0.089 mm-mrad quoted for NANOGAN-II (cf. Section 7.2.2) considering that the factor 4 used to transform from 99% to RMS emittance is valid only for K-V beams and could easily be higher for realistic beams (meaning the RMS value of 0.089 could easily be lower). As it became clear that the diode system did not produce sufficient beam quality, the tetrode system (see Figure 7.7, bottom) was used in IGUN with a plasma aperture diameter of 6 mm. The resulting laminar beam flow can be seen in Figure 7.13. The final beam diameter for $^4He^{1+}$ at z = 88.25 mm (where particles are loaded into WARP) was 4.38 mm (∼34% smaller than with diode) with a normalized RMS emittance of 0.0527 mm-mrad (comparable to diode system) and a beam current of 0.92 mA.

7.4.2 Front End and Accelerator Tube

This part of the simulations was carried out with WARP [36] in XY slice mode (cf. Subsection 3.1.3). This means space-charge is taken into account, but only in the two transversal directions (x,y). Longitudinal space-charge effects are assumed to be negligible, because the beam is continuous. An overview of the system can be seen in Figure 7.10. Particle distributions (10000 macro-particles per species) are obtained from the previous IGUN simulations and loaded into WARP at z = 88.25 mm after the plasma aperture of the source.

All the electrostatic fields (einzel lens, immersion lens, accelerator column, electrostatic quadrupole triplets) were calculated by modeling the electrodes in WARP and calculating the fields beforehand in 3D mode with 4-fold symmetry (only a quarter has to be calculated due to symmetry of the elements). The magnetic field of the 30°dipole was calculated beforehand in 3D as well, using the finite element software Opera3d [121]. The magnetic field was then transformed into Frenet-Serret coordinates [42, pp. 22] (coordinate system that follows the ideal particle trajectory through the magnet) and saved to a file. The transformation is necessary because WARP also transforms the coordinates inside a bending element to follow the design trajectory (cf. subsection 3.1.3). The 90°dipole was approximated by using WARP's internal hard-edge model.

The particle transport simulation was carried out by setting up the simulation space, loading the respective fields and the particles and running the simulation step-by-step. The results were analyzed with the PostProcessor (cf. Subsection 3.2). Field calculation and particle transport during tuning of the elements were done in 2 mm/grid-cell resolution and then confirmed with a higher resolution of 1 mm/grid-cell.

Four test cases were picked to represent the wide range of desired beam energies:

- **14B**: $^{4}He^{1+}$, 3 MeV
- **15B**: $^{4}He^{1+}$, 1 MeV
- **16B**: $^{4}He^{1+}$, 300 keV
- **17B**: $^{12}C^{2+}$, 600 keV

Table 7.5 lists the relevant settings of source, einzel lens, and electrostatic quadrupole triplets (ESQ1-A/B/C, ESQ2-A/B/C) for the four different cases. Beam contaminants were taken into account as well ($^{4}He^{2+}$ in 14B, 15B, 16B; $^{4}He^{1+/2+}$ and $^{12}C^{1+/3+/4+/5+}$ in 17B).

Table 7.5: Simulations - Test case parameters. (case numbers kept consistent with other documentation) The number of shorted rings corresponds to the positions in Figure 7.9.

Parameter	**Case 14B**	**Case 15B**	**Case 16B**	**Case18B**
HV terminal (kV)	2981	981	281	281
Source (kV)	19	19	19	19
Einzel Lens (kV)	15.15	15.15	15.15	15.90
Shorting (# of rings)	0	90	114	114
ESQ1-A (kV)	0.0	0.0	6.0	6.0
ESQ1-B (kV)	0.0	0.0	6.0	6.0
ESQ1-C (kV)	0.0	0.0	5.25	5.25
ESQ2-A (kV)	26.0	11.0	3.1	3.1
ESQ2-B (kV)	30.0	11.0	3.1	3.1
ESQ2-C (kV)	36.5	11.8	3.35	3.3

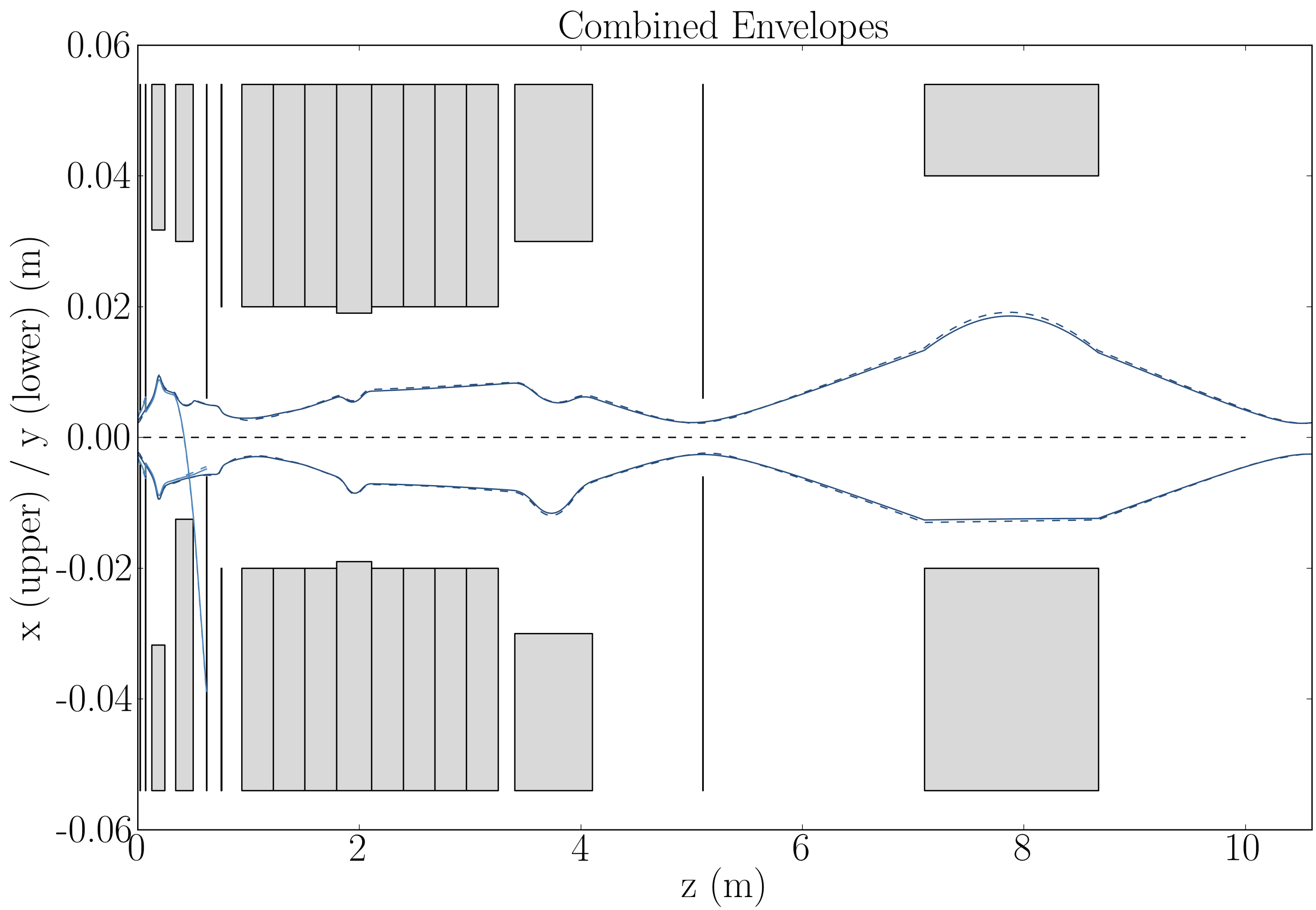

Figure 7.14: DIANA - WARP simulation results of a 300 keV $^{4}He^{1+}$ beam: Horizontal (upper half) and vertical (lower half) beam envelopes.

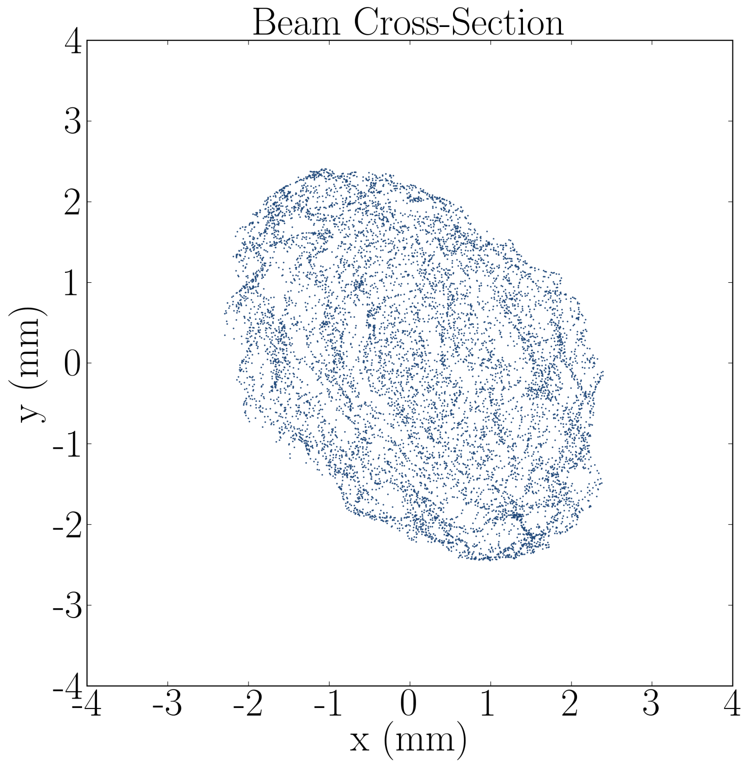

Figure 7.15: DIANA - WARP simulation results of a 300 keV $^4He^{1+}$ beam: Cross section.

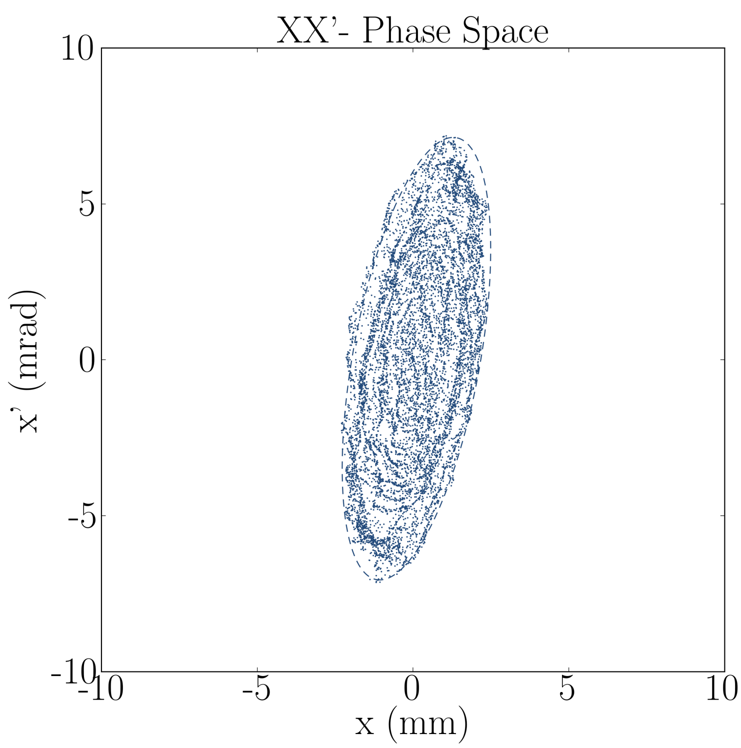

Figure 7.16: DIANA - WARP simulation results of a 300 keV $^4He^{1+}$ beam: Horizontal phase space.

As an example, the resulting beam envelopes for case 16B ($^{4}He^{1+}$, 300 keV) are shown in Figure 7.14 and the beam cross-section and horizontal phase space in Figures 7.15 and 7.16. The results (beam size, emittance, and filling of the dipole) are listed in Table 7.6.

Conservatively, the simulations can be summarized to: The presented setup is able to create and transport $^{4}He^{1+}$ beams of up to 850 μA beam current in the regime of 300 keV - 3 MeV to the image point of the 90° dipole, with normalized RMS emittances < 0.06 mm-mrad and diameters < 5 mm, filling the 90° dipole less than 75%.

Table 7.6: DIANA simulations - test case results. In case 16B it can be seen that the beam current decreases by ~ 7% du to the use of a collimator. The beam diameters are <5 mm, and no case fills the 90° dipole more than 75%. (case numbers kept consistent with other documentation)

Parameter	**Case 14B**	**Case 15B**	**Case 16B**	**Case18B**
Energy (keV)	3000	1000	300	600
Initial Current (mA)	0.92	0.92	0.92	0.25
Final Current (mA)	0.92	0.92	0.86	0.24
$\varepsilon^{xx'\text{-norm-rms}}$ **(mm-mrad)**	0.048	0.049	0.045	0.033
$\varepsilon^{yy'\text{-norm-rms}}$ **(mm-mrad)**	0.055	0.054	0.051	0.036
X-diameter (mm)	3.0	3.3	4.7	3.8
Y-diameter (mm)	3.5	2.8	4.8	3.6
90° **dipole fill**	35 %	70 %	68 %	75 %

7.5 Conclusion

The DIANA high energy accelerator presented an interesting opportunity to use the experience obtained during the earlier parts of this thesis, the same simulation software, and the utility programs developed in this thesis, to model and improve a commercial 3 MV electrostatic accelerator system. The requirements for the DIANA high energy accelerator are to deliver H^{1+} and He^{1+} beams of close to 1 emA beam current throughout the energy range of 300 keV to 3 MeV, as well as selected heavier ions at lower currents. In order to achieve this, extensive simulations using IGUN and WARP have been performed and custom modifications were proposed to the vendor (NEC). Good communication with the vendor was established and, after going through a few design iterations, a final version was approved for technical feasibility by the vendor. It is an off-the-shelf model of a 3 MV NEC Pelletron with modified ion source extraction system, an adjusted voltage gradient in the first unit of the accelerator column, shorting rod technique, and an additional electrostatic quadrupole triplet inside the column. Simulations of four test cases were carried out in order to test the final version of the modified accelerator. It could be shown that this design is able to deliver beams close to the DIANA requirements. Only in the case of the lowest energy the maximum obtainable beam current is reduced due to the use of a collimation system for preserving beam quality. The particle distributions created in this work were used by another group in the DIANA collaboration to simulate the final transport of the beam to the targets with good results. DIANA has concluded the preliminary design report (PDR) stage and a proposal for a 6-year plan to build and commission the facility is being put forward at the moment.

Chapter 8

Conclusion

As discussed in the introduction, simulations are an important tool for designing and testing extraction systems and LEBT systems for ECR ion sources. In order to be able to accurately simulate these, the initial conditions inside the plasma need to be known. Furthermore, a triangular structure of the beam due to the sextupole confinement field, multispecies extraction and the presence of a strong solenoidal magnetic field at the plane of extraction increase the difficulty of such extraction simulations. To accurately transport the ion beam through the LEBT, the level of space charge compensation needs to be known. I addressed these concerns and challenges through novel simulation methods and measurements. The following summary and outlook are essentially recapitulations of the respective conclusion sections at the end of the major chapters of the thesis.

8.1 Summary

8.1.1 Space Charge Compensation Measurements

To answer the question about space charge compensation in typical ECRIS LEBT systems, I presented neutralization measurements at two different locations: in the beam line of the LEDA injector source and in the beam line of the SuSI superconducting ECRIS.

The LEDA measurements agree with previous measurements at the same source with a similar detector and show neutralization values around 80-90 %, which depend on beam intensity. It is possible to calculate the beam radius from the RFA spectra alongside the neutralization. In case of the LEDA source this yielded very large beam radii which could not be explained. A similar discrepancy showed up in previous measurements at the same source by Ferdinand *et al.* [7]. Theoretical calculations using reasonable beam radii compared well with the measured neutralization, however.

The measurements in the beam line of SuSI suggest overall low neutralization factors (0 % - 50 %) which compare reasonably well with the theoretical model introduced by Gabovich [51] and discussed in detail in Chapter 2. They follow the prediction of higher neutralization with higher residual gas pressure, larger beam radii and higher beam density. For typical ECRIS LEBT settings, where the beam line pressure is kept as low as possible to prevent losses due to charge exchange, this means very low neutralization factors and beam lines should be designed accordingly. The reasonable agreement of the model with the measurements suggested incorporating the simple theoretical treatment into the simulation of low energy beam transport.

8.1.2 ECRIS Extraction and Beam Line Simulations

In this chapter, I presented the three parts of the ECRIS extraction suite using the particle in cell code WARP. The initial conditions are obtained semi-empirically from plasma markings inside the source. The particles are then extracted from the plasma by means of a relaxation process in which the steady state solution and the plasma meniscus form self-consistently. The hybrid RZ-3D model called 2D+ saves computation time and space and compares reasonably well with full 3D simulations. The use of the same simulation code (WARP) for the two parts of the ion source simulation and the beam transport together with a number of python utility programs and GUI's lets the user seamlessly go from one step to the next thereby obtaining a end-to-end simulation of an ECRIS driven accelerator frontend. As will be shown in chapter 7 sometimes it is even possible to include the accelerator into the simulation.

First tests of the extraction simulations with uranium and helium beams extracted from VENUS suggest the simulation model can be used for medium to heavy ions of medium to high charge states, but the approach to obtain the initial conditions breaks down for very light singly ionized ions. A more self-consistent model of the plasma as e.g. suggested by Mironov *et al.* [20] might help obtaining more realistic initial distributions for the subsequent extraction simulation.

The implementation of the multispecies extension of the formula derived by Gabovich *et al.* [51] as part of the LEBT beam transport simulation yielded promising first results and gave interesting insights in the distribution of space charge compensation along the beam line. It might be possible that in the region before the analyzing magnet, space charge compensation is as high as 90% due to the high beam current and large average beam radius. This has to be confirmed by future measurements, though.

8.1.3 The DIANA High Energy Accelerator

The DIANA high energy accelerator presented an interesting opportunity to use the experience obtained during the earlier parts of this thesis, the same simulation software, and the utility programs developed in this thesis, to model and improve a commercial 3 MV electrostatic accelerator system. The requirements for the DIANA high energy accelerator are to deliver H^{1+} and He^{1+} beams of close to 1 emA beam current throughout the energy range of 300 keV to 3 MeV, as well as selected heavier ions at lower currents. In order to achieve this, extensive simulations using IGUN and WARP have been performed and custom modifications were proposed to the vendor (NEC). Good communication with the vendor was established and, after going through a few design iterations, a final version was approved for technical feasibility by the vendor. It is an off-the-shelf model of a 3 MV NEC Pelletron with modified ion source extraction system, an adjusted voltage gradient in the first unit of the accelerator column, shorting rod technique, and an additional electrostatic quadrupole triplet inside the column. Simulations of four test cases were carried out in order to test the final version of the modified accelerator. It could be shown that this design is able to deliver beams close to the DIANA requirements. Only in the case of the lowest energy the maximum obtainable beam current is reduced due to the use of a collimation system for preserving beam quality. The particle distributions created in this work were used by another group in the DIANA collaboration to simulate the final transport of the beam to the targets with good results. DIANA has concluded the preliminary design report (PDR) stage and a proposal for a 6-year plan to build and commission the facility is being put forward at the moment.

8.2 Outlook

Whenever a question is answered, at least two more arise and so it is not surprising that there are a number of possibilities to continue this work.

8.2.1 Space Charge Compensation Measurements

As pointed out in Section 5.4, the data sets taken at the two additional locations (Artemis beam line, SuSI diagnostic box Q001) may still yield useful results upon further investigation and especially the SuSI/Q001 data might result in a validation of the 90% neutralization predicted by the simple Gabovich formula. The analysis methods presented in this chapter can be extended to accommodate multispecies ion beams and similar collimator transmission curves as used in the LEDA injector source analysis can be obtained for SuSI Q001. Preliminary analysis of data from the two locations suggests similar findings as at the other locations (neutralization of 0% to 50% depending on beam size, beam current, and residual gas pressure).

In order to settle questions of beam aspect ratio and to improve the statistics of the measurement by increasing the total measured current, a second identical detector put perpendicular or under 45°to the existing detector might prove useful. The beam current monitors used at the NSCL already provide two input channels and electron suppressor (V_3) as well as retarding field (V_2) could be provided in parallel by the same power supplies. Q014 in the SuSI beam line with the perpendicular ports for the Allison emittance scanners would be an ideal starting point.

The RFA setup as it is is certainly improvable as well. Possible changes that could benefit the setup are

- Applying a bias to the collector plate to suppress oscillations.
- Exploring the option of heating the detector in order to suppress insulating film deposition on the grids.
- Trying different combinations of apertures in the collimation system (e.g. taking out the inner aperture, using smaller apertures).

In addition, one might envision the use of NeMo as non-invasive beam diagnostic device. If all processes are well understood and pressure and residual gas composition are known, a

RFA could be used to measure the beam current, beam radius, and beam stability.

8.2.2 ECRIS Extraction and Beam Line Simulations

While progress has been made in this thesis towards obtaining realistic initial particle distributions, they are still an approximation based on measured plasma markings. Here it would be a great step forward to use the results of realistic ECR plasma simulations as initial conditions which can self-consistently provide triangular distributions of varying size for the different ion species according to the plasma parameters. Since arbitrary particle distributions can readily be loaded into the simulation, the extraction simulation and beam transport could immediately be upgraded if a working plasma model was presented.

The theoretical model for the neutralization of multispecies ion beams would greatly benefit from a further generalization to beams with different beam radii for each species. Unfortunately, this is not a trivial task and maybe even the scope of another PhD thesis.

Of course, the GUI programs developed for the ECRIS WARP simulations can be extended in any number of ways from conveniently shifting electrodes in the electrode designer to a full-blown GUI frontend for WARP, the possibilities are endless.

8.2.3 The DIANA High Energy Accelerator

Unfortunately, a few weeks ago, the decision was made to discontinue the DIANA project for now. At this point I can only say: I really hope funding will be found at some point, this is a great project!

APPENDICES

Publications and Proceedings

Papers and Refereed Proceedings

2012

Progress towards the development of a realistic electron cyclotron resonance ion source extraction model
D. Winklehner, D. Leitner, J. Y. Benitez, C. M. Lyneis, M. M. Strohmeier
Rev. Sci. Instrum. 83, 02B706 (2012)

DIANA - A Deep Underground Accelerator for Nuclear Astrophysics Experiments
D. Winklehner, A. Lemut, D. Leitner, M. Couder, A. Hodgkinson, M. Wiescher
AIP Proceedings CAARI (2012)

2011

Ion beam properties for ECR ion source injector systems
D. Leitner, D. Winklehner, M. Strohmeier
JINST 6 P07010 (2011) (http://jinst.sissa.it/jinst/)

Design of a 400 kV deep underground, high detector efficiency, high target density, high beam intensity accelerator facility
A. Lemut, M. Couder, D. Winklehner, U. Greife, A. Hodgkinson, D. Leitner, M. Leitner, J. S. Saba, P. A. Vetter, W. L. Waldron, M. Wiescher
Phys. Rev. ST Accel. Beams 14, 100101 (2011)

2010

Comparison of extraction and beam transport simulations with emittance measurements from the ECR ion source VENUS

D. Winklehner, D. Todd, J. Benitez, M. Strohmeier, D. Grote and D. Leitner
JINST 5 P12001 (2010) (http://jinst.sissa.it/jinst/)

Conferences and Workshops

2012

Space Charge Compensation Measurements of Multi-charged Ion Beams Extracted from ECR Ion Sources
D. Winklehner, D. Leitner, G. Machicoane, F. Marti, D. Cole, L. Tobos
Oral presentation: 20th Int. Workshop on ECR Ion Sources (ECRIS 2012) Sydney, Australia (2012)

DIANA - A Deep Underground Ion Accelerator for Nuclear Astrophysics Experiments
D. Winklehner, A. Lemut, D. Leitner, M. Couder, A. Hodgkinson, M. Wiescher
Oral presentation: MSU Graduate Academic Conference, East Lansing, USA (2012)

2011

ECRIS extraction and LEBT simulations with the PIC code WARP
D. Winklehner, D. Leitner
Poster: 3rd DITANET School on beam diagnostics, Stockholm, Sweden (2011)

2010

Plasma-to-target WARP simulations of Uranium beams extracted from VENUS compared to emittance measurements and beam images
D. Winklehner, D. Todd, D.Grote, D. Leitner, J. Benitez, M. Strohmeier
Oral Presentation: 19th International Workshop on ECR Ion Sources (ECRIS 2010) Grenoble, France (2010)

Comparison of extraction and beam transport simulations with emittance measurements from the ECR ion source VENUS
D. Winklehner, D. Todd, D. Grote, D. Leitner, J. Benitez, M. Strohmeier, F. Aumayr
Poster: 14th Beam Instrumentation Workshop (BIW 2010), Santa Fe, NM, USA (2010)

DIANA - Resistor Values

The full set of resistor values, both for the idealized case where all values are unique and the practical case that approximates the ideal case piecewise linearly by using only 5 different resistor values (not counting immersion lens), is shown here in Table 1.

Table 1: DIANA - Resistor values.

Element #	**Z** (m)	**R ideal** (normalized to 1)	**R practical** (MΩ)
Total	-	1	-
Immersion lens	0.00025	0.013418	734
1	0.01320	0	0
2	0.02615	0.000498	40
3	0.03910	0.000756	40
4	0.05205	0.000899	40
5	0.06500	0.001006	75
6	0.07795	0.001095	75
7	0.09090	0.001171	75
8	0.10385	0.001238	75
9	0.11680	0.001298	75
10	0.12975	0.001354	75
11	0.14270	0.001405	75
12	0.15565	0.001452	75
13	0.16860	0.001497	100
14	0.18155	0.001539	100
15	0.19450	0.001579	100
16	0.20745	0.001618	100
17	0.22040	0.001654	100

Continued on next page...

Table 1 (cont'd)

Element #	Z (m)	R (norm.)	R (MΩ)
18	0.23335	0.001689	100
19	0.24630	0.001722	100
20	0.25925	0.001754	100
21	0.27220	0.001785	100
22	0.28515	0	0
23	0.28515	0	0
24	0.29810	0	0
25	0.31105	0.001816	124
26	0.32400	0.001845	124
27	0.33695	0.001873	124
28	0.34990	0.001900	124
29	0.36285	0.001927	124
30	0.37580	0.001953	124
31	0.38875	0.001978	124
32	0.40170	0.002002	124
33	0.41465	0.002026	124
34	0.42760	0.002050	124
35	0.44055	0.002073	124
36	0.45350	0.002095	124
37	0.46645	0.002117	124
38	0.47940	0.002138	124
39	0.49235	0.002160	124
40	0.50530	0.002180	124
41	0.51825	0.002200	124
42	0.53120	0.002220	124
43	0.54415	0.002240	124
44	0.55710	0.002259	124
45	0.57005	0	0
46	0.57005	0	0
47	0.58300	0	0
48	0.59595	0.009185	555
49	0.60890	0.009185	555
50	0.62185	0.009185	555

Continued on next page...

Table 1 (cont'd)

Element #	**Z (m)**	**R (norm.)**	**R (MΩ)**
51	0.63480	0.009185	555
52	0.64775	0.009185	555
53	0.66070	0.009185	555
54	0.67365	0.009185	555
55	0.68660	0.009185	555
56	0.69955	0.009185	555
57	0.71250	0.009185	555
58	0.72545	0.009185	555
59	0.73840	0.009185	555
60	0.75135	0.009185	555
61	0.76430	0.009185	555
62	0.77725	0.009185	555
63	0.79020	0.009185	555
64	0.80315	0.009185	555
65	0.81610	0.009185	555
66	0.82905	0.009185	555
67	0.84200	0.009185	555
68	0.85495	0	0
69	1.17205	0	0
70	1.18500	0	0
71	1.19795	0.009185	555
72	1.21090	0.009185	555
73	1.22385	0.009185	555
74	1.23680	0.009185	555
75	1.24975	0.009185	555
76	1.26270	0.009185	555
77	1.27565	0.009185	555
78	1.28860	0.009185	555
79	1.30155	0.009185	555
80	1.31450	0.009185	555
81	1.32745	0.009185	555
82	1.34040	0.009185	555
83	1.35335	0.009185	555

Continued on next page...

Table 1 (cont'd)

Element #	Z (m)	R (norm.)	R (MΩ)
84	1.36630	0.009185	555
85	1.37925	0.009185	555
86	1.39220	0.009185	555
87	1.40515	0.009185	555
88	1.41810	0.009185	555
89	1.43105	0.009185	555
90	1.44400	0.009185	555
91	1.45695	0	0
92	1.45695	0	0
93	1.46990	0	0
94	1.48285	0.009185	555
95	1.49580	0.009185	555
96	1.50875	0.009185	555
97	1.52170	0.009185	555
98	1.53465	0.009185	555
99	1.54760	0.009185	555
100	1.56055	0.009185	555
101	1.57350	0.009185	555
102	1.58645	0.009185	555
103	1.59940	0.009185	555
104	1.61235	0.009185	555
105	1.62530	0.009185	555
106	1.63825	0.009185	555
107	1.65120	0.009185	555
108	1.66415	0.009185	555
109	1.67710	0.009185	555
110	1.69005	0.009185	555
111	1.70300	0.009185	555
112	1.71595	0.009185	555
113	1.72890	0.009185	555
114	1.74185	0	0
115	1.74185	0	0
116	1.75480	0	0

Continued on next page...

Table 1 (cont'd)

Element #	**Z (m)**	**R (norm.)**	**R (MΩ)**
117	1.76775	0.009185	555
118	1.78070	0.009185	555
119	1.79365	0.009185	555
120	1.80660	0.009185	555
121	1.81955	0.009185	555
122	1.83250	0.009185	555
123	1.84545	0.009185	555
124	1.85840	0.009185	555
125	1.87135	0.009185	555
126	1.88430	0.009185	555
127	1.89725	0.009185	555
128	1.91020	0.009185	555
129	1.92315	0.009185	555
130	1.93610	0.009185	555
131	1.94905	0.009185	555
132	1.96200	0.009185	555
133	1.97495	0.009185	555
134	1.98790	0.009185	555
135	2.00085	0.009185	555
136	2.01380	0.009185	555
137	2.02675	0	0
138	2.02675	0	0
139	2.03970	0	0
140	2.05265	0.009185	555
141	2.06560	0.009185	555
142	2.07855	0.009185	555
143	2.09150	0.009185	555
144	2.10445	0.009185	555
145	2.11740	0.009185	555
146	2.13035	0.009185	555
147	2.14330	0.009185	555
148	2.15625	0.009185	555
149	2.16920	0.009185	555

Continued on next page...

Table 1 (cont'd)

Element #	**Z (m)**	**R (norm.)**	**R (MΩ)**
150	2.18215	0.009185	555
151	2.19510	0.009185	555
152	2.20805	0.009185	555
153	2.22100	0.009185	555
154	2.23395	0.009185	555
155	2.24690	0.009185	555
156	2.25985	0.009185	555
157	2.27280	0.009185	555
158	2.28575	0.009185	555
159	2.29870	0.009185	555
160	2.31165	0	0

BIBLIOGRAPHY

BIBLIOGRAPHY

[1] A. Müller and E. Salzborn, "Scaling of cross sections for multiple electron transfer to highly charged ions colliding with atoms and molecules," *Physics Letters A*, vol. 62, no. 6, pp. 391 – 394, 1977.

[2] P. Zavodszky, B. Arend, D. Cole, J. DeKamp, G. Machicoane, F. Marti, P. Miller, J. Moskalik, J. Ottarson, J. Vincent, and A. Zeller, "Design of SuSI - superconducting source for ions at nscl/msu - ii. the conventional parts," *Nuclear Instruments and Methods in Physics Research Section B: Beam Interactions with Materials and Atoms*, vol. 241, no. 1 - 4, pp. 959 – 964, 2005.

[3] D. Leitner, C. Lyneis, S. Abbott, D. Collins, R. Dwinell, M. Galloway, M. Leitner, and D. Todd, "Next generation ECR ion sources: First results of the superconducting 28 ghz ECRIS VENUS," *Nuclear Instruments and Methods in Physics Research Section B: Beam Interactions with Materials and Atoms*, vol. 235, no. 1 - 4, pp. 486 – 493, 2005.

[4] C. Braams, "Edge effect in charged-particle analyzing magnets," *Nuclear Instruments and Methods*, vol. 26, no. 0, pp. 83 – 89, 1964.

[5] W. Rogowski, "Die elektrische Festigkeit am Rande des Plattenkondensators," *Archiv für Elektrotechnik*, vol. 12, pp. 1–15, 1923.

[6] PANTECHNIK, "Pantechnik.com - Equipment for particle accelerators - ECR ion sources." `http://www.pantechnik.com/`, Accessed: January 2013.

[7] R. Ferdinand, J. Sherman, R. R. Stevens Jr, and T. Zaugg, "Space-charge neutralization measurement of a 75-keV, 130-mA hydrogen-ion beam," in *Particle Accelerator Conference, 1997. Proceedings of the 1997*, vol. 3, pp. 2723–2725, IEEE, 1997.

[8] D. Leitner, C. M. Lyneis, T. Loew, D. S. Todd, S. Virostek, and O. Tarvainen, "Status report of the 28 GHz superconducting electron cyclotron resonance ion source VENUS (invited)," *Review of Scientific Instruments*, vol. 77, no. 3, p. 03A302, 2006.

[9] M. Leitner, D. C. Wutte, and C. Lyneis, "Design of the extraction system of the superconducting ECR ion source VENUS," in *Particle Accelerator Conference, 2001. PAC 2001. Proceedings of the 2001*, vol. 1, pp. 67–69 vol.1, 2001.

[10] T. Zaugg, C. Rose, J. Schneider, J. Sherman, and R. Stevens Jr, "Operation of a microwave proton source in pulsed mode," in *Proc. LINAC98 (Chicago, 24-28 August 1998) pp*, pp. 893–895, 1998.

[11] G. Machicoane, D. Cole, J. Ottarson, J. Stetson, and P. Zavodszky, "ARTEMIS-B: A room-temperature test electron cyclotron resonance ion source for the national superconducting cyclotron laboratory at michigan state university," *Review of Scientific Instruments*, vol. 77, no. 3, p. 03A322, 2006.

[12] D. Leitner, D. Winklehner, and M. Strohmeier, "Ion beam properties for ecr ion source injector systems," *Journal of Instrumentation*, vol. 6, no. 07, p. P07010, 2011.

[13] P. Sortais, C. Bieth, P. Foury, N. Lecesne, R. Leroy, J. Mandlin, C. Marry, J. Pacquet, E. Robert, and A. Villari, "Developments of compact permanent magnet ecris," in *Proceedings of the 12th International Workshop on ECR Ion Sources (RIKEN, Institute for Nuclear Study, University of Tokyo, Tanashi, Tokyo 188, Japan)*, pp. 44–52, 1995.

[14] R. Geller, *Electron cyclotron resonance ion sources and ECR plasmas*. Taylor & Francis Group, 1996.

[15] R. York, G. Bollen, M. Doleans, W. Hartung, M. Johnson, G. Machicoane, F. Marti, X. Wu, Q. Zhao, S. Assadi, *et al.*, "Status and plans for the facility for rare isotope beams at michigan state university," in *Proceedings of the XXV Linear Accelerator Conference (LINAC10)*, pp. 12–17, 2010.

[16] D. Leitner, J. Benitez, M. Galloway, T. Loew, C. Lyneis, D. Todd, and L. Berkeley, "Progress and perspective for high frequency, high performance superconducting ecr ion sources," in *18th Int. Conf. Cyclotron and Their Applications, Giardini Naxos*, p. 265, 2007.

[17] C. M. Lyneis, D. Leitner, D. S. Todd, G. Sabbi, S. Prestemon, S. Caspi, and P. Ferracin, "Fourth generation electron cyclotron resonance ion sources (invited)," *Review of Scientific Instruments*, vol. 79, no. 2, p. 02A321, 2008.

[18] C. Lyneis, J. Benitez, D. Leitner, J. Noland, M. Strohmeier, H. Koivisto, and O. Tarvainen, "Charaterization of the microwave coupling to the plasma chamber of the lbl ecr ion source," *Proceedings of ECRIS'10*, pp. 162–164, 2010.

[19] C. Lyneis, B. J, M. Strohmeier, and T. D, "Coupling microwave power into ecr ion source plasmas at frequencies above 20 ghz," in *Proceedings of the 20th International Workshop on Electron Cyclotron Resonance Ion Sources (ECRIS'12)*, 2012.

[20] V. Mironov and J. P. M. Beijers, "Three-dimensional simulations of ion dynamics in the plasma of an electron cyclotron resonance ion source," *Phys. Rev. ST Accel. Beams*, vol. 12, p. 073501, Jul 2009.

[21] S. Gammino, G. Ciavola, L. G. Celona, D. Mascali, and F. Maimone, "Numerical simulations of the ecr heating with waves of different frequency in electron cyclotron resonance ion sources," *Plasma Science, IEEE Transactions on*, vol. 36, no. 4, pp. 1552–1568, 2008.

[22] P. Suominen, O. Tarvainen, and H. Koivisto, "The effects of gas mixing and plasma electrode position on the emittance of an electron cyclotron resonance ion source," *Review of scientific instruments*, vol. 75, no. 5, pp. 1517–1519, 2004.

[23] Y. Higurashi, T. Nakagawa, M. Kidera, T. Aihara, M. Kase, and Y. Yano, "Effect of plasma electrode position on the beam intensity of heavy ions from a riken 18 ghz electron cyclotron resonance ion source," *Review of scientific instruments*, vol. 73, no. 2, pp. 598–600, 2002.

[24] I. V. Izotov, A. V. Sidorov, V. A. Skalyga, V. G. Zorin, T. Lamy, L. Latrasse, and T. Thuillier, "Experimental and theoretical investigation of the preglow in ecris," *Plasma Science, IEEE Transactions on*, vol. 36, no. 4, pp. 1494–1501, 2008.

[25] O. Tarvainen, H. Koivisto, T. Ropponen, V. Toivanen, Y. Higurashi, and T. Nakagawa, "Time evolution of plasma potential in pulsed operation of ECRIS," in *19th International Workshop on ECR Ion Sources (ECRIS'10)*, 2010.

[26] V. Mironov, G. Shirkov, O. Strekalovsky, and N. Tokareva, "Exploration of the afterglow of the pulsed electron cyclotron resonance source under the injection of neutral fluxes," *Review of scientific instruments*, vol. 69, no. 2, pp. 1129–1131, 1998.

[27] P. Sortais, "Pulsed ecr ion source using the afterglow mode," *Review of scientific instruments*, vol. 63, no. 4, pp. 2801–2805, 1992.

[28] O. Tarvainen, P. Suominen, and H. Koivisto, "A new plasma potential measurement instrument for plasma ion sources," *Review of scientific instruments*, vol. 75, no. 10, pp. 3138–3145, 2004.

[29] C. Lyneis, D. Leitner, D. Todd, S. Virostek, T. Loew, A. Heinen, and O. Tarvainen, "Measurements of bremsstrahlung production and x-ray cryostat heating in venus," *Review of scientific instruments*, vol. 77, no. 3, pp. 03A342–03A342, 2006.

[30] J. Noland, O. Tarvainen, J. Benitez, D. Leitner, C. Lyneis, and J. Verboncoeur, "Studies of electron heating on a 6.4 ghz ecr ion source through measurement of diamagnetic current and plasma bremsstrahlung," *Plasma Sources Science and Technology*, vol. 20, no. 3, p. 035022, 2011.

[31] R. Becker, "Numerical simulation of ion-beam formation," *Review of scientific instruments*, vol. 67, no. 3, pp. 1132–1137, 1996.

[32] R. Becker and W. B. Herrmannsfeldt, "IGUN - A program for the simulation of positive ion extraction including magnetic fields," *Review of Scientific Instruments*, vol. 63, no. 4, pp. 2756–2758, 1992.

[33] R. Becker and W. B. Herrmannsfeldt, "The design of electron and ion guns, beams, and collectors," in *Journal of Physics: Conference Series*, vol. 2, p. 152, IOP Publishing, 2004.

[34] T. Kalvas, O. Tarvainen, T. Ropponen, O. Steczkiewicz, J. Arje, and H. Clark, "IBSIMU: A three-dimensional simulation software for charged particle optics," *Review of Scientific Instruments*, vol. 81, no. 2, pp. 02B703–02B703, 2010.

[35] P. Spädtke, "Kobra3-inp user manual, version 3.39," 2000.

[36] D. P. Grote, A. Friedman, J.-L. Vay, and I. Haber, "The WARP code: Modeling high intensity ion beams," in *16th Intern. Workshop on ECR Ion Sources* (M. Leitner, ed.), vol. 749, AIP, 2004.

[37] D. Leitner, M. L. Galloway, T. J. Loew, C. M. Lyneis, I. Castro Rodriguez, and D. S. Todd, "High intensity production of high and medium charge state uranium and other heavy ion beams with VENUS," *Review of Scientific Instruments*, vol. 79, no. 2, pp. 02C710–02C710, 2008.

[38] P. A. Zavodszky, B. Arend, D. Cole, J. DeKamp, G. Machicoane, F. Marti, P. Miller, J. Moskalik, J. Ottarson, J. Vincent, and A. Zeller, "Design of SuSI - superconducting source for ions at nscl/msu - i. the magnet system," *AIP Conference Proceedings*, vol. 749, no. 1, pp. 131–134, 2005.

[39] P. A. Zavodszky, B. Arend, D. Cole, J. DeKamp, G. Machicoane, F. Marti, P. Miller, J. Moskalik, J. Ottarson, J. Vincent, A. Zeller, and N. Y. Kazarinov, "Status report on the design and construction of the superconducting source for ions at the national superconducting cyclotron laboratory/michigan state university," *Review of Scientific Instruments*, vol. 77, no. 3, p. 03A334, 2006.

[40] P. A. Zavodszky, B. Arend, D. Cole, J. DeKamp, M. Doleans, G. Machicoane, F. Marti, P. Miller, J. Moskalik, W. Nurnberger, J. Ottarson, J. Vincent, X. Wu, and A. Zeller, "Design, construction, and first commissioning results of superconducting source for ions at nscl/msu," *Review of Scientific Instruments*, vol. 79, no. 2, p. 02A302, 2008.

[41] M. Reiser, *Theory and design of charged particle beams*. Weinheim: Wiley-VCH, 2 ed., 2008.

[42] H. Wiedemann, *Particle Accelerator Physics*. Berlin: Springer, 3 ed., 2007.

[43] S.-Y. Lee, *Accelerator physics*. World Scientific Publishing Company, 2004.

[44] I. Brown, ed., *The physics and technology of ion sources*. New York: John Wiley and Sons Inc., 1 ed., 1989.

[45] I. Brown, ed., *The physics and technology of ion sources*. Weinheim: Wiley-VCH, 2 ed., 2004.

[46] A. A. Vlasov, "On the kinetic theory of an assembly of particles with collective interaction," *J. Phys. (USSR)*, 1945.

[47] I. Kapchinsky and V. Vladimirsky, "Limitations of proton beam current in a strong focusing linear accelerator associated with strong space charge," in *Proc. of the II. Int. Conf. on High Energy Accel*, 1959.

[48] I. Soloshenko, "Physics of ion beam plasma and problems of intensive ion beam transportation (invited)," *Review of scientific instruments*, vol. 67, no. 4, pp. 1646–1652, 1996.

[49] I. Soloshenko, "Space charge compensation of technological ion beams," in *Discharges and Electrical Insulation in Vacuum, 1998. Proceedings ISDEIV. XVIIIth International Symposium on Discharges and Electrical Insulation in Vacuum*, vol. 2, pp. 675–678, IEEE, 1998.

[50] I. A. Soloshenko, "Transportation of intensive ion beams," *Review of scientific instruments*, vol. 69, no. 3, pp. 1359–1366, 1998.

[51] M. Gabovich, L. Katsubo, and I. Soloshenko, "Selfdecompensation of a stable quasineutral ion beam due to coulomb collisions," *Fiz. Plazmy*, vol. 1, pp. 304–309, 1975.

[52] M. D. Gabovich, "Ion-beam plasma and the propagation of intense compensated ion beams," *Soviet Physics Uspekhi*, vol. 20, no. 2, p. 134, 1977.

[53] J. D. Jackson, *Classical Electrodynamics*. John Wiley and Sons Inc., Hoboken, NJ, USA, 3 ed., 1999.

[54] I. H. Hutchinson, "Electromagnetic Interactions." Lecture Notes, MIT Open Courseware, 1999.

[55] C. Barnett, J. Ray, E. Ricci, M. Wilker, E. McDaniel, E. Thomas, and H. Gilbody, "Atomic data for controlled fusion research," tech. rep., Oak Ridge National Lab., TN (USA), 1977.

[56] R. Ito, T. Tabata, T. Shirai, and R. A. Phaneuf, "Analytic cross sections for collisions of H, H2, He and Li atoms and ions colliding with atoms and molecules.III." `http://www-jt60.naka.jaea.go.jp/english/JEAMDL/code/95008.html`, 1995.

[57] C. Barnett, H. Hunter, M. Kirkpatrick, I. Alvarez, and R. Phaneuf, "Atomic data for fusion. Collisions of H, H2, He and Li atoms and ions with atoms and molecules." `http://www-cfadc.phy.ornl.gov/redbooks/redbooks.html`, 1990.

[58] I. D. Kaganovich, E. A. Startsev, R. C. Davidson, S. R. Kecskemeti, A. Bin-Nun, D. Mueller, L. Grisham, R. L. Watson, V. Horvat, K. E. Zaharakis, and Y. Peng, "Ionization cross-sections for ion-atom collisions in high-energy ion beams," *Nuclear Instruments and Methods in Physics Research Section A: Accelerators, Spectrometers, Detectors and Associated Equipment*, vol. 544, no. 1 - 2, pp. 91 – 97, 2005.

[59] I. D. Kaganovich, E. A. Startsev, and R. C. Davidson, "Scaling cross sections for ion-atom impact ionization," *Physics of Plasmas*, vol. 11, no. 3, pp. 1229–1232, 2004.

[60] I. D. Kaganovich, E. A. Startsev, and R. C. Davidson, "Comparison of quantum-mechanical and classical trajectory calculations of cross sections for ion-atom impact ionization of negative and positive ions for heavy-ion fusion applications," *Phys. Rev. A*, vol. 68, p. 022707, Aug 2003.

[61] J. Thomson, "Xlii. ionization by moving electrified particles," *Philosophical Magazine Series 6*, vol. 23, no. 136, pp. 449–457, 1912.

[62] Z. Xie and C. Lyneis, "Two-frequency plasma heating in a high charge state electron cyclotron resonance ion source," *Review of scientific instruments*, vol. 66, no. 8, pp. 4218–4221, 1995.

[63] A. Girard, D. Hitz, G. Melin, and K. Serebrennikov, "Electron cyclotron resonance plasmas and electron cyclotron resonance ion sources: Physics and technology (invited)," *Review of Scientific Instruments*, vol. 75, no. 5, pp. 1381–1388, 2004.

[64] S. Gammino, G. Ciavola, R. Harkewicz, K. Harrison, A. Srivastava, and P. Briand, "Effects of frequency and magnetic field scaling on the superconducting electron cyclotron resonance ion source at msu-nscl," *Review of scientific instruments*, vol. 67, no. 12, pp. 4109–4113, 1996.

[65] P. Suominen, O. Tarvainen, H. Koivisto, and D. Hitz, "Optimization of the halbach-type magnetic multipole for an electron cyclotron resonance ion source," *Review of scientific instruments*, vol. 75, no. 1, pp. 59–63, 2004.

[66] G. Melin, A. G. Drentje, A. Girard, and D. Hitz, "Ion behavior and gas mixing in electron cyclotron resonance plasmas as sources of highly charged ions," *Journal of Applied Physics*, vol. 86, no. 9, pp. 4772–4779, 1999.

[67] A. Müller, E. Salzborn, R. Frodl, R. Becker, H. Klein, and H. Winter, "Absolute ionisation cross sections for electrons incident on O^+ , Ne^+ , Xe^+ and Ar^{i+} (i=1,...,5) ions," *Journal of Physics B: Atomic and Molecular Physics*, vol. 13, no. 9, p. 1877, 1980.

[68] W. Lotz, "An empirical formula for the electron-impact ionization cross-section," *Zeitschrift für Physik*, vol. 206, no. 2, pp. 205–211, 1967.

[69] W. Lotz, "Electron-impact ionization cross-sections and ionization rate coefficients for atoms and ions from hydrogen to calcium," *Zeitschrift für Physik*, vol. 216, no. 3, pp. 241–247, 1968.

[70] P. C. Stangeby, "The bohm-chodura plasma sheath criterion," *Physics of Plasmas*, vol. 2, no. 3, pp. 702–706, 1995.

[71] P. C. Stangeby, "The plasma sheath," *Physics of plasma-wall interactions in controlled fusion*, vol. 131, pp. 41–97, 1986.

[72] Z. Q. Xie, *The Effect of Space Charge Force on Beams Extracted from Ecr Ion Sources.* PhD thesis, Michigan State University, 1989.

[73] P. Allison, J. Sherman, and H. Smith Jr, "Comparison of measured emittance of an H^- ion beam with a simple theory," tech. rep., Los Alamos National Lab., NM (USA), 1981.

[74] A. Septier and edited by Albert Septier, *Focusing of charged particles*, vol. 1. Academic Press New York, 1967.

[75] W. Krauss-Vogt, H. Beuscher, H. Hagedoorn, J. Reich, and P. Wucherer, "Emittance and matching of ECR sources," *Nuclear Instruments and Methods in Physics Research Section A: Accelerators, Spectrometers, Detectors and Associated Equipment*, vol. 268, no. 1, pp. 5–9, 1988.

[76] T. Thuillier, J. C. Curdy, T. Lamy, A. Lachaize, A. Ponton, P. Sole, P. Sortais, and J. L. Vieux-Rochaz, "High current beam transport with Phoenix 28 GHz: Experiment and simulation," *AIP Conference Proceedings*, vol. 749, no. 1, pp. 41–46, 2005.

[77] D. Clark, "Emittance measurements on the LBL ECR source," in *International conference on ECR ion sources and their applications*, 1987.

[78] L. Panitzsch, M. Stalder, and R. F. Wimmer-Schweingruber, "Spatially resolved measurements of electron cyclotron resonance ion source beam profile characteristics," *Review of Scientific Instruments*, vol. 82, no. 3, pp. 033302–033302, 2011.

[79] D. Manura and D. A. Dahl, *SIMION 8.0 User Manual*. Scientific Instrument Services, 2007.

[80] D. P. Grote, *WARP Manual*, 2000.

[81] A. Friedman, D. P. Grote, and I. Haber, "Three dimensional particle simulation of heavy ion fusion beams," *Phys. Fluids B.*, vol. 4, p. 2203, 1992.

[82] A. Friedman and S. P. Auerbach, "Numerically induced stochasticity," *Journal of computational physics*, vol. 93, no. 1, pp. 171–188, 1991.

[83] T. E. Oliphant, *A Guide to NumPy*, vol. 1. Trelgol Publishing USA, 2006.

[84] J. D. Hunter, "Matplotlib: A 2d graphics environment," *Computing in Science & Engineering*, pp. 90–95, 2007.

[85] J. Finlay, "PyGTK 2.0 tutorial," *ozone-friendly. ru, Published April*, vol. 13, 2005.

[86] A. Tuininga, "cxFreeze." `http://cx-freeze.sourceforge.net/index.html`, Accessed: July 2013.

[87] C. Fai Chan, W. S. Cooper, J. W. Kwan, and W. F. Steele, "Dynamics of skew beams and the projectional emittance," *Nuclear Instruments and Methods in Physics Research Section A: Accelerators, Spectrometers, Detectors and Associated Equipment*, vol. 306, no. 1, pp. 112–122, 1991.

[88] T. Taylor and J. F. Mouris, "An advanced high-current low-emittance dc microwave proton source," *Nuclear Instruments and Methods in Physics Research Section A: Accelerators, Spectrometers, Detectors and Associated Equipment*, vol. 336, no. 1 - 2, pp. 1 – 5, 1993.

[89] J. Sherman, G. Bolme, L. Hansborough, D. Hodgkins, M. Light, E. Meyer, J. Schneider, H. Smith Jr, M. Stettler, R. Stevens Jr, *et al.*, "Development of a 110-mA, 75-keV proton injector for high-current, cw linacs," *Energy (keV)*, vol. 75, p. 75, 1996.

[90] J. Sherman, A. Arvin, L. Hansborough, D. Hodgkins, E. Meyer, J. D. Schneider, J. H. Vernon Smith, M. Stettler, J. Ralph R. Stevens, M. Thuot, T. Zaugg, and R. Ferdinand, "Status report on a dc 130 mA, 75 keV proton injector (invited)," *Review of Scientific Instruments*, vol. 69, no. 2, pp. 1003–1008, 1998.

[91] P. A. Zavodszky, H. Koivisto, D. Cole, and P. Miller, "Emittance studies of ARTEMIS - the new ECR ion source for the coupled cyclotron facility at NSCL/MSU," *AIP Conference Proceedings*, vol. 576, no. 1, pp. 619–622, 2001.

[92] H. Koivisto, J. DeKamp, and A. Zeller, "Cooling of the plasma chamber for the AECR-U type electron cyclotron resonance ion source ARTEMIS," *Nuclear Instruments and Methods in Physics Research Section B: Beam Interactions with Materials and Atoms*, vol. 174, no. 3, pp. 373 – 378, 2001.

[93] G. Machicoane, C. Benatti, D. Cole, M. Doleans, O. Kester, F. Marti, X. Wu, P. Zavodszky, and C. Zhang, "Performance investigation of the nscl 18 ghz superconducting ecr ion source susi," in *in Proceedings of the 2009 Particle Accelerator Conference (Vancouver, Canada 2009)*, 2009.

[94] M. A. Leitner, C. M. Lyneis, D. C. Wutte, C. E. Taylor, and S. R. Abbot, "Construction of the superconducting ECR ion source Venus," *Physica Scripta*, vol. 2001, no. T92, p. 171, 2001.

[95] C. M. Lyneis, D. Leitner, D. S. Todd, G. Sabbi, S. Prestemon, S. Caspi, and P. Ferracin, "Fourth generation electron cyclotron resonance ion sources (invited)," in *PROCEEDINGS OF 12TH INTERNATIONAL CONFERENCE ON ION SOURCES (ICIS 2007)*, vol. 79, p. 02A321, AIP, 2008.

[96] J. Bergoz, "Bergoz instrumentation." `http://www.bergoz.com`, Accessed: April 2013.

[97] G. F. Knoll, *Radiation detection and measurement.* Wiley, 2010.

[98] L. Y. Lin, C. Benatti, G. Perdikakis, D. Leitner, S. W. Krause, and J. Yurkon, "Scintillation degradation of yag: Ce under low-energy ion bombardment," *Journal of Instrumentation*, vol. 8, no. 01, p. P01001, 2013.

[99] J. Kolata and R. Surratt, "A rapid emittance scanner," *Nuclear Instruments and Methods*, vol. 87, no. 1, pp. 141 – 144, 1970.

[100] P. Rose, A. Wittkower, R. Bastide, and A. Galejs, "Quantitative measurements of ion beam properties," *Nuclear Instruments and Methods*, vol. 14, no. 0, pp. 79 – 82, 1962.

[101] P. H. Rose, R. P. Bastide, N. B. Brooks, J. Airey, and A. B. Wittkower, "Description of a device used to measure ion beam emittance," *Review of Scientific Instruments*, vol. 35, no. 10, pp. 1283–1285, 1964.

[102] P. W. Allison, J. D. Sherman, and D. B. Holtkamp, "An emittance scanner for intense low-energy ion beams," *Nuclear Science, IEEE Transactions on*, vol. 30, no. 4, pp. 2204–2206, 1983.

[103] H. R. Kremers, J. P. M. Beijers, and S. Brandenburg, "A pepper-pot emittance meter for low-energy heavy-ion beams," *Review of Scientific Instruments*, vol. 84, no. 2, p. 025117, 2013.

[104] M. Strohmeier, J. Benitez, D. Leitner, C. Lyneis, D. Todd, and M. Bantel, "Development of a pepper-pot device to determine the emittance of an ion beam generated by electron cyclotron resonance ion sources," *Review of Scientific Instruments*, vol. 81, no. 2, pp. 02B710–02B710–3, 2010.

[105] S. Kondrashev, A. Barcikowski, B. Mustapha, P. Ostroumov, and N. Vinogradov, "Development of a pepper pot emittance probe and its application for {ECR} ion beam studies," *Nuclear Instruments and Methods in Physics Research Section A: Accelerators, Spectrometers, Detectors and Associated Equipment*, vol. 606, no. 3, pp. 296 – 304, 2009.

[106] W. Hanson, D. Frame, and J. Midgley, "Errors in retarding potential analyzers caused by nonuniformity of the grid-plane potential," *Journal of Geophysical Research*, vol. 77, no. 10, pp. 1914–1922, 1972.

[107] W. Hanson, S. Sanatani, D. Zuccaro, and T. Flowerday, "Plasma measurements with the retarding potential analyzer on ogo 6," *Journal of Geophysical Research*, vol. 75, no. 28, pp. 5483–5501, 1970.

[108] Y. Sakai and I. Katsumata, "An energy resolution formula of a three plane grids retarding field energy analyzer," *Jpn. J. Appl. Phys*, vol. 24, p. 337, 1985.

[109] M. Newville and T. Stensitzki, "Lmfit-py: Least-squares minimization with constraints for python." `http://cars9.uchicago.edu/software/python/lmfit/index.html`, 2012.

[110] V. Afrosimov, G. Leiko, Y. A. Mamaev, and M. Panov, "Elementary processes of change of charge states in the interaction between protons and hydrogen molecules," *Soviet Physics JETP*, vol. 29, no. 4, 1969.

[111] J. Sherman, M. Olivo, and E. Mariani, "H^+ beam neutralization measurements at 870 keV beam energy," *Review of scientific instruments*, vol. 63, no. 4, pp. 2776–2778, 1992.

[112] V. Toivanen, O. Tarvainen, J. Komppula, and H. Koivisto, "Oscillations of ecr ion source beam current along the beam transport of the jyfl k-130 cyclotron," *Journal of Instrumentation*, vol. 8, no. 02, p. T02005, 2013.

[113] J. Sherman, E. Pitcher, and P. Allison, "H^- beam neutralization measurements with a gridded-energy analyzer, a noninterceptive beam diagnostic," tech. rep., Los Alamos National Lab., NM (USA), 1988.

[114] K. Poole, "Electrode contamination in electron optical systems," *Proceedings of the Physical Society. Section B*, vol. 66, no. 7, p. 542, 1953.

[115] J. Sherman, E. Pitcher, R. Stevens, and P. Allison, "H beam neutralization measurements in a solenoidal beam transport system," in *AIP Conference Proceedings*, vol. 287, p. 686, 1992.

[116] J. E. Boers, "An interactive version of the PBGUNS program for the simulation of axisymmetric and 2-D, electron and ion beams and guns," in *Particle Accelerator Conference, 1995., Proceedings of the 1995*, vol. 4, pp. 2312–2313, IEEE, 1995.

[117] L. Zhao, J. Kim, and B. Cluggish, "Modeling ecris plasma using 2d gem," in *ECRIS08 workshop, Chicago, IL*, 2008.

[118] D. Mascali, L. Neri, S. Gammino, L. Celona, G. Ciavola, N. Gambino, R. Miracoli, and S. Chikin, "Plasma ion dynamics and beam formation in electron cyclotron resonance ion sources," *Review of Scientific Instruments*, vol. 81, no. 2, pp. 02A334–02A334, 2010.

[119] S. Saminathan, *Extraction and transport of ion beams from an ECR ion source*. PhD thesis, University of Groningen, The Netherlands, 2011.

[120] D. S. Todd, D. Leitner, C. M. Lyneis, M. Leitner, J. Qiang, and D. P. Grote, "Comparison of particle-in-cell simulation with experiment for the transport system of the superconducting electron cyclotron resonance ion source venus," *RSI*, vol. 77, no. 03A338, 2006.

[121] OPERA3D, "Cobham plc: Aerospace and security, antenna systems, kidlington." `http://www.cobham.com/`, Accessed: February 2013.

[122] I. E. Software, "LORENTZ - Particle trajectory: 3D full-wave electromagnetic simulator." `http://www.integratedsoft.com/Products/Lorentz`, Accessed: July 2013.

[123] D. Todd, D. Leitner, C. M. Lyneis, and D. P. Grote, "Simulation and beamline experiments for the superconducting electron cyclotron resonance ion source venus," in *PROCEEDINGS OF 12TH INTERNATIONAL CONFERENCE ON ION SOURCES (ICIS 2007)*, vol. 79, p. 02A316, AIP, 2008.

[124] M. Leitner, D. Leitner, A. Lemut, P. Vetter, and M. Wiescher, "DIANA - A new, deep-underground accelerator facility for astrophysics experiments," tech. rep., Ernest Orlando Lawrence Berkeley National Laboratory, Berkeley, CA (US), 2009.

[125] A. Lemut, M. Couder, D. Winklehner, and A. Champagne, "The DIANA underground accelerator facility project at DUSEL laboratory," in *11th Symposium on Nuclei in the Cosmos, NIC XI, Heidelberg, Germany*, Proceedings of Science, 2010.

[126] D. Leitner, M. Leitner, D. Winklehner, A. Hodgkinson, A. Lemut, J. Saba, M. Couder, and M. Wiescher, "DIANA, a next generation deep underground accelerator facility," in *Proceedings of 2011 Particle Accelerator Conference, New York, NY, USA*, 2011.

[127] A. Lemut, M. Couder, D. Winklehner, U. Greife, A. Hodgkinson, D. Leitner, M. Leitner, J. Saba, P. Vetter, W. Waldron, *et al.*, "Design of a 400 kV deep underground, high detector efficiency, high target density, high beam intensity accelerator facility," *Physical Review Special Topics-Accelerators and Beams*, vol. 14, no. 10, p. 100101, 2011.

[128] M. Wiescher, F. Käppeler, and K. Langanke, "Critical reactions in contemporary nuclear astrophysics," *Annual Review of Astronomy and Astrophysics*, vol. 50, pp. 165–210, 2012.

[129] C. Broggini, D. Bemmerer, A. Guglielmetti, and R. Menegazzo, "Luna: nuclear astrophysics deep underground," *arXiv preprint arXiv:1010.4165*, 2010.

[130] NEC, "NEC National Electrostatics Corp." `http://www.pelletron.com/`, Accessed: February 2013.

[131] R. J. van de Graaff, J. G. Trump, and W. W. Buechner, "Electrostatic generators for the acceleration of charged particles," *Reports on Progress in Physics*, vol. 11, no. 1, p. 1, 1947.

[132] P. Sortais, M. Bisch, P. Bricault, P. Lehérissier, M. Lewitowicz, R. Leroy, C. Liang, J. Pacquet, P. Paris, J. Putaux, *et al.*, "NANOGAN: An ultra compact ECRIS for online and high voltage applications, kvi report 996," in *Proceedings of the 11th ECRIS Workshop, Groningen*, p. 97, 1993.

[133] A. Villari, "ECR development for accelerated radioactive ion beams," *Nuclear Instruments and Methods in Physics Research Section B: Beam Interactions with Materials and Atoms*, vol. 126, no. 1, pp. 35–44, 1997.

[134] M. Menzel and H. Stokes, "Users guide for the POISSON/SUPERFISH group of codes," tech. rep., Los Alamos National Lab., NM (United States), 1987.

[135] J. Billen and L. Young, "Poisson/superfish on pc compatibles," in *Particle Accelerator Conference, 1993., Proceedings of the 1993*, pp. 790–792, IEEE, 1993.